3D multi-scale characterization and modelling of damage in ceramic matrix composites



A thesis submitted for the degree of

Doctor of Philosophy

Shixiang Zhao

Trinity College

University of Oxford

Michaelmas term 2018

3D multi-scale characterization and modelling of damage in ceramic matrix composites

Shixiang Zhao, D.Phil Thesis

Trinity college, Michaelmas term 2018

Abstract

The SiC/SiC composite has been proposed as a candidate material for the fuel cladding component in advanced nuclear reactors. The present thesis aims to characterize the damage evolution within a SiC/SiC composite in different conditions and then validate a multiscale damage model. In order to gain insight into the damage mechanisms, *in situ* experimental methods are required to detect damage development and quantify the mechanical response at different scale to support the reliability assessment and simulation modelling of the components.

In this thesis, *in situ* 3D laboratory and synchrotron X-ray computed tomography and quantitative digital volume correlation have been applied to characterize the damage evolution in a SiC/SiC composite, with respect to its heterogeneous microstructure and macroscale mechanical response. The quantified information from tomography further helps the development of an advanced multiscale model with the microstructure sensitivity. Experimental methods for the direct *in situ* observation of damage have been developed for SiC/SiC C-ring specimens at both room temperature and elevated temperature. The time-resolved tomography allows the continuous observation of the damage within the heterogenous microstructure and the macroscale deformation. The development of the damage in the composite depends on the loading history, and the high temperature (900°C) in air degenerates the mechanical properties of the SiC/SiC composite as shown in the observations of the crack paths. The hoop pressurization test of the SiC/SiC composite tube via an expanding plug revealed the distribution of the matrix cracks at both the interior and outer surfaces of tube sample for the first time. The full-field multiscale *in situ* observation quantifies the non-uniform deformation of the composite tube under internal pressure with the corresponding strain measurement. It also allows a more accurate experimental measurement of the mechanical response in the composite tube component. Damage simulations have been performed in the finite-element microstructure meshfree (FEMME) model. The 3D experimental observation provided the statistical description of the microstructure for the model. The virtual damage simulated by the FEMME model is compared with the experimental observations in both the C-ring and hoop pressurization tests. The capability of the microstructure sensitive model has been demonstrated with a high fidelity of the simulated damage evolution and mechanical response in the composite. This coupled experimental and simulation studies could provide a more comprehensive understanding of the damage mechanisms in the SiC/SiC composite.

Acknowledgments

First and foremost, I would like to thank my supervisor Prof. T. James Marrow for the guidance and support throughout my DPhil study. His comments and suggestions are truly invaluable. His passion for science has always been inspiring for me. I feel very lucky to be one of his students. I am also grateful to have Dr. Luis Saucedo-Mora for the help in the simulation work. I would also like to thank my collaborators Dr. Biao Cai and Prof. Peter Lee for making the high temperature experiment possible.

I also appreciate all of the Marrow's group members for giving me a great working expereince for the passed four years. I couldn't ask for more than what I have. I would like to express my special thanks to Matthew Jordan and Dr. Selim Barhli for the training and help at the beginning of my DPhil, Phil Earp and Liye Yan for helping me go through the synchrotron experiments. Certainly, the great time when 'team crack' was out for drinking, playing, hiking, cycling and surfing would stay in my memory for good.

The work in this thesis cannot be done without the assistance from the beamline scientists, Dr. Thomas Connolley and Dr. Christina Reinhard, on I12 in the Dimond Light Source (UK). Their overnight help is sincerely appreciated. Furthermore, I thank all the MFFP group members in Oxford for the valuable discussion I have on each Friday morning, where I learnt a lot about nuclear materials.

I would also like to thank all other friends I have in Oxford over my four-year study: Jing and Hang are always supportive and are indeed mentors to me. Yang and Xue provided a lot of amazing food while I missed Chinese food. There were also so many enjoyable memories with Xiangwen, Hongjia, Xixi, Rui, Yakun, Qifeng and Diana… I also thank my friends in the TCBC. The beautiful time we had on the ISIS river is the best refreshment on every early morning.

My deepest gratitude goes to my parents. I am sorry for not being along with you two for many years while I have been aboard, but you are always being trusting, supporting and loving me. No words can fully express my gratitude.

Acronyms

light water reactors (LWRs)

gas-cooled fast reactor (GFR)

lead-cooled fast reactor (LFR)

very-high-temperature reactor (VHTR)

molten salt reactor (MSR)

sodium-cooled fast reactor (SFR)

supercritical water reactor (SCWR)

oxide dispersion strengthened (ODS)

digital volume correlation (DVC)

computed tomography (CT)

ceramic matrix composite (CMC)

acoustic emission (AE)

pyrocarbon (PyC)

proportional limit stress (PLS)

microstructure-based meshfree (MAM) model

Finite Element Microstructure Meshfree (FEMME) model

cellular automata (CA)

Contents

Abstract I
Acknowledgments II
Acronyms III
Chapter 1. Introduction 1
1.1 Overview 1
1.2 Engineering background 2
1.3 Objectives 5
1.4 Thesis structure 6
Chapter 2. Literature review 8
2.1 SiC/SiC composite materials 8
2.1.1. Material Elements 8
Fibres and architecture 9
Interphases 12
Matrix 13
2.1.2. Processing 14
2.2 Mechanical behaviours and damage in the composite 15
2.2.1 Microscale damage phenomena 15
2.2.2 Minicomposite Testing 17
2.2.3 2D woven composites 19
2.3 *In situ* experimental methods for damage characterization 21
2.3.1 Acoustic Emission 22
2.3.2 Surface imaging 23
2.3.3 X-ray computed tomography 24
2.3.4 Digital volume correlation 28
2.4 Concluding remarks 33
Chapter 3. Multiscale quantitative characterization of the SiC/SiC composite structure by X-ray tomography 34
3.1. Introduction 34
3.2. Materials and methods 34
3.2.1. Materials 34
3.2.2. X-ray computed tomography 35
3.2.3. Coordinate systems 37
3.2.4. Unwrapping code 38

3.3. Results 40
3.3.1. Multiscale tomographic study 40
3.3.2. Fibre braid structure in the composite tube 42
3.3.3. Porosity analysis 44
3.4. Discussion 52
3.5. Concluding remarks 55
Chapter 4. *In situ* synchrotron X-ray studies of C-ring diametral compression 56
4.1. Introduction 56
4.2. Materials and methods 58
4.2.1. Materials 58
4.2.2. Experimental setups 59
4.2.2.1. Static scan *in situ* diametric C-ring experiment 59
4.2.2.2. Continuous (time-resolved) scan of a diametric C-ring (room temperature) 62
4.2.2.3. Continuous (time-resolved) scan of a diametric C-ring (High Temperature) 67
4.2.2.4. Loading state of the C-ring. 71
4.3. Results 73
4.3.1. Overall observation 73
4.3.1.1. Static scan with cycling loading 73
4.3.1.2. Continuous scan under monotonic loading (Room Temperature) 78
4.3.1.3. Continuous scan at high temperature 87
4.3.2. Digital volume correlation analysis 91
4.3.2.1. Static scan with cycling loading 91
4.3.2.2. Continuous scan with monotonic loading 97
4.3.2.3. Continuous scan at high temperature 100
4.3.3. Bulk deformation 102
4.3.4. Localized strain distribution 105
4.3.5. Elastic properties 106
4.4. Discussion 108
4.4.1. Elastic properties 108
4.4.2. Matrix cracks 110
4.4.3. Deformation behaviour and damage observation 111
4.4.4. Cycling loading and monotonic loading 113
4.4.5. High temperature properties 114
4.5. Conclusions 116
Chapter 5. *In situ* synchrotron study of hoop pressurization tests 118

5.1 Introduction 118
5.2 Materials and Methods 119
5.2.1 Materials and Mechanical Experiment Setup 119
5.2.2 Synchrotron X-Ray Tomography 122
5.2.3 Strain measurement by Digital Volume Correlation 124
5.3 Results 125
5.3.1 Fracture of the SiC/SiC composite 125
5.3.2 General observation from the tomography with quantitative crack analysis 127
5.3.3 Microscale damage evolution 132
5.3.4 Quantitative study of the deformation 138
5.3.4.1 Coordinate system conversion and rigid body movement 138
5.3.4.2 Macroscale deformation 141
5.3.4.3 Displacement field and hoop strain measurement 144
5.3.5 Non-linear stress-strain behaviour 149
5.4 Discussion 151
5.4.1 Anisotropic deformation behaviour 151
5.4.2 Damage evolution 155
5.5 Conclusions 160
Chapter 6. 3D multiscale microstructure-based modelling of the fracture behaviour in nuclear graded SiC/SiC composite 161
6.1 Introduction 161
6.2 Structure of the FEMME model 165
6.3 Image-informed reproduction of the SiC-SiC composite microstructure in the FEMME model 170
6.4 C-ring Case Studies 182
6.5 Internal Pressurization Case Study 192
6.6 Discussion 196
6.7 Conclusion 199
Chapter 7. Conclusions and future work 201
7.1 Conclusions 201
7.2 Suggestions for future work 202
Bibliography 204

Chapter 1. Introduction

1.1 Overview

A rapid development focusing on the fabrication of the SiC/SiC composites for advanced nuclear reactors has been witnessed over the recent decades among several international collaboration programs, in Japan *(JAERI* and *Kyoto University*) [1]–[3], Korea (*Korea Atomic Energy Research Institute*) [4], [5], EU (*European Framework Program*) [6], [7] and USA(*General Atomics* and *Oak Ridge National Laboratory*)[8], [9]. The research in this thesis is driven from the European Energy Research Alliance Joint Program on Nuclear Materials, within the MatISSE European Commission project (Materials' Innovations for a Safe and Sustainable nuclear in Europe) [10]. A general objective of this research is to characterize the mechanical damage development in a SiC/SiC composite that is proposed for the nuclear fuel cladding. The project aimed to observe when and where the damage initiates; investigate the influence of the microstructure and the effect of loading conditions, such as tensile and hoop stress, on the damage development. Innovative methods have been developed using high-resolution X-ray tomography to monitor the mechanical tests *in situ* with strain mapping by digital volume correlation, which aimed to provide the vital information on the critical strain at which the damage starts to occur and how the microstructure affects the damage development. Such data can provide essential information including the internal porosity, fibre weaves and their interaction with the damage, which have been utilized and verified in an advanced microstructure-sensitive modelling. Such simulations to reliably predict damage are needed for the composite design.

1.2 Engineering background

Currently the dominating type of the civil fission nuclear reactors in operation throughout the world is the Generation II light water reactors (LWRs) [11]. The popularity of LWRs is also expected to continue for at least in the 21st century as most commercial nuclear reactors in construction or planning are also LWRs (Gen III type) [12]. The next Gen IV reactors are still in the conceptual stage with six main reactor systems and the aim for installation is in around 2040 [6], [13]. The Gen IV reactors are designed for a safer, cleaner and more efficient use of the nuclear fuel [14]. The fuel burn-up is improved by increasing the operating temperature with higher neutron fluence. For example, the typical operating temperatures and the effective irradiation damage for different Gen IV systems and current Gen II reactors are shown in figure 1.1 [15]. This demonstrates a clear trend of a more extreme environment in the new generation reactors.

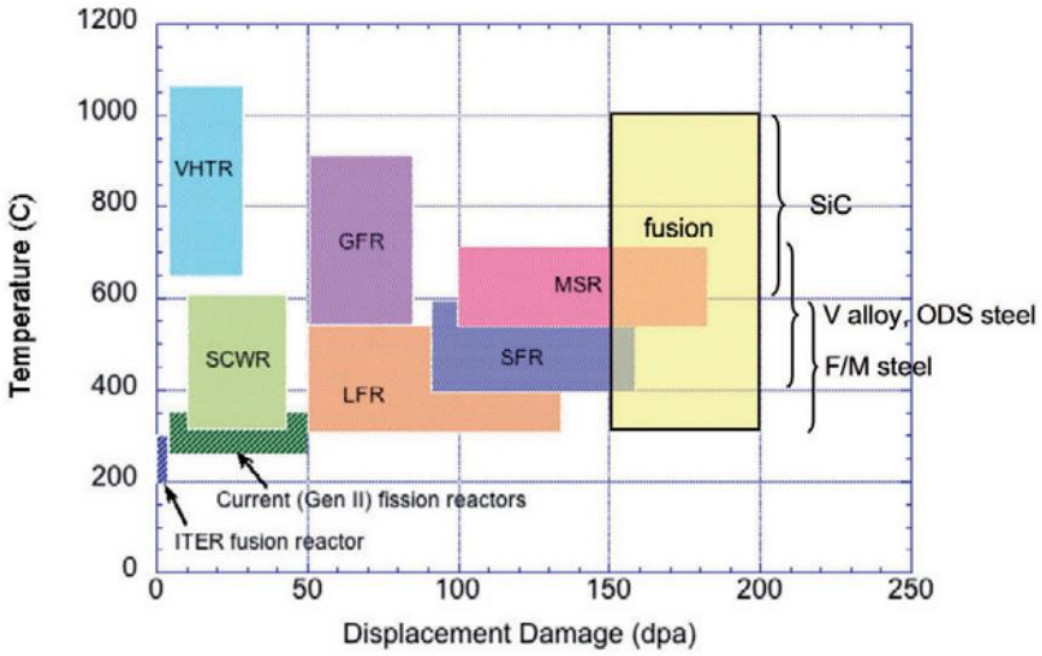


Figure 1.1: The required operating temperature and displacement damage dose regimes for structure materials in different advanced reactor systems and current Gen II rectors. [15], [16]

The designed operation environment determines the options of the structural materials. The fuel cladding is one of the most critical components in the fission reactor (figure 1.2). Currently, all the commercial LWRs are using a Zirconium alloy fuel cladding. The more demanding constraints require a further development in the cladding materials. Those include a low effective neutron cross section absorption; an outstanding radiation damage resistance; improved corrosion resistance in service; and acceptable mechanical properties at a higher operating temperature. The selection of the fuel cladding materials also needs to consider their performance during normal and accident conditions.

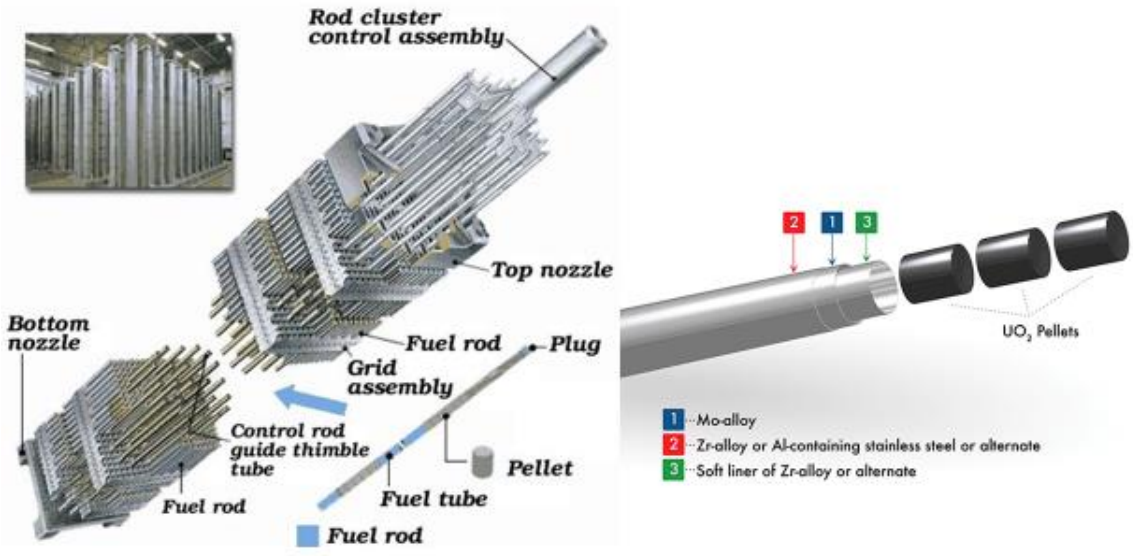


Figure 1.2: The typical fuel assembly system a LWR nuclear reactor and the structural of the fuel cladding tube[17], [18]

The current Zr alloys have served as the fuel cladding for over 50 years [12]. A great development in the alloy design and processing of the Zr alloys has also been witnessed. However, its maximum service temperature is still limited at around 400°C [11]. The Gen IV reactors generally aim for an

operation temperature higher than 500°C [19]. For example, in the conceptual gas-cooled fast reactor (GFR), lead-cooled fast reactor (LFR) and very-high-temperature reactor (VHTR), the potential cladding materials will experience a temperature above 850°C in normal operation [13]. Therefore, the Zr alloys will be replaced with an alternative. Among all the potential materials for the fuel cladding, the SiC-based materials are considered as a primary candidate [11], [19] due to SiC's excellent properties in thermal and radioactive environments. Besides, it has around 25% lower absorption of neutrons compared to Zr alloys with a similar geometry [12], which can provide a better nuclear fuel efficiency.

The Fukushima accident in 2011 drew serious issues concerning the safety of the fuel cladding in the current LWRs. This leads to the concept of an accident-tolerant fuel (ATF) system in both current and future fission reactors where the cladding should be capable of enduring a much longer allowable time in the loss of coolant accident (LOCA) [20], [21]. For example, in GFRs, the accident condition is designed to be over 1600°C [11], [22]. However, other candidate materials such as steel melt at 1450°C. A typical Zr alloy has a melting point at around 1850°C but it reacts violently with steam and generates hydrogen gas [12]. However, this is no serous reaction between the steam and SiC ceramics. Therefore, the SiC-based composites are also expected to substitute Zr alloys in a ATF cladding as well as SiC-based composites can retain their strength and corrosion resistance (without the generation of the gaseous hydrogen) at elevated temperature [23].

The remarkable advance of SiC-based composites in nuclear fission applications has benefited from the previous international fusion research programs where they found application in the breeder blanket [3], [6], [7], [24] and also the development of SiC fibres [25] for high temperature structural applications in the aerospace industry [26]. Other applications in the fission rectors such as guide tubes and channel boxes in the fuel assembly have also been reported [4], [27]. The types

of the application will determine geometry of the prototype component. In this project and within the European nuclear fission programme, a tubular pin-type GFR fuel cladding geometry has been designed [6], [22] with essentially the same geometry proposed for the ATF cladding in the LWRs [8].

1.3 Objectives

Even though SiC/SiC has been used for high temperature structural applications [26], a reliable application of SiC/SiC composites in nuclear fuel cladding still need some efforts. It requires a better understanding of its component properties. Those include gas tightness, mechanical properties and thermal properties. Among those properties, a fundamental understanding of its mechanical behaviour, especially the damage behaviour, is mandatory to ensure the structural integrity of the critical components made of SiC/SiC composites.

The purpose of this research is to characterize the damage evolution in a nuclear grade SiC/SiC composite. This includes when (real time macroscale stress and strain curve) and where (microstructure, stress state) the crack initiates; the influence of the microstructure and the loading conditions on the initiation, propagation and accumulation. The thesis aims to facilitate the understanding of the damage mechanisms in the SiC/SiC composite by providing direct experimental evidence using novel methods. Additionally, the quantified results offer an experiment benchmark for the theoretical models. Specifically, the objectives of the project are to offer

- feasibility evaluation of using high-resolution X-ray tomography during the mechanical tests with the strain mapping by the image correlation for damage characterization;

- macroscale stress/strain behaviour of SiC/SiC composite cladding with damage evolution under different loading condition;
- the characterization of the cladding properties at high temperature;
- quantified foundations for the microstructure-based modelling of the damage in composite with the input and validation from the characterization results.

1.4 Thesis structure

The thesis structure is organized as follows: Chapter 2 provides the theoretical background of the SiC/SiC composite materials and researches on the mechanical behaviour of the composite will be reviewed. It then describes development of the experimental methods regarding the *in situ* characterization of damage in the composite. The background of the X-ray tomography and the use of the digital image correlation method will then be introduced. Chapter 3 describes the use of laboratory X-ray tomography to characterize the microstructure of the SiC/SiC composite, with the emphasis on the porosity and fibre tow structure to provide a benchmark study for the subsequent *in situ* synchrotron experiments and microstructure sensitive modelling. In Chapter 4, a series of *in situ* mechanical tests have been developed in the C-ring geometry from the composite tube. A time-resolved study is presented which allows the continuous observation of the damage in the composite at both room temperature and high temperature. Chapter 5 describes a study of the mechanical responses of the composite tube under internal pressure that includes the quantified study of damage and deformation at both macroscale and microscale. In Chapter 6, the microstructure information from the previous experimental characterization is applied in advanced microstructure modelling. The virtual simulation results are then presented in comparison with the

previous *in situ* experimental observations. Chapter 7 summarizes the conclusion remarks of the studies in this thesis and point out the potential future work.

Chapter 2. Literature review

2.1 SiC/SiC composite materials

Since the work done by Rovner and Hopkins back in the 1970s [28], silicon carbide (SiC) has been proposed for nuclear applications due to many attractive properties [28], [29]. As a ceramic, the high-purity chemical vapour deposited SiC can maintain its strength up to around 1500°C under an irradiation dose of 18.7 dpa [29]. However, the monolithic SiC is brittle, which limits its application in engineering components. The combination of SiC-fibre and SiC matrix offers non-linear deformation and improved toughness [30], [31]. The relatively high toughness was found by introducing an engineered bonding between the fibre and the matrix, which is termed an "interphase" [32]–[35]. The current nuclear-grade SiC/SiC composites consist of near-stoichiometric and crystalline beta-phase SiC for both fibres and matrix and a small amount of interphase layer(s) between the fibres and the matrix. Each element will be introduced. Then, the processing techniques will be briefly described.

2.1.1. Material Elements

Ceramic Matrix Composites (CMCs) are normally designed to serve in severe environments, such as high temperature engines and nuclear reactors. To meet the specific requirement at elevated temperature and/or in strong irradiation, CMC composites are deliberately designed in the aspect of the fibres, the interphase and the matrix. Each element exhibits its own properties. The fibres and the interphase dominate the mechanical properties. The interphase controls the toughness of the composites.

Fibres and architecture

The fibre is the major load bearing element in the continuous fibre CMCs. Its architecture is also an important designing factor. In the 1980s, the advance in the processing technology enabled the production of fine SiC fibres with a diameter to around 10 μm, which opened its potential in many applications [36]. Since then, a remarkable advance in processing the SiC fibre has been witnessed in the recent decades, which can be highlighted by the three generations of the SiC fibres as shown in the figure 2.1. Table 2.1 also summarized some key properties of different types of commercially available SiC fibres.

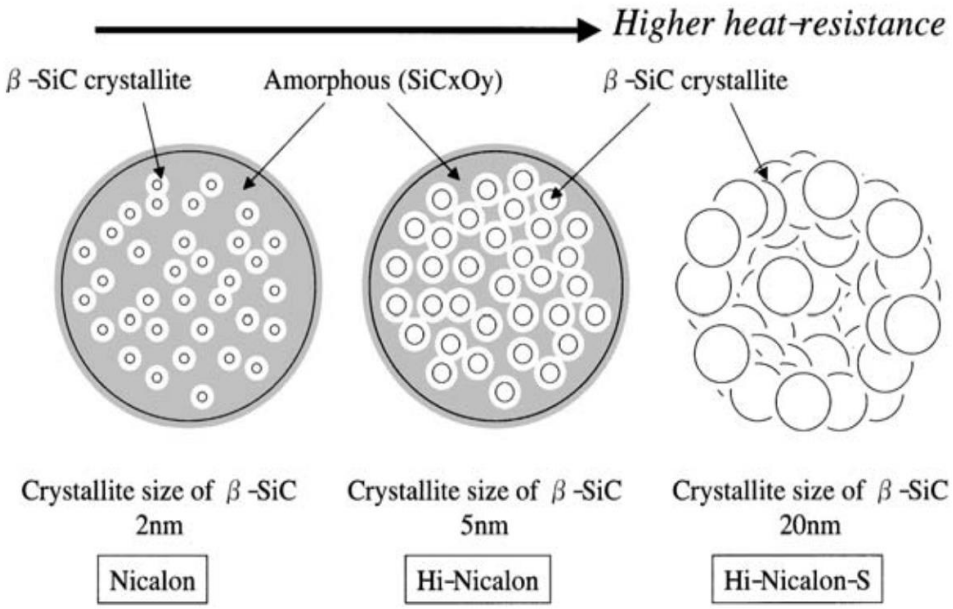


Figure 2.1: The general microstructure of the three generation fibres [36].

Table 2.1: properties of some commercial SiC fibres in three generations [27], [37]

SiC fibre generation	Trade name	C/Si atomic ratio	Elastic modulus RT (GPa)	Tensile strength RT (GPa)	Elongation (%)	Approximate max. production temperature
Gen I	CG-Nicalon 202	1.31	220	3.0	1.4	1200°C
Gen II	Hi-Nicalon	1.39	270	2.8	1.0	1300°C
Gen III	Hi-Nicalon Type S	1.05	420	2.6	0.6	>1500°C
	Tyranno SA	1.07	380	2.8	0.7	>1700°C
	Sylramic	1.00	380	3.2	0.8	>1700°C
(CVD SiC)	Pure β-SiC	1.00	450	~0.4	~0.1	

The impurities such as carbon and oxygen in the first and second generations of SiC fibres limited their use in the nuclear industry as it suffered from a noticeable volume change under the irradiation [38]. The SiC fibres of third generation (Gen III), e.g. Hi-Nicalon Type S *(Nippon Carbon)*, Tyranno SA *(Ube industries)* and Sylramic *(Dow Chemical)*, eliminate the oxygen and contain only the high pure quasi-stoichiometric crystallite β-SiC. The Gen III fibres exhibit a higher Young's modulus, ~400 GPa that is close to the pure SiC. They also demonstrate exceptional heat resistance up to nearly 2000°C as well as the best dimensional stability under irradiation due to its oxygen-free and stoichiometric character [36], [38]. The relatively large β-SiC grain size in the Gen III fibres is also beneficial, which gives a less smooth fibre surface that will influence the later interphase bonding and friction [27]. It is obvious that development in the microstructure improves the mechanical properties and irradiation resistance. Therefore, even though the Gen III fibres are expensive, currently the fibres proposed for Nuclear application are mainly the third generation fibres, due to their substantially improved properties [3], [38]–[40]. In this study the composite was made from the Gen III Hi-Nicalon type S fibres.

Given the fact that a certain type of fibre is chosen, the composite's properties are also controlled by the fibre tow architecture. Some typical fibre architectures is shown in the figure 2.2. Each fibre tow normally consists of a group of hundreds of single filaments [41]. The types of the architecture have a noticeable effect on the mechanical properties, with the highest uniaxial strength in the unidirectional composites [27]. In nuclear grade composites, a two-dimensional (2D) woven architecture is often employed in a planar structure, commonly either by plain-weave or satin-weave [27]. Both of them offer similar composite properties, but for the tubular structure as in the fuel cladding component, a satin-weave with ± 45° or ± 30° stacking is more popular in the open literature [3], [27], [42], [43]. The three-dimensional (3D) braiding structure were also seen to tailor the anisotropic properties [44]. However, a 3D structure is more commonly found in thermostructural components [45], [46]. By contrast, it is less common to apply the 3D architecture in the nuclear tubular structure as the wall thickness is normally small compared with the tube diameter [27]. Thus, when comparing the similarity or difference in mechanical properties of the composites with same fibres, it is important to address their fibre tow architecture.

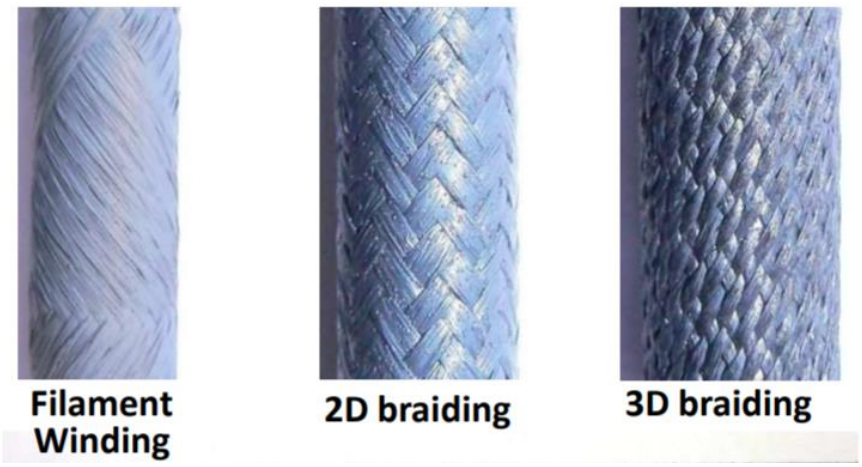


Figure 2.2: The typical fibre architectures in the tubular shape [47]

Interphases

The engineered interphase is an important thin film structure in SiC/SiC composite. Its structure is responsible for the non-brittle behaviour of the ceramic composite materials as the interphases can arrest, deflect and/or branch the cracks that initiated from the matrix [34], [48]. Additionally, the interphases can also inhibit the damage propagation by energy dissipation from friction force between the fibre and matrix. [26]. The bonding of the interphase should be both strong enough to provide the load transfer and weak enough to deflect the cracks within the interphase instead of directly from the matrix to the fibre.

For such purposes, in the SiC/SiC composites, pyrocarbon (PyC) and hexagonal boron nitride (BN) are the most two common interphase materials. The anisotropic PyC was claimed to be the best interphase material from a mechanical viewpoint by Naslain [49]. Meanwhile, BN offers better oxidation resistance at high temperature (over 500°C) [50], [51]. Furthermore, BN is not compatible with neutron irradiation as it will transform and generate helium [38]. Therefore, in nuclear applications PyC is more commonly used [3], [7], [38], [41], while BN has been found in high temperature components in the aerospace industry [45], [51], [52].

The interphase may exhibit a single layer or layers structure. A layered crystal structure (PyC, BN with SiC) or a layered microstructure ($(PyC\text{-}SiC)_n$, $(BN\text{-}SiC)_n$) has been considered as the best interphase [26], [32]. The structure of the interphase controls the crack deflection mechanisms, where the deflection of the crack within the interphase rather than fibre/interphase interface is preferable. Another important engineering parameter in the interphase structure is its thickness. The variation in the interphase thickness results in a difference in the fracture behaviour. The optimum thickness of a single layer carbon interphase was found out to be submicron [33], [35], [51]. Further, Katoh et al. suggested that the thickness of the PyC in SiC/SiC composites should

be as small as around 50 nm (the smallest in their study), which provides better short-time mechanical properties in the nuclear applications (with high strain rate) [53]. Moreover, considering the irradiation damage, the thickness of the PyC interphase should also be as small as possible to minimize dimension change in neutron irradiation environment [26]. The deposition of interphase achieved a thickness down to 1 nm decades ago [32], but a too thin interphase gives a too large debonding and friction stress that would lead to a brittle fracture [54].

Matrix

The matrix in a nuclear SiC/SiC composite protects the fibre and interphase from the oxidising environments. The beta-form of SiC gives good high temperature mechanical properties, excellent oxidation resistance up to 1500°C, excellent stability in irradiation environment, and high thermal conductivity [29], [38]. However, the monolithic matrix is normally the first constituent to crack under loading. A relatively low stress level (generally less than 100 MPa) could be enough to induce microcracks in the matrix [9], [26], [53], [55]. Although those microcracks could be stabilized by the interphase in the composites, significant matrix cracks will limit the mechanical properties such as stiffness. The network of matrix cracks also provides the diffusion channel for oxidation atmosphere to the interphase and potentially for the release of fission products in nuclear applications (i.e. hermeticity of fuel cladding).

Other important properties including thermal conductivity are also related to the matrix. The structure of the matrix is controlled by the processing method. Each processing routine yields a SiC/SiC composite with typical properties, which will be described in the following Section.

2.1.2. Processing

During manufacturing procedures, the fibre tows are first braided to form the layered fibrous preform [56]. In this study, regular braiding, where each yarn crosses over and below two yarns, of the fibre tows was used. Both braided [57]–[60] and filament wound [5], [21], [47] sublayers (figure 2.2) are commonly superimposed to form a preform in cladding applications. The fibrous preforms are then deposited with the PyC interphase and the SiC matrix via the Chemical Vapour Infiltration (CVI) process. The CVI method is widely employed in the nuclear application to produce a high purity polycrystalline microstructure [3], [61].

In this route, the fibrous preform is first either self-standing or supported by the designed tooling, e.g. a cylindric mandrel. Subsequently, the other constituents, interphases and matrix, are consecutively deposited on the fibre preform at a controlled high temperature (over ~1000°C) and under a reduced pressure or a near vacuum pressure [26], [62], [63]. Firstly, the pyrocarbon (PyC) was deposited on the fibre by the decomposition of a hydrocarbon precursor, typically propane (C_3H_8) or methane (CH_4), according to reaction 2.1[64]:

$$2C_xH_y\ (g) \rightarrow 2xC(s) + yH_2\ (g) \qquad 2.1$$

Then, the coated fibrous preform is densified with the SiC matrix by the decomposition of the gaseous phase process. The process consists of the deposition reaction of the precursor methyltrichlorosilane (MTS) in the gaseous hydrogen flow at a temperature over 1000°C, according to the equation. 2.2 [65].

$$CH_3SiCl_3(g) \xrightarrow{H_2\ (g)} SiC\ (s) + 3HCl\ (g) \qquad 2.2$$

The exact and detailed processing parameters of the processing were normally not reported for the industrialized products. However, a relatively low processing temperature is believed that can reduce the damage during processing by minimizing the residual stress after cooling [27].

The gaseous reaction in the CVI processes of the matrix yields a non-negligible residual porosity. As shown in the equation 2.2, the volume of the gaseous product is larger than that of the reactant. Thus, the new reactant gas phases must diffuse against the outflow of the products, which causes the porosity. The typical value of the residual porosity in the CVI-SiC/SiC composite produces is approximate 10 - 25% [26], [63], [64], [66], [67].

Another common process to produce dense SiC/SiC is the Melt Infiltration (MI) process [4], [26], [68], [69], during which the open pores are filled with liquid silicon (T_m=1410°C) that reacts with carbon at a temperature above 1500°C [4], [69]. Without the gaseous products, the residual porosity is normally negligible or less than 2% in MI-SiC/SiC products [49]. However, the inevitable residual silicon in the matrix limits the irradiation resistance. Therefore, such composites are commonly found in aero-engine applications [45], [46], [69].

2.2 Mechanical behaviours and damage in the composite

2.2.1 Microscale damage phenomena

Even though the monolithic ceramic is generally a brittle ceramic, the fracture toughness of the fibre reinforced ceramic composites is considerably improved. The toughness is generally determined by the energy required for the crack to propagate in a material. In the SiC/SiC composite, the improvement in the toughening is largely reliant on the interphase between the

matrix and fibres. Specifically, extra energy is required for crack propagation that imposed by the interphase and this originates from the fibre debonding and sliding energy.

The β-SiC matrix is normally the first constituent to crack, as the failure strain of the matrix is lower than that of the fibres [70], [71]. The matrix crack will eventually reach the coated fibres. The fibre coating, which is the weakly bonded interphase, can then deflect the crack along the interphase direction, causing the debonding of the interphase [55] as shown in figure 2.3. Besides, the interphase can also blunt the crack tip, which means a further increased energy required for the crack propagation.

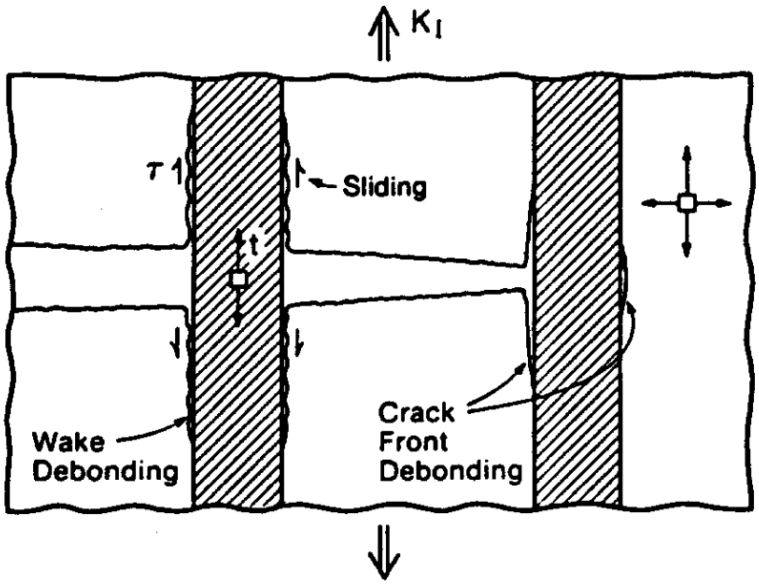


Fig. 2.3: Illustration of the initial debonding at the crack front and the wake debonding with the sliding interaction [55]

Additionally, due to the different degrees of deformation between the fibre and matrix, there is a sliding (friction) force. The sliding force contributes to the load transfer between the matrix and the fibre [55]. Meanwhile, a further increase in the stress leads to the propagation of the existing cracks and/or the fracture of the fibres. However, the fibre breakage is not necessarily in the matrix

crack plane. The fibre fracture is determined by the variation in the strength along the fibre, described as Weibull Modulus, due to the relative random distribution of the flaws in the ceramic material [72], [73].

This ‘out of plane’ fracture of the fibre leads to the main energy-absorbing mechanism in toughening of the fibrous composite, fibre pull-out [71], [74]. As shown in figure 2.4, the fractured fibre can still transfer its load to the matrix via the friction force at the interphase. The bridged fibres behind the crack tip causes a crack closure force against the crack opening. As the crack advances, extra dissipation energy is required to pull the fibres out of their sockets in the matrix.

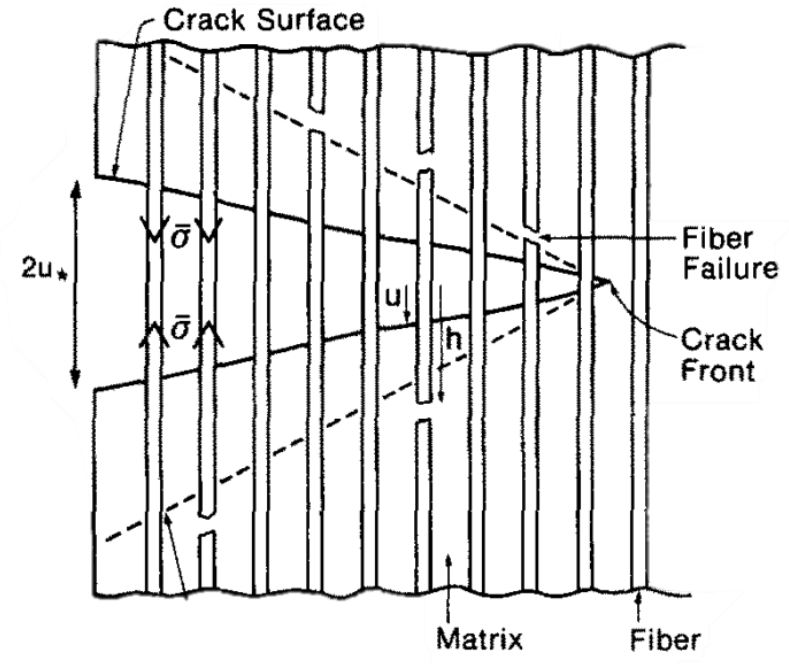


Fig. 2.4: A schematic illustrating fibre pull-out from the fractured fibres and the fibre bridging by the intact fibre [75]

2.2.2 Minicomposite Testing

The theoretical damage phenomena in the SiC/SiC were first studied in unidirectional minicomposites [41], [76], [77]. These minicomposites exhibit the same microstructure as a fibre

tow in the braided composites. Experimental damage observation of minicomposites at the microscale was previously studied *ex situ* or after the ultimate failure [76], [78]. The first comprehensive *in situ* investigation was carried out by Chateau et al. to characterize the damage in the matrix and fibres at the local scale [79], [80]. Their results were further confirmed in the 3D *in situ* study in a different SiC/SiC minicomposite by Bale et al. [81]. Those 3D *in situ* observations provided new insight of the damage evolution in matrix and fibre breakage in the minicomposite.

They found out that cracks generally initiated at the periphery of the minicomposite [79], [81]. The different cracks normally initiated at different position. The matrix cracks might grow into a main crack but most of them were observed to be isolated. The cracks were generally perpendicular to the tensile loading direction, with a spiral propagation kinetics [79]. The final matrix cracks could cross the whole minicomposite. Chateau et al. also reported the saturation of the matrix crack density at a global strain level of 0.3% in the minicomposite, which then failed at a global strain of ~ 0.7%. After the propagation of the matrix crack, the fibre breakage occurs [79]. Different fracture points might be found in one single fibre. They were generally homogeneously distributed with a preference to be near to the matrix cracks.

The interphase properties were normally measured separately. There have been several approaches proposed to quantify the debonding stress and sliding stress, including the direct displacement measurements and indirect methods. The direct displacement measurements use indentation on a single fibre, while the matrix is fixed at the other end [71], [82]–[84]. After linear elastic deformation, debonding occurs and then the fibre slides. The indirect methods involve the interpretation of the hysteresis loops with loading-unloading in the macroscopic stress-strain curve [27], [39]. The *in situ* damage observation of the interphase is very difficult due to its submicron

size. Bale et al. captured the interphase in an 3D X-ray tomographic study of the minicomposite [81]. However, it needs to mention that in their study, the interphase of the SiC/SiC minicomposite was as thick as 2 μm, which is much higher than what is normally found in SiC/SiC composites.

2.2.3 2D woven composites

Engineering components are normally made to meet their specific thermal/structural requirements as a textile SiC/SiC composite, which consists of fibre bundles [3], [23], [49]. In the nuclear industry and this study, 2D woven composites are commonly used [3]. Compared with the unidirectional minicomposite, there have been fewer theoretical and experimental studies about the microscale mechanical behaviours, especially the damage mechanisms, of braided fibres. Fibre braiding introduces more complexity due to the anisotropy and heterogeneity. To ensure the structure integrity of engineering applications, mechanical properties data are essential for engineering design. However, the reported studies have been normally focused on macroscale tests. Their key mechanical properties will be discussed in this section. Those properties include elasticity, proportional limit stress (PLS), and ultimate failure stress and strain.

Figure 2.5 shows the stress-strain evolutions of some 2D (0°/90°) CVI-SiC/SiC composites with common third generation SiC fibres in a 0° tensile loading given by Katoh et al. [85] and compared with the study by Nozawa et al. [53]. The elastic modulus was found to be within the range of 200-280 GPa [3], [27]. The tensile modulus could be predicted by the simple rule of mixture or the ply theory [86], [87]. This could explain the findings from Katoh et al. that an unusually high porosity lead to a low modulus value (HNL/PyC150-A in figure 2.5) [27]. Further, anisotropy of the modulus has shown in their study such that the minimal modulus at the ±45° orientation is about 15% lower than that in the major fibre direction (0°/90°) [27], [88]. However, the elastic modulus

seem to be unaffected by the loading states in many studies where the modulus for tension and compression were very similar before the non-linearity [43], [88].

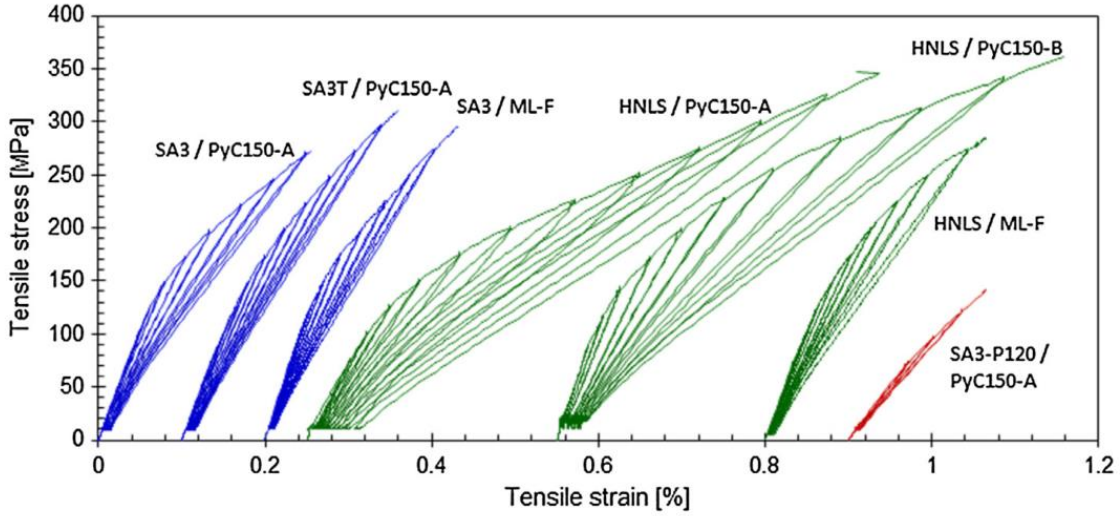


Fig. 2.5: Representative stress-strain curve during the tensile testing in some typical SiC/SiC composites with Gen III fibres [27]

The proportional limit stress (PLS) is the first non-linearity in the stress-strain curve that is associated with the development of the matrix microcracks. The typical PLS value of a 2D CVI-composite falls in the range of 100-150 MPa in the major axial tensile tests [3], [27], [38], [89]. The variation in the ceramic strength leads to a scattering in the values of PLS, which is also influenced by the composite microstructure and testing methods [9]. Nozawa et al. argued that the highest PLS is in the major fibre direction (116±16 MPa at 0°/90°), but the difference compared with off-axial strength is relatively small (112±16 MPa at 45°) [88]. Katoh et al. suggested the high mass density (low porosity) might attribute to an increased tensile PLS [27], which agreed with the interrupted observation of the matrix cracks associated with the large pores slightly above the PLS in Zhu et al.'s study [90]. The study by Droillard et al. demonstrated a 30% increase in PLS in 2D composites by adopting a stronger interphase [51]. The comprehensive study of

multiaxial testing on a tubular composite by Bernachy-Barbe showed the PLS is also controlled by the loading state [43]. Similar results were reported in [88], where the highest PLS was found in compression.

The ultimate failure state indicates what the composite can withstand beyond which the composite components losts most of its strength and shape. The tensile strength (UTS) is normally the highest point in the stress-strain curve (as in figure 2.5) [27]. The typical value of UTS in a 2D CVI-SiC/SiC under tensile tests generally lay in the range of 250-350 MPa [27], [35], [91]. It is worth noticing that the composites not necessarily have zero strength immediately after the matrix cracking or fibre failure as the broken fibres can be held by the interphase sliding force [92]. Therefore, the point of ultimate tensile strength is an important engineering design parameter but its correlation with the microstructure damage requires further study. There have been extensive studies on microscale damages based on the fractography after the failure [60], [77], [90]. A few studies tried to observe the damage *in situ* utilizing the surface technology [43], [93]. Other attempts include the loading-unloading hysteresis loop to indirect measure the damage in the interphase (as in the figure 2.5) [27]. However, generally, the damage mechanisms are poorly known in the 2D composite, and so to obtain new insights of the damage evolution an advanced method is needed.

2.3 *In situ* experimental methods for damage characterization

To understand the microscale damage phenomena corresponding to the macroscale response, several non-destructive evaluation methods have been used to study damage development in SiC/SiC composites. The common methods in the literature include acoustic emission, surface imaging and x-ray computed tomography (XCT). In this study, *in situ* X-ray tomographic

observation of the damage for the composite will be used, which is a capable tool offering 3D visualisation of the microstructure with the macroscale behaviour. In this section, the other commonly used methods will be briefly described. Then XCT will be introduced in more detail.

2.3.1 Acoustic Emission

Acoustic emission (AE) can be used to investigate the damage evolution during mechanical tests. In principle, the damage releases strain energy in the material which generates characteristic stress waves, known as acoustic emissions [94]. Those are recorded by AE piezoelectric sensors (transducers) which are surface mounted on the material to convert the emissions into electric signals [95]. The signals describe an acoustic event by its maximum amplitude, duration, counts, energy etc. The rate and intensity of the AE signals may indicate the initiation or propagation of damage in the materials [96], [97]. Due to its simplicity and low cost, AE has been widely used to study the damage mechanism in the SiC/SiC composite. For instance, Shiwa et al.'s study showed the different acoustic events with characteristic AE amplitude distributions to indicate the matrix cracking, interphase debonding and fibre damages in tensile tests of a 2D CVI-SiC/SiC woven composite [96].

The AE method offers *in situ* global damage information along the gauge length. Multiple sensors could provide the location of the damage onset in the component with a simple geometry [98]. However, while the accuracy of the damage detection in AE is generally robust, it is affected by background noise. Moreover, the similar elementary constituents (fibre and matrix) in the SiC/SiC composite make the accurate differentiation difficult. Therefore, the AE technique is normally combined with other *in situ* surface observation to provide more complementary information [43], [60], [99].

2.3.2 Surface imaging

Surface imaging techniques could provide direct observation of damage initiation and development in the composites. The common methods utilize optical illumination or electrons (scanning electron microscope, SEM). The accuracy is predominantly determined by the resolution of the obtained digital images and the field of view (FOV) that is related to the detector. The resolution or pixel size in the images determines the capability of the damage characterization, while the FOV controls the monitored area. The FOV should be large enough to capture a representative area of the microstructure in ceramic composites.

The interpretation of the images involves processing of the digital images. The damage normally gives a feature with distinct contrast compared with the material background, which exhibits a discontinuity in the grey level in digital images. Apart from the manual selection of the damage characteristics, the smaller damage features can be quantified by image correlation [43], [100]. A series of images may be captured at the same location. Using a series of *in situ* images, correlation can be made to quantify the full-field displacement at the observed surface. This method is called digital image correlation (DIC).

Optical imaging coupled with DIC has been widely used with conventional macroscale tests to provide extra information about localized heterogenous deformation. In the case of SiC/SiC composites, Rajan et al. demonstrated the capability of this technique in the use of 2D woven SiC/SiC composite that revealed the strain distribution at the sub-tow sale [101]. Bernachy-Barbe et al. used this method to demonstrated the matrix cracking orientation that is relevant to different loading conditions [57]. In their further study, they proposed fibre tow reorientation mechanisms based on their observations [43]. However, there is a physical resolution limit in the optical images. Thus, the observation of the damage at microscale can be difficult. Some studies used scanning

electron microscopy (SEM) techniques to resolve the microscale information [79], [100]. In a multiscale characterization study of damage presented by Tracy [100], microscale *in situ* mechanical tests were performed in an SEM, where the damage evolution at the interphase was observed. Nevertheless, even though the SEM provides quite precise observations, the FOV is generally small (typically 500µm to show all the elementary material constituents). Several observations or stitched images might be required to make the observation representative of the composite.

In SiC/SiC composites, surface observation provides an important tool for damage observation. However, surface observation is not representative enough of the bulk damage evolution as the composite structure is highly heterogeneous. This has been demonstrated in the 3D minicomposite studies [79], [81]. To thoroughly understand the damage mechanisms in the woven composite, a 3D characterization of the damage with respect to its microstructure is essential. X-ray computed tomography, which offers high resolution 3D characterization, is therefore well suited and will be used in this study.

2.3.3 X-ray computed tomography

X-ray computed tomography (XCT) is a non-destructive technique that allows the 3D visualization of the sample's internal structure. It utilizes numerical computation to reconstruct a series of slices through the object from the systematic set of X-ray radiographs obtained at different viewing angles. This technique has two steps, acquisition of the radiographs and reconstruction of the 3D images. The principles of radiographs from X-ray illumination will first be described.

X-rays from a radiation sources interact with the object and are then collected by the detecting system. X-ray sources can be lab-based (X-ray tubes) or synchrotron. The majority of the current tomography uses the electrical X-ray source where accelerated electrons strike a metal target to

produce X-ray photons [102]. Lab-based sources give a fan or cone-shape X-ray beam while the synchrotron source provides a parallel beam as illustrated in the figure 2.6.

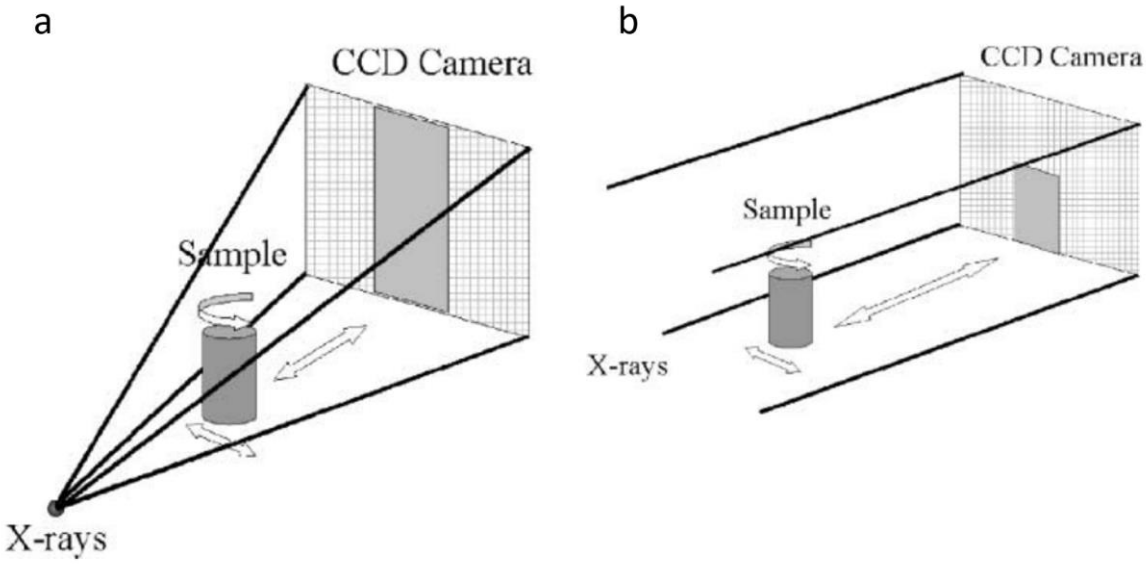


Figure 2.6: The principles of the (a) lab-based X-ray sources with a cone-beam geometry and (b) the synchrotron source with a parallel X-ray beam. [103]

The X-ray flux then interacts with the object when it travels through where the attenuation of its intensity occurs. The attenuation of the X-ray can be caused by any process that involves scattering or absorption of the incident X-ray [104]. The intensity decreases of a monoenergetic (monochromic) incident X-ray can be mathematically expressed in Beer-Lambert Law, and is proportional to the object's thickness (x):

$$\frac{dI}{I} = -\mu dx \qquad 2.3$$

where I is the intensity of the incident X-ray and μ is a material (atomic number and density) dependent linear absorption coefficient. The integration of equation 2.3 can lead to the description of a penetration though a heterogenous material:

$$I = I_o e^{-\int \mu(s) ds} \qquad 2.4$$

where $\mu(s)$ is the linear absorption coefficient at the point s and I_o and I are the intensities of the original and transmitted X-ray.

X-ray computed tomography (XCT) collects the transmitted X-ray on the detector, which provides radiographs or 'projections'. A number of radiographs are then collected as the sample is rotate to different angular positions. Eventually, the reconstruction process generates the virtual slices from those radiographs, such as via the back-projection method. Thus, the 3D image of the object is obtained that describes the spatial heterogeneity of the local absorption coefficient. The standard acquisition mode of the radiographs is the absorption mode, which based on equation 2.4. The contrast, expressed as the grey level in the images, is essentially the distribution of the linear absorption coefficient in the object. Other contrast mechanisms in materials science include the phase contrast mode and holographic mode [103], [105]. The phase contrast mode is acquired with a larger sample-detector distance. The enhanced contrast comes from the interference at the phase interphases, which highlighted the interphases but may raise difficulties in the quantitative analysis. The holographic mode requires several scans at different sample-detector distances, which allows the observation of the low absorption phases in the materials with a special reconstruction algorithm [79], [105]. In the current study, the standard absorption mode will be used with lab and synchrotron X-ray sources.

The XCT technique can be divided into two groups based on the source system, the laboratory XCT and the synchrotron XCT [106]. The laboratory X-ray emitted from the metallic tube generates a divergent cone-beam while a parallel beam is provided in the synchrotron source, as shown in figure 2.5. The synchrotron X-ray offers a number of advantages [103], [107]:

- A high flux X-ray (at least 1000 times larger than the lab X-ray tubes) that makes a short exposure time possible with a higher signal-to-noise ratio;
- The high energy monochromatic beam is available with a monochromator;
- The parallel, coherent X-ray that could minimize some geometric and beam hardening artefacts;
- The proportion of the X-ray photons illuminating the detector is practically unaffected by the sample-detector distance.
- Large experimental hutches [108] normally in the synchrotron make it possible to perform the *in situ* experiments in complex thermal and/or mechanical sample environments.

Laboratory X-rays are generally more common and accessible. Commercialized systems with controlling and reconstruction software makes it relatively easy to use. Additionally, apart from the resolution determined by the detector system, the X-ray images from the lab sources are also enlarged in some systems by geometric magnification.

One major purpose of this project is to investigate the damage in SiC/SiC composites using X-ray tomography. The use of X-ray tomography in the material research has increased extensively over the last decades, thanks to the advance of XCT technology. This technique is of particular interests to shed light upon materials with complex microstructure where the surface or sectioning characterization is not representative enough. For instance, Stock et al. reported a series of studies

in a natural composite (bones), which demonstrated the applicability of the XCT to reconstruct the 3D images of a composite material [109], [110]. It is therefore possible to observe the characteristic microstructure evolution as well as the cracks in 3D, as shown for example in the study of damage in metal matrix composites [111], and polymer matrix composites [112]–[114].

As for SiC/SiC composites, initial research by XCT focussed on the 'static' observation of the specimen [115]–[117] to analysis the microstructure in the composite. The improvement of the micro-XCT (with a resolution less than 50 μm [110]) with *in situ* methods has made damage observation in SiC/SiC composites achievable [79]. Research focused on damage observation in SiC/SiC composites has started quite recently. Chateau et al. showed the observation of the cracks in a unidirectional SiC/SiC minicomposite sample under the tensile test in 2011 [79]. The quantification studies of the fibre and matrix damages evolution were also reported at elevated temperature in the synchrotron source [81]. Furthermore, XCT with other image processing technique (digital volume correlation) was also applied in composite indentation tests and other heterogenous materials [118]–[121]. The limited open literature for SiC-SiC composites has already demonstrated that X-ray CT is a powerful tool that opens the possibility to investigate the microscale damage mechanics which will be used in the composite materials in this study.

2.3.4 Digital volume correlation

The results obtained from X-ray CT are essentially volumetric digital images. Digital imaging processing can extract further information regarding the internal structure based on the different grey levels of the features. With *in situ* experiments, image correlation was first applied to the 2D surface observations, using digital image correlation (DIC) [122]. DIC is a relatively well-established method to measure the displacement and strain (displacement gradients). Fundamentally, digital volume correlation (DVC) share the same principles as DIC, which extends

the 2D method into 3D for the displacement measurement [123]. The basic principles of DVC of the volumetric images that are normally acquired from the X-ray CT or magnetic resonance imaging systems can be summarized into the following steps [124], [125]:

I. A series of *in situ* volumetric images with the same dimensional size are divided by a grid into smaller units, named as 'correlation windows' for the correlation analysis.
II. The displacement and deformation of the correlation window is calculated by comparing the reference images and deformed images. Each displacement vector is obtained via the tracking of the corresponding locations of each correlation windows in the images.
III. 3D strain field is derived from the displacement field by using an appropriate differentiation approach [125], [126].

The key procedure in the DVC is resolving the displacement field between two images to obtain the motion of each correlation window. More advanced methods also consider the deformation and rotation of the window. The resulting displacement can be represented as a shift vector that is required to match the pattern in the reference image to that in the deformed image. The real images may have illumination differences (grey level intensity), and so this intensity function is generally resolved by a cross-correlation algorithm with a normalised correlation coefficient [127]–[129]. The correlation coefficient C based on grey level differences can be represented as:

$$C = \frac{\sum_{A\in VOI}^{1} f(A)\cdot g(B)}{\sqrt{\sum_{A\in VOI}^{1} f(A)^2 \cdot \sum_{B\in VOI}^{1} g(B)^2}} \qquad 2.5$$

where A and B are the spatial coordinates of each voxel in the volume of interest (VOI) from reference image and deformed image respectively and f and g represent the grey levels in initial and deformed VOI.

The highest level of correlation coefficient helps to locate the best matching position of each correlation window in the deformed state (perfect match has a value of 1). The shift can be defined as the vector connecting the centre of the subvolume, as shown in the figure 2.7 [123], [124]. Each subvolume gives one displacement vector. Subsequently, the size of the subvolumes is related to the spatial resolution of the vector field. However, practically the smaller subvolumes yield increased noise due to the limited information provided [130]. When processing the data, a sufficient size of the subvolumes is required to capture the essential features with an acceptable accuracy.

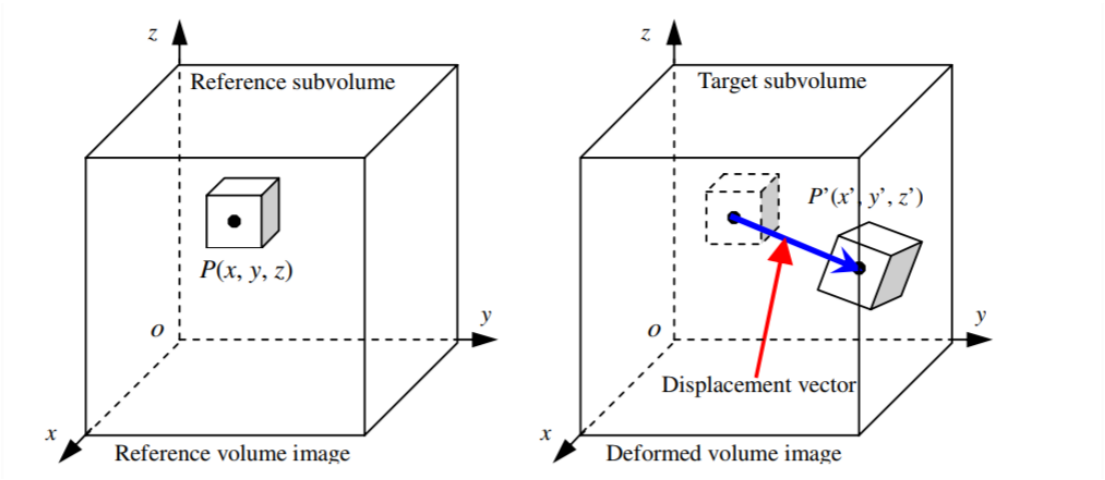


Figure 2.7: Basic principle of the DVC: the cubic subvolume at the position P in the reference image and tracked at P' in the deformed image; the coordinate difference between the P' and P gives the displacement vector [123].

The change (gradient) of the displacement vectors along the certain directions is then calculated. Mathematically, the displacement gradient (E) is represented from the vector component (V_i) along the j axis as

$$E_{ij} = \frac{\partial V_i}{\partial j} \quad (i \in \{x, y, z\}; j \in \{x, y, z\}) \tag{2.6.}$$

Therefore, the distribution of the localized deformation can be mapped within the entire 3D volume.

The availability and accuracy of the DVC is reliant on its robust algorithm development [107]. Recently, it is benefited from a number of the available commercial DVC softwares [126], [127], [131], [132]. The DVC method used in this study is from LaVision GmbH, Germany. In its algorithm, a discrete grid of displacement vectors is obtained based on the subdivided correlation volume, so the calculation of the strain tensor components (Equation 2.6) is approximated to be $\Delta V_i / \Delta j$ [130]. Accordingly, the magnitude of the localized strain may depend on the size of the subvolume grid. For example, if there is a sudden change of displacement occurred between two adjacent subvolumes, a smaller subvolume might yield a larger value of the localized strain.

The discontinuity of the displacement, which leads to a high localized strain magnitude, shows the localized deformation in a material that normally indicates the present of damage. The evolution and distribution of the damage can then be linked with microstructure with the help of the XCT images. One major issue at the early stage for the application of the DVC was the restriction to suitable materials with optimum absorption properties and sufficient local contrast for the subsequent feature tracking. The first study of damage applying DVC was published by Bay in a porous bone material in 1999 (figure 2.8) [124]. With the development of the X-ray tomography and the available commercial DVC software, the coupling of the XCT and DVC has become applicable to study damage in other materials, such as alloys [129], ceramics [121], [133] and engineering composites [107], [118].

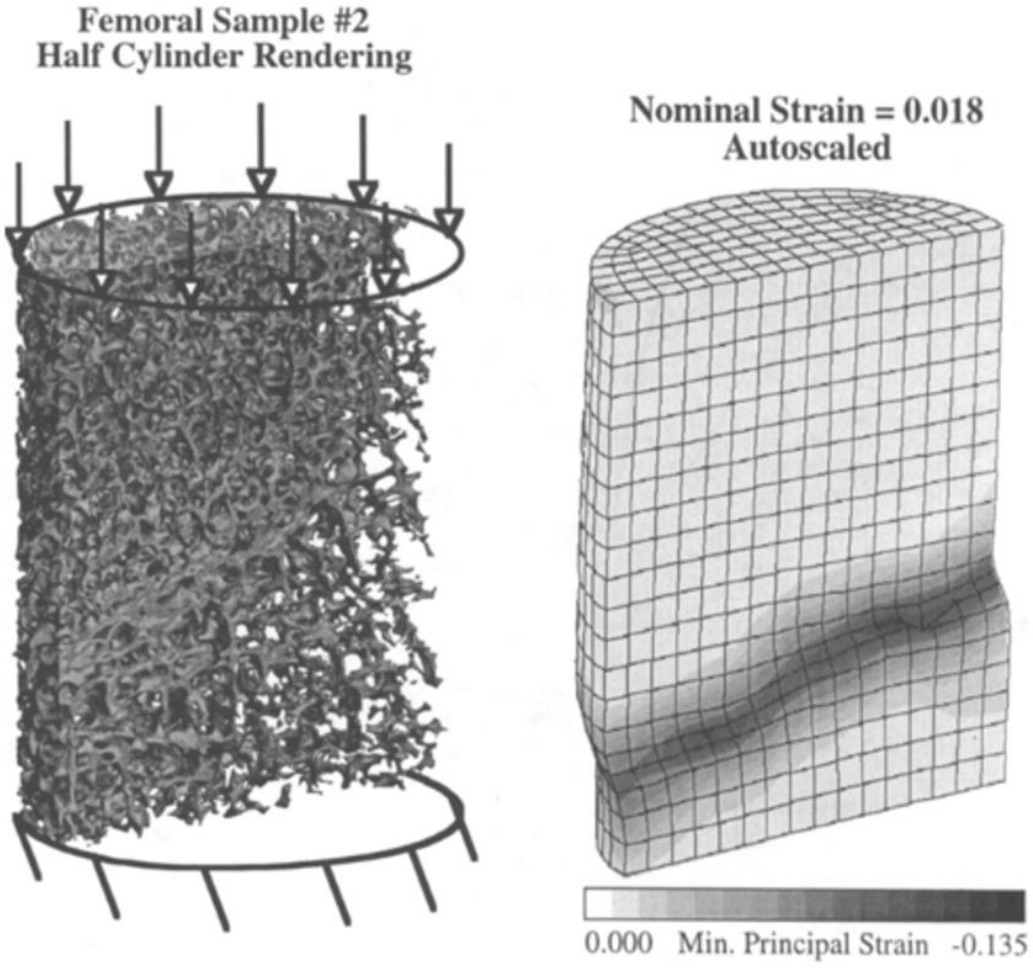


Figure 2.8: illustration of damage in femoral bone in Bay's paper. The damaged region is highlighted by the localized strain features of high strain values [124].

2.4 Concluding remarks

This chapter has summarized the background information and literature regarding the SiC/SiC ceramic composite that will be studied in this thesis. The importance and processing of the material constituents such as fibres, interphases and matrix are reviewed. The mechanical behaviours and damage characterization of such ceramic composite have been reviewed. Most damage characterization relies on *ex situ* or post-mortem analysis. Direct observation is required to reveal damage evolution in the composites. The *in situ* experiential methods for this observation have been reviewed, with specific focus on X-ray computed tomography. *In situ* three-dimensional observations also allow the quantitative analysis of the deformation and damage via digital volume correlation. In the following chapters, combined X-ray computed tomography and digital volume correlation will be used to reveal the microstructure and damage evolution within ceramic composite *in situ*.

Chapter 3. Multiscale quantitative characterization of the SiC/SiC composite structure by X-ray tomography

3.1. Introduction

The X-ray computed tomography can provide the 3D images of the sample non-destructively. In this chapter, laboratory X-ray tomography has been used to characterize the structure of the tubular SiC/SiC at different length scales. The main objective is to reveal the microstructure features, including pore structure and its distribution with respect to the fibre architecture. The image-based analysis will provide valuable quantitative information for the later *in situ* mechanical tests and the advanced microstructure-sensitive modelling. This is also the preliminary preparation study for the subsequent *in situ* synchrotron X-ray studies.

3.2. Materials and methods

3.2.1. Materials

The SiC/SiC composite material used in this study is provided by the MatISSe consortium [13]. The composite materials received are in the tubular shape of the nuclear grade cladding, fabricated by the CEA (*French Alternative Energies and Atomic Energy Commission*). The given information of the material from the manufacturer is as follows. The ceramic composite was based on third generation HNS SiC fibres (*Hi-Nicalon™ Type-S, Nippon Carbon Co.*), with an average diameter of 12µm. The fibre architecture consists of three layers. The interior layer is a filament winding layer with a ± 45° stacking configuration. The intermediate and outer layers are both 2 x 2 (± 45°) 2D braided structure. The fabric preform was then deposited with a 100 nm pyrolytic carbon (PyC) and then densified with the monolithic SiC matrix by the CVI process. The cladding tubes have a

grit blasted smoothed interior surface with a diameter of 7.80 mm, and outer surface, which was not ground, has diameter of 9.75 mm with a ± 0.05 mm fluctuation due to surface roughness measured from a Vernier scale. The outer undulant surface of the received samples shows the 2D structure of the outer fibre braids structure.

3.2.2. X-ray computed tomography

The multiscale non-destructive characterisation was performed in an Xradia Versa 510 X-ray microscope (*Carl Zeiss Microscopy GmbH, Göttingen, Germany*) in University of Oxford. The principle apparatus is shown in figure 3.1. In a laboratory tomography, even though the resolution is largely determined by the detector systems, the geometric magnification generated by the cone X-ray beam allows a certain range of resolution via changing the distance of the source and the detector. Three typical scans were performed to characterise the structure of the composite at different length scales, from the size of the tube (macroscale) to the size of each material constituent (microscale). The important parameters, such as voltage, field of view, pixel size etc., are summarized in table 3.1.

The experiment was controlled by the Scout-and-Scan™ Control Software from the Xradia, Inc.. All the scans have 3201 projections (one projection is a reconstruction reference, while the remainder are used to reconstruct the 3D microstructure) over 360° rotation, with an equivalent angular step of 0.12°. The reconstruction was performed using Zeiss Reconstructer software, which checks the central rotation position and removes obvious ring artefacts and beam hardening effects using the automatic correction mode. The reconstruction software also automatically applied a 3D Gaussian filter with a parameter of 0.5 (pixel) to the final reconstructed results, but no further spatial filter was applied in this study. The 3D images were then post-processed using

the ImageJ software (*https://imagej.net/*) and the 3D results were visualized using Avizo software 8.2 (*FEI VSG3d*).

Table 3.1 the experimental parameters in each scan at different length scale

Scans	Macroscale	Mesoscale	Microscale
Pixel Size	12 µm	3.3 µm	0.7 µm
Approximate Field of view	12 × 12 × 12 mm	3 × 3 × 3 mm	1.4 × 1.4 × 1.4 mm
	1000 × 1000 (pixels)	1000 × 1000 (pixels)	2000 × 2000 (pixels)
Binning	2	2	1
X-ray energy	60.0 KeV	60.0 KeV	80.0 KeV
Data Type	16 bits	16 bits	16 bits
Scanning time	~ 2 hr	~ 10 hr	~ 28 hr

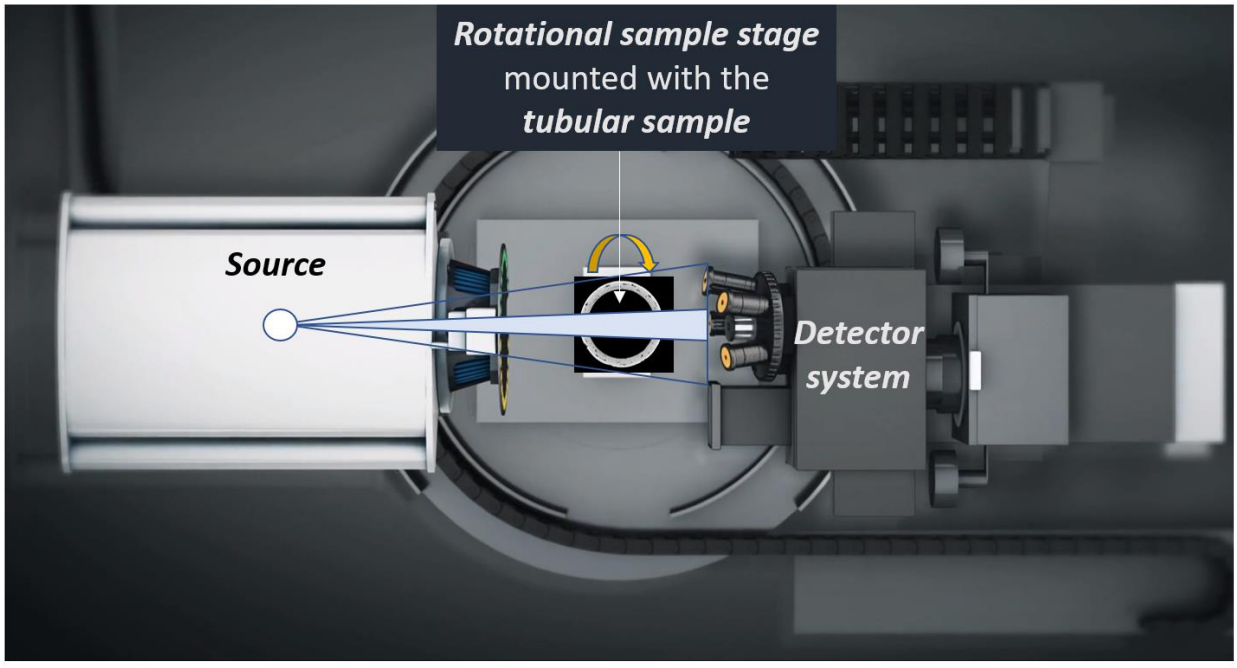


Figure 3.1: A schematic of the experimental apparatus for characterization in the laboratory X-ray tomography, Xradia Versa 510. The blue line highlights the cone X-ray beam from the source. Sample is enlarged for illustration. Background image adapted from the manufacturer's website (https://www.zeiss.com/microscopy/int/products/x-ray-microscopy.html).

3.2.3. Coordinate systems

It is important to note that there were three coordinate systems used in this study to describe the 3D tomographic images of the tubular (i.e. cylindrical) specimen and in the quantitative analysis. The different coordinate systems can be transformed to each other, as shown in figure 3.2, and they are defined as follows.

- Image Cartesian coordinate system (x, y, z). This is registered with the detector (i.e. the Xradia microscope) and is the coordinate system of the final 3D reconstructed images obtained directly from the reconstruction. The camera detector records the radiographs at each angular step, and the reconstruction mathematically uses the inverse Radon transformation. The z axis of the reconstructed image is parallel to the rotation axis. The origin is also not necessarily on the rotation axis. It is the top left corner of the image that defines relative position of each voxel.
- Tube Cartesian coordinate system (X, Y, Z). This is registered with the tubular (cylindrical) specimen. The Z axis of tube coordinate system is parallel with longitudinal axis of the tube. This transformation is especially important when the tube axis is not perfectly aligned with the rotation centre during the scanning. The origin of the tube Cartesian coordinate system (X, Y, Z) is not necessarily on the tube axis, as the reconstructed images might be cropped to reduce the image size for the later quantification analysis. The transformation between the image and tube Cartesian coordinate systems was generally performed by image processing, such as the functions of *reslice, rotation* and *crop* in ImageJ.
- Tube Cylindric coordinate system (R, θ, Z). The tube cylindric system is fundamentally the same as the tube Cartesian system, with the tube axis (Z) being parallel in both. The

tube cylindric system sets the origin (O_t) at the base of the tube and at the centre of the tube cross-section. The transformation was done mathematically using the equations below:

$$R = \sqrt{X^2 + Y^2} \quad 3.1$$

$$\theta = \tan^{-1}\frac{Y}{X} \quad 3.2$$

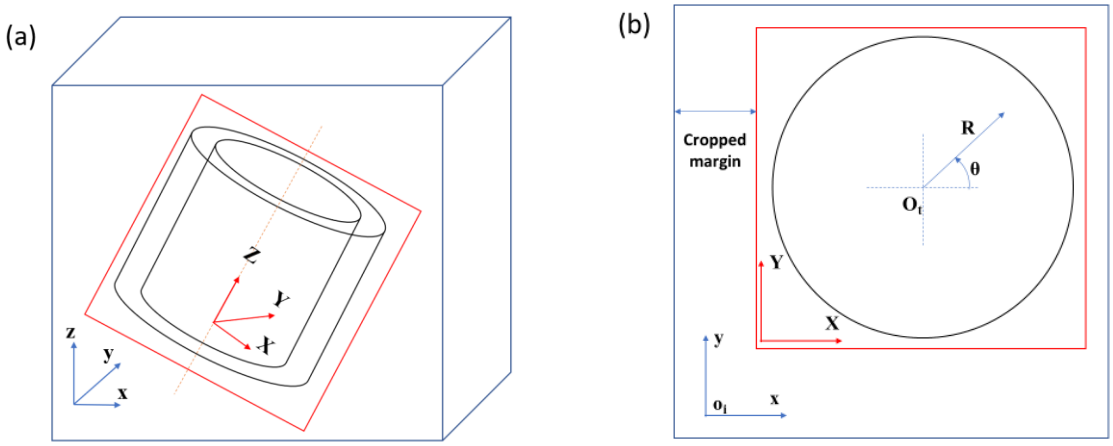


Figure 3.2: illustration of the three different coordinate systems. (a) the spatial relation of the image coordinate (x, y, z) in blue and the tube coordinate (X, Y, Z) in red, (b) the XY projection showing the tube Cartesian system (R, θ, Z).

3.2.4. Unwrapping code

In the post-processing analysis, it is useful to transform the 3D tubular images into a 2D image by unwrapping the cylinder to obtain a (θ, Z) image. A MATLAB algorithm code 'unwrapping' was developed to do this. The code was adapted from the study by Ye et al. that used 3D immunofluorescence images of a biomaterial [134] (the core code is available in the reference's attachment [134]). The adapted workflow is described briefly as follows (figure 3.3): (1) The image with the tube Cartesian coordinate (shared centre along Z axis) was imported as a 3D matrix; The planes near the top and bottom of the tube were selected (along Z direction); (2) Using a fitting

function proposed by Taubin [135], over 10 points were manually selected on braids in a circular cross section (X-Y plane) to define a fitted circle based on selected points. The fitting procedure was applied using the cross-section images at the top and bottom of the tube to obtain the averaged values for the centre point and radius of the fitted circle, which provide the reference parameters for the unwrapping. (3) The unwrapping function was then applied based on the fitted circle in the previous procedure to show the radius sectioning in the cylindric coordinate.

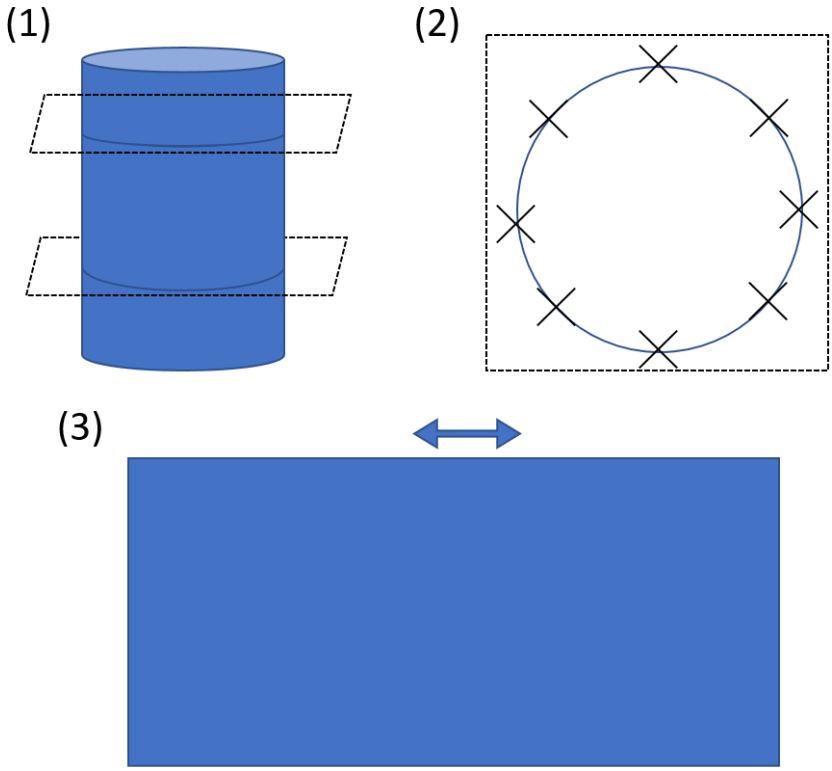


Figure 3.3: The illustration of the workflow of the Unwrapping code

The images for this unwrapping were first converted from 16 bits into 8 bits (i.e. 256 levels of grey) to reduce the processing time. The downscaling is conducted after the dynamic optimisation of the grey scale range of the original volume to minimize the loss of information. Still, the converted 8 bits images are typically around 2.5 GB. The ‘unwrapping’ to obtain one (θ, Z) slice

(i.e. constant radius) took about 1 hr in a workstation with a Intel® Xeon® Processor E5-2699 v3 (2.30 GHz) and 512 GB installed RAM (minimal of 56GB Memory required for each unwrapped slice), so the algorithm was not developed to obtain an unwrapped 3D image, and was used only to unwrap selected sections.

3.3. Results

3.3.1. Multiscale tomographic study

The multiscale structure of the composite tube from the entire tube of each elementary constituent is illustrated in figure 3.4. Macroscale images (12 µm voxel) of figure 3.4(a) show the 3D volume of the entire tube rendered based on the grey level. Examples of horizontal and longitudinal sections at the same resolution are shown in figure 3.4(b) and (c). At the macroscale, the composite component sample can be treated as a homogeneous tube, disregarding the pores or the fibre architecture. This assumption is possible as the composite tube manufacture has good control of the diameter and the roundness. Manufacturing problems that were common in earlier composites [8], such as open pores on the periphery of the cylindrical tube and the large variation in the diameter along the tube height were not observed in this sample. At the mesoscale (figure 3.4(d), 3.3 µm voxel), the structure of fibre tows is revealed. The woven fibre tows form three sublayers, and large pores between the sublayers are also observed. The microscale refers to the elementary constituents within a single fibre tow, and the sub-micron tomographic image (0.6 µm voxel) figure 3.4(e) successfully shows the individual SiC fibres among the SiC matrix, with the small pores observed inside each fibre tow. The thin PyC interphase (100 nm thickness) cannot be resolved in these tomographs due to the limitation of the spatial resolution of the Xradia microscope.

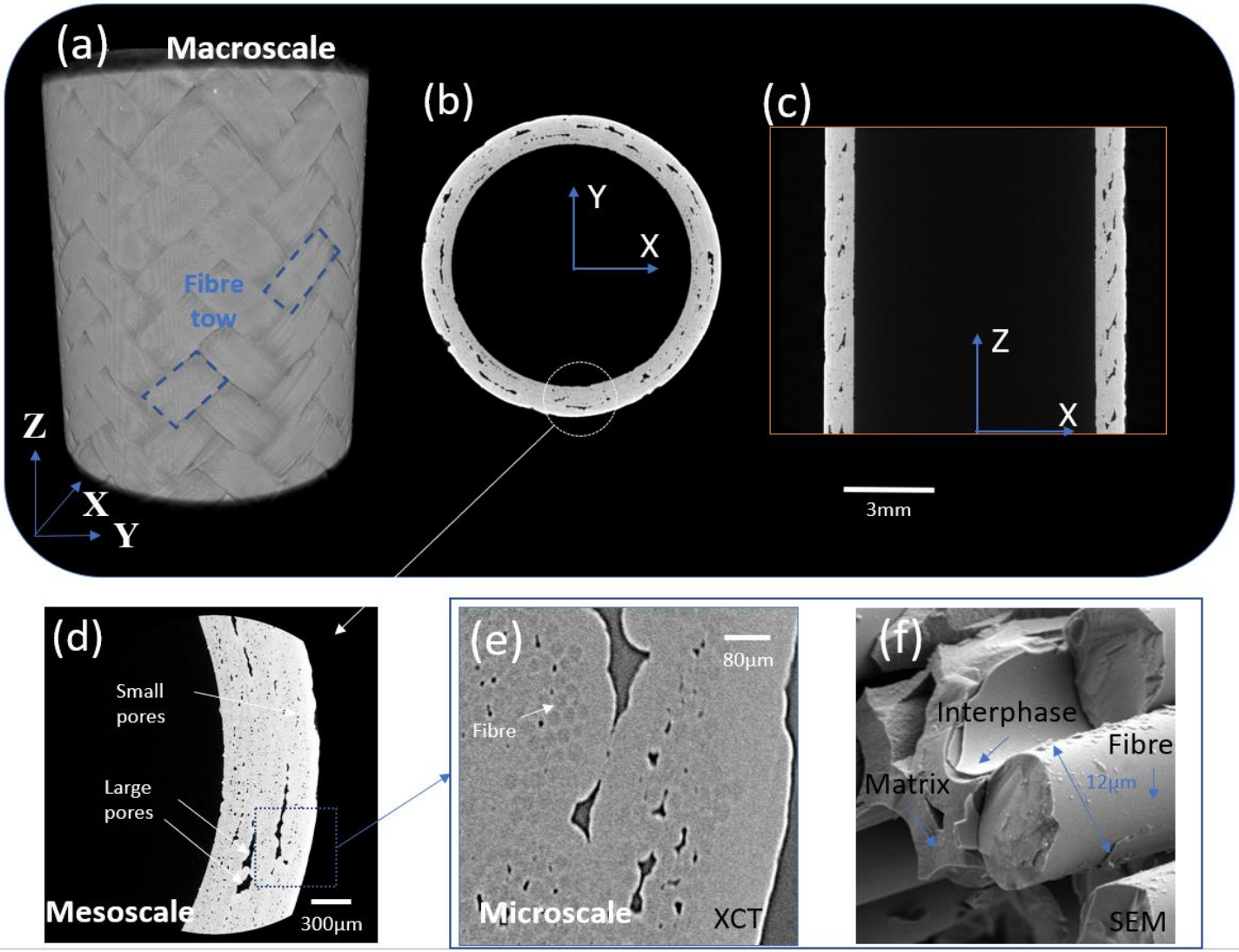


Figure 3.4: The multiscale visualization of the composite tube. (a) - (c) show the macroscale scan (12 µm voxel), with (a) 3D rendering with (b) axial and (c) longitudinal cross section view. The mesoscale image (d with 3.3 µm voxel size) shows the layered structure with the small and large pores. The microscale scan (0.6 µm) reveals the individual fibre with the comparison of the SEM image (f).

3.3.2. Fibre braid structure in the composite tube

The layered braided structure is also of interest. The outer layer of fibre tow braids can be visualized from the undulating surface as shown in figure3.4(a). However, it is difficult to illustrate or quantify the tubular fibre architecture as most commercial software only visualise the data using Cartesian sections. Therefore, to analysis the fibre structure at each layer, the unwrapping procedure was implemented using the 'unwrapping' MATLAB code.

The planar images after applying the 'unwrapping' to the cylindric composites tube at different radius corresponding to the different sublayers. Each layer was selected via the manual selection of the points at the same layer with the same radius in the (R, θ) cross section. An example of the circle representing intermediate layer was illustrated in the figure 3.5. With the same method, the unwrapped three sublayers were illustrated in figure 3.6. It shows the structure of the fibre tows at each ply layer. The outer layer and the intermediate layer are both 2x2 braided with a constant periodicity. This periodicity can be measured from the radial projection images, which is about 1.7 mm in axial direction and around 21° in the theta direction. The direction of the +45° fibre tows were reversed to -45° and then overlaid at the subsequent layer, which are highlighted in yellow quadrangle in figure 3.5 (a) and (b). This periodicity of the braids ought to be linked with the distribution of the pores, which will be addressed in the following sections.

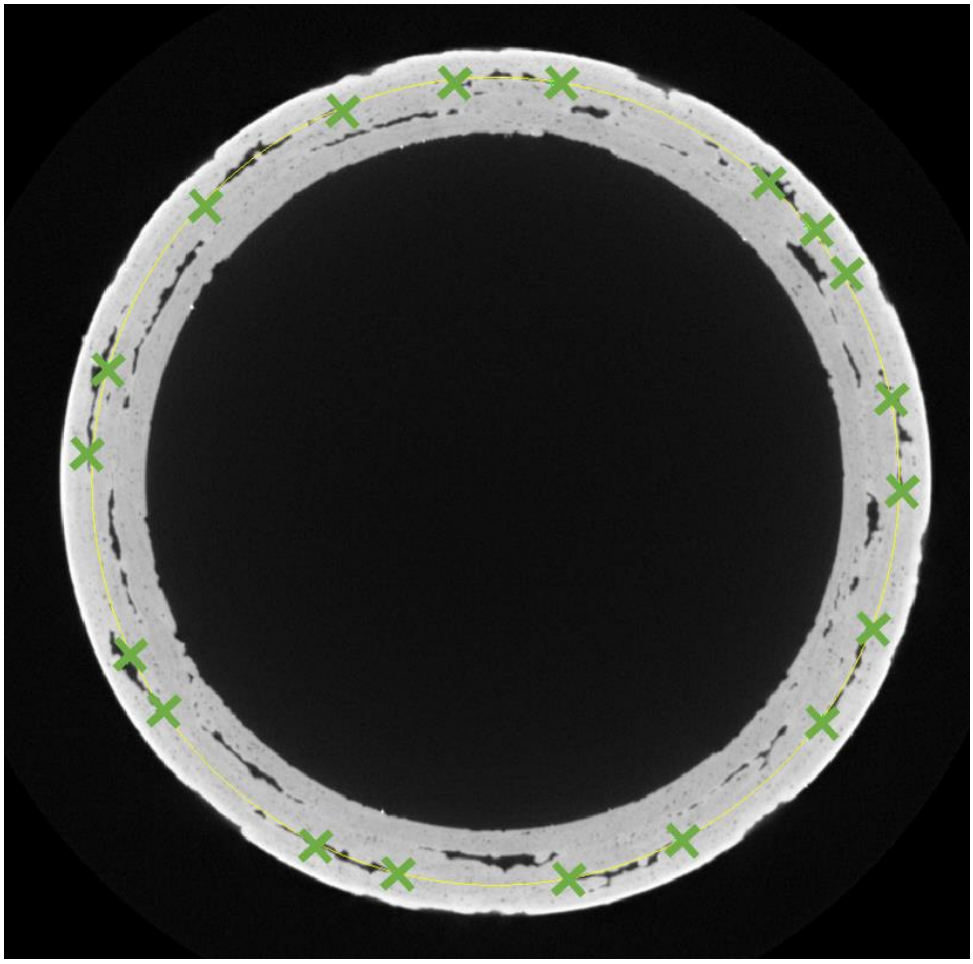


Figure 3.5: An example of the position represents the intermediate layer that was selected for the unwrapping. The green '+' marks were the manual selected points and the fitted yellow circle is based on the green marks though the Taubin function [135].

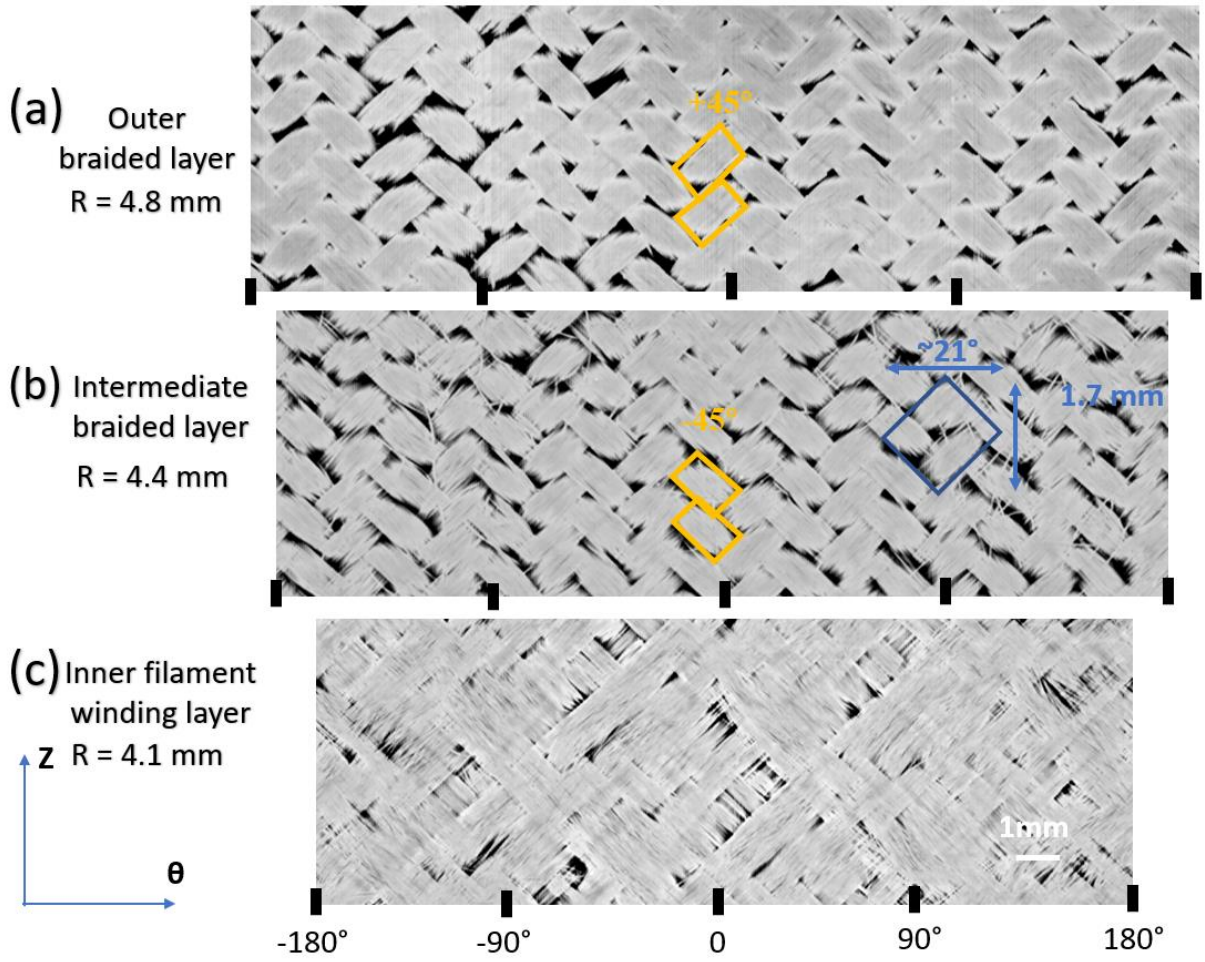


Figure 3.6 the unwrapped radial projection images showing the different layer structure in the composite tube from the 3D image with a voxel size of 3.3 µm. Three layers were illustrated at different radius as (a) the outer braided layer, (b) the intermediate braided layer, and (c) the inner filament winding layer. The blue rectangular indicate a typical braid unit, and the difference of tow orientation is highlighted in yellow.

3.3.3. Porosity analysis

The dark phase inside the composite tube in the tomographic images represents the porosity. As shown in figure 3.4, there are two types of pores with differences shapes and sizes; the large pores between the fibre tows and the small pores within each fibre tow. The small pores exhibit a needle shape with a typical diameter smaller than ~10 µm and the same orientation as the neighbouring fibres. It is also interesting to find that those small pores are generally distributed towards the centre of each tow as shown in the figure 3.4(e), which may due to the densification process during

the deposition. The large pores are normally next to the boundaries between the braided layers. They also preferably locate at the crossover points of the fibre tows. The 2D section view in figure 3.3(c) shows those large pores have a periodic repetition with the distance of this repetition (~1.7 mm) being the same as the length of a fibre braiding unit. It indicates the complicated structure of the large pores that may be related to the architecture of the fibres.

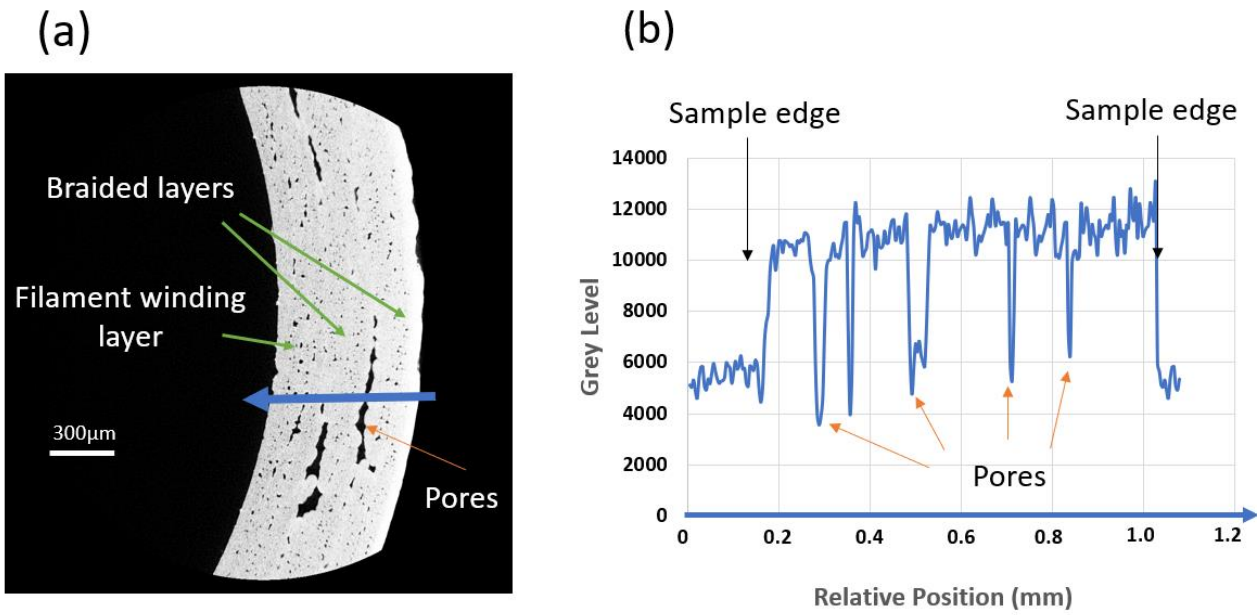


Figure 3.7: An example of the composite showing the layers structure and pores from an XCT virtual slice with 3.3 µm voxel size. The profile of the grey level of probe blue line in (a) is showing in (b).

From a quantitative point of view, the porosity analysis was based on the distinct difference in the grey level between the air and solid in the images. the segmentation procedures were applied using the ImageJ software as follows. Firstly, the sample edges of the outer and interior surfaces are defined by two concentric circles to select the composite tube. A greyscale threshold is then manually applied to segment the pores (small pores, large pores) from other solid materials constituents (fibres, matrix, and interphases). Those two phases have a substantial grey levels difference, as shown in the grey level profile (figure 3.7(b)). Due to the high contrast between of

the solid and air, the segmented pores and the quantitative analysis were insensitive to the threshold value (a typical value of around 8000 was used for 16 bits data). The segmented images of the pores were then binarized to save computational time. Those binarized images were utilized to study the structure and distribution of the porosity.

The structure study of the porosity focused on its size and interconnectivity. The segmentation of the large pores from the previous binarized pores images was found to be successful by using the *propagating contour* function in the Avizo software (figure 3.8). It autoselects all the spatially connected neighbouring voxels with same value from an initial arbitrary seed voxel. Different selection of the initial point in any large pore from the section view gave the same result, which confirmed the high connectivity of the large pores (figure 3.8(b)). In contrast, the small pores within each fibre tow are generally not connected to each other nor with the large pores. Figure 3.9 (c) and (d) shows the 3D rendered volumes of the segregated interconnected larges pores and isolated small pores, respectively. The large pores were found to be interconnected spatially. From the 3D view, it was also found that the small pores were relatively evenly distributed among the samples. In contrast, the network of the interconnected large pores situated between the network of the fibre bundles. It is also worth noticing that the interconnected pores have a closed structure which are not connected to the outside air. Those barriers are provided by densified the outer and inner surface. This also means the composite tube can provide a good gas-tightness.

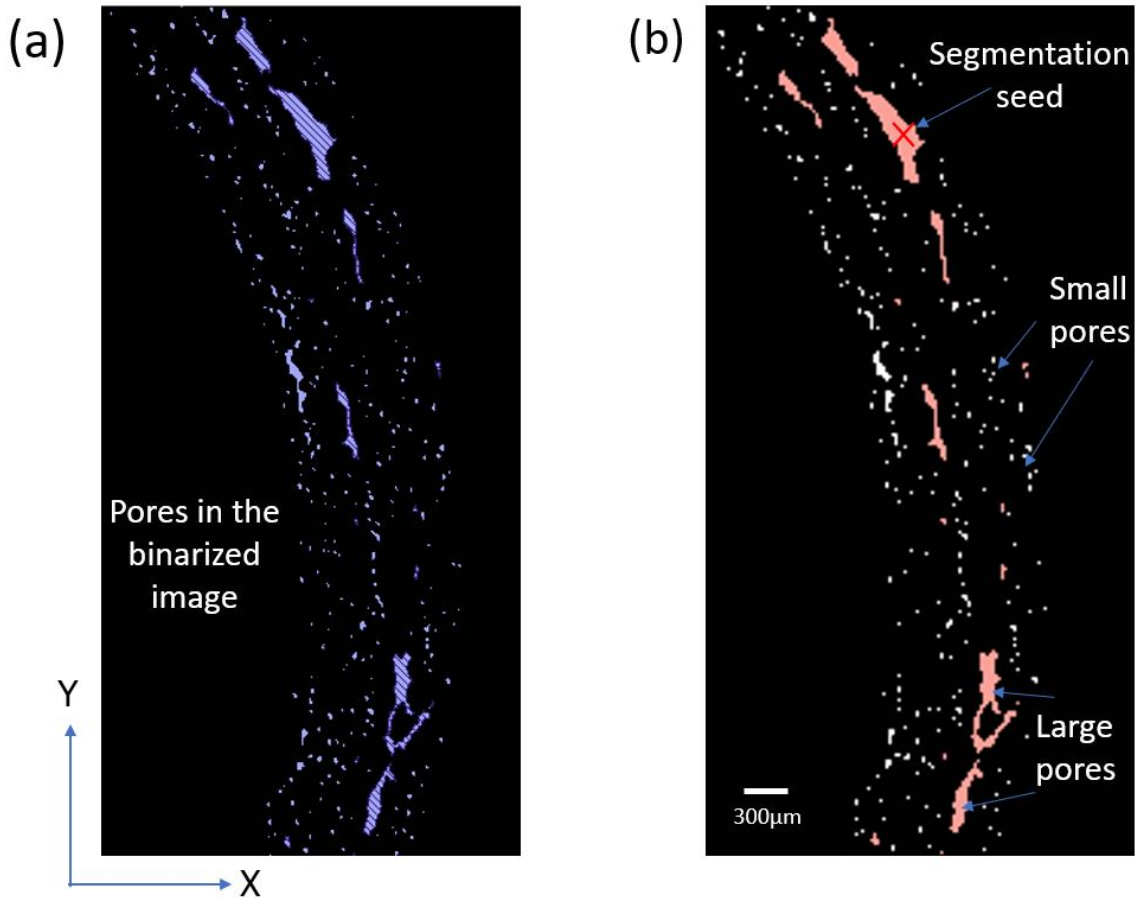


Figure 3.8 (a) Segmentation by image intensity thresholding showing the pores, (b) the propagated seeding thresholding of the binarized pores to segment the large pores from one separated pore in 2D section view. The red cross indicates a typical seed and all the pink labelled pores are interconnected with the seeded pores in 3D, while the remaining unconnected pores are shown in white.

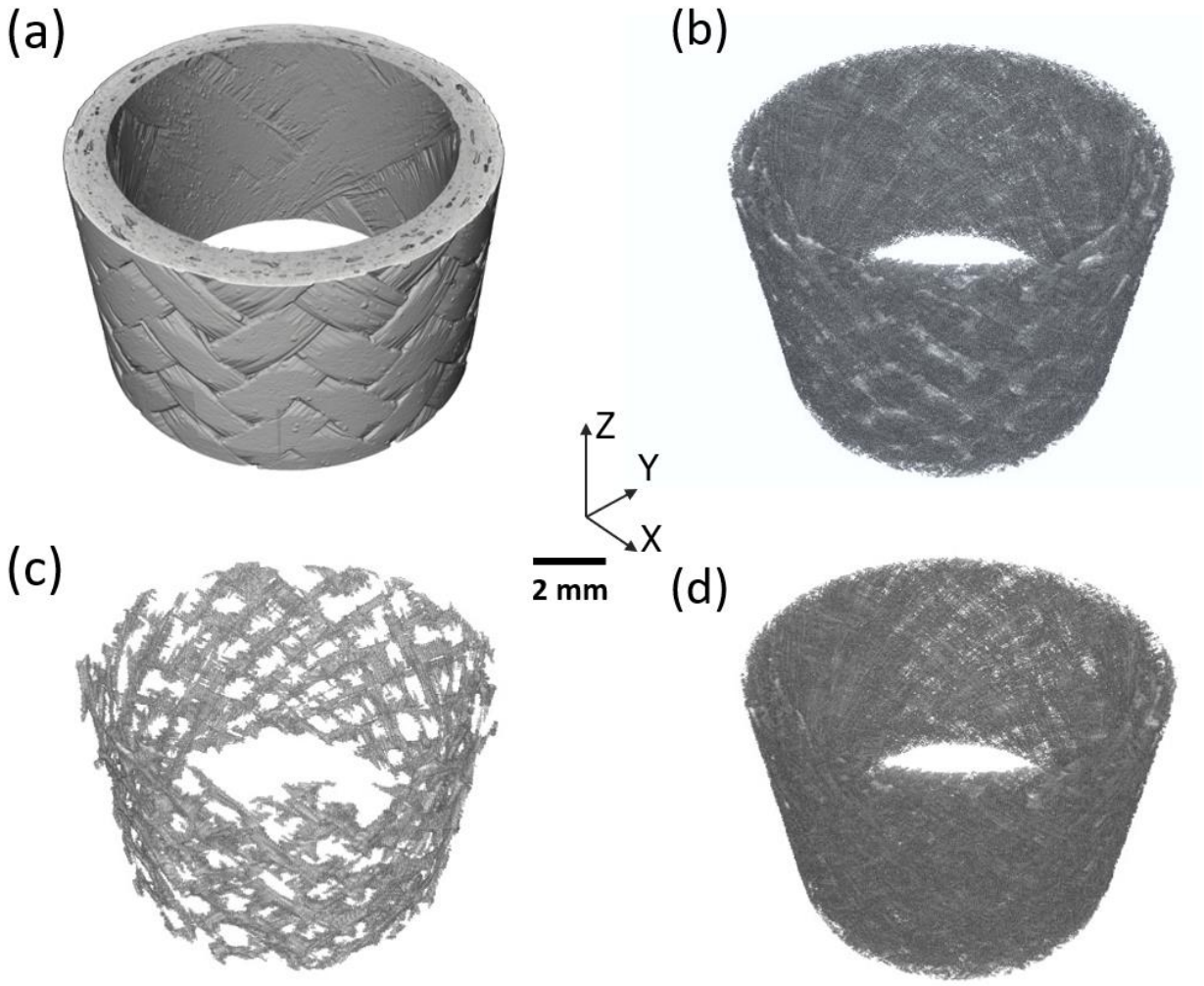


Figure 3.9: 3D visualizations of (a) the solid phase, (b) pores network with both large and small pores, (c) the large pores in the composite tube to show their structure and distribution and (d) the unconnected small pores in the composite.

The binary images were also used for the statistical analysis of porosity distribution in the composite. The total porosity was measured as the number of the segmented voxels compared with overall number of voxels of the tube sample. As the surfaces of the cylindric tube are relatively dense, the pores images were cropped by the outer and internal surfaces via a manual section of a fitted circle. The results of the variation of porosity measured along the axial direction are summarized in figure 3.10 with data obtained at the macroscale, mesoscale and microscale of a

same specimen with different voxel sizes (12 µm, 3 µm and 0.7 µm as slice images shown in figure 3.4) in a measured sampling volume of approximately 340 mm^3, 15 mm^3 and 2.5 mm^3 respectively. A similar value of the averaged porosity (~5.4%) was found from the composite tube with different resolution of the tomographic scans. A larger fluctuation was found in the data of high-resolution scans (with 0.7 µm voxel size) as the corresponding field of view only covers a very small portion of the sample, but all the data are in the range between 5.0 to 6.0%.

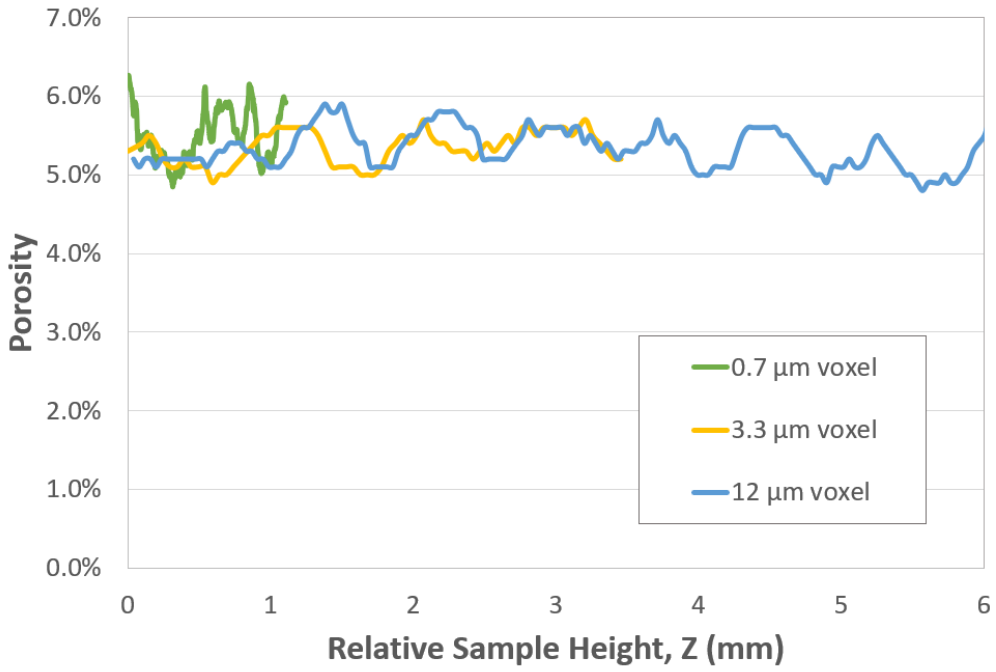


Figure 3.10: the distribution of the total porosity along the axial direction at different voxel resolutions (from data as shown in figure 3.4).

Even though the average porosity is similar in different scans with different voxel size, as illustrated in the table 3.1 and figure 3.4, the FOV of the microscale scan (0.7µm) can only covers the through-thickness length (1.4mm) of the tube and that of the mesoscale scan cannot cover the entire angular direction (figure 3.4(d)) without further stitching. Therefore, the spatial distribution of the pores utilized the data obtained from the tomographs that covers the entire cylinder (12 µm

voxel size, figure 3.4(a)). The corresponding variation of the porosity measured along the radial, angular and axial directions are shown in figure 3.11. The most noticeable fluctuation was observed along the radial (R) direction. The local peak mainly due to the large pores locates at the boundary of the sublayer, which is about 11%. The local minima in figure 3.11(a) is close to the porosity of the small pores within each fibre tow, which is about 2%. This shows the local porosity is associated with the direction at which fibre layers are stacked. Compared with the distribution in radius direction, the distributions show a relatively small fluctuation in the theta and axial direction (figure 3.11(b) and (c)). In fact, the fluctuation in the axial direction is shown to be also associated with the microstructure. The periodicity in the fluctuation is close to the unit length (~1.7 mm in axial direction) of the woven braids. Nevertheless, a much larger fluctuation was observed along the radius direction that is determined by the distribution of the large pores. In contrast, the pores along the theta and axial direction which is liked with fibre textiles structure are much more homogeneous distributed.

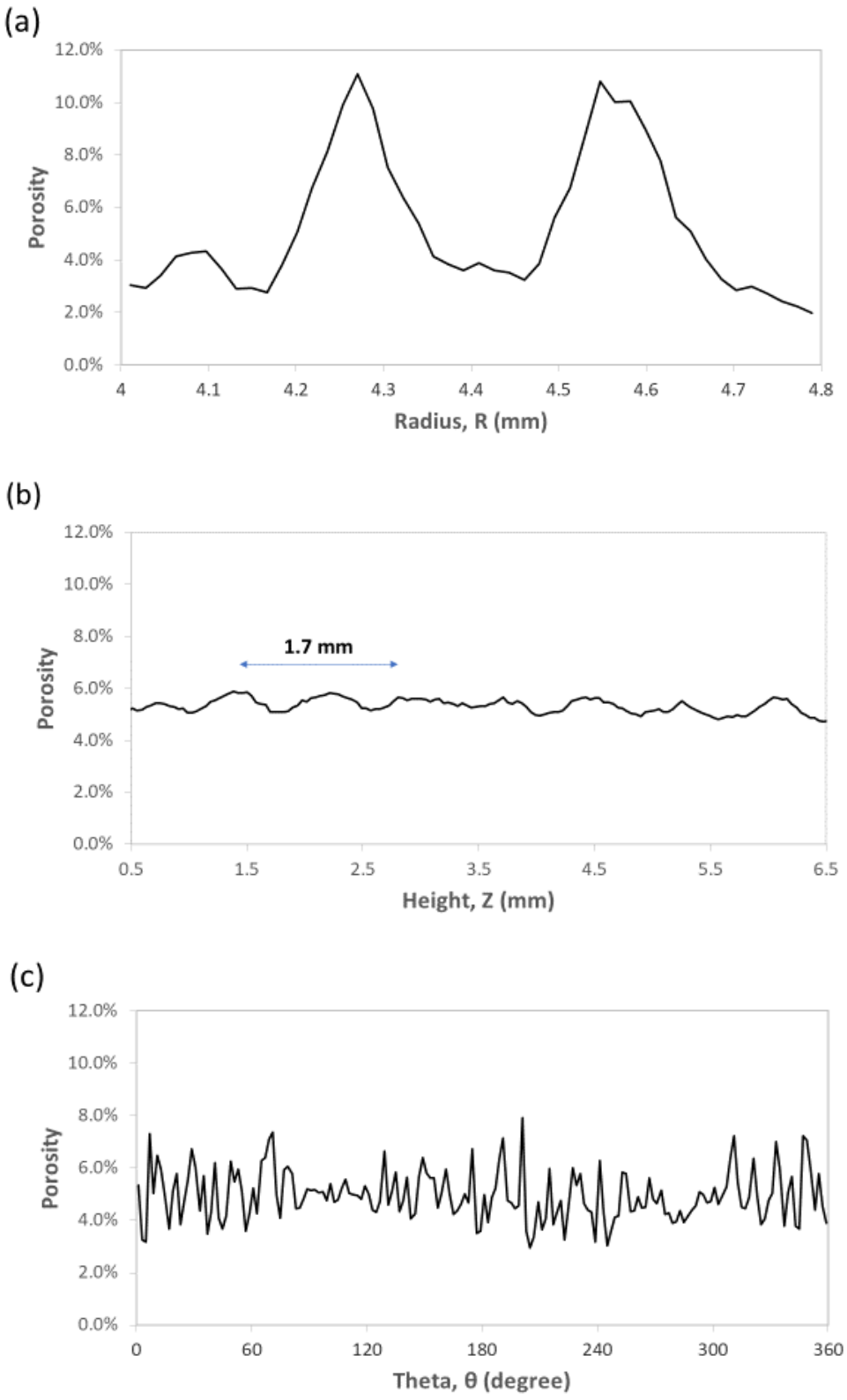


Figure 3.11: Variation of the total porosity at the (a) radius, (b) height and (c) theta direction of the composite tube of the tomographic images with a voxel size of 12 µm

3.4. Discussion

The characterization of the studied SiC/SiC composite tube at different scales (figure 3.4) demonstrates the capability of X-ray tomography to provide useful quantitative information of the microstructure features, such as pores and fibre braids, which have the size a few times larger than the voxel size. One aim in manufacturing the nuclear SiC/SiC composite is to reduce its porosity, which increases its thermal conductivity [38], [47], [136] and may improve the mechanical properties [35].

The total measured porosity from the tomographic images was around 5.5% of the received sample in this study. The measured value is larger than that (~11%) in the study from Bernachy-Barbe et al. of a similar tubular shape composite also provided by *CEA* [57]. Even though the details of the images used for the porosity analysis was not stated in their study, an obviously more densified and smoother SiC/SiC composite was received in our study (figure 3.12). In fact, the received CVI-SiC/SiC composite sample also has a relatively low porosity level compared with that in other studies (typical value 10 to 20%) [67], [116], [137], which may be owing to the development of the manufacturing process. Even though the detailed procedures were normally not stated in the literature, the noticeable difference of the grey levels between the pores and materials (figure 3.4) means the porosity characterization is relatively insensitive to the threshold value and segmentation methods [138]. In addition, the similar value that was coincided from different measurements with various resolution (figure 3.11) gives more confidence of the obtained porosity data.

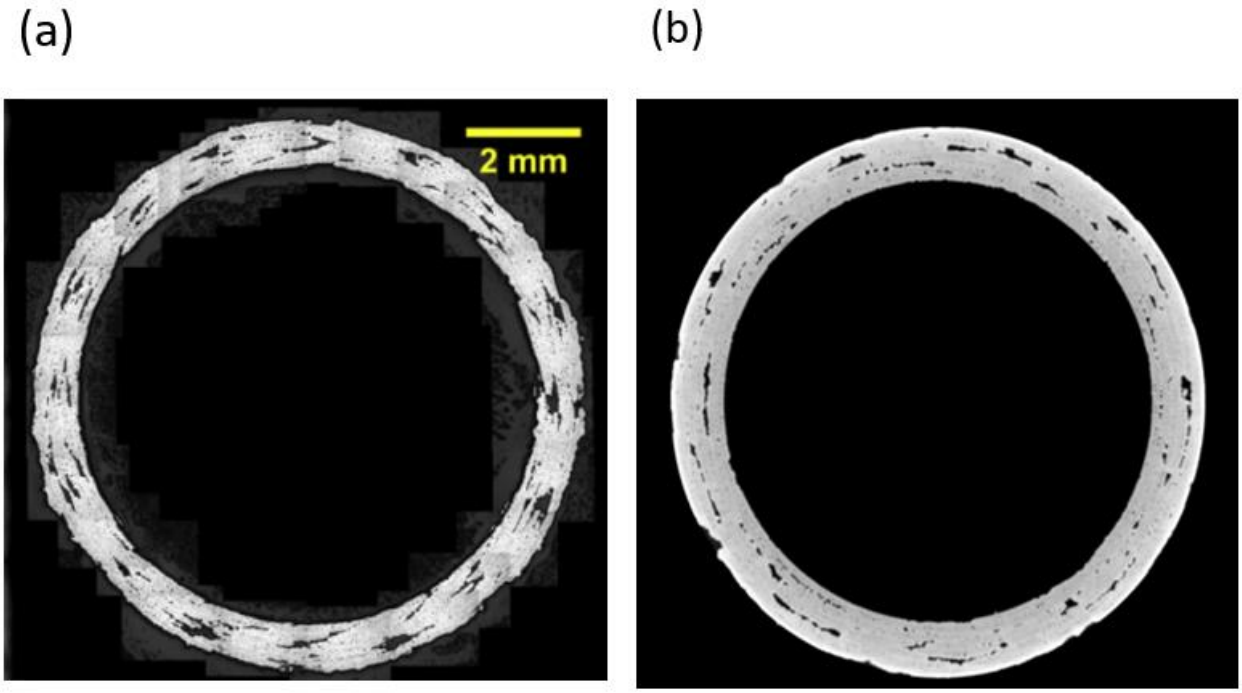


Figure 3.12: The sliced images of the tubular SiC/SiC composite in (a) reference [57] and (b) this study, both materials provided by *CEA.*

The 3D X-ray tomography can also reveal the internal residual network of the porosity, which may not be representative from the sectioning or surface 2D section image. A 3D interconnected network of the large pores, which are typically isolated in the 2D image (figure 3.4), is demonstrated in figure 3.9(c). The volume of those interconnected large pores constitutes around 70% of the total porosity, which predominantly control the level of the total porosity in the composite. Furthermore, they are preferably distributed at the inter-ply regions of the composite, which explains the local peaks in the radial direction (figure 3.11(a)). Similar results of a strong variation in the porosity fraction profiles at the ply direction were also reported of a representative volume in the bulk SiC/SiC [116], [139]. and C/SiC [137] composite samples. This indicates that

the stacking of the fibrous plys and layout of the fibre tows are of importance in controlling the porosity level of the textile composite and the network of the pores.

Apart from the overall porosity, the structure and the interconnectivity of pores in the SiC/SiC composite is also important as it could strongly affect the gas hermeticity. It is one of the most important parameters in the fuel cladding application of the composites, as the fission gas must be contained during the reactor operation thought the cladding life [8]. However, a significant residual porosity is generally expected in the CVI composite [4]. Theoretically, the interconnected pores could provide an easy path for the air flow. Even though those interconnected large pores are found to be closed and sealed by the surface ply of the composite, their interconnected residual pores structure means that to keep the hermeticity is challenging once the matrix cracks occur in the composite. In the nuclear industry, this has led to a 'sandwich' concept that has been proposed by the CEA with a heavy metal (Ta) liner to ensure the gas tightness [47], where the metal liner ensures the gas hermeticity and the composite layer provides mechanical properties. The experimental study of the permeability is beyond the scope of this thesis. However, as stated when discuss the gas permeability, it should consider not only the level of the total porosity but also the structure of the pores, where the X-ray tomography is a very powerful method.[1]

For this thesis, the laboratory X-ray tomographic results also provide the benchmark for the following *in situ* experiments in Chapter 4 and 5. It demonstrated the heterogeneous microstructure of the composite at the different resolution. Since the quantitative observation the deformation from the digital volume correlation (DVC) of the *in situ* tomographic images is based on the correlation of the grey-scale voxels, it requires heterogeneous features (contrast patterns) to track

[1] XCT of composite tubes with a Ta sandwich liner was attempted in this project, but the high attenuation of the liner prevented successful tomographs of the full tube thickness.

the displacement within the materials [124], [130]. In the SiC/SiC composite the combined micropores and macropores provided the naturel heterogenous structure that is suitable for DVC, which make the image correlation theoretically possible.

3.5. Concluding remarks

In summary, the method of using laboratory X-ray tomography at different scale provides a convenient and useful non-destructive characterization method to study the internal structure of the SiC/SiC composite tube. The heterogenous structure of the fibre tows and pores were successfully revealed. The large pores and small pores have different connectivity. The large pores were found to be spatially interconnected. The porosity is quantified, and its distribution is different at different directions. The local increase in the porosity are related the large pores, which is associated with the stacking direction of the fibre plys. Those understandings of the pores structure are important for the successful engineering application of the composite. It also provides the valuable microstructure information that is useful for the future experiment design and microstructure-based modelling.

Chapter 4. *In situ* synchrotron X-ray studies of C-ring diametral compression

4.1. Introduction

The SiC/SiC ceramic matrix composite in this study is proposed as a fuel cladding material for the nuclear fission reactors. In the current reactors and future reactor designs, a tubular SiC/SiC cladding is used to hold the fuel pellets. The cladding as one of the most critical components in the reactor needs to meet strict requirements over service. During operation, due to a combination of the swelling of fuel pellets, a through-thickness thermal gradient and irradiation-based swelling of the cladding, a complex stress state is expected on the cladding component [13], [140]. In some specific reactors, such as the LWRs, additional stress may come from the prefilled helium gas in the tube and the build-up of the fission gas [22]. Furthermore, in accident scenarios, rapid change of the temperature environment can also induce an abrupt stress rise [21]. Therefore, it is important to demonstrate the SiC/SiC composites have the required strength and also essential to understand their fracture mechanisms in different situations before they can be qualified for reactor applications.

Component testing is crucial for the evaluation of structure integrity in engineering applications, and could be beneficial for composite developments to optimise the manufacturing process as well [8]. Previously, SiC/SiC composites with unidirectional fibres and 2D plates were typically studied with a planar geometry [38], [53]. They were based on a well-established and standardised method to assess the mechanical properties of a planar composite [141]. However, the geometric shape of the components affects the manufacturing process of the composites and thereby the

microstructure such as the fibre architecture [51], [79], which may also change their mechanical behaviour.

Adaption of the conventional regular beam or sheet shape samples for tubular cladding components requires further machining procedures, which inevitably alter the intrinsic flaws or introduce defects into the sample while the measurement of mechanical properties in ceramics is defect sensitive. Therefore, the results obtained from a small bending bar may not represent the behaviour of the larger tubular composite components. For the tubular ceramic composite component, techniques to measure a reliable strength value are relatively lacking in the open literature. A simple geometry that can be easily machined is required for the tubular component tests.

In the tubular component, an axial direction test is relatively straightforward [43]. By contrast, difficulties are normally associated with the properties in hoop direction. For the monolithic ceramic, the simple tubular specimens such as C-ring [142] and O-ring [143] have been used to measure the hoop properties. A diametrical compression C-ring test from a tubular component is also standardized to measure the ultimate hoop tensile strength [144]. The sample specimen preparation and associated loading requirements make them also particularly attractive to be explored in the composite application. For example, Jacobsen et al. investigated the feasibility of the C-ring test for a SiC/SiC cladding prototype [145]. Their successful macroscale tests demonstrated the accessibility of the C-ring specimens in the composite.

Such macroscale tests provide valuable data for engineering design. They may also be used to evaluate the variation in the properties due to fabrication and the effects of the fibre textile weaves at the onset of the damage and final failure [60], [146]. However, macroscale tests yield an average response of the material along the gauge length. The heterogeneity nature of the SiC/SiC

composites suggests that their mechanical behaviour is sensitive to the microstructure [43]. The complicity of the microstructure may arise from of the fibre textile and the different ply in the composites. The post-mortem analysis of the fractured composite also indicates that damage is affected by the microstructure [145]. Therefore, a more reliable method to investigate the microstructure damage during the mechanical and thermal environment is needed.

A few recent studies have reported the microstructure characterization [67] and damage observation [79] in the SiC/SiC minicomposites via the X-ray tomography, which showed its advantages. This chapter presents studies combining the use of X-ray tomography and image correlation to detect and quantify damage evolution during *in situ* mechanical tests of SiC/SiC C-ring specimens from the tubular cladding. The testing method here is further developed to perform a thermomechanical test with high speed X-ray tomography, which allows continuous observation of the experiment. The customized loading rigs are capable at both room temperature and high temperature (900°C). With this approach, the macroscale response and the evolution of the microstructure damage of the composite cladding sample could be simultaneously investigated.

4.2. Materials and methods

4.2.1. Materials

The same batch of tubular cladding SiC/SiC composite fabricated by CEA (French Alternative Energies and Atomic Energy Commission) was used as in the previous study (section 3.2). The C-ring sample preparation follows the international standard for advanced ceramics [144]. The samples were first cut into 4 mm width, then sectioned into the C-ring shape using a 1 mm thick Buehler circular diamond cutting blade with a water-based coolant. To minimize the damage during the machining, the sample was waxed into the holder before the cutting. The wax was then

dissolved completely by immersing in Acetone for about three hours. The machined surfaces were then ground with abrasive SiC paper (to 800 grit sizes) and checked by optical microscopy to ensure any visible cutting defects were removed.

4.2.2. Experimental setups

Three *in situ* experiments were performed on C-ring samples on the JEEP (Joint Engineering, Environmental and Processing) I12 beam line at the UK Diamond synchrotron. The X-ray tomography was performed in the static mode, when mechanical test was paused, and continuous mode, where images were recorded continuously with a constant loading rate. The first two experiments were carried out at room temperature, then a third experiment was performed at 900°C.

4.2.2.1. Static scan *in situ* diametric C-ring experiment[2]

The first diametric compression test of a C-ring sample was performed using the *in situ* Deben Load Rig (2.5 kN capacity, figure 4.1(a)), which was kindly provided by University of Manchester. The C-ring sample was attached at the base end of the sample stage by a commercial cyanoacrylate superglue (figure 4.1(b)). Loading applied on the top end of the C-ring sample via the rig's crosshead. The applied loading from the crosshead (displacement control mode) with a progressively increasing amplitude was shown in figure 4.1 (c). Between each increment in the loading, there was an unloading scan (to approximately 5 N). The experiment was stopped after the load peaked at 123 N. After this point, further diametric compression by the crosshead

[2] Beam line number EE10106 in Jan 2015.
All the Synchrotron tests require 24 hours operation without any stop to make the best of the awarded beamline time, which means almost all the Marrow's group members were there to help each other with assistance from the beamline scientist (sometime from other collaborators). For this test, Group members Dr. L. Saucedo-Mora and Mr. S. Barhli (Dr. now) performed the test and did the reconstructions using the Diamond code. I did all the data analysis for all the results presented in this thesis.
Part of the results in this experiment has been published in *Journal of Nuclear Materials* 481 (2016) 13-23. Saucedo-Mora, L., Lowe, T., **Zhao, S.,** Lee, P. D., Mummery, P. M., & Marrow, T. J. (2016). In situ observation of mechanical damage within a SiC-SiC ceramic matrix composite.

movement did not cause any further increment in loading. The profile of peak load versus displacement of the crosshead is also shown in figure 4.1(d).

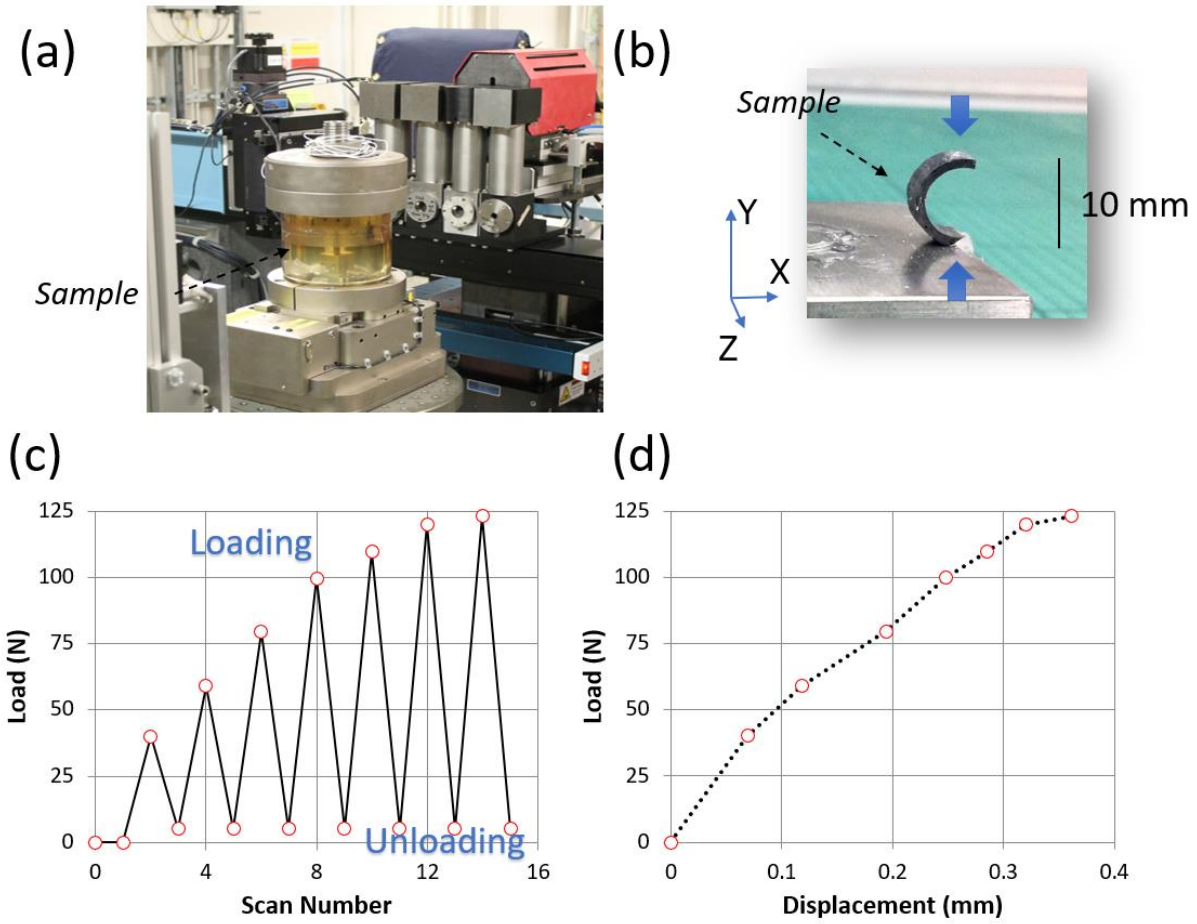


Figure 4.1: (a) The Deben Load Rig (2.5 kN load cell) on the JEEP-I12 beam line; (b) the C-ring SiC/SiC sample for diametric compression test mounted on the sample stage; (c) the cycling load history of the compression test a, hollow red circles indicate the paused X-ray scans points at that load; (d) force-displacement curve (displacement of the crosshead readout) of the loaded states from *in situ* tests.

The *in situ* tomographic scans were performed once the C-ring sample was compressed to the designated load, with the corresponding applied displacement held constantly during the scan (figure 4.1 (c)). All the radiographic images were recorded by the Module 3 optics in the JEEP-I12 with a pixel resolution of 3.25 μm [108]. The recorded images have 2560 × 2160 pixels. The resulting field of view can cover an area of 8.5 mm × 7 mm, which covers all the middle part of

the C-ring sample along entire sample width (Z direction). The scanned volume, with a typical longitudinal virtual slice, is illustrated in figure 4.2. The effective radiographic width is around 4/3.25 = 1230 pixels. Following a rule of thumb [147], 1800 (1.5×effective image length in pixels) projections is required. In this experiment, for each tomographic image, 1800 radiographs were thus recorded over a 180° rotation, with a monochronic X-ray energy of 56 keV. This yields an angular step of 0.1° for each radiograph. The acquisitions were performed in the standard absorption mode, with reference images (flat and dark images) collected before each scan when sample were moved out of the detector's field of view. Adding the manually manoeuvring time and necessary security check for the synchrotron hutch, each tomographic scan took around 18 mins.

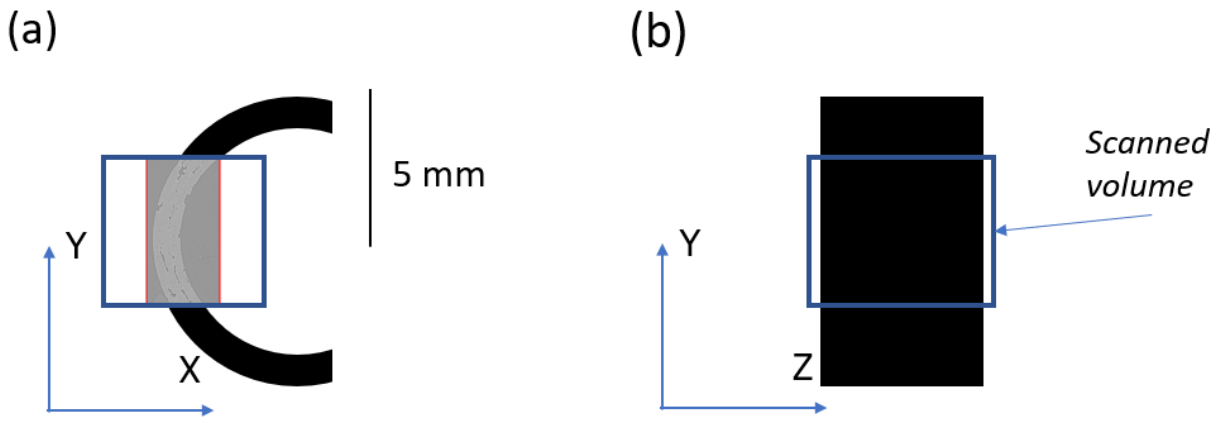


Figure 4.2: (a) The scanned volume of the C-ring sample using the Module 3 optics in (a) the X-Y slice projection and (b) the Z-Y slice projection. The C-ring sample shows in black, and the scanned volume shows the in the blue rectangular and the latter cropped volume in red.

The reconstruction of the tomographic images used the standard back-filtered projection code provided by Diamond I12, without the ring artefact remover [108]. The resulting stacks of 2D tiff images (reduced to 8-bits) from Diamond were then converted into a 3D raw data file using ImageJ

software. Further cropping was also applied in ImageJ to reduce the data size. Additionally, a standard Gaussian filter (with a parameter of 1 × 1 × 1 pixel) was also applied to reduce the noise.

It needs to be mentioned that during the experiment, there was a GDA (general data acquisition) software error between the 40 N-60 N scans. Due to the failure of the controlling system, no flat and dark field image (reference image) was taken, and the number of radiographs at 40 N is insufficient for a standard reconstruction. The 60 N scan was taken once again after the software error was fixed. Therefore, the 40 N image was discarded, and all the data presented in this chapter were obtained after the software crash was fixed.

4.2.2.2. Continuous (time-resolved) scan of a diametric C-ring (room temperature)[3]

Only recently it has become possible to apply a constant loading rate while recording the tomography images continuously. It requires a high-precision apparatus allowing exposure of the sample to X-ray over 360° while rotating the sample with a relatively high angular speed under a designated loading. To meet those requirements, a bespoke loading rig (called P2R) was generously provided by Prof. P.D. Lee [148], [149]. The mechanical test rig (figure 4.3(a)) allows the continuously rotation of the specimen up to 1 Hz over 0-360° with a loading capacity of 500 N (0-150 mm extension). A customized fixture (figure 4.4) was designed and manufactured for this experiment from Pyrophyllite Ceramit 14 (Aluminium Silicate, maximum temperate over 1250°C) to permit the diametric C-ring compression test via the P2R's loading arms. The fixture includes a seated platen for the C-ring sample and a close fit on the other loading arm end. The

[3] Beam line number EE12581-2 in Dec 2016.
For this test, I designed the experiment with the customized load mounting stages. I conducted the experiment with the help from collaborator Dr. B. Cai from University of Manchester (Lecturer in University of Birmingham now).

groove size of the sample holder is marginally larger (approximately 0.2 mm) than the sample width to avoid any possible thermal expansion effects. The C-ring sample, mounted with top and bottom holders, was placed on the loading rig. The C-ring sample was carefully handled and preloaded with 5 N in the fixture. Then, before the start of the *in situ* experiment, the rotation axis of P2R stage was manually aligned with the centre of the detector, using the 0° and 90° radiographic images. Once started, the compression loading of C-ring sample was set at a continuous rate of 0.5 μm/s. In the meantime, the recording of the tomography commenced.

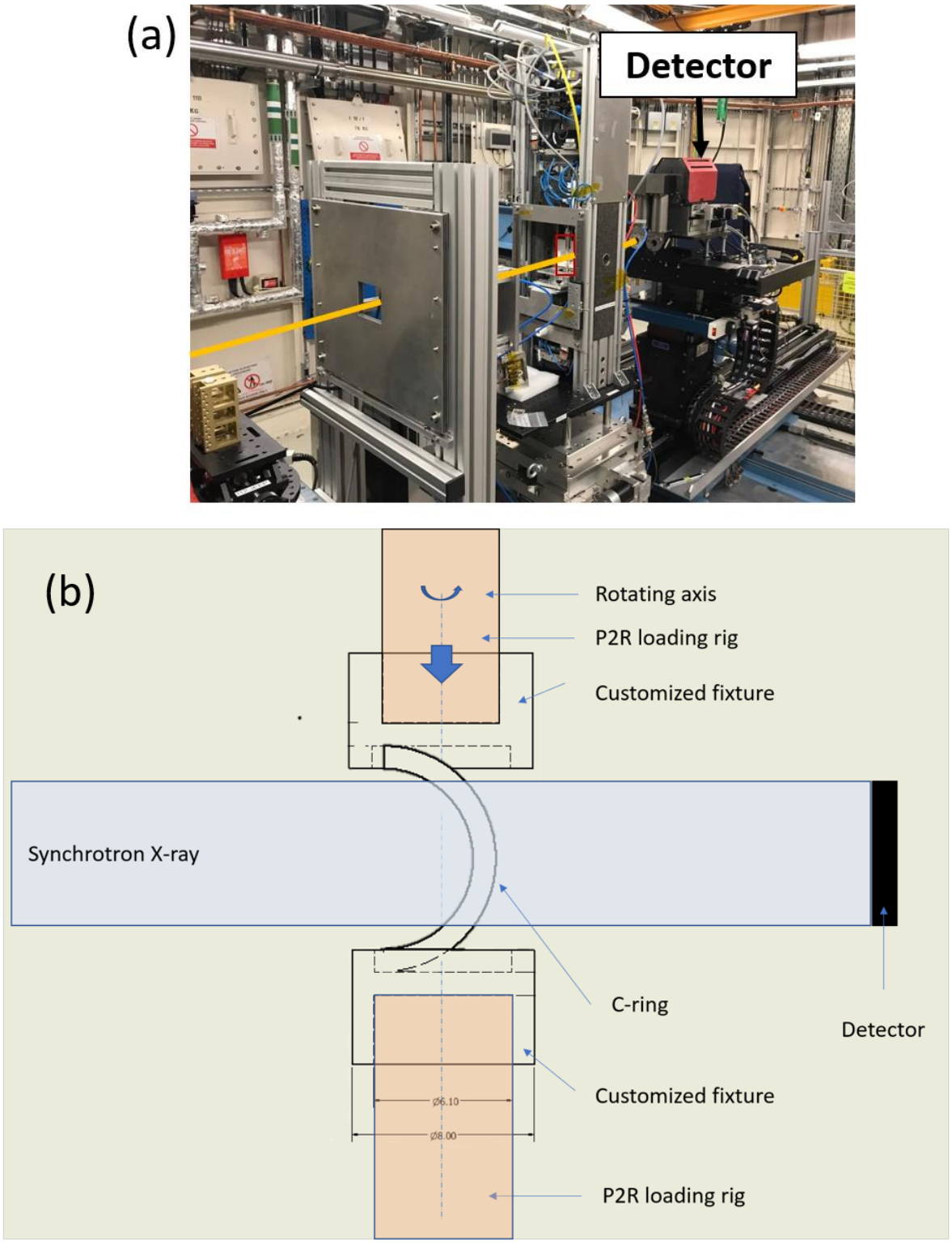


Figure. 4.3: (a) The photo of the bespoke P2R loading rig at the Dimond I12 beamline; (b) Schematic of the experiment setup with the customized fixture for bespoke loading rig in the C-ring compression test.

The time-resolved high-resolution X-ray tomography was also carried out in the Joint Engineering, Environmental and Processing (JEEP – I12) beam at the Diamond Light Source. The radiography was recorded by the high speed PCO.edge camera [108]. The optics was selected as Module 3 with a field of view (FOV) covering 8.5 mm × 7 mm and a pixel size of 3.25 μm, which is same as the previous 3D *in situ* experiment (figure 4.2). However, in the time-resolved mode, each three-dimensional tomogram consists of 900 projections over a full angle of 180° rotation, with the exposure time for one projection being 0.01 s. With user-defined rotation and data transferring, the time for each cycle was 20 s. This allows continuous recording of the C-ring during the diametrical compression.

When the C-ring lost 80% of its ultimate strength (i.e. 80% of peak load), the experiment was stopped manually. In total, 38 tomograms were collected during the continuous C-ring compression experiment, over a period of 760 s, during which the travel of the crosshead was 0.38 mm. Each tomogram is reconstructed using a filtered back-projection algorithm with a ring remover method [150] from Diamond.

With the help of the high-speed camera, the pictures can capture the key features in the sample continuously. Figure 4.4 shows the reconstructed images of the C-ring specimen at the same location from a continuous scan (4D) and a subsequent static scan recorded using the same parameters. There is no noticeable difference between the qualities of the images between those two modes. Therefore, no further procedure was taken to improve the quality of the 4D images. The stacks of tomogram images were converted from 32 bits to 16 bits and then post-processed in the ImageJ software with a Gaussian filtered (spatial resolution of 1 pixel) applied, as in the previous experiment.

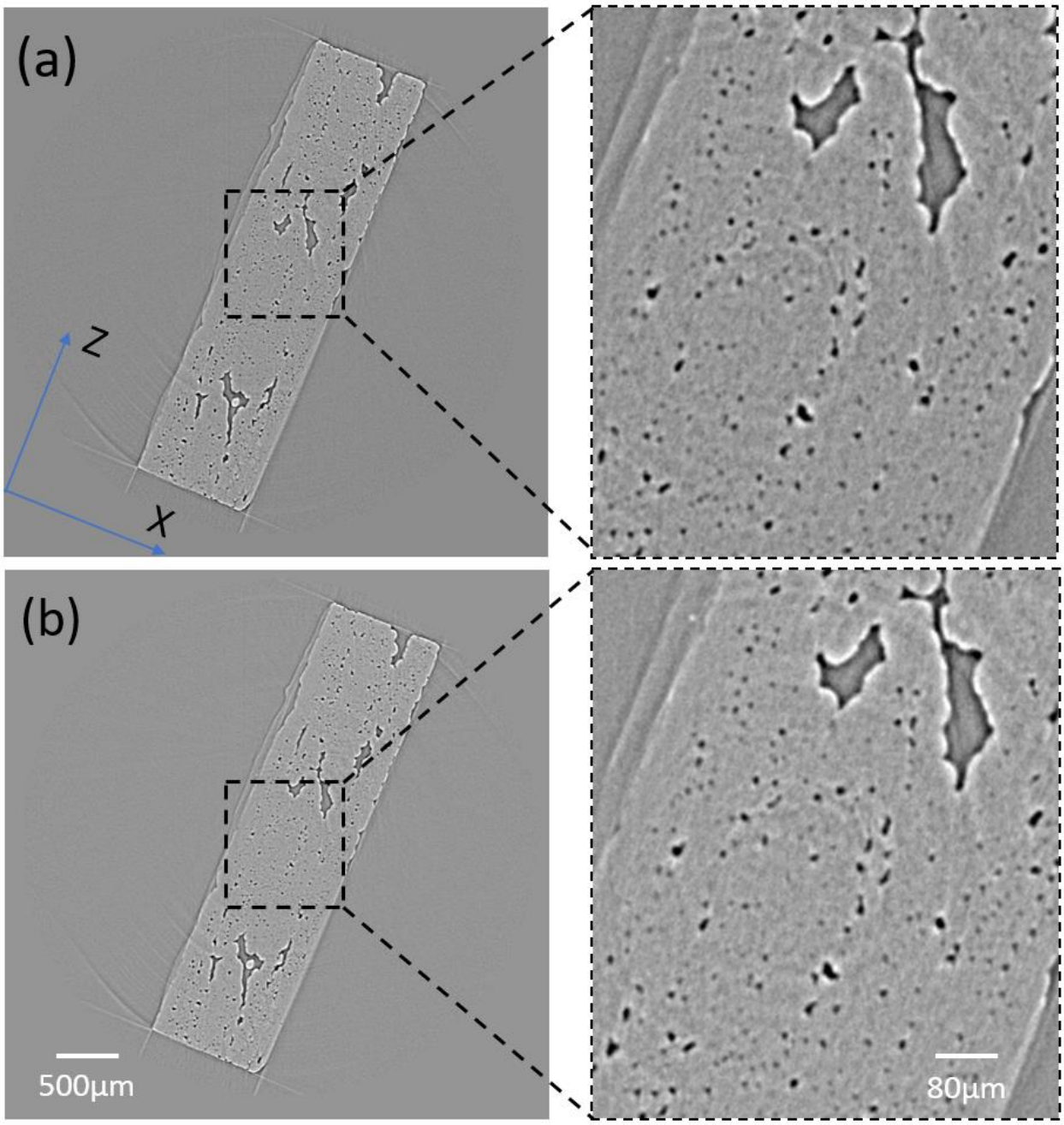


Figure. 4.4:(a) The reconstructed slice image of a static tomography without the movement of the crosshead during the scanning; (b) the reconstructed slice images of the 4D tomography with a crosshead speed of 0.5µm/s during the scanning at the same location as (a) in C-ring specimen. All the acquisition and reconstruction parameters are the same in (a) and (b).

4.2.2.3. Continuous (time-resolved) scan of a diametric C-ring (High Temperature)[4]

The sample preparation and the loading fixture are the same as in the previous time-resolved experiment at room temperature. The sample was equipped in a resistance furnace during the *in situ* testing, with the furnace wall shown in the figure 4.5 (b). Due to the spatial restriction caused by the furnace wall, a commercial double-sided adhesive paper (3M Company) was applied to mount the C-ring sample to the fixture. The adhesive paper burned up soon after the temperature reached around 200°C, which was confirmed with the real-time X-ray radiographic images (figure 4.5 (c)). The X-ray beam passes through the furnace via two aligned aluminium 'windows' in the furnace wall. Three separate K type thermocouples were placed on the top, bottom and near (about 10 mm away) the middle of the sample to control and monitor the temperature in the furnace chamber during the experiment. The thermal insulation was also used to fill the spacing between the rotating loading rigs and furnace. It should be mentioned that the experiments were conducted in an *air atmosphere* without inert gases in the furnace. The heating rate was set at 40 °C/min. During the heating, due to the thermal expansion of the composite, there was compression force applied to the specimen. This heating-induced force was released by continuous manual control of the crosshead displacement to ensure the pre-load force on the sample never exceeded 10 N. The heating stage finished at 900 °C, followed by an isothermal holding time of 10 mins to ensure an isothermal environment before the start of the compression test. Once started, the compression

[4] Beam line number EE12581-2 in Dec 2016.
For this test, I designed the experiment and the customized load mounting stages. I conducted the experiment with the help from collaborator Dr. B. Cai.

loading of C-ring sample was set at a continues non-stop rate of 0.5µm/s. In the meantime, the recording of the tomography commenced.

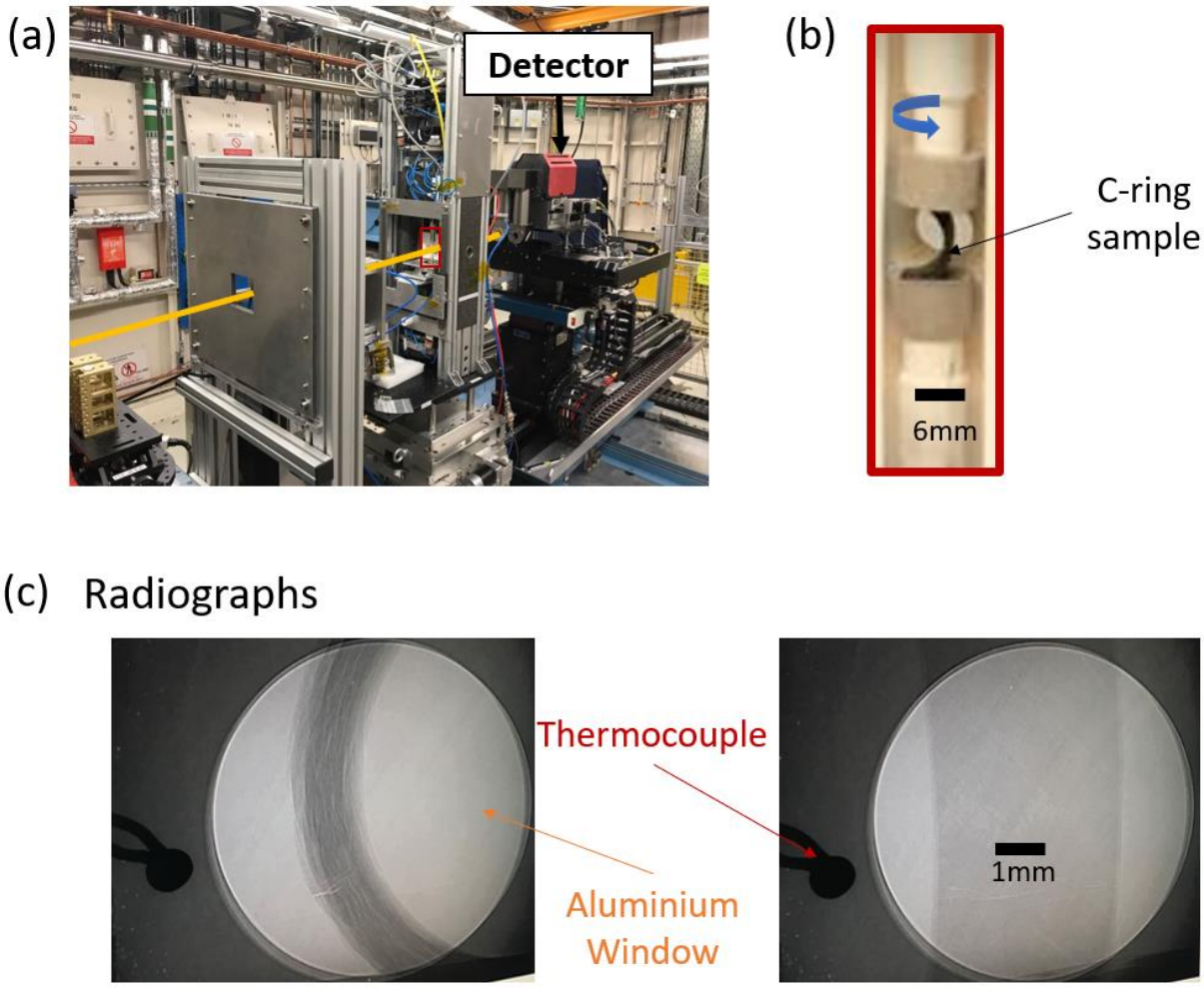


Figure. 4.5 (a) The bespoke mechanical testing rig with the resistive furnace at Diamond Light Source I12. (b) Photo of the C-ring on loading fixtures with inbuilt rotation in the furnace. (c) Examples of real-time radiographs during experiments.

The synchrotron X-ray observations at elevated temperature was also carried out on the JEEP – I12 beamline at the Diamond Light Source. The same settings were used as in the previous test at room temperature. Due to the geometric restriction by the furnace window, as shown in figure 4.5(c) and (d), the field of view (FOV) was further cropped into Φ 6.0 mm. Nevertheless, the

region of interest was covered entirely throughout the sample width, and the final cropped images are in the similar size as the room temperature test. All the synchrotron tomographic images have a pixel size of 3.25 μm, with an acquisition time per tomograph of 20 s.

The tomographic setting and loading configuration were the same as the 4D experiment at room temperature. The same number of tomograms were collected during the continuous C-ring compression for a good comparison. The reconstructed images at elevated temperature with a smaller mean grey level due to attenuation from the aluminium windows. After adjusting the brightness and contrast, the images show no detectable difference before any image filter has been applied, as in figure 4.6. Therefore, no specific procedure was taken to improve the high temperature image quality.

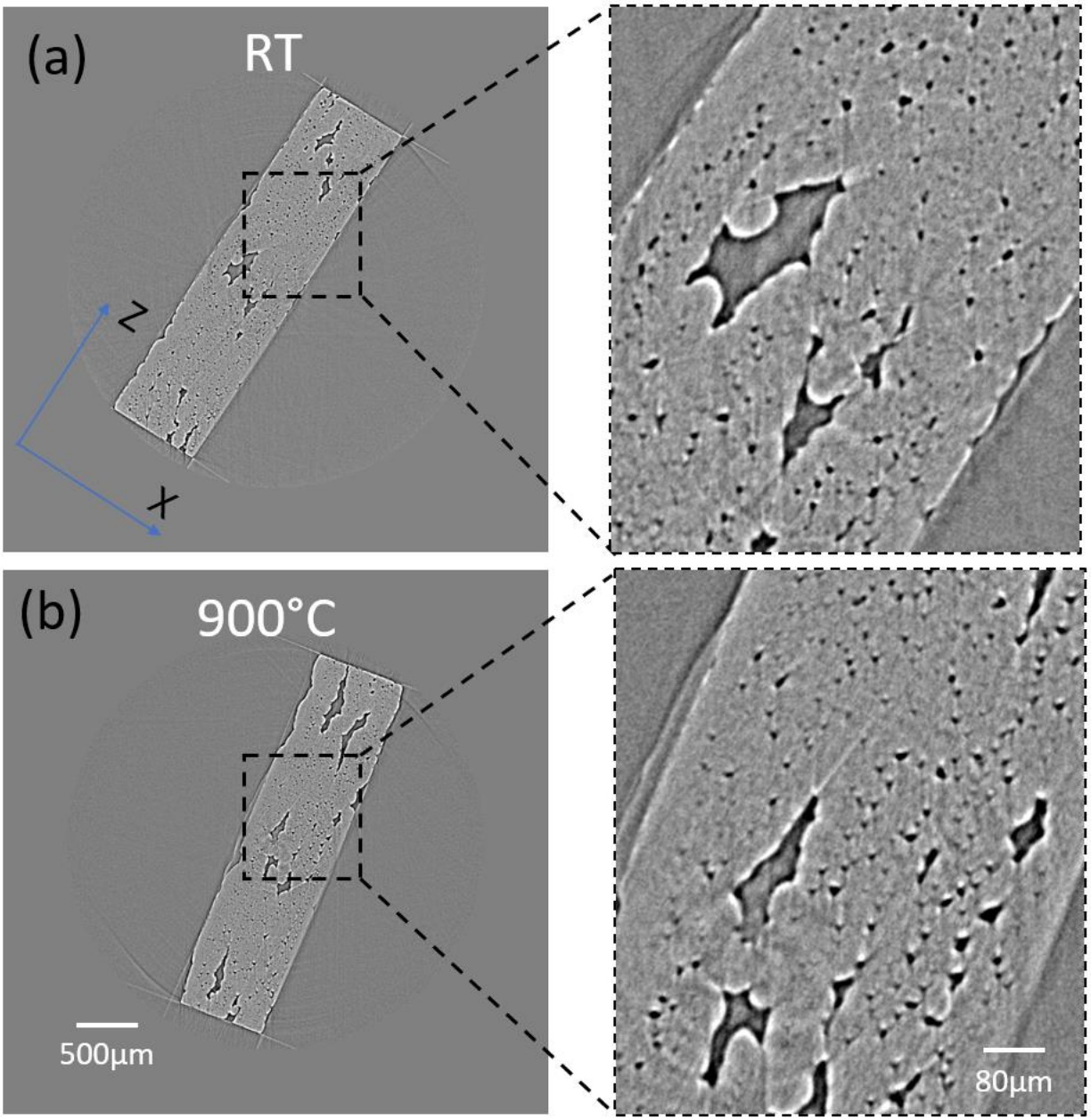


Figure. 4.6: The reconstructed image slice of in the experiment at (a) room temperature (RT) without the furnace and (b) at 900°C with the furnace.

4.2.2.4. Loading state of the C-ring.

In the C-ring diametric tests, the compressive force is applied via the crosshead of the loading rig to initiate damage in the middle of the C-ring sample. The elastic properties of the SiC/SiC composite C-ring sample can also be obtained using a simple curved-beam theory stress solution. The method used in this study is derived from a standard test method to evaluate the strength of the *advanced ceramics* in tubular form, ASTM C1323-10 [144]. Due to the geometry of the C-ring and the relatively small size of the C-ring sample, the use of strain gauges may not be applicable. However, the stress state could still be calculated based on the simple curved-beam theory. In this study, with the help of the *in situ* X-ray tomography, the method can be further improved with real time monitoring. The corresponding real-time tomography images were also examined to ensure there is no damage in the sample, to ensure the stress state is still in the elastic region.

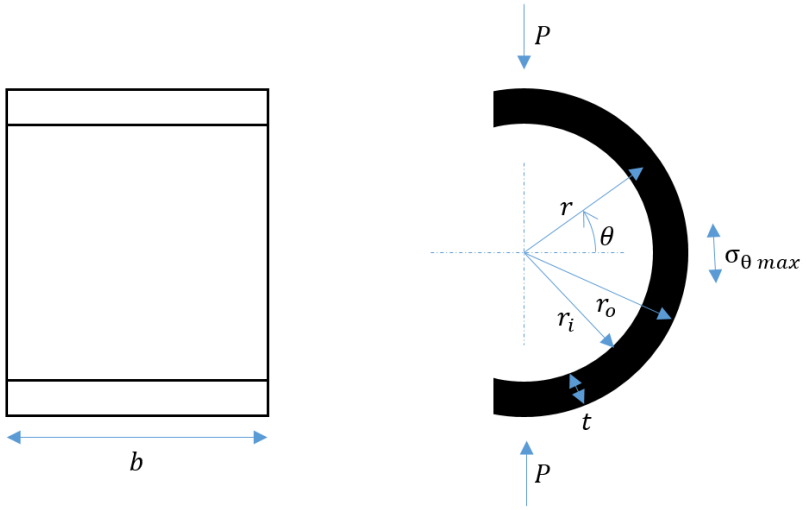


Figure 4.7: C-ring test specimen and defined geometry parameters, the radius r and angle θ refer to the position of the damage (after the ASTM standard [144])

The stress state of the C-ring, such as shown in figure 4.7, can be computed from the force-displacement data of the crosshead via curved-beam theory, from the following expressions [144]. Equation 4.1 calculates the strain rate ($\dot{\varepsilon}$) from the crosshead speed ($\dot{d}$). Equation 4.3 shows the predicted tensile stress (σ_θ) in the C-ring sample from the applied compressive load, P. Eventually, the elastic modulus (E) can be defined as in Equation 4.4 from the previous two expressions. Other variables are shown in Figure 4.7, where r_o is the outer C-ring radius, r_i is the inner C-ring radius, b is the sample width, t is the sample thickness, θ is the reference angle and the term R is defined in Equation 4.2. Based on equation 4.3, the maximum tensile stress is expected at the middle part of the C-ring on the convex side, where it should be vulnerable to the damage initiation.

Strain rate

$$\dot{\varepsilon} = \frac{(r_o - r_i)^2}{6\pi r_a^3}\left[\frac{R\left(r_o - \frac{r_o + r_i}{2}\right)}{r_o\left(\frac{r_o + r_i}{2} - R\right)}\right]\dot{d} \tag{4.1}$$

$$R = \frac{r_o - r_i}{\ln(\frac{r_o}{r_i})} \tag{4.2}$$

Tensile stress

$$\sigma_\theta = \frac{PR}{btr_o}\left[\frac{r_o - r_i}{r_i - R}\right]\cos\theta \tag{4.3}$$

Elastic Modulus

$$E = \frac{d\sigma}{d\varepsilon} \tag{4.4}$$

4.3. Results

4.3.1. Overall observation

4.3.1.1. Static scan with cycling loading

Under the cycling diametric loading, the 3D rendered images (figure 4.8) show the cracks in the C-ring while it was mechanically loaded to the peak stress and also after the loading. The extensive cracks are obvious at the surface when the sample reaches the high loads. The damage evolution within the C-ring under loading is also illustrated by the *in situ* virtual slice images in figure 4.9, which illustrate the cracks inside the C-ring sample 1.5 mm from the cut edge. Matrix cracks were first observed in the images at 60 N (cracking may have occurred at lower load, however). The surface crack appeared at the outside convex surface as shown in figure 4.9(b) (60N). It is interesting to find that more than one crack was observed at the surface. Three separate surface cracks are observed at the same time near the middle plane. The multiple cracks became more noticeable when the loading increased to 110 N as shown in figure 4.9(c). At this stage (figure 4.9(c)), the number of surface cracks also increased. All the surface cracks span the entire sample width at the outer surface (in Z direction) (figure 4.8(b)).

By contrast, the fractured sample (figure 4.9 (e)) shows the extensive matrix cracks are associated with the pores, indicating the paths of the matrix cracks may be linked with the microstructure. The path of the critical crack is also confirmed in the fractured image (figure 4.9 (e)) showing that the critical crack propagation tends to deflect along the fibre tow boundaries. Delamination between the fibre tows were also observed as the crack is linking the large pores. However, there is no damage observed at the concave side of the C-ring sample even after the peak loading. The cracks from the convex side seem to be dissipated inside the sample. Eventually, even after the peak loading, with the further compression, the C-ring sample was still in one piece.

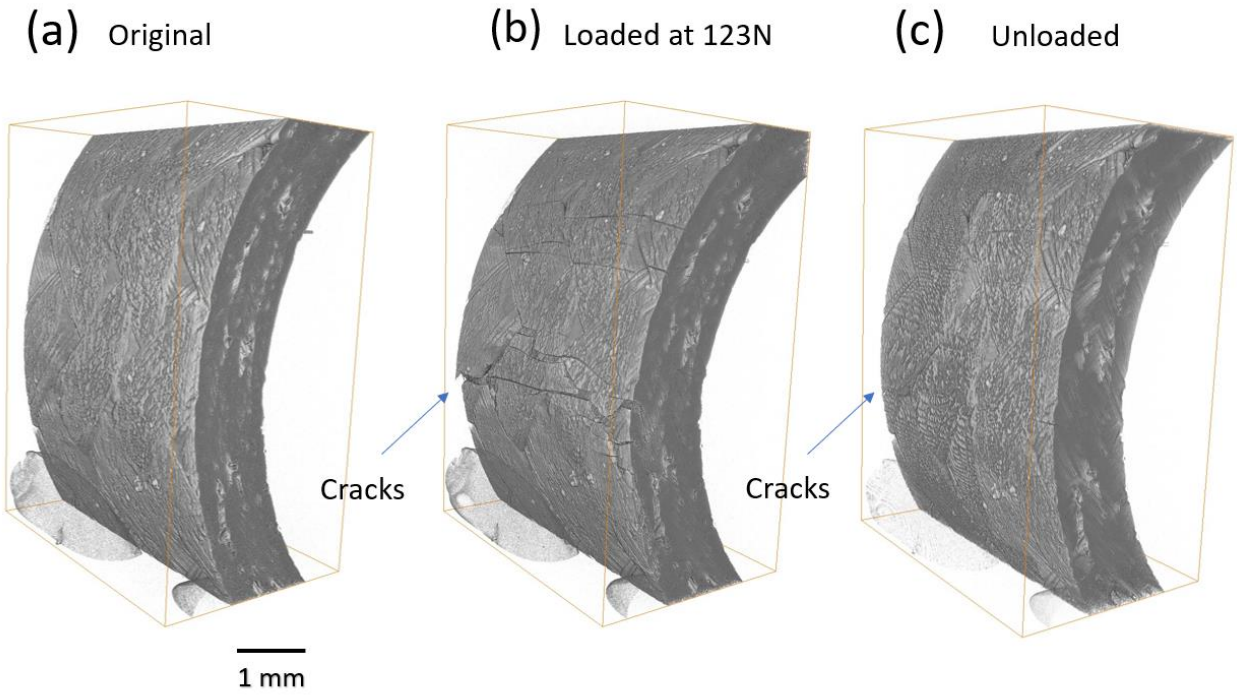


Figure. 4.8: 3D rendering of the in situ XCT data show (a) the original C-ring, (b) the peak loading the 123N with the obvious cracks, and (c) the unloaded sample after the peak loading.

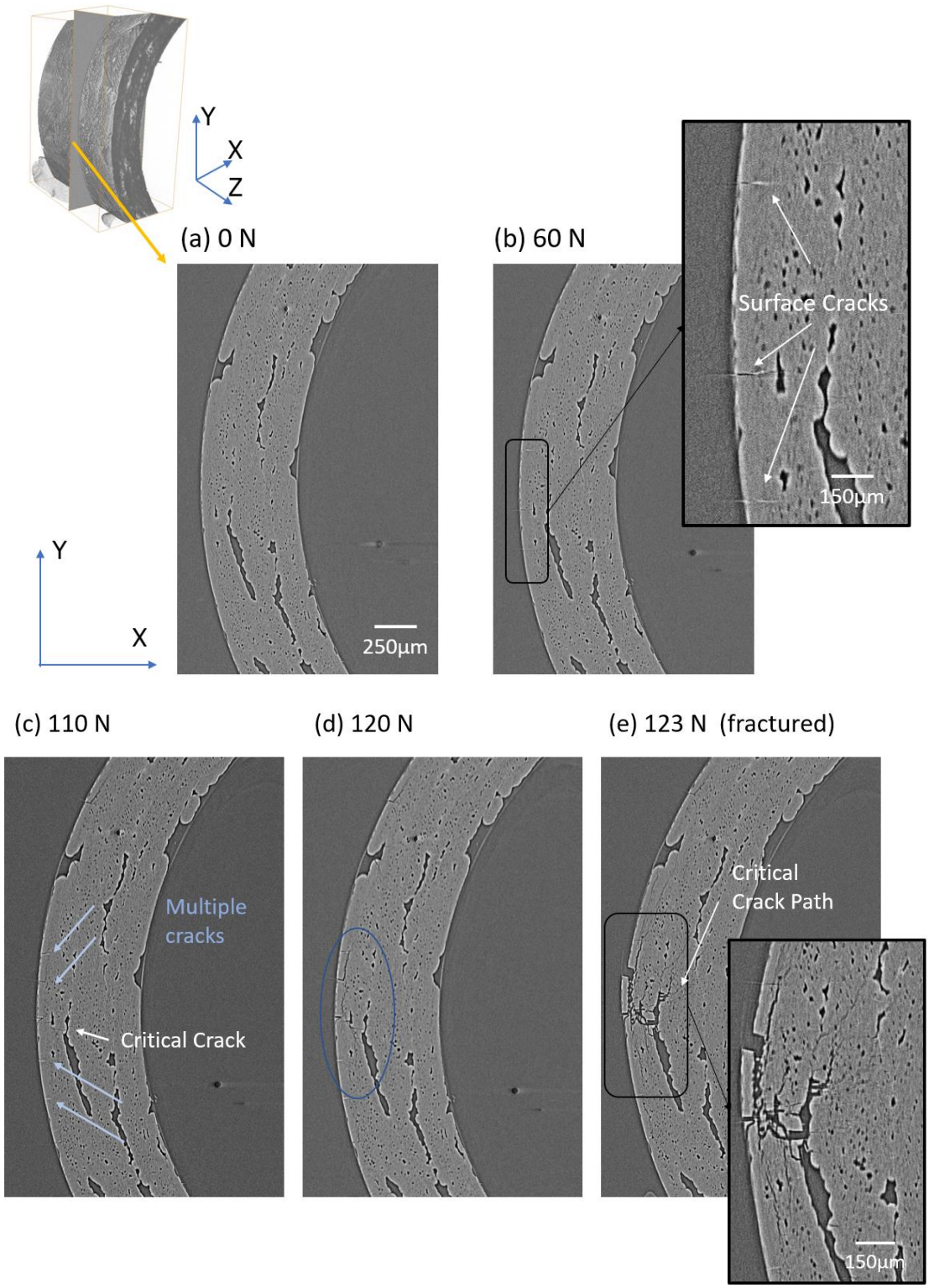


Figure. 4.9: The in situ XY virtual slices (1.5mm from the edge) of the C-ring sample showing the damage evolution inside the C-ring sample at each loading stage, (a) the original state, 0N; (b) surface cracks, 60N; (c) multiple damages, 110N; (d) crack propagation, 120N; and (e) fractured sample, 123N.

The 3D structure of the crack path can be visualised using the *Avizo* software with a suitable segmentation method. However, due to the complicated microstructure of the pores in different sizes and interacting damage, automated segmentation could not be applied directly in this study. To illustrate the spatial relationships of the matrix cracks and pores, a manual selection was applied. A typical large pore located at the middle part of the C-ring, between the first and second braided layers, is shown in figure 4.10(a). The surrounding matrix cracks were presented in red in the 3D images figure 4.10(b) with the pores. Even though some cracks were bridged by the large pore, most matrix cracks propagate across the pore without any deflection effect as shown in figure 4.10(b).

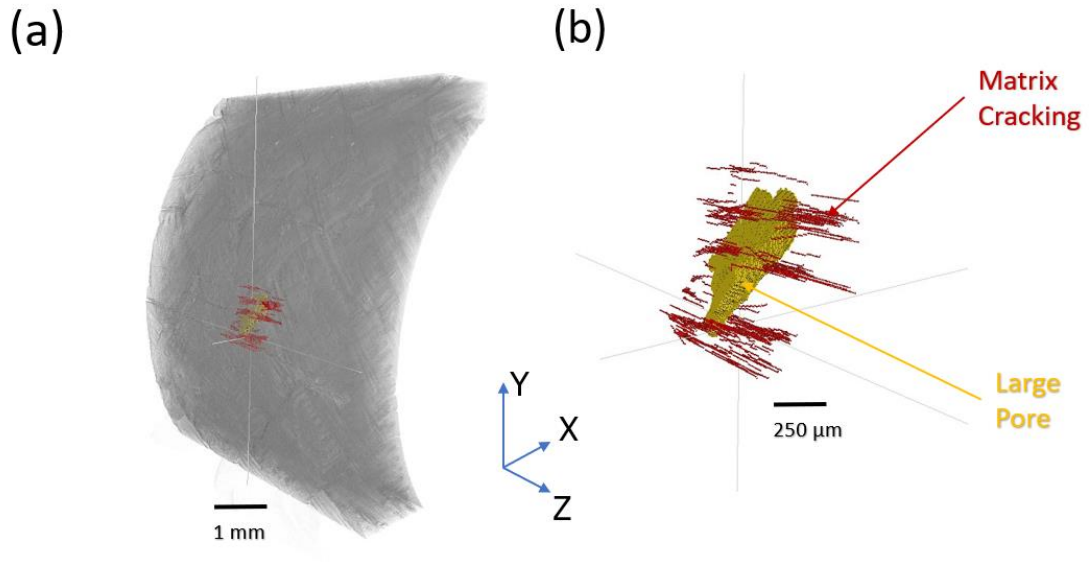


Figure. 4.10: The 3D view (b) of three adjacent matrix cracking (in red) around a segmented large pore (in yellow) at 120 N. Its location in the C-ring specimen is shown in the (a).

To understand the accumulative damage in the cycling loading, the loading-unloading sequential images were also compared. During the unloaded stages, the C-ring sample recovered some of the applied deformation. Generally, partial closure of the axial cracks was observed when the load was

removed (figure 4.11). Meanwhile, when the load was sufficiently high (120 N), one interesting phenomenon was not previously reported that the axial crack closure can be accompanied by circumferential crack propagation near the surface region, which is parallel to the previous applied tensile stress. The progressive delamination effect is shown in the figure 4.11(b). This indicates quite complex behaviour during the unloading process. Nevertheless, the maximum crack opening is generally smaller in the unloaded images compared with that under loading. Some of the partially closed cracks in unloading states can barely be distinguished, especially within the sublayer structure in the XCT images. However, even though the damage was relatively very small, here, by comparing the two *in situ* sequential images at the same location, this phenomenon is successfully observed.

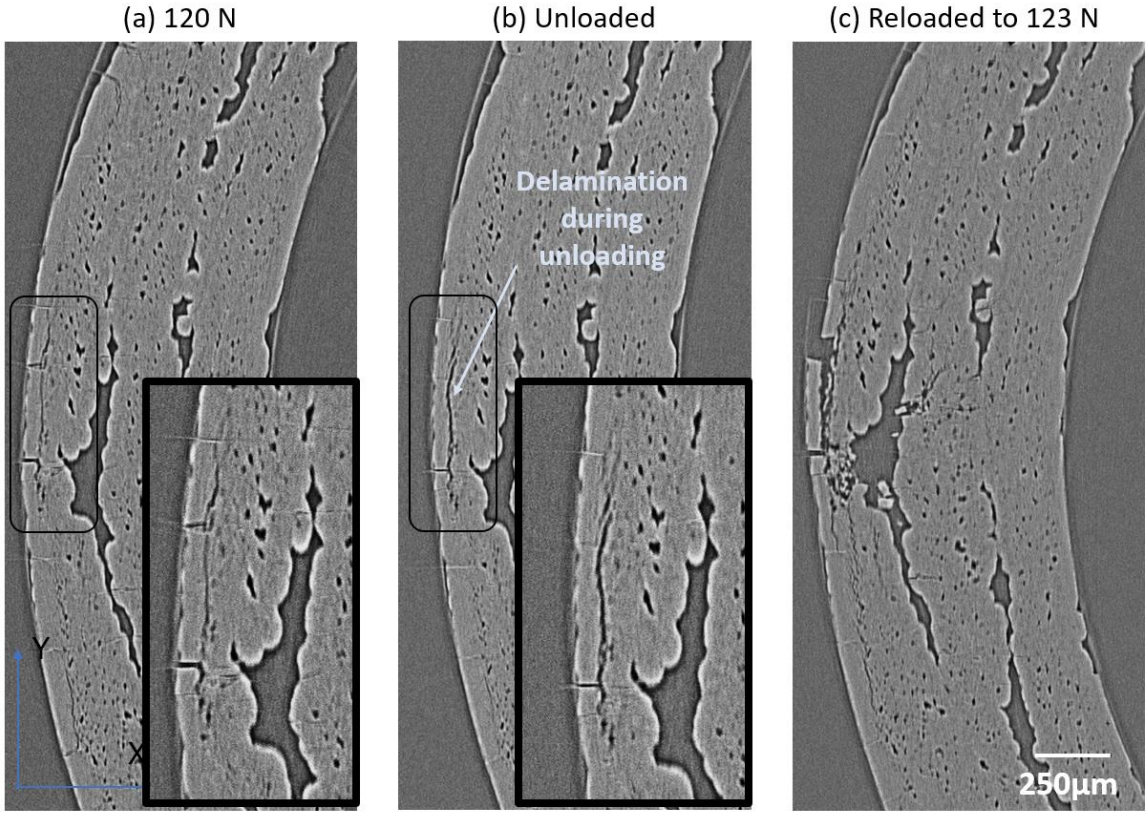


Figure. 4.11: The XY virtual slices of show the damage during the sequential cycling loading at (a) 120N (b) unloading, and (c) reloaded to 123N.

4.3.1.2. Continuous scan under monotonic loading (Room Temperature)

In the continuous scan mode, the sample is kept spinning while exposed to the X-rays. There was a regular fluctuation in the loading readout as the sample span during the experiment, as shown in the Fig. 4.12(a). Data for one typical loading versus angular position history (scan No. 20) is enlarged in the inset (top left). The loading rig is rotating at an angular rotation speed of ~17.7 °/s. The regularity of the fluctuation corresponds to the rotation of the rig. The average standard deviation of the load in each scan or a full cycle of rotation is approximately 2.5 N, which is considered as the uncertainty of the load measurement in this study. For demonstration purposes, in each full cycle rotation, the data were then filtered using an arithmetic moving filter in MATLAB for a sine wave. Each cycle of the sine wave was then replaced by the four moving quadrantal average of sine curve. The averaged points were set to be 40°, 120°, 210° and 300° in each full rotation. This method preserves the sudden increases or drops in the curve effectively. The filtered load versus displacement curve is illustrated in Fig. 4.12(b) and the original data is illustrated in Fig. 4.12(a).

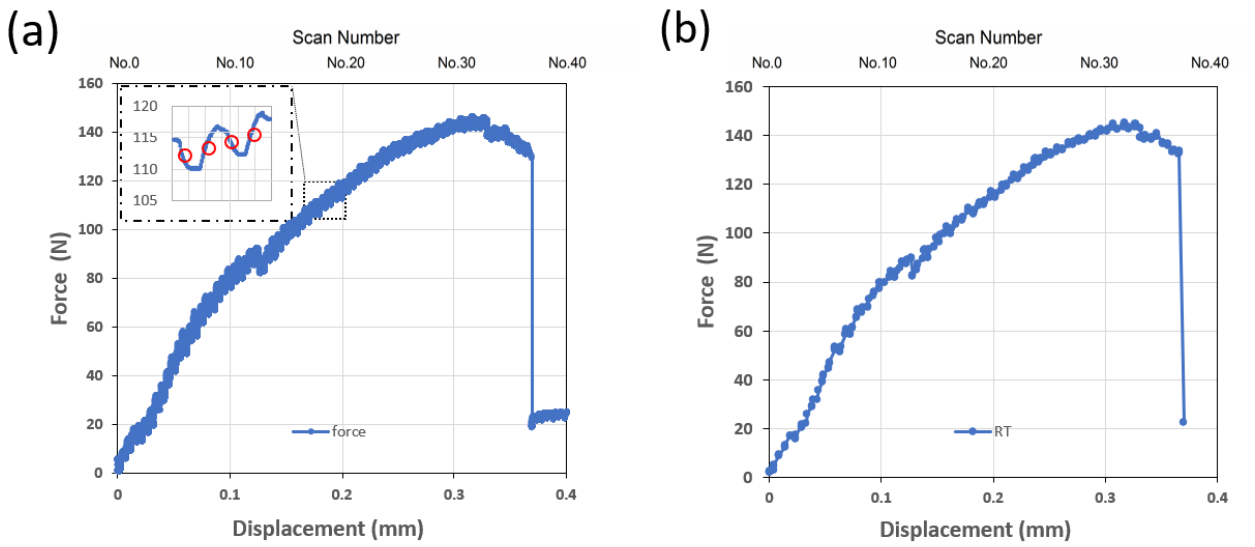


Figure. 4.12: (a) The raw force development during the continuous experiment; the periodic fluctuation of force due to rotation is shown in the enlarged window; the red hollow circles indicate the selected data from a moving average filter, (b) the filtered curve of the force versus displacement.

Figure 4.13 shows the force and displacement applied by the crosshead. The curve can be arbitrarily divided into four regions. In the first region, the load gradually increases linearly from the beginning until around 55 N. Then, in the second region, there is a non-linear behaviour observed with a gradual decrease in the gradient before a sudden load drop is witnessed at 87N, 0.13 mm. Between this load drop, the gradient increased slightly when it enters the third region. Then the non-linear behaviour continuous, with a peak load at 145 N and 0.33 mm. Finally, shortly after the peak loading, in the fourth region, the C-ring failed at the point 137N, 0.37 mm. The final fractured C-ring sample lost over 85% of its peak capability in load but it failed gracefully and remained in one piece even after the unload. Figure 4.14 shows the 3D rendered view of the fractured C-ring after the peak loading.

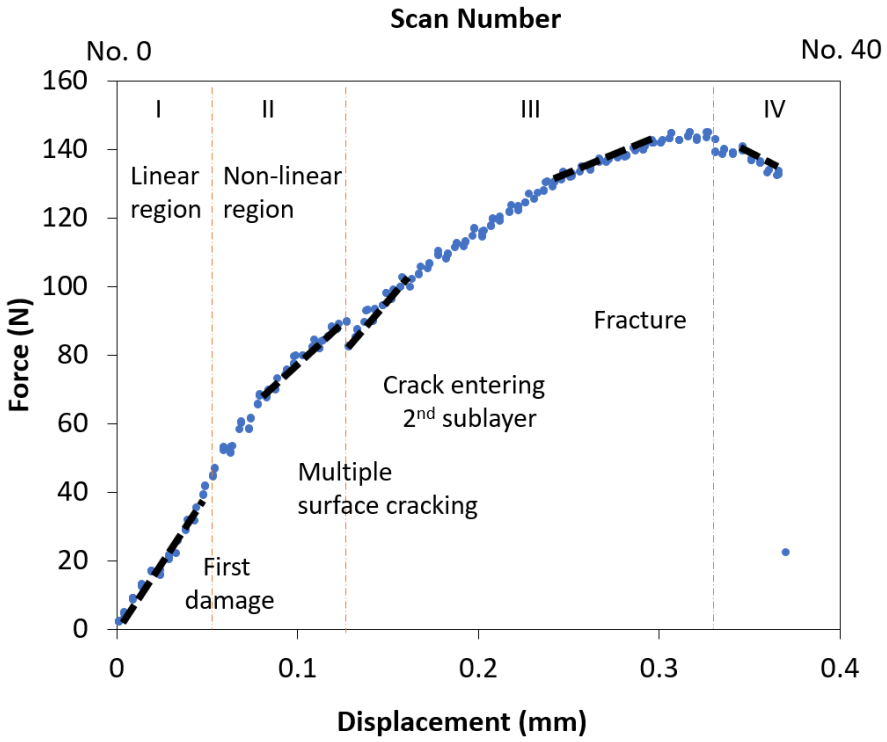


Figure 4.13: Force and displacement curve applied by the crosshead in the continues experiment

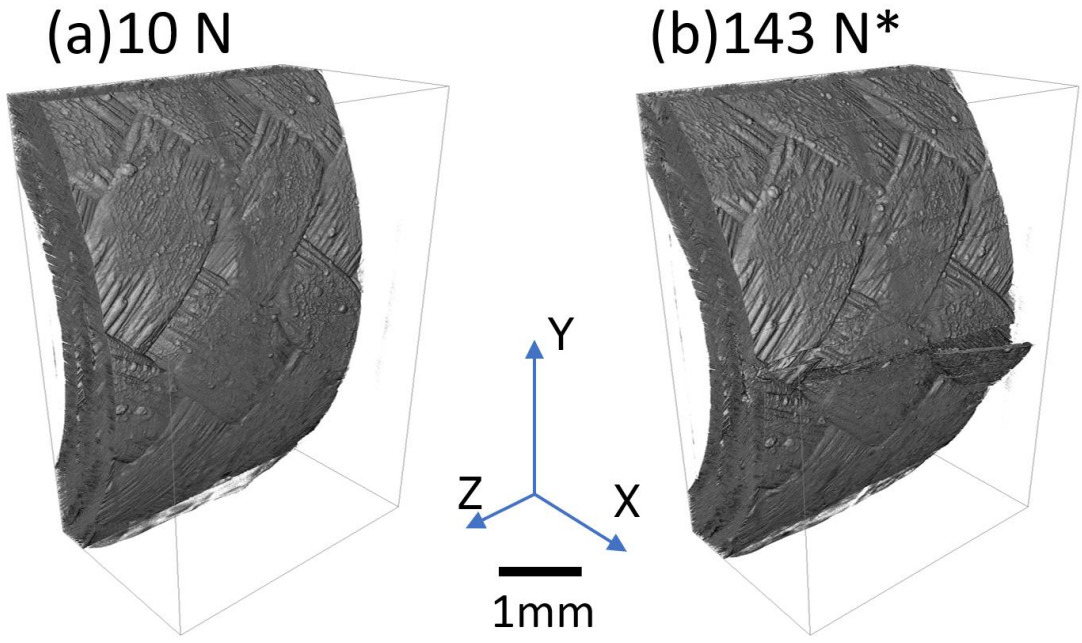


Figure 4.14: 3D rendering view of the C-ring tomographic image at the (a) original state and (b) the fractured state (* peak loading value).

The corresponding virtual sections of the 3D tomographic images of the load versus displacement curve (figure 4.13) are presented in the Figure 4.15, to illustrate the accumulative damage. The vertical slices were taken at the position of 1.5 mm from the sample edge. Figure 4.14(a) shows the image of the sample at the original state. As the load increased to 55N, 0.07 mm, the first crack initiated at the middle plane of the convex surface (i.e. where the stress is maximum, figure.4.14(b)). Then, as the non-linear behaviour began in the load profile, multiple matrix cracks occurred at the outer surface. The crack also propagated into the fibre-rich region in the first ply layer of the C-ring composite. Those phenomena correspond to the non-linear region in figure 4.13, where there was a decreased gradient, before the first sudden drop. In the third region of the load profile, the image (figure 4.15(c)) shows further crack propagation including an increase of the matrix crack density at the surface and propagation of the critical crack. Cracks near the middle plane start to be observed in the second ply layer. In the second ply layer, the damage was not necessarily as the same location as in the first sublayer nor connected to the pre-existing cracks from this virtual slice images. Images obtained just before the fracture and after the fracture are presented in figure 4.15(e) and figure 4.15(f), respectively. Before fracture, the cracks became connected between the ply layers and the path preferably follows the boundaries between the fibre tows as in figure 4.15(e). After its peak loading at 143 N, the sample fractured. The fractured sample of figure 4.15(f) shows excessive damage, with the crack path being deflected by the fibre architecture. Interestingly, its critical crack path is different from where the most intensive damage was observed before the fracture in figure 4.15(e).

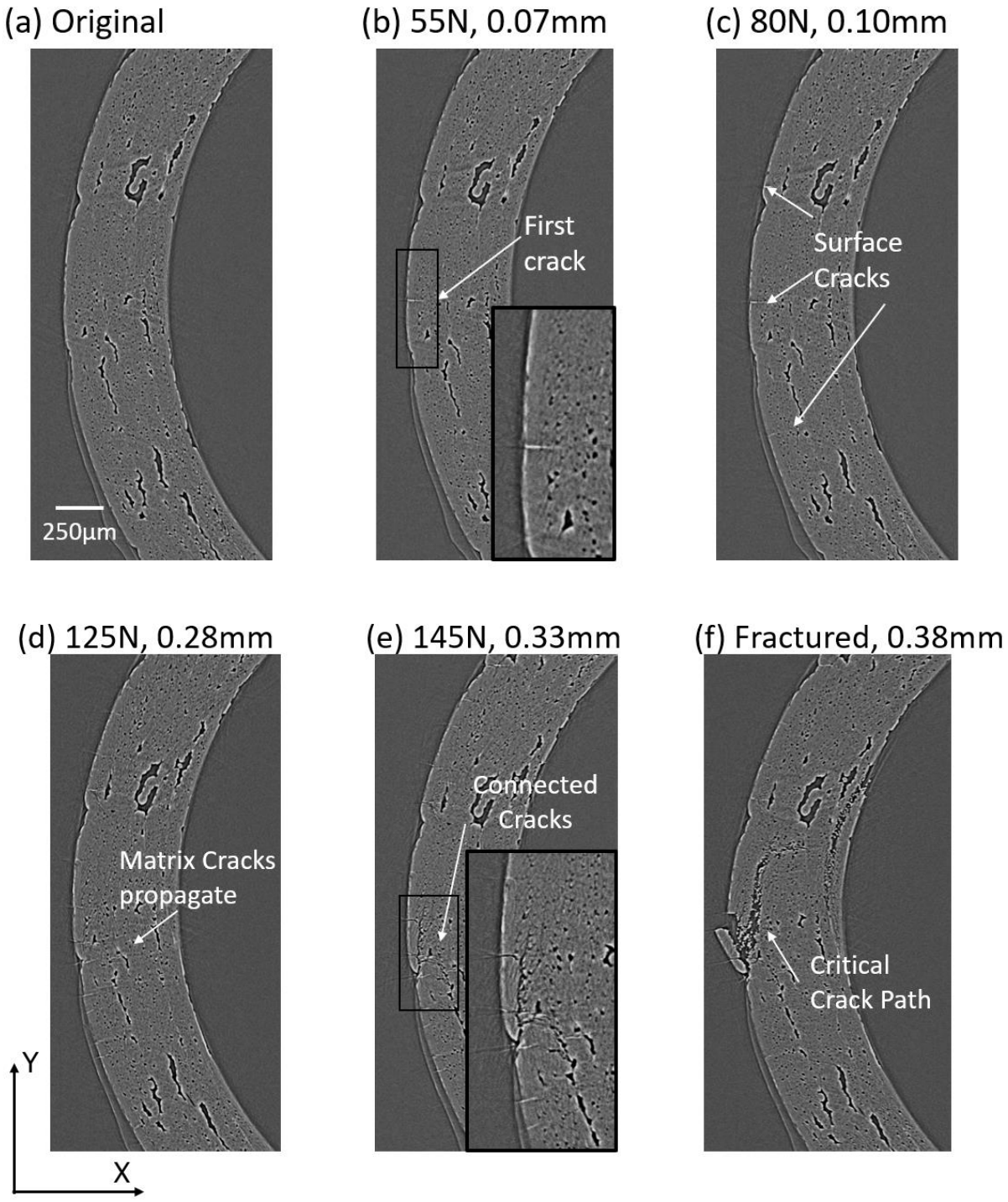


Figure 4.15: The *in situ* X-Y virtual slices (1.5mm from the edge) of the C-ring sample in the 4D tomography images showing the damage evolution inside the C-ring sample. (a) the original state, 0N; (b) first crack, 55N; (c) multiple cracks, 80N; (d) crack propagation, 125N; (e) peak loading at 145N and (e) fractured sample.

The Y-Z slices of the images just before and after fracture are also presented in figure 4.16 and figure 4.18. They show how the crack is affected by the fibre tows along its propagation direction. Figure 4.16 shows the features of the matrix damage just before the final fracture. The path of each matrix crack, showing little effect from the fibre architecture, was flat at the surface and within the C-ring. As there were multiple matrix cracks opening, the critical crack paths could connect to each another at the location of the fibre tow crossover (figure 4.16(a)). Within each of the fibre tows, the matrix crack become less obvious in the tomography images, but fibre breaking with pull-out within the composite layers along the crack path was observed (figure 4.16(b) and enlarged in figure 4.17). It is also interesting to note that the heterogeneous distribution of the fibre-break cluster and the fibre-bridging near the path of the matrix cracking.

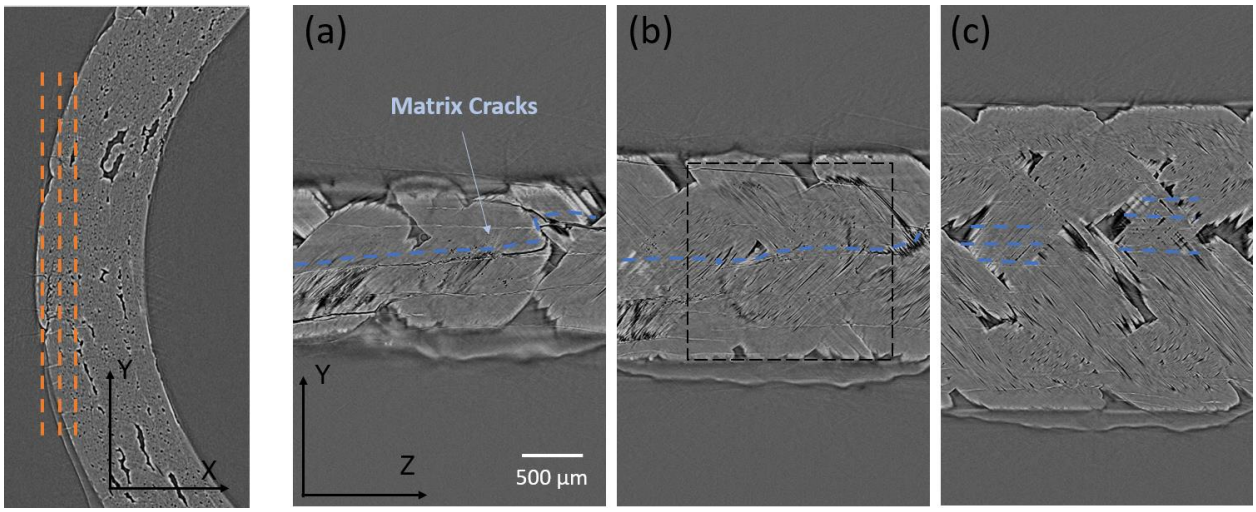


Figure 4.16: Y-Z virtual slice of the images before the final fracture (d = 0.36mm) showing the damage in different layers. The offset dashed blue line for increased visibility of the crack path.

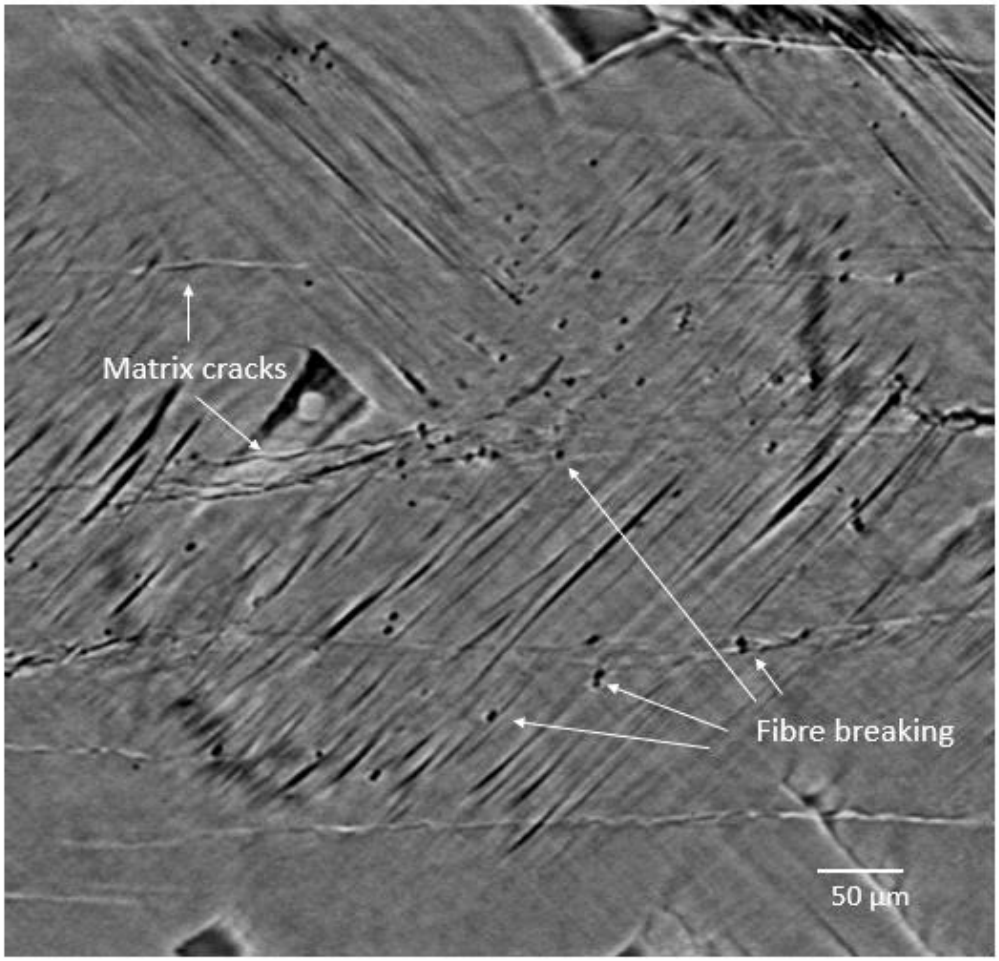


Figure 4.17: The enlarged picture of the black region in figure 4.16 (b).

The Y-Z images of figure 4.18 displays the more excessive damage within the composite after the fracture. The critical crack path that follows the matrix crack initiated from the surface (figure 4.18(a)). However, its final crack path then shows a strong effect of the fibre architecture, when it propagates into the composite as shown by the blue line in figure 4.18(b) and figure 4.18(c). The crack path gradually switched to follow the crossover of fibre tows from a relatively flat shape at the surface. Within the fibre tows, the cracks were associated with extensive fibre breakages. Interestingly, as the crack propagated in a different ply layer, the deflection become less obvious as the matrix crack becomes smoother shown in the figure 4.18(d). In brief, the accumulative

damage process was observed to be associated with the fibre architecture. The ‘Zigzag’ path of the critical matrix crack due to deflection is observed both in the scale of the fibre tows as it follows the fibre tow boundaries and in the scale of individual fibres which is observed next to the fibre breakages.

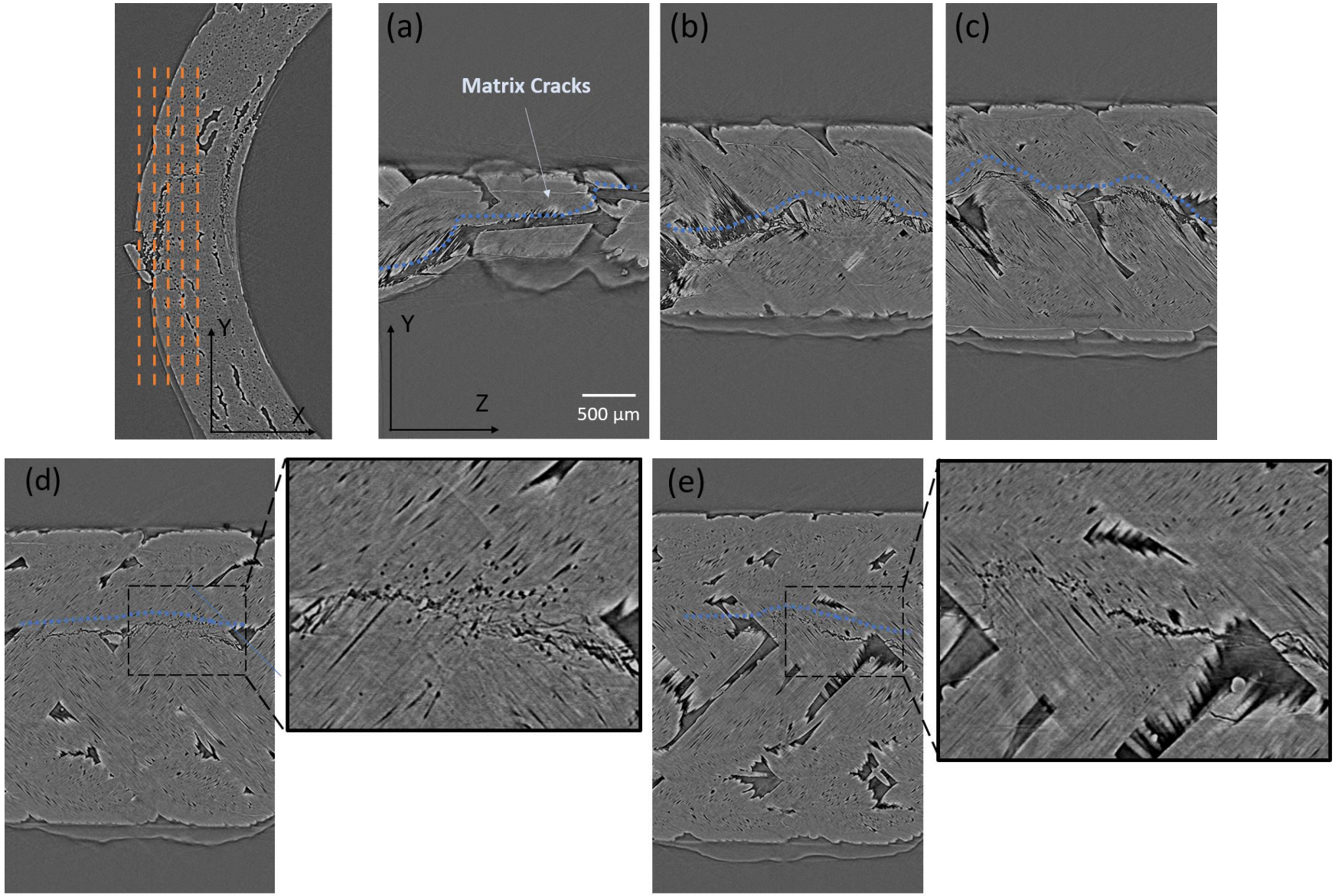


Figure 4.18: YZ virtual slice of the images after the fracture (d = 0.38mm) showing the critical crack path along the sample thickness. The offset dashed blue line for increased visibility of the crack path.

4.3.1.3. Continuous scan at high temperature

With the constant compression rate, the force-displacement profile from the loading rig is shown in figure 4.19 at 900°C. At this high temperature, the C-ring sample failed at around 83 N, but C-ring remained in one piece, as shown in the tomographic image in figure 4.20. Inside the C-ring, figure 4.21 of the reconstructed longitudinal slices illustrated the crack evolution at 900°C. The cross-section images are 1 mm away from the edge. The first detectable surface cracking occurred at ~30 N (d=0.05mm, figure 4.21(b)), at the middle of the outer surface. Then, as in figure 4.21(c) multiple cracks initiated from the outer surface, with the opening of the exiting cracks. Meanwhile, there is a gradual decease of the gradient in the force-displacement curve (figure 4.19). At ~60 N (d=0.15mm, figure 4.21(c)), the matrix crack propagating into the C-ring's second ply layer was detected. It is located in front of the previous matrix cracks in the first layer, but they were not connected in this slice of the image yet. As the load increased, the crack propagates, and the crack opening became more noticeable. The load peaked at 83 N (d=0.26mm, figure 4.21(d)), where extensive cracks was observed. Unlike the sudden fracture point observed at room temperature, the C-ring experienced some stepped drops after the peak loading. In the fractured sample, with a remaining load of 50 N (further increased displacement to d=0.30mm, figure 4.21(e)), the crack opening is obvious in the cross section, showing the crack path throughout the first and second ply layers. It was also interesting to note that the critical crack in the fractured C-ring (figure 4.21(e)) is around 500 μm from where the first damage observed as in figure 4.21(b).

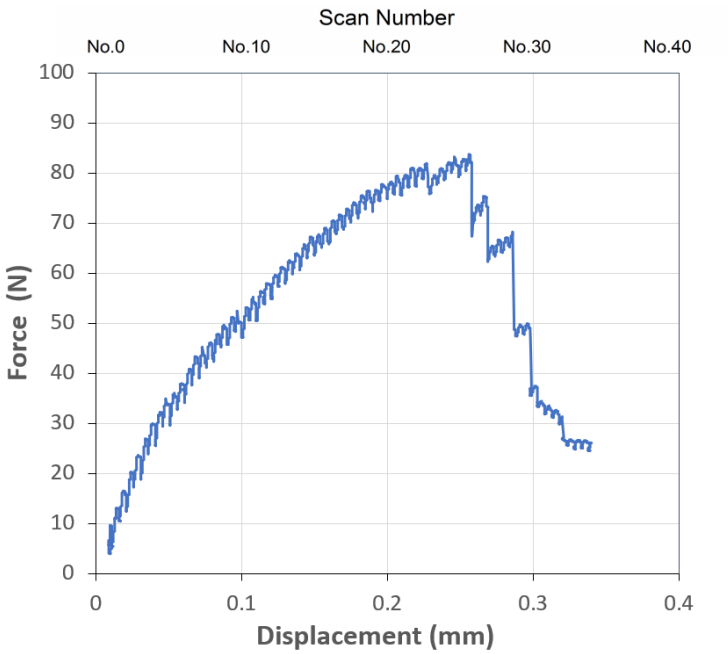


Figure 4.19: The force-displacement profiles of the C-ring experiment at 900°C

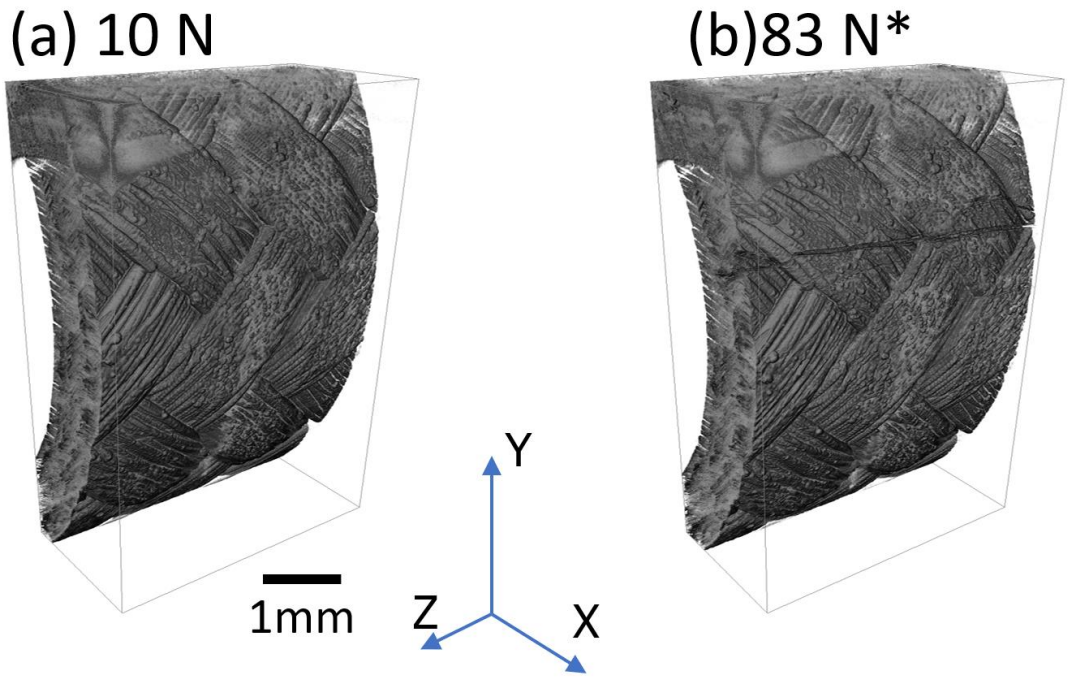


Figure. 4.20: 3D volume-rendered tomographic images of the C-ring sample under continuous loading of the (a) the original state and (b) the fractured state (* peak loading value) at 900°C.

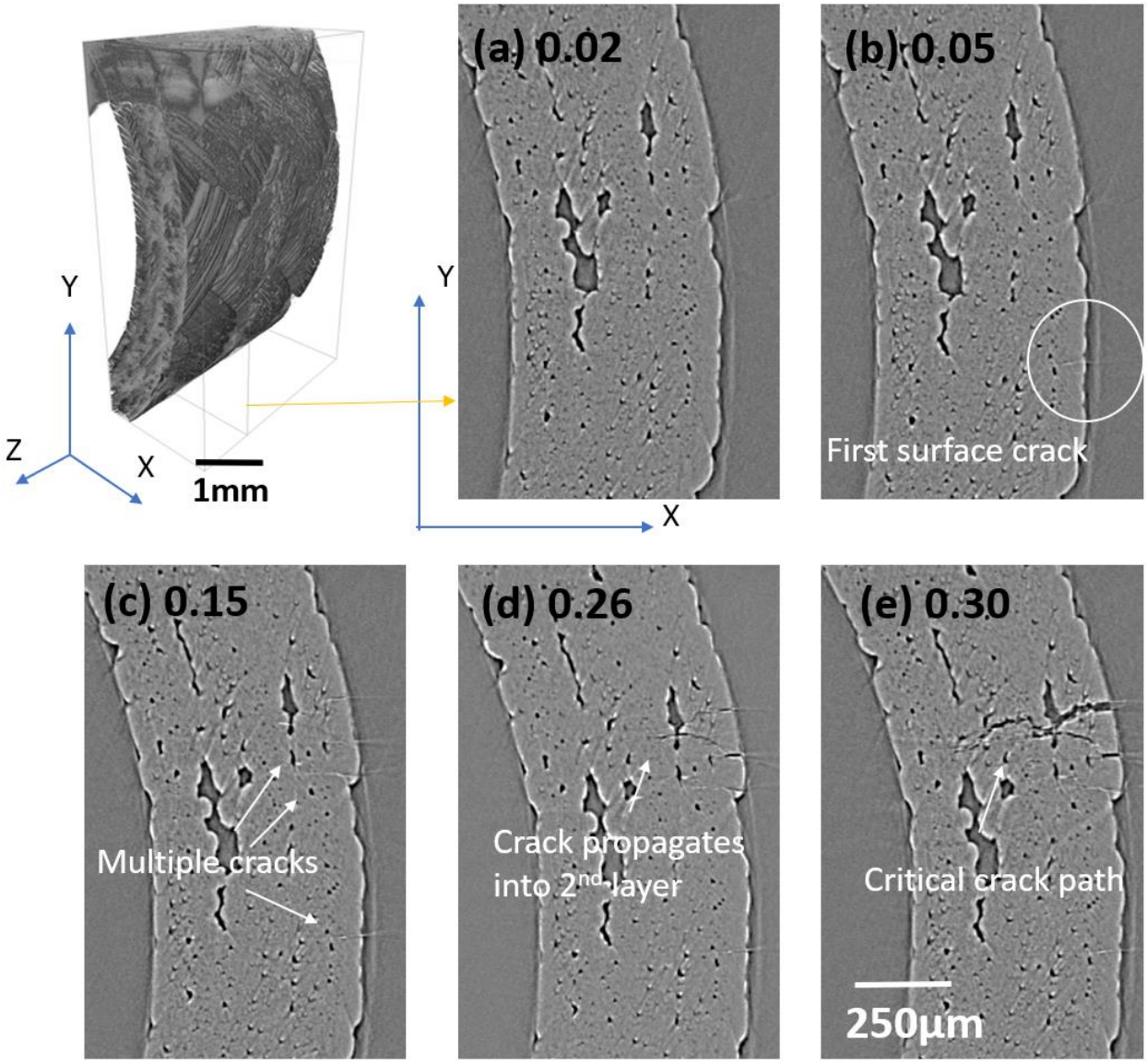


Figure. 4.21: 2D longitudinal slice (XY) of the C-ring sample under different diametric displacement.

Three vertical slices from the Y-Z plan of the fractured sample were presented in figure 4.22 to show the critical crack path. In the first slice at the crack root (figure 4.22a), the matrix damage path was sharp and flat with the little fibre pull-out phenomenon in the fibre tows. In the second slice of the first ply layer (figure 4.22b), few of the 'zigzag' pattern of damage were observed

inside the fibre tows. The damage in the middle layer of the composite is illustrated in figure 4.22(c). It shows the fibre breakage ahead of the crack tip and the crack opening were not constant along the sample width (Z direction). More extensive crack opening appears at the edges of the C-ring sample. Additionally, throughout the matrix cracks, the fibre breaking points were located preferably near the matrix cracks as shown in figure 4.23.

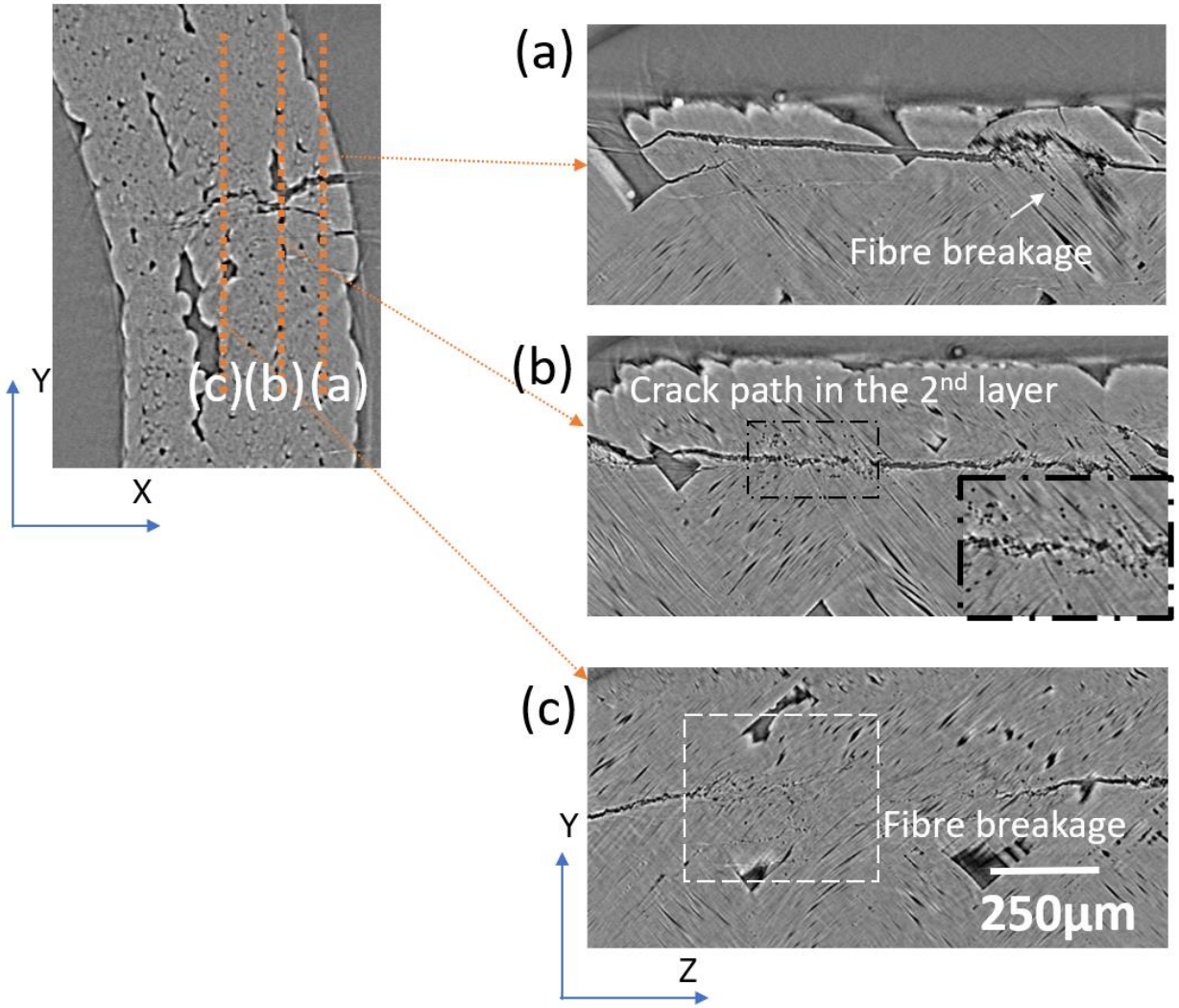


Figure. 4.22: 2D slices (YZ) of the fractured sample (d = 0.30 mm)

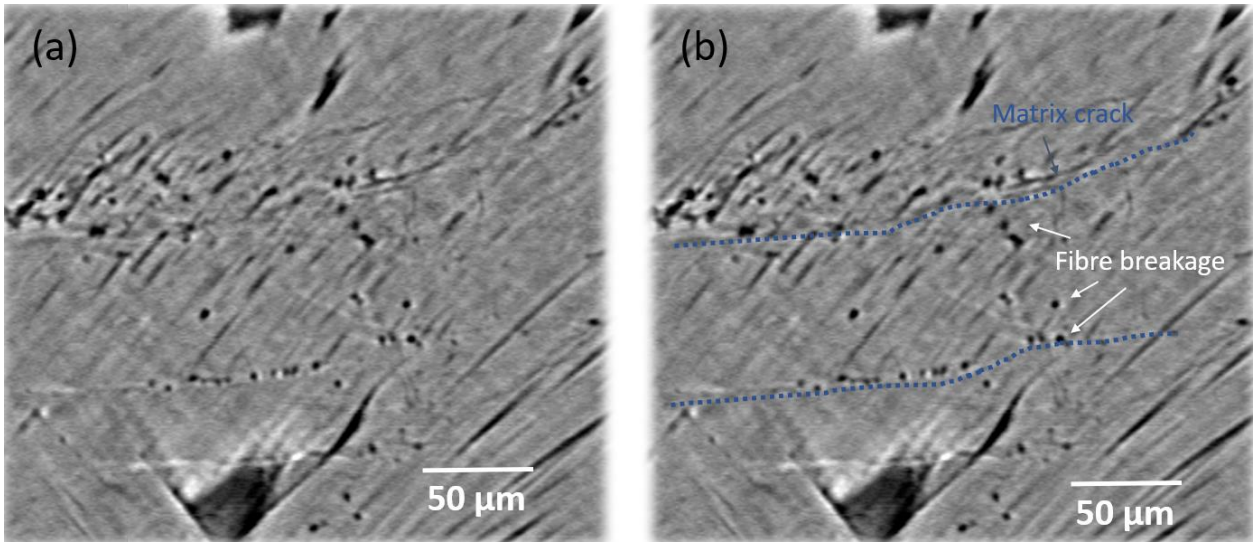


Figure. 4.23: (a) The magnified image of the white rectangular region from figure 4.22(c). The blue lines highlight two matrix cracks in (b).

4.3.2. Digital volume correlation analysis

4.3.2.1. Static scan with cycling loading

DVC analysis has been applied to all the three *in situ* experiment tomographs (3.25 µm voxel) to obtain the full-field displacements. For the static scan data at room temperature, the DVC was performed in Lavision Davis 8.1 software [130] with the OUMS-Lavision workstation with a 128 GB memory and an Intel Xeon E5-2560 processor. The reference image was the tomograph of the original unloaded sample. A geometric mask was applied on the C-ring to include the 4 mm middle part by a manual selection of the boundaries before the correlation.

The uncertainty analysis was conducted by correlating *another scan* of the physically translated unloaded sample with an applied displacement of 50 µm at x direction with the reference scan. The size of the correlation window was selected in the uncertainty analysis as the window is as small as possible to illustrate the details of the deformation but large enough that the calculated strain is close to zero. Ideally, the calculated strain from the physical translation should be zero,

but the uncertainty that is associated with the number of the valid data in each correlation window gradually increased with the decreasing window size as shown in figure 4.24. Therefore, the final correlation having a windows size of 96 × 96 × 96 (voxels) was selected for this experiment, with an 75% overlap and 2 passes. The required valid voxels per correlation window was set to 50% to give a more detailed result at the sample surface, and the threshold of correlation coefficient for each window was 90%. It yields a spatial resolution of 78 μm for the displacement field. The calculated displacement field in x, y and z direction in the uncertainty analysis is listed in table 4.1. In each orthogonal direction the standard deviation is around 0.4 μm that is approximately 12% of the voxel size. In total, the displacement uncertainty for a 50 μm displacement is around 0.9 μm. With this applied setting. each set of DVC calculations took about 6 hours.

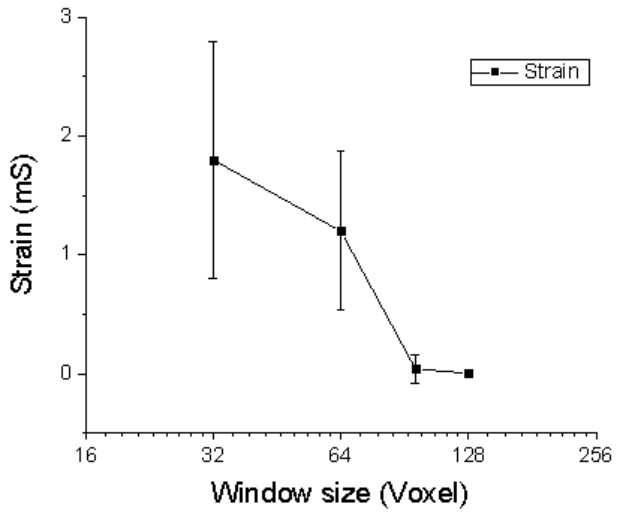


Figure. 4.24: the principle strain calculated from the DVC versus the size of the final correlation widow of the physically translated dataset

Table 4.1: the displacement uncertainty of the DVC analysis in the static scan with the window size of 96 × 96 × 96 voxels

Direction	Physical translation (μm)	DVC analyse	
		Average (μm)	Standard deviation (μm)
x	50	50.16	0.47
y	0	0.95	0.43
z	0	0.79	0.36
Total	50	50.17	0.74

The displacement field (V_i) of the *in situ* tomographic dataset can then be used to calculate the displacement gradient e_{ij} in each correlation window at each orthogonal direction:

$$e_{ij} = \frac{\partial V_i}{\partial j} = \begin{bmatrix} e_{xx} & e_{xy} & e_{xz} \\ e_{yx} & e_{yy} & e_{yz} \\ e_{zx} & e_{zy} & e_{zz} \end{bmatrix} \quad (i \in \{x, y, z\}; j \in \{x, y, z\}) \qquad 4.5$$

The principal strains here are defined as the eigenvalues of the matrix in equation 4.1. The maximum principal strain is therefore the maximum the eigenvalues on any plane that is independent of the orientation of the coordinate system.

An example of the displacement field, illustrated in figure 4.25(a), shows the macroscale deformation of the C-ring by the displacement vectors under diametric compressive loading. Those data with a correlation coefficient less than 0.8 were discarded. The displacement arrows are scaled with a factor of 20 for illustration purposes. The orthogonal strains e_{xx}, e_{yy} and e_{zz} are also presented in figure 4.25 with the maximum principal strain maps in figure 4.25(e).

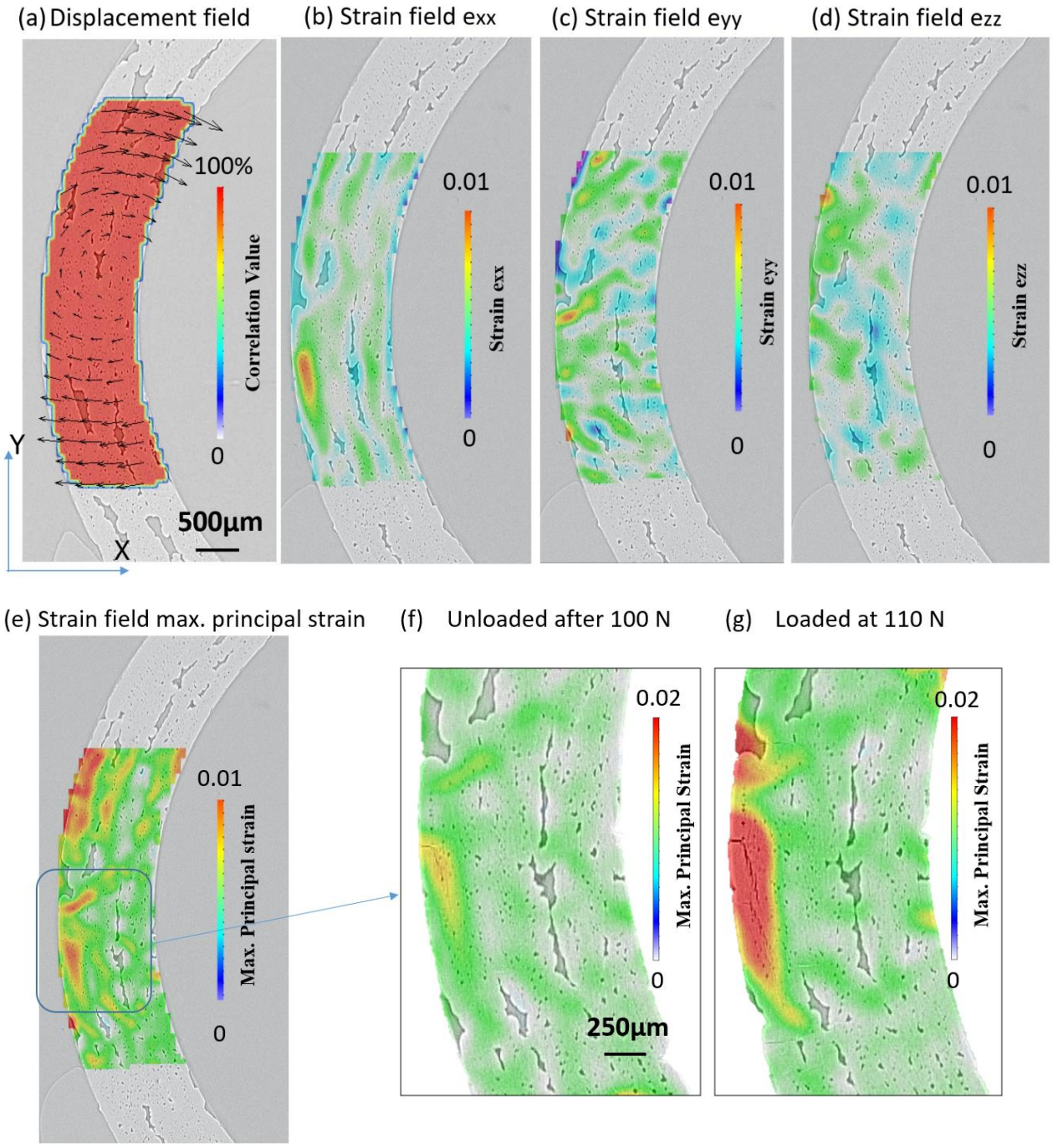


Figure. 4.25: (a) The geometry mask applied throughout the C-ring sample width, the vector indicating the deformation of the C-ring under 100N (scale factor = 20), the background colour showing the correlation coefficient for each correlation window; the strain maps of (b) e_{xx}, (c) e_{yy}, (d) e_{zz} and (e) the maximum principle strain at the unloaded state after 100 N with the superimposed images of the microstructure; the strain development is highlighted at (f) unloaded stage and (g) subsequent loaded stage respectively.

As shown in figure 4.25(f), it is very difficult to locate the damage solely from the unloaded tomography images due to reduced crack opening distance in unloading. With the 3D strain maps, those cracks can be successfully resolved. For example, figure 4.25(f) and figure 4.25(g) show the superimposed images of strain map with the microstructure of the unloaded state after 100 N and then reloaded to 110 N, respectively. The residual damage and the successive damage progression were both highlighted with the maximum principle strain. In the unloaded state, the local strain at the crack is slightly above 0.01, while in the loaded stage, the localized strain is generally larger than 0.02 with a more extensive damaging zone.

Figure 4.26 shows the strain map evolution with the C-ring tomographic images under cycling loading. A progressive evolution of the localized strain distribution was observed as the load increased (Figure 4.26(a)), showing the cumulative damage process. The strain distribution is far less homogenous, which is consistent with the tomographic observation. In fact, extensive strain appears at the surface during the loading stage that spans across the sample width. The localised strain widely spreads out at the outer surface with some penetration into the specimen at the higher load. At the unloading stages, some of the previous strain pattern remains, showing the resolved permanent damage. For instance, at the final stages, the critical crack path was still highlighted near the middle sample height. The dispersed damage was also spotted by the other localized strain features. Overall, those 3D strain distributions illustrate the permanent damaged areas at the surface and inside the sample.

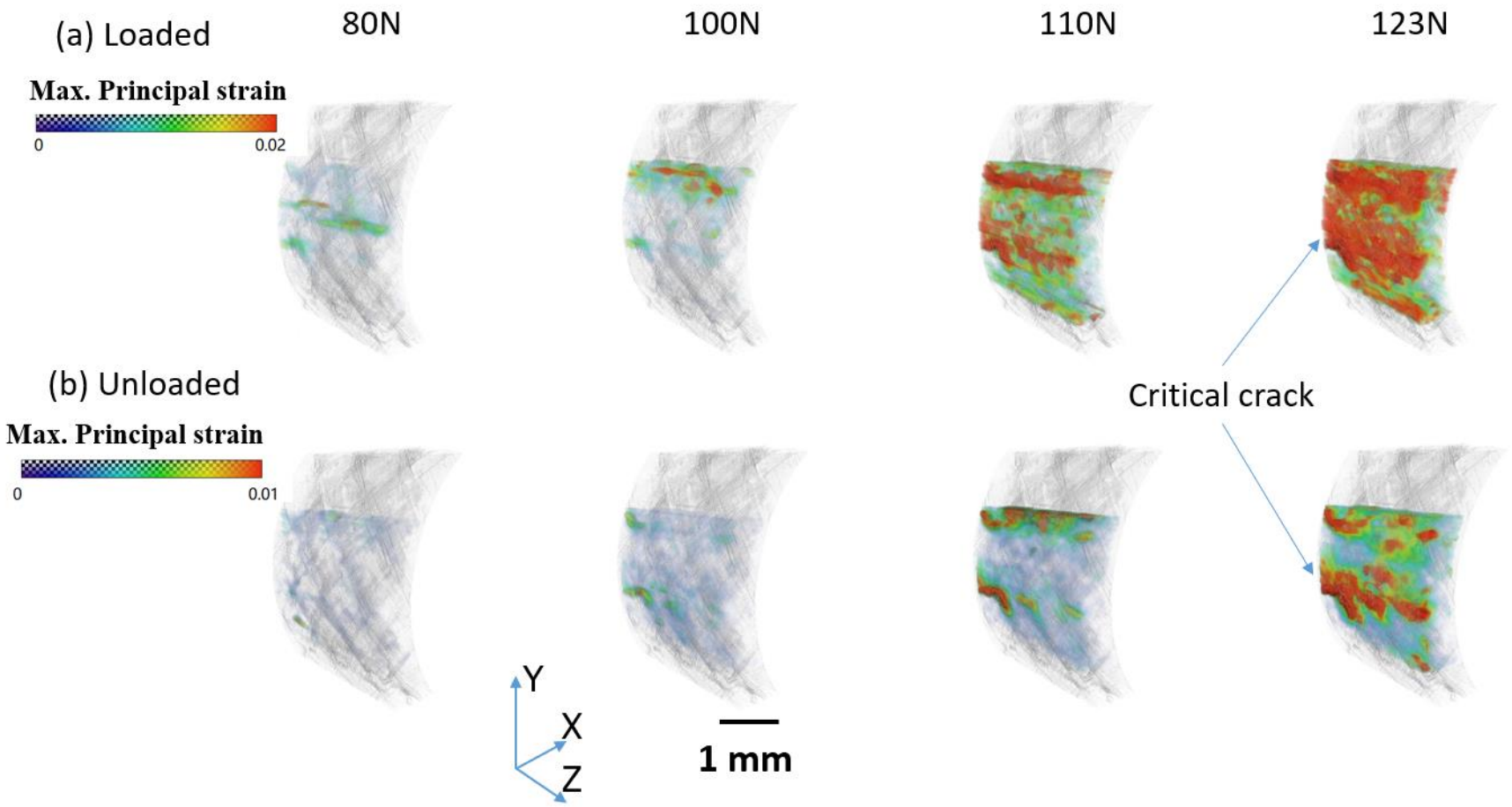


Figure 4.26: 3D visualization of the maximum principle strains showing the damage evolution in the C-ring sample at (a) loaded stages and (b) unloaded stages, from 80N to 123N. The strains were calculated from the displacement field measured relative to the original state before loading. The red colour indicates the damages. The superimposed images of the fibre and matrix materials have been set transparent for damage illustration.

4.3.2.2. Continuous scan with monotonic loading

DVC analysis was applied for the continuous experiment to measure its mechanical response. It was performed in the Lavision Davis 8.4 software with an upgraded workstation, OUMS-ARES, with 512 GB memory and an Intel Xeon E5-2699 processor. The procedure of the DVC is the same as described the previous section. Here, the final correlation window has a spatial resolution of 64 pixel with 75% overlaps with 2 passes. Before the start of the compression, a physical translation of 60 µm of the sample was applied vertically (y direction) at the unloaded stage to estimate the uncertainty in the displacement measurement from the DVC and its subsequent strain value. This analysis yields the magnitude of standard deviation in the measurement of displacement of 0.76 µm. The uncertainties of displacement measurement at different orthogonal directions are listed in table 4.2. The corresponding error in the average strain measurement from this physically translation analysis is 0.023%. All other settings in the DVC calculation were the same as in the previous experiment.

Table 4.2: The displacement uncertainty of the DVC analysis in the continuous scan with the window size of 64 × 64 × 64 voxels at room temperature

Direction	Physical translation (µm)	DVC analyse	
		Average (µm)	Standard deviation (µm)
x	0	0.36	0.13
y	60	59.48	0.19
z	0	0.07	0.08
Total	60	59.48	0.24

The inhomogeneous distribution of the strain is illustrated in the superimposed 3D images of the strain maps correlate to the original state as in figure 4.27 with the microstructure. Specifically, the crack opening of the tensile failure mode was observed as the region with high tensile strain

among the C-ring. Initially, very little localized strain is observed, and it is preferably aligned with the fibre tow orientation (figure 4.27(a)). Then, the high nominal strain (>0.02) was observed in the middle part of the C-ring (figure 4.27(b)) after the onset of the matrix crack. This high localized strain region is highly heterogeneously distributed. The strain spanning the sample width is associated with the matrix cracking damages initiated at the surface. Then, with the increasing load, a progressive development in magnitude and extent of the localized strain distribution was observed (figure 4.27 (b-e)). The increase in the magnitude of the localized strain is associated with the crack opening and crack propagation into the C-ring sample, which can be confirmed with the slice image of the microstructure. Moreover, the multiple cracks as in figure 4.15 were highlighted by the extensive localized strain at the middle part of the sample. Nevertheless, once damages were observed, an accumulative damage evolution was shown from the development of the localized strain distribution.

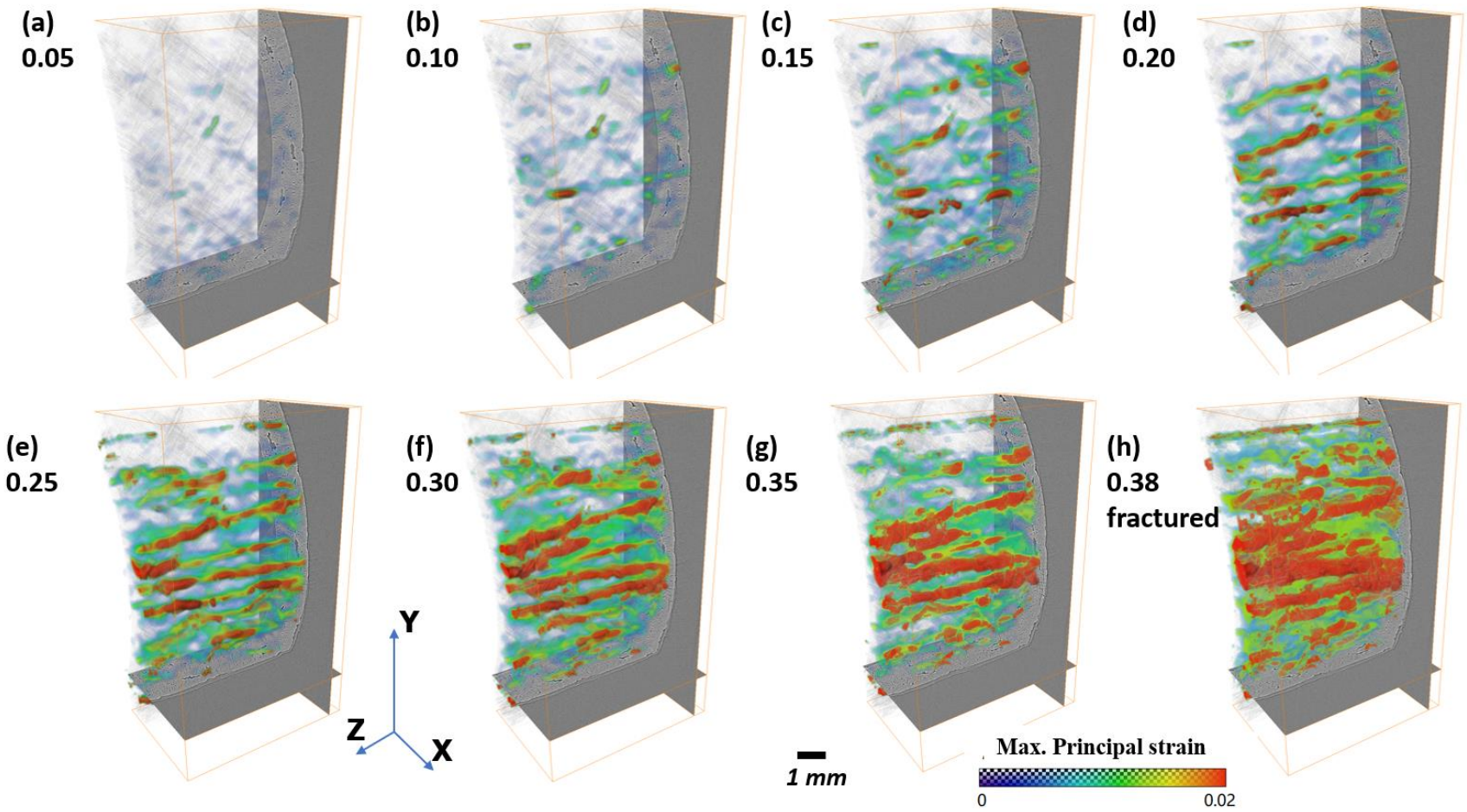


Figure 4.27: 3D visualization of the strains showing the damage in the C-ring sample with the increasing diametric compression at room temperature. The number is the crosshead displacement (mm) showing the evolution of the strain. The strains were calculated from the displacement field measured relative to the original state. The red colour indicates the damages. The 3D superimposed tomographic images of the fibre and matrix materials have been set transparent. The corresponding orthogonal slices of tomographic images shows the location of the damage related to the microstructure.

4.3.2.3. Continuous scan at high temperature

The same DVC analysis was also applied to measure the full field displacements of the continuous synchrotron X-ray tomographs at high temperature with the same setting as that in the room temperature in the Lavision Davis 8.4 software, using the same OUMS-ARES workstation. The final correlation subset window has 64 × 64 × 64 voxels with 75% overlaps for 2 passes. The standard deviation of a physically translated sample by 60 µm rigid body moved scan at 900°C is around 0.83 µm, with the detail of the analysis list in table 4.3. The equivalent uncertainty in strain measurement is 0.027%.

The corresponding 3D localized strain evolution from the DVC analyse with the reference being the original state is illustrated in figure 4.28. The first high strained feature was captured in figure 4.28(c) at the middle height. Then, there are few more non-uniformly strain features observed with multiple damages. They are concentrated in few surface damages and they tend to span across the sample width. Just before and after the final fracture, the extensive strain highlights the critical damage path that developed into the C-ring sample. It is also interesting to find that the location of the highest strain at the fracture of the sample 4.28(h) is different from where the first surface crack was observed.

Table 4.3: The displacement uncertainty of the DVC analysis in the continuous scan with the window size of 64 × 64 × 64 voxels at 900°C

Direction	Physical translation (µm)	DVC analyse	
		Average (µm)	Standard deviation (µm)
x	0	0.98	0.42
y	60	60.19	0.46
z	0	0.81	0.55
Total	60	60.20	0.83

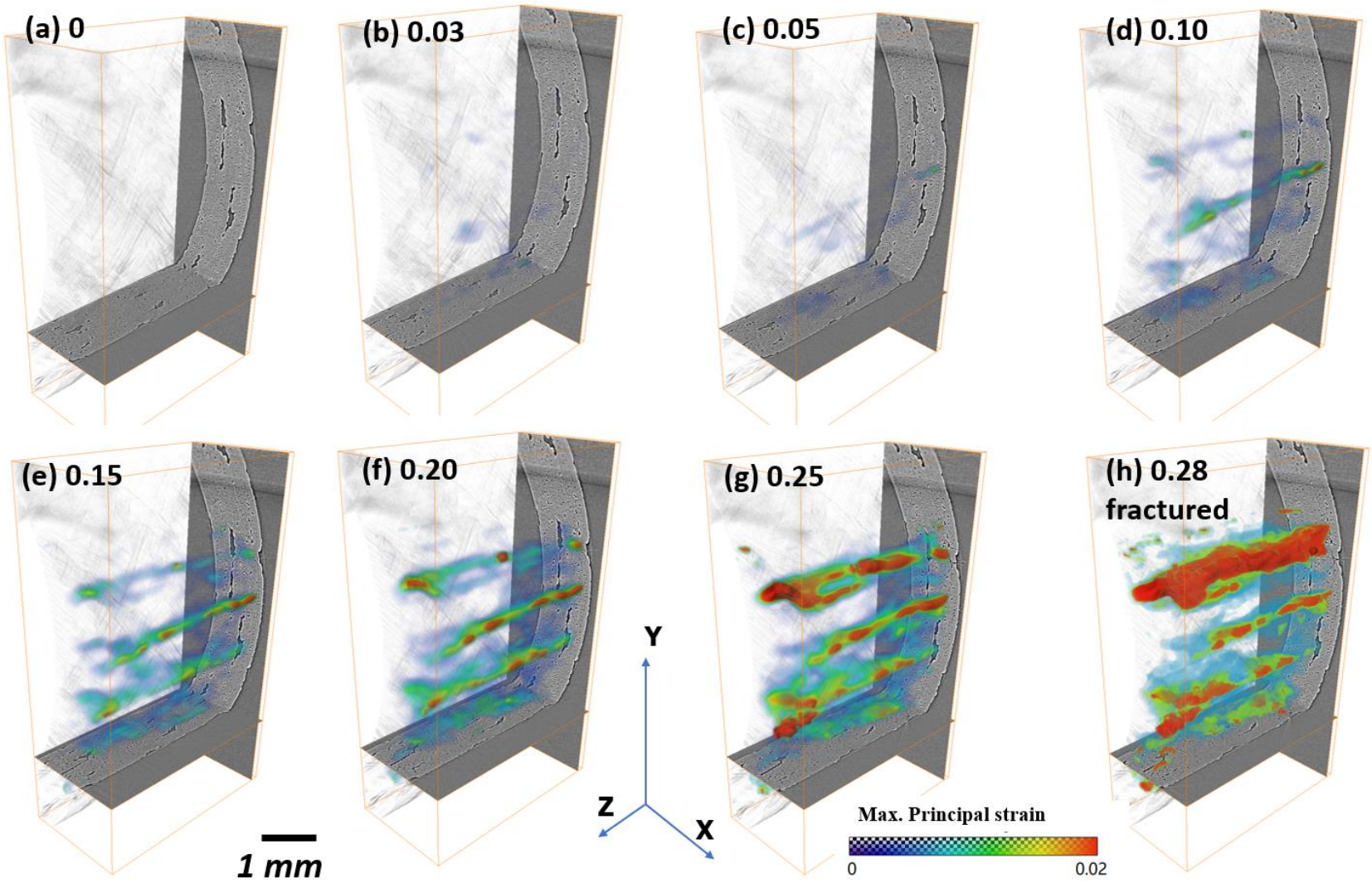


Figure 4.28: 3D visualization of the strains showing the damage evolution in the C-ring sample at 900°C with the increasing diametric compression. The number is the crosshead displacement (mm). The strains were calculated from the displacement field measured relative to the original state

4.3.3. Bulk deformation

The bulk deformation of the C-ring under the diametric compression can illustrated by the displacement vector field. An example of displacement map of a virtual slice in the middle of the sample (1.8mm from the edge) when the load was approximately 80 N is illustrated in figure 4.29 for the continuous experiments at room temperature and 900°C. A symmetric deformation between the middle plane was observed when the C-ring was continuously compressed. As a result, in an analogue to a bending test, the maximum bending moment and the maximum deflection were expected to be at the middle plane.

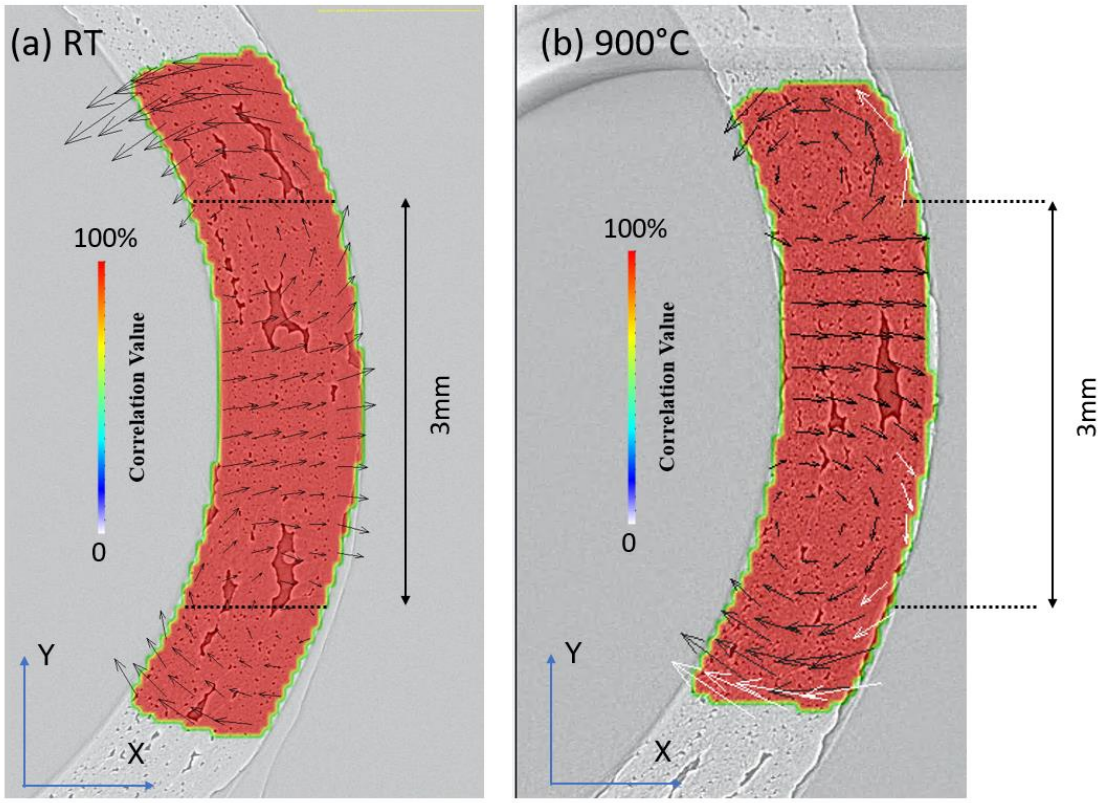
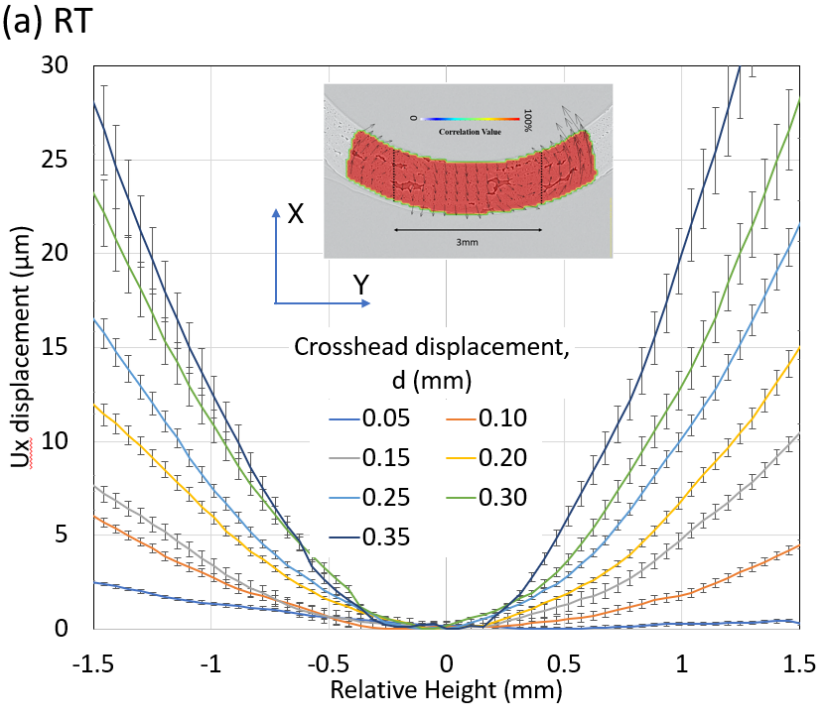


Figure 4.29: The deformation of the C-ring shown by the displacement vectors (scale factor = 20) at (a) room temperature and (b) 900°C. The red colour background showing the geometry mask applied.

Due to the high-speed angular rotation and the X-ray transparency requirement of the *in situ* experiments, the use of a physical strain gauge is impractical. However, the displacement results from the DVC analysis can be used to quantify the deformation (i.e. deflection). The relative X displacements in the C-ring, caused by the diametric compression at Y direction, were measured over a virtual distance of 3 mm at the middle height of the C-ring sample where the maximum stress was expected. Its virtual boundaries and the relative position to the C-ring is shown in the figure 4.29. The evolution of the deflections is quantified at different stroke displacements with a constant compression rate, which is plotted in figure 4.30 at the room temperature test and 900°C test. The degree of the deflection (represented as the displacement at x direction) increases gradually during the compression. The increased standard deviation at higher loads indicates a more heterogeneous deformation with the progression of the damages. Additionally, similar deflection patterns were observed from the at room temperature and 900°C data before the fracture (C-ring sample fracture at around d=0.25mm at 900°C).



(continue on the next page)

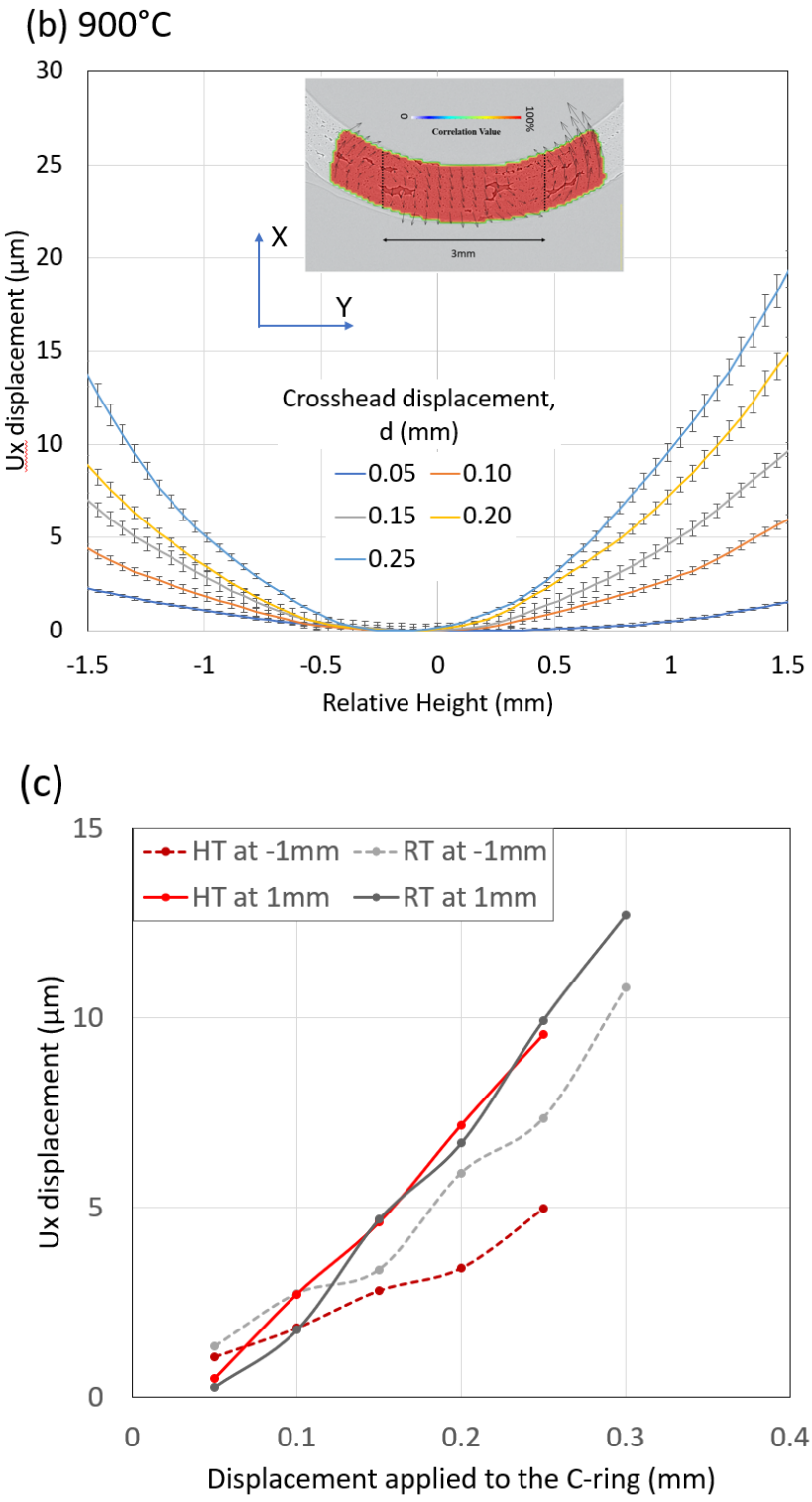


Figure 4.30: Plots of the deflections along the sample height of the C-ring from its original shape during in different stage of the (a) room temperature and (b) 900°C experiments; (c) the deflection as Ux displacement of the C-ring at the position of ±1 mm in the C-ring test at room temperature (RT) and 900°C (HT).

4.3.4. Localized strain distribution

The displacement field can be used to calculate the directional mechanical response. One important use of the diametric compression in C-ring sample is to investigate the properties of the tubular component in the hoop direction [143], [145]. For instance, the hoop strain can be represented by the strain in the Y direction at the middle height of the C-ring under diametric compression. As shown in equation 4.5, the Eyy strain can be calculated from the y displacements obtained by DVC. Example data of the Eyy strain distribution at the middle height (relative 0 position in figure 4.29) along the width of the C-ring are illustrated in figure 4.31. The localized Eyy strain was initially very small (when d = 0.05 mm). The distribution of the localized strain appears to be far from uniform with increasing load. The positive strain indicates a deformation caused by the tensile force that is concentrated near the outer surface of the C-ring, with the compression strain near the inside. Moreover, significant localized tensile strain was observed concentrated in the area near the outside surface. The strain pattern remains similar as the load increases, which suggests a progressive damage evolution in the same location.

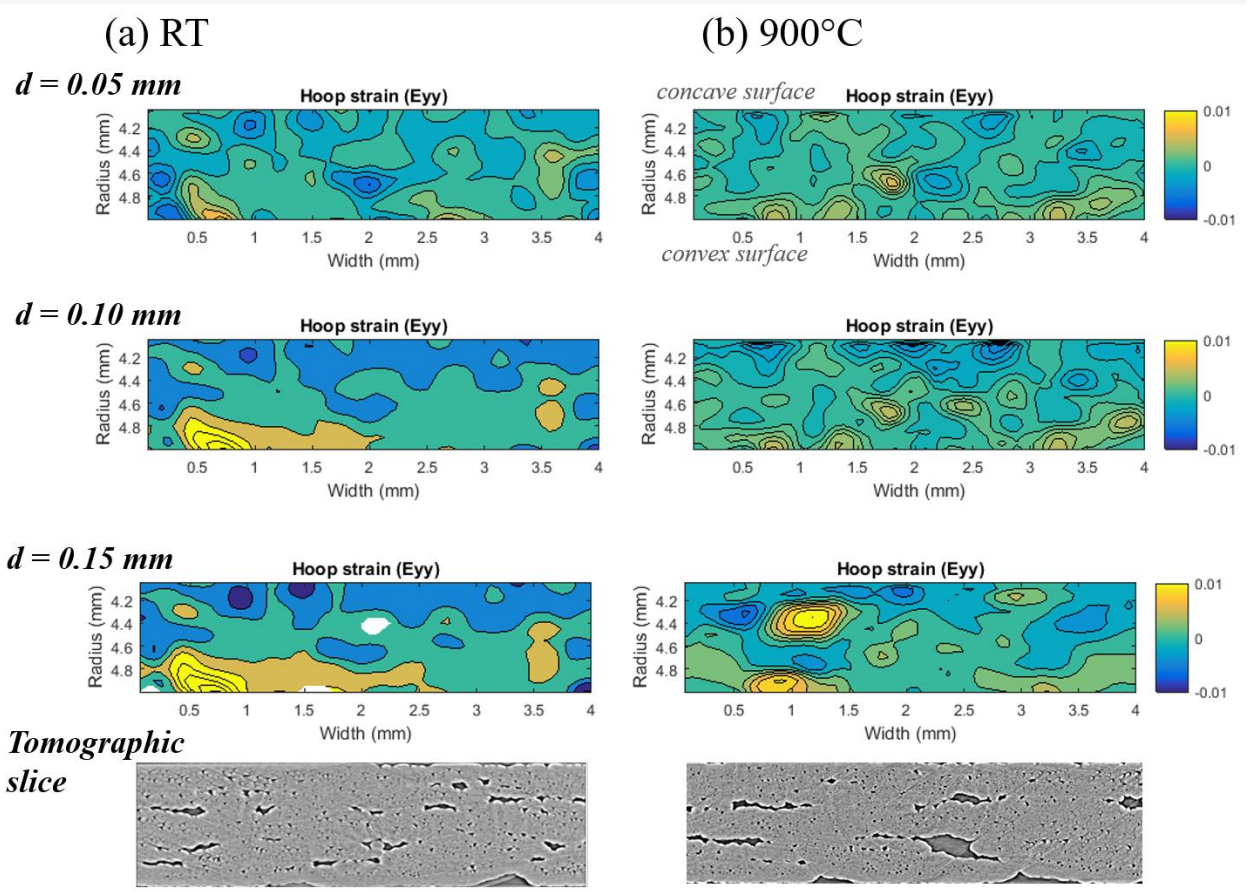


Figure 4.31: The strain distribution (Eyy) at the middle plane of the C-ring under increasing loading. (a) the 2D maps showing the locations are with the same scale bar.

4.3.5. Elastic properties

The force history in the real-time imaging with a constant loading rate can also provide information for the elastic properties via curved-beam theory [144] assuming the C-ring deformed elastically. The records of the continuous loadings with the displacement from the crosshead at both room temperature and 900°C are illustrated in the figure 4.32. The two loading profiles experienced a coincidental linear region from the beginning up until 35 N, where the high temperature curve starts to depart from the linear region and the first matrix crack was observed in the tomographic images (figure 4.21(b)). It was then followed by a gradually decrease of gradient until the ultimate

load with multiple damages imitated. The elastic modulus [144] based on equation 4.1-4.4 was calculated at room temperature and 900°C when there is no damage observed in the tomographic images (figure 4.16 and figure 4.21) and where the force-displacement curve (figure 4.32) stays linear. The calculated elastic modulus was 335 ± 25 GPa and 327 ± 21GPa at room temperature and 900°C respectively (table 4.4). The corresponding proportional limit stresses are 247 ± 15 MPa at room temperature and 170 ± 12 MPa at 900°C.

Table 4.4: The elastic properties of the SiC/SiC composite measured from the continues experiments at room temperature and 900°C

Temperature	Elastic modulus (GPa)	PLS (MPa)
25°C	335 ± 25	247 ± 15
900°C	327 ± 21	170 ± 12

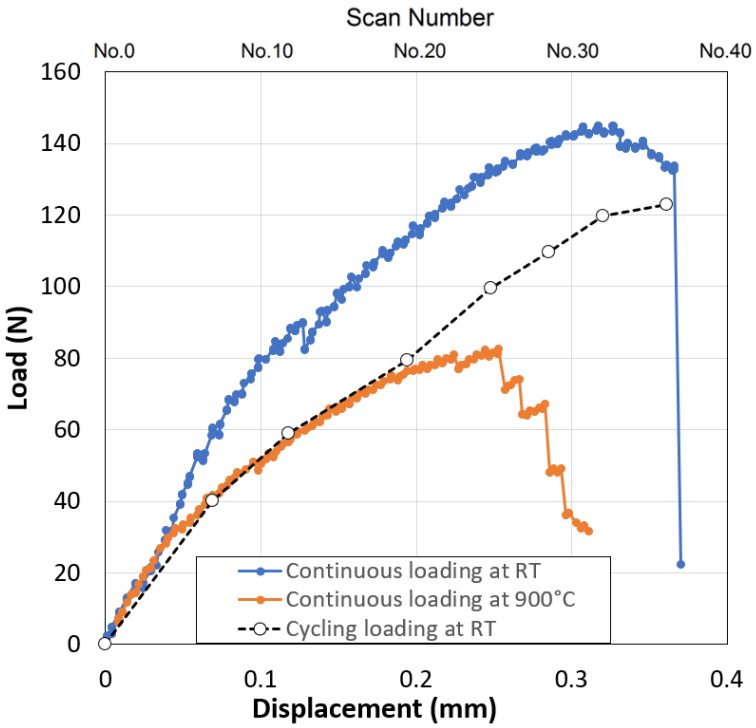


Figure 4.32: the force versus cross-head displacement of the diametric compression test with the continuous loading at room temperature and 900°C; and the cycling loading at room temperature.

4.4. Discussion

4.4.1. Elastic properties

The SiC/SiC composites undergo several stages of deformation under the applied stress as descripted in figure 4.13 and 4.19. A significant parameter for design guidelines of a composite application is the proportional limit stress (PLS) .When the load is smaller than the PLS, the composites were expected to behave liner-elastically without any irreversible damage[151]. Therefore, the concept of the PLS is fundamentally associated with the onset of irreversible damage (i.e. matrix cracking in tension). In some other studies the PLS is also corresponds to the matrix cracking stress [85], [151]. In this study, it has been demonstrated with observation of the first crack in the real time tomographic images at both room temperature (figure 4.15) and high temperature (figure 4.21).

For most structure integrity tests, the PLS is determined by the threshold stress level in the curve or an offset auxiliary line [152]. In tensile tests of minicomposites [79] or an individual fibre tow [81], the PLS can be clearly found in the force displacement curve. However, for the 2D woven structure composites, the stress state is more complicated[153]. The effect of microstructure was well demonstrated in that the PLS is strongly affected by the fibre orientation, with the highest PLS found at the most 0° directional SiC/SiC, in a typical unidirectional tensile test [152]. For the tensile test involving a progressive cycling loading, the data monitored from the crosshead or a strain gauge were sometimes too noisy to provide an accurate measurement of PLS [8], [60], [93], [153]. Another variation could also arise from the sample geometry as the 2D woven tubular composites makes the standard sample preparation more difficult compared with a planar composite.

In addition, the PLS is affected by the specific macroscale load state. The comprehensive study [43] of the tubular sample by Bernachy-barbe et al. used the acoustic emission technique with *in situ* surface imaging. Its axial deformation results show that the PLS from the stress strain curve could be different from the onset of surface damage occurrence, depending on the loading conditions (i.e. tension or compression).

In the non-standard test of C-ring compression of woven composites, a relatively complex loading state was expected within the sample. In this study the method of 4D (time-resolved) tomographs allows the continuously detection of the damage without interruption. It confirms the coinciding time of the non-linear departure in the force-displacement data and the onset of the damage initiation at the surface. The overall deformation (figure 4.29) also gives confidence in the application of the simple-curve beam theory to calculate the elastic properties of the composite. Derived from the figure 4.32, using the equation 4.1-4.4, the calculated PLS is 247 ± 15MPa with elastic modulus is about 335 ± 25 GPa at room temperature.

The measured PLS is approximately 30% larger than a typical reported value in tensile test of a similar composite material [43], [85]. Firstly, the difference could be that only a relatively small volume was measured in the C-ring test. The region under tensile stress is located at the outer surface of the C-ring composite. Therefore, the results are largely dependent on the distribution of defects and flaws, especially near the surface. In this test, the C-ring surface has a thin layer of monolithic SiC from the CVI process, which means a relatively dense and defect-free region was at the surface. The densified region might lead to an increased measured PLS of the composite [29], [152]. Secondly, a mixed mode with of tension/compression stress state was expected in the C-ring sample along the radius. In the curved-beam theory, it is assumed that there is the same modulus in tension and compression. However, the axial strength of SiC/SiC tube were much

stronger in compression than in tension [43], which indicates that tensile damage should occur first and such damage would reduce the elastic modulus in the tensile loaded region. Similar observations of the overestimation in the flexural strength were also reported in the monolithic SiC [29], where the flexural strength from the O-ring compression were found to be higher than that from a flexural bar.

Nevertheless, despite the general assumptions in the calculation and the limitation of the testing method, with the help of the *in situ* method, the measured values can be interpreted as the elastic hoop tensile properties of the SiC/SiC composites, especially for the outer surface region.

4.4.2. Matrix cracks

As the PLS is exceeded, the associated development of the matrix cracking is well resolved in the tomographic images. For a monolithic SiC C-ring, once a crack has initiated at the outer surface, it soon propagates through the entire sample and causes the fracture[145]. In contrast, in the studies of composite, the surface crack is also the initiation site for the sub-surface damages as observed in the 4D studies (figure 4.15). The crack initiation was observed to occur very quickly and soon after the first initiation several other cracks initiated to form a group of cracks. This means constant monitoring is of importance and the *ex situ* post fracture studies may only describe the limited evolution of the damage [60], [145].

The multiple cracks initiated and the further propagation of the previous crack in the composite are resisted by fibre bridging [154]. With further increased loading, multiple matrix cracks were both observed in the C-ring test under cycling loading and monotonic loading as shown in figure 4.9 and figure 4.15. The open cracks were counted before the final fracture over a gauge distance of 6.5 mm. The average spacings of the cracks from the C-ring tests are 0.46 mm (i.e. 2.2 mm^{-1})

for cycling loading and 0.38 mm (i.e. 2.6 mm^{-1}) for monotonic loading. The value is similar to the crack density (2 mm^{-1}) reported previously of a similar composites under tension [57].

The relatively decreased crack density in the cycling loading might be explained due to the lesser fibre bridging effect. In the cycling loading, the residual strain as shown in the figure 4.25(f) and (g) indicates there is permanent damage with cracks that did not close during unloading. The partial crack closure must be accompanied by fibre sliding and/or damage in the PyC interphase[71], [151]. This can weaken the fibre bridging strength, which results in a lower matrix crack density with further crack propagation under a given degree of deformation. Therefore, the overall failure strain with cycling loading is also smaller than that in monotonic loading mode. Another contributing factor could be the propagation of delamination cracks observed in the cycling loading (figure 4.11), which was not observed under monotonic loading. The measured crack density only accounted the cracks that were perpendicular to the tensile direction. The decreased crack density could also arise from the other types of damage in the specimen. Nevertheless, it still needs to be mentioned that those phenomena were observed from a very limited number of *in situ* synchrotron C-ring tests. More studies are needed for the generalization of the difference in different loading conditions.

4.4.3. Deformation behaviour and damage observation

The digital volume correction of the *in situ* tomographs gives a quantitative information of the bulk deformation behaviour (figure 4.29). The calculated strain from the displacement field can also illustrate the cracking in the sample as shown in (figure.4.26-28). The *in situ* tomographic images show a complicated cracking path with the crack branching and crack deflections by the fibre tows. How the crack propagated inside the sample is very different compared with that

observed from the surface. Therefore, the surface observation were not fully representative for the bulk damage in the composites [43], [60], [67].

Generally, the cracks propagated through two woven ply layers (about two thirds of the total thickness) prior to the final fracture (figure 4.9, figure 4.15 and figure 4.21). The strain maps with the superimposed tomographic images (figure 4.26-28) also show the network evolution of the damages. The damage caused a discontinuity in two adjacent measurements of the displacement field, which leads to a high local strain. Thus, the damage was visualized as high local strain. It needs to be noted that those local strain features arise from crack opening that is different from the real or global strain in the specimen [118], [121].

Nevertheless, the progressive development of the damage and the extent and magnitude can be observed real time until the final fracture. Given the force-displacement curve, the coupled real time images gave a new insight to explain the corresponding momentary drops. Previous post-mortem analysis [145] tried to correlate the drops to the fibre fracture. However, these 3D real time observations indicate it is associated with substantial matrix crack propagation with the branched cracking at the fibre tow boundaries. The misinterpretation in previous studies may due to matrix crack closure from the unavoidable unloading in the *ex situ* analysis, which would have made it difficult to visualise the cracks. This unloading might also change the loading state as shown in the cycling loading results (figure 4.8).

The understanding of the accumulative damage is also important to prevent the overinterpretation of results obtained using the curved beam theory. The curved beam theory assumes a linear and uniform elastic behaviour of the material [142], [144]. The multiple damages observed once the stress exceeds the PLS means a deviation from the curved beam theory. This deviation is mostly obvious at the peak stress where extensive damages were observed. The damage, i.e. matrix cracks,

introduce a local stress concentration. Therefore, the ultimate tensile strength (UTS) calculated from C-ring test is significantly higher than the actual value. Some studies [8], [145] stated the similar value of UTS of the fabricated composites measured from C-ring and hoop tests but the equation[145] presented was mathematically erroneous in the radius terms compared with that from the ASTM standard [144], which might explain their surprisingly low value of UTS obtained from the macroscale C-ring test.

The deformation data from the displacement fields also allow a quantified study of the C-ring (figure 4.30). The C-ring responded heterogeneously along the sample width as shown in the maps of the tensile strain (Eyy) figure 4.31. Its pattern corresponds to the shape of the fibre tow structure that the typical strain feature generally stays in the single fibre tow, which may be due to the fibre tows reorientation mechanism under load [43], [57]. This proposed damage mechanism needs to be confirmed with other preconditions, i.e. internal damages, that were not observed but proposed in [43]. In this study, internal damage between the fibre tows and between the ply layer was well visualised in the *in situ* X-ray tomography images.

4.4.4. Cycling loading and monotonic loading

The *in situ* tomographic images further revealed the damage evolution in the ceramic composites that is observed to be different between cycling loading and monotonic loading. The crack propagation under cycling loading was discussed in other ceramic materials [107], [155]. The toughening mechanism can be classified to be intrinsic or extrinsic, which is the primary mechanism ahead of the crack front or behind the crack respectively. The crack propagation is normally governed by a mutual competition of intrinsic mechanism and extrinsic mechanism. As for ceramics, crack deflection was observed to be identical in the cycling loading and monotonic loading [156], with no degradation of the intrinsic mechanism under cycling loading. By contrast,

the extrinsic mechanism, such as crack bridging, could undergo severe degradation in cycling loading in fibrous composite.

Crack bridging by fibres has been observed to be an essential mechanism that shields the crack propagation and affects the crack opening in composites. The bridging stress can be determined by the fibre pull-out length and the sliding force at the interphase [55]. The unloading procedure causes the corresponding reverse sliding that is associated with a macroscale deformation such as observed crack closure (figure 4.8). This reverse sliding may cause further damage in the interphase, which leads to the degradation in the cycling loading. In the C-ring sample, the tensile region is at the convex side under loading, with the crack tip facing the concave side. The crack path generates an extensive fibre bridging especially in the outer ply layer. The reverse sliding during unloading makes a non-uniform deformation with in the sample, which could also explain why there were a dispersed crack path and delamination between the fibre tows observed in the sample under cycling loading compared with that under monotonic loading.

4.4.5. High temperature properties

The novel loading fixture allows the continuous three-dimensional (3D plus time) observation at the elevated temperature that simulates the real service condition. Combined with the DVC analysis, the *in situ* results, both at room temperature and at 900°C, show a similar elastic behaviour and the first matrix crack was observed both initiated at the outer surface. This is consistent with the studies in a melt infiltrated (MI) SiC/SiC from Morscher [52], [157] in which the cracks nucleated in the matrix-rich region. The recent *in situ* test from Mazars [158] also observed the crack initiated from the free surfaces at 25°C and at 1250°C, in another MI SiC/SiC composite. Even though there is no open literature that has discussed crack initiation of the CVI

SiC/SiC composite at the elevated temperature, the results in this thesis show the matrix-rich surface is a possible region for the crack initiation.

After the damage initiated, compared with the previous room temperature test, the results at 900°C revealed a different damage evolution in many aspects. A relatively 'easy' path for the crack propagation was observed in the composite C-ring (figure 4.22). Specifically, the crack path showing a lack of influence from the fibre tows with little crack deflection. A more concentrated damage region in the evolution was observed which could be attributed to the high temperature oxidation of the material. Moreover, in contrast to the results at room temperature (figure 4.18), all the fibre fracture was observed to be very close to the main crack path at 900°C. It leads to a much smaller fibre pull-out length that is generally comparable to the dimension of a fibre diameter at 900°C.

Oxidation is anticipated to play a very important role in the CVI SiC/SiC at such high temperature without protection from an insert gas [159], [160]. Even though the oxygen can penetrate into the sample at both temperatures due to the structure of the interconnected pores (as shown in the Characterization Chapter 3), the oxidation kinetics only became considerable at the elevated temperature [159]. These oxidation effects are different for different materials constituents. The differences from the oxidizing environment at high temperature are much smaller in the MI SiC/SiC composite with a BN interphase [161], [162]. For example, the difference in the stress-strain curves of the tensile tests at toom temperature and at 1200°C was less than 10% in air from the Gowayed's study[161].

The studied SiC/SiC has a near-stoichiometric composition matrix and third generation SiC fibre. Thus, there should be no or negligible degradation in their strength at such temperature (<1200°C) [26], [87]. However, a different oxidation behaviour would be expected in the PyC interphase [26],

[77], [152]. At 900°C, it is expected that once the carbon (PyC) interphase is in contact with air, the carbon is soon oxidized and evaporated. Consequently, there is a reduction in the fibre-matrix interfacial sliding stress and the fibre can move more freely with the possibility being directly in contact with the matrix. Thus, when one or more fibres fractured at or near the matrix crack plane, extra loads simultaneously applied to the adjacent fibres. The movable fibres then experience a local stress concentration due to the matrix cracks, which results in the final smoother fracture surface. This assumption is also supported by the observation that the fibres have approximately no pull-out at the final crack surface (figure 4.22).

Additionally, this earlier rupture of the fibres can be one of the reasons for the reduction in the macroscale strength and elongation (figure 4.32). The degree of this degradation could be related to the affected area. For instance, an approximately 30% difference in tensile strength was reported from Hironaka of a similar SiC/SiC composite with a PyC interphase at 1300°C [152]. Its fractography show the effected region was limited to the surface of the specimen. In the tests reported in this thesis, the entire C-ring is assumed to be affected by the oxidation due to the network provided by the porosity, which is also consistent with the *in situ* observation that the damage evolution was concentrated at some specific matrix cracks at 900°C.

4.5. Conclusions

The study demonstrates the capability of the X-ray tomography to observe the damage evolution in SiC/SiC composite during the mechanical test. The *in situ* tomography method has been developed to observe the C-ring composites from the tubular cladding continuously at both room temperature and elevated temperature. The crack was observed to have initiated at the surface of the C-ring composite at both room temperature and elevated temperature. The occurrence of the

damage is associated with the departure of the macroscale liner elasticity (PLS). The elasticity is similar at both room temperature and elevated temperature (335 ± 25 GPa and 327 ± 21GPa, respectively), but a degenerated strength and ductility were observed at elevated temperature in air. The digital volume correlation of the tomographic image allows the quantitive full-field study of the mechanical response of composite sample in the designed environment in both macroscale and microscale, which could not be obtained by the visual examination of the tomographs. The damage evolution highlighted as strain features in the composite from the digital volume correlation was also found highly heterogeneous and microstructure dependent in the C-ring composite.

Chapter 5. *In situ* synchrotron study of hoop pressurization tests

5.1 Introduction

The fuel cladding components as the most critical core structure must have a reliable performance in both operation conditions and accident scenarios [20], [22]. The structural integrity of the component is largely reliant on its mechanical properties. For the candidate material, SiC/SiC composite, the intrinsically brittle properties of the ceramic determine that its mechanical behaviour is strongly dependent on the microstructure heterogeneities, such as the pores, defects and fibre architectures [61], [163]. The pores and defects population that is irregularly distributed in the composite can also lead to the failure initiation of the component [101]. The fibre architecture might also lead to an anisotropic mechanical behaviour in the composite [52]. Therefore, a feasible approach to evaluate the mechanical properties of the tubular cladding is important.

The C-ring experiments described in the preceding chapters have demonstrated XCT is a useful method to investigate the damage development in the composite cladding tubes. The critical crack initiated at the surface region where the tensile stress was concentrated due to the geometric factor of the C-ring. In fact, an extensive damage was discovered in a relatively small sampling area in the C-ring method samples. How the composites response with a larger sampling area in the scale of tubular component size still needs to be revealed.

Several other methods have been proposed to evaluate the hoop strength in the cladding tubes [164]. They were first applied to evaluate the current fuel cladding material, Zircaloy, in potential accident scenarios [165]. The internal pressure could be generated inside the cladding tubes from a gas or liquid fluid to investigate the tensile hoop behaviour [166]. More commonly, the

compression of an elastomeric plug insert [167], [168] or an expanding solid surrogate [99] could also be utilized. In those experiments, the stress state is normally calculated based on the thick-wall or thin-wall cylinder assumptions [167], [169]. This approximation might be valid in the isotropic metal material as Zircaloy. However, it is unclear whether this approximation is still valid and can be applied in the anisotropic SiC/SiC composites.

The validation study would require a 3D comprehensive measurement of the mechanical deformation. In this chapter, a study is presented using coupled X-ray computed tomography (XCT) and digital volume correlation (DVC) of an *in situ* synchrotron pressurization test of the SiC/SiC fuel cladding. The study intends to provide a multi-scale volumetric measurement of mechanical response of the SiC/SiC composite and investigate the damage evolution in the fuel cladding component under internal pressure.

5.2 Materials and Methods

5.2.1 Materials and Mechanical Experiment Setup

The material used in this study is the same batch of the SiC_f/SiC composite tube provided by *CEA* as in the previous studies. The composite tubes were cut into sections with a length of 11 mm, using a diamond cutting saw. The cutting surfaces were then ground and examined in an optical microscope and by X-ray tomography up to a voxel resolution of around 2.5 μm to ensure there was no detectable machining damage.

Pressurization tests were performed using a Shimadzu AGS-X precision (10 kN capacity) universal testing machine (figure 5.1(a)), which was transported to the Diamond Light Source from University of Oxford for this experiment. The test machine was set in displacement-controlled mode such that there is no movement during rotation of each X-ray tomographic scan. A

customized loading stage was designed to generate pressurization upon the tube specimen, as shown in figure 5.1(b) and (c). Two end punches were made from an aluminum alloy, which offers a satisfactory combination of yield strength and X-ray penetration rate. A trial and error procedure of the punch manufacturing ensured a close fit to the tubular cladding that was less than 0.02 mm. The core of the schematic, which fits within the tubular cladding specimen, is a Viton® (tradename of an extrusion resistant fluorocarbon elastomer in *DuPont-Dow*) rubber plug with a diameter of 8 mm. The rubber was selected as it has a Poisson's ratio of nearly 0.5, to generate a uniform expansion and could tolerate small-scale misalignment [170]. The plug was compressed axially by moving the aluminium punch at the top end, which generated predominantly a radial displacement upon the inner diameter of the tube specimen until its final fracture. The compressive strength of the Viton rubber was not provided from the supplier, but the rubber remained intact after the fracture of the composite tube.

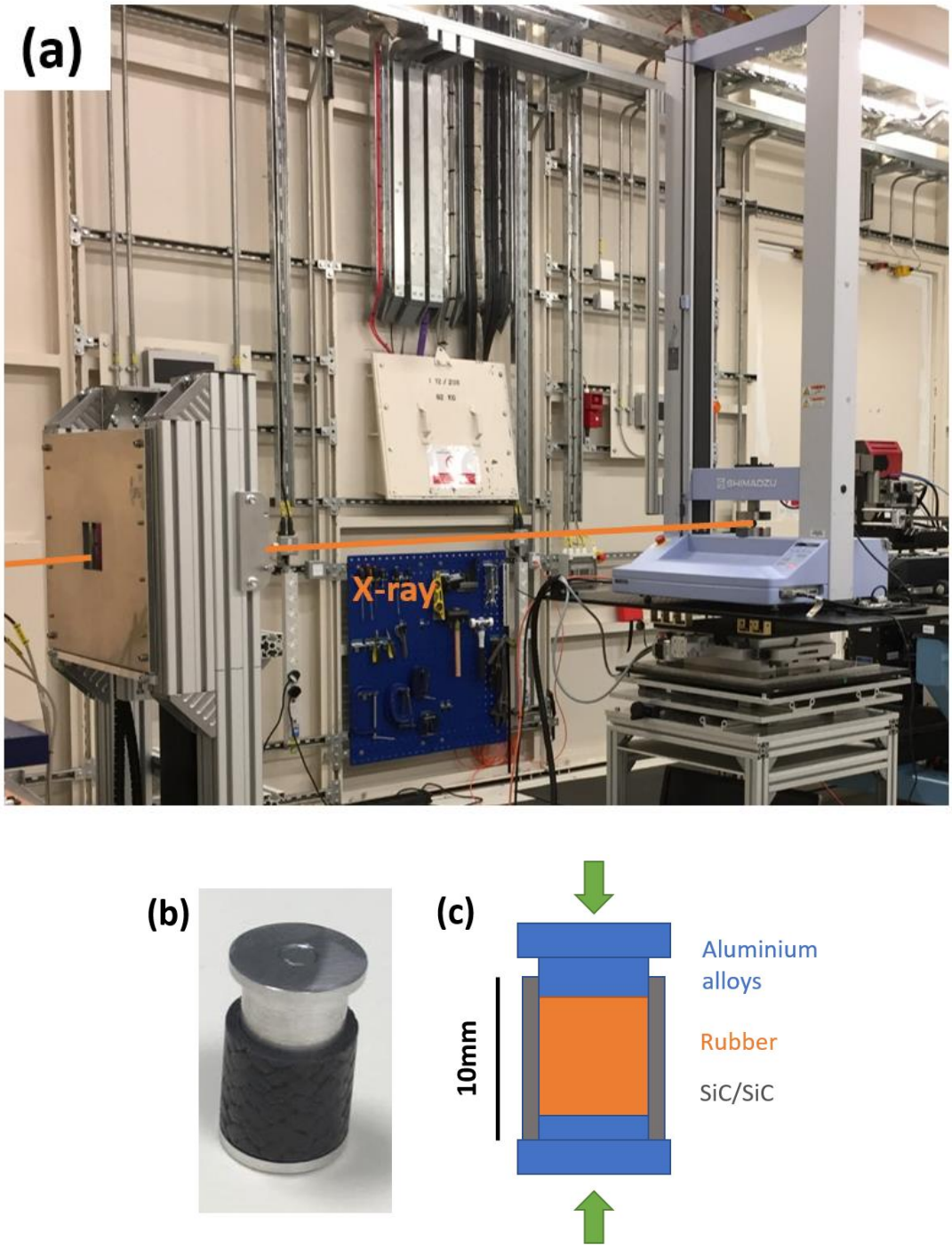


Figure 5.1 (a) The Shimadzu test machine (from University of Oxford) mounted on the Diamond I12 EH2 rotation stage. (b) the image of the tube composite sample placed on the customized loading stage before the tests. (c) the schematic section view of the customized loading stages.

5.2.2 Synchrotron X-Ray Tomography[5]

This *in situ* mechanical testing was performed at the I12 Joint Engineering, Environmental and Processing (JEEP) beamline in Diamond Light Source, UK as shown in figure 5.1(a). The high energy synchrotron monochromatic X-ray beam line was set at 60 keV. The observation adopted the limited-angle tomography mode (from -74.4° to 71.8°), due to the geometric limitation imposed by the arms of the Shimadzu universal tensile machine. Two modules of optics [108] were utilized to obtain radiographic pictures of the entire sample in each load increment with different resolution. Their spatial relation is illustrated in figure 5.2. The first scan (module 2) captures the entire specimen in one scan with the pixel size of 7.91μm, with an exposure time of 0.05 s for each radiograph. The length of its spatial field of view is approximately 20 mm. The second set of scans (module 3) has 3.25 μm pixel size detecting more detailed structure in the localized region of interest, but it can only offer the limited field (around 8 × 8 × 8 mm). Therefore, four scans at module 3 with an overlapped distance of 1.5 mm were conducted to observe the entire specimen. The exposure time for module 3 is 0.8 s per radiograph. All those tomographic images were obtained *in situ* while the displacement of the crosshead was fixed. One full set of scans took about one hour in total at each scanning point of the designated displacement.

[5] Beam line number EE12585-2 in Oct 2016.

For this test, I designed the experiment and machined the customized load mounting stages. I conducted the experiment with the help from group members (Mr. S. Barhli and Mr. P. Earp).

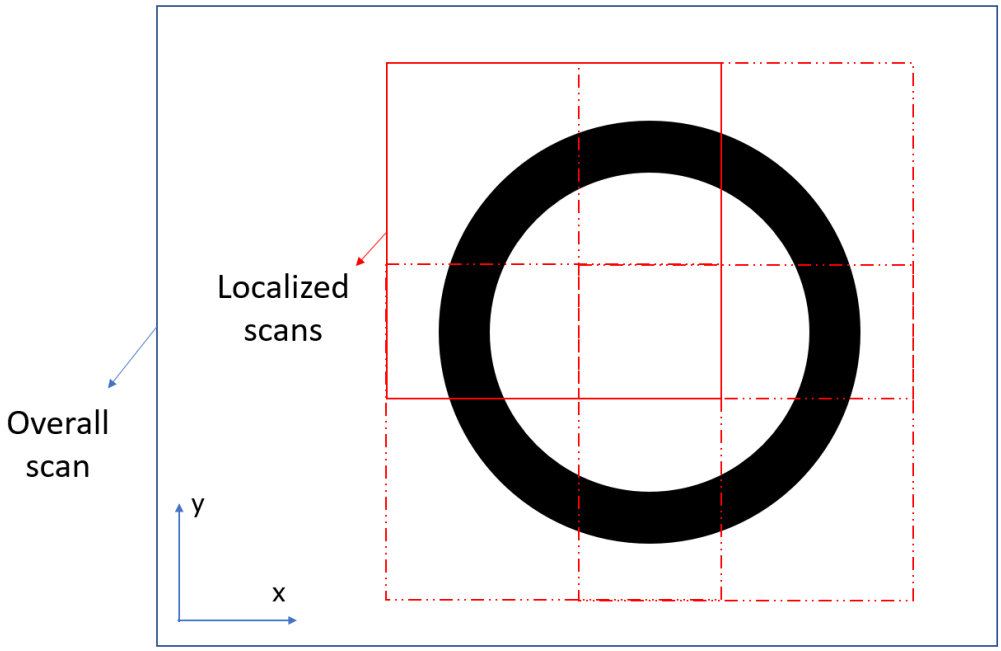


Figure 5.2: The spatial relation of the overall scan (in blue, Module 2) and the localized scans (in red, Module 3) employing two optical modules. The black indicates the composite tube samples.

Each 3D synchrotron tomographic image was then reconstructed from 2501 radiographic projections. The reconstruction used the in-house back-filtered projection code with a ring artifacts remover Fourier-wavelet algorithm provided by I12, Diamond [171]. The ring artifact due to the faulty scintillator pixels (~10 pixels) was corrected in the code by replacing the averaged neighboring pixels values. Although the data were not collected over 180°, no further correction was applied to reconstruct the limited angle tomographic data as key features were captured in the reconstructed images. After the synchrotron X-ray tomography, the fractured sample was also examined in the Zeiss Xradia Versa 510 at University of Oxford. A 60 keV X-ray energy was used, and 3201 projections were collected over 360° to produce the post-mortem tomographic picture with a voxel size of 8.2 µm and 3.1 µm. The 3D images were processed in ImageJ and visualized using the Avizo Fire software.

5.2.3 Strain measurement by Digital Volume Correlation

In order to quantify the mechanical response of the composite tube in different length scales, the DVC analysis was applied to the tomographic images from two optical modules separately. The analysis was performed in the commercial software LaVison DaVis StrainMaster 8.2 with the OUMS-ARES workstation. The calculation used the direct correlation mode, with the reference image being the undeformed sample (50 N preload on the rubber). The final correlation window has a subset size of 64×64×64 voxels, with 75% overlap for 2 passes. The required valid voxels per window was set to at 50% to give a more detailed result at the sample surface, and the threshold of correlation coefficient for each window was 90%. The analysis yields a full field displacement field with a resolution of 126.5 µm and 52 µm for the scans with the resolution of 7.91 µm and 3.25 µm respectively. To estimate the uncertainty in the displacement measurement, a physical translation of around 98 µm was applied to the sample stage (details in table 5.1). This yields an uncertainty in the displacement measurement of around 0.37 µm that is approximately 5% of the voxel size and the error in the strain calculation is 0.025%.

Table 5.1: The displacement uncertainty of the DVC analysis in the continuous scan with the window size of 64 × 64 × 64 voxels at room temperature

Direction	Physical translation (µm)	DVC analyse	
		Average (µm)	Standard deviation (µm)
x	40	39.42	0.20
y	40	39.58	0.20
z	80	80.58	0.16
Total	98	98.05	0.32

5.3 Results

5.3.1 Fracture of the SiC/SiC composite

Before the *in situ* tests, six SiC/SiC composite tubes were tested using the customized loading stage (figure 5.1(a)) in the Shimadzu universal test machine without tomography. They all fractured when the loading on the rubber insert reached 4000 ± 400 N with a steep decline in the force. The records of the force from the crosshead are shown in the figure 5.3. The loading history imposed on the rubber insert in the ***in situ* mechanical test** is shown in figure 5.4(a) that is quite similar. The loading increased gradually and paused at each designated load until the tube specimen fractured at 4052 N. Each dot in the profile represents the point at which loading was paused for a set of tomographic scans. The loads for tomography were set at 1000 N, 2000 N, 2800 N, 3400 N and 3800 N, based on the previous experiment. During each scan the relaxation of the rubber leads to a small load drop. The maximum drop was less than 70 N during the scanning and they were generally negligible (< 20 N) when the loading force was less than 3000 N.

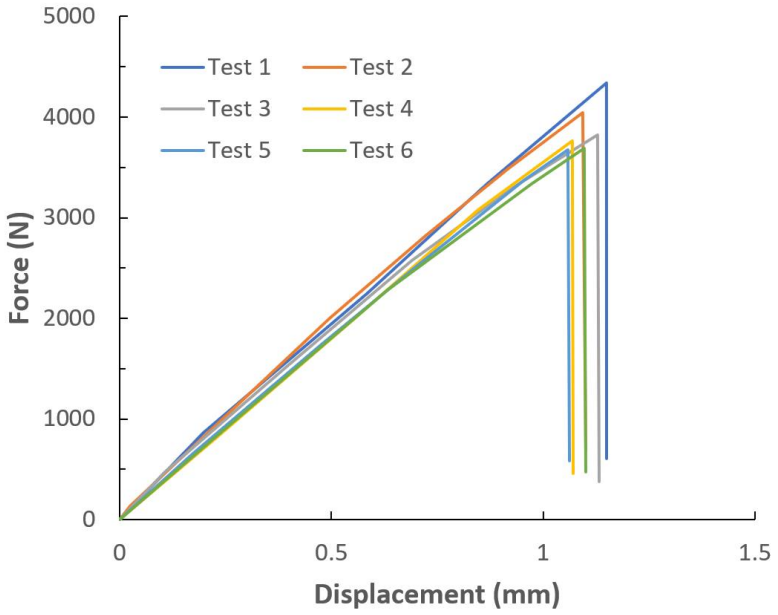


Figure 5.3: The force and displacement data of six trail tests of composite tube with the loading stage.

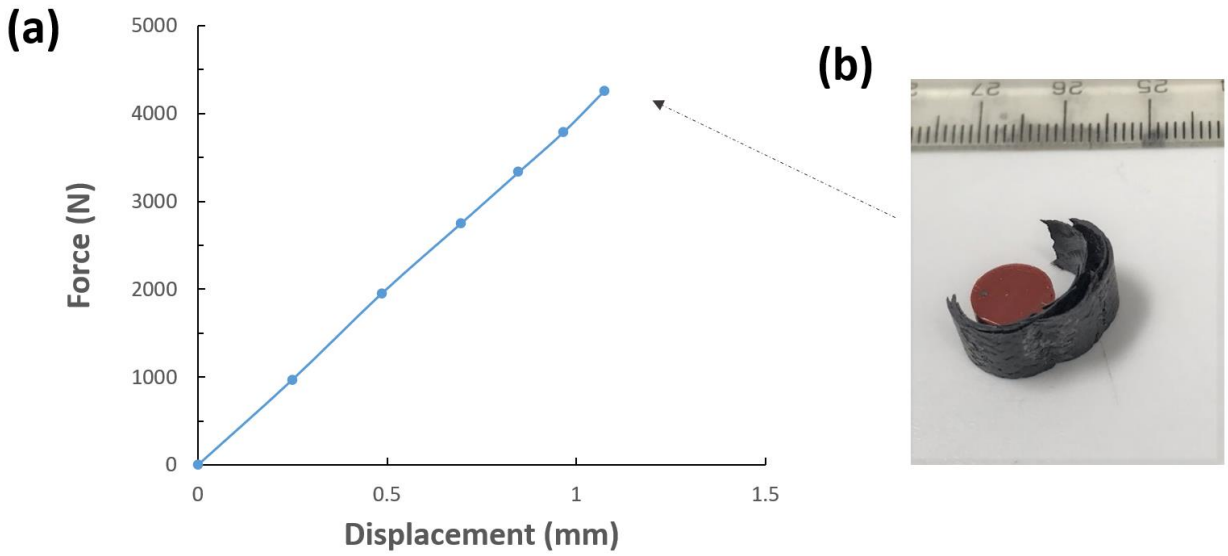


Figure 5.4: (a) The force and displacement data that were recorded imposing on the rubber with each dot noted the paused loading level for a set of *in situ* tomographic scans. (b) the shape of the fractured sample.

At the ultimate loading, the fractured samples showed a through-thickness critical crack along the tube axis direction (figure 5.3(b)). Due to the sudden expansion of the compressed rubber when the composite tube fractured, the tube was enlarged with the longest diameter almost doubled. The fibre pull-out and laminated delamination were also obvious without any aid of the microscope. Despite the clear delamination of the three layers and two other cracks spread in the tube, all the fractured tubes remained a single piece. Nevertheless, the shape of fractured tube indicated a failure mode that was dominated by the hoop stress.

5.3.2 General observation from the tomography with quantitative crack analysis

The example images of the spatial relationship scans from the two optical modules (resolutions in 7.91µm and 3.25µm) from the synchrotron tomographs are shown in figure 5.5. The virtual slices illustrate how the entire volume of the composite tube was covered in the 7.91 µm scan and four overlapped localized scans with a voxel size of 3.25 µm in each scan set. The *in situ* observation of the original state of the composite tube in the deformed state is shown in the figure 5.6(a) and figure 5.6(b) respectively. In the X-ray tomographic images at the deformed states, axial matrix cracks at the surface of the composites could be observed (figure 5.6(b)).

An example of the cracks seen from the horizonal plane is shown in the figure 5.7. The *in situ* image was captured when the load reached 2000N, which is also where the first matrix cracks were observed from the tomographic observation. The crack opening was generally very small and is close to the magnitude of the voxel size (7.91µm). The sharp edges of those cracks also caused the artifact streaks which makes the quantitative analysis of each crack difficult. However, the streak line associated with each crack makes the detection of each crack straightforward and the counting of the crack distribution possible (figure 5.7). Figure 5.8 shows the 3D view of the scan image at 2000 N (as in figure 5.7). The path of the cracks appeared on the surface was generally spanning axially at the same angular direction along the composite tube. The cracks from both outside surface and inside surface are also shown in the enlarged views in figure 5.8(b) and figure 5.8(c) respectively.

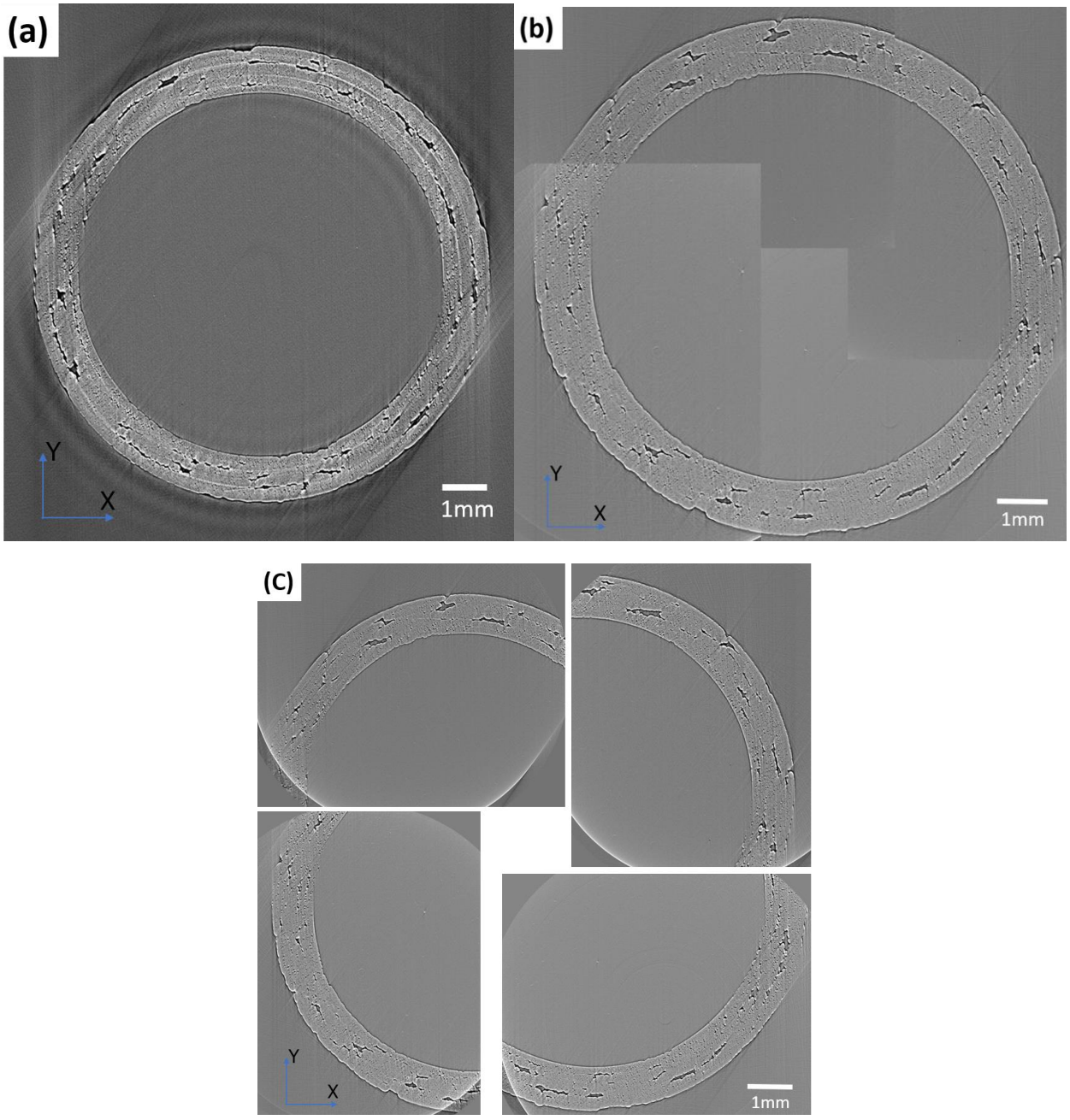


Figure 5.5: The horizontal (X-Y) virtual slice of the composite tube in the (a) 7.91µm scan and (b) the overlapped 4 scans in the resolution of 3.25 µm. (c) the original 3.25 µm scans in the overlapped image (b).

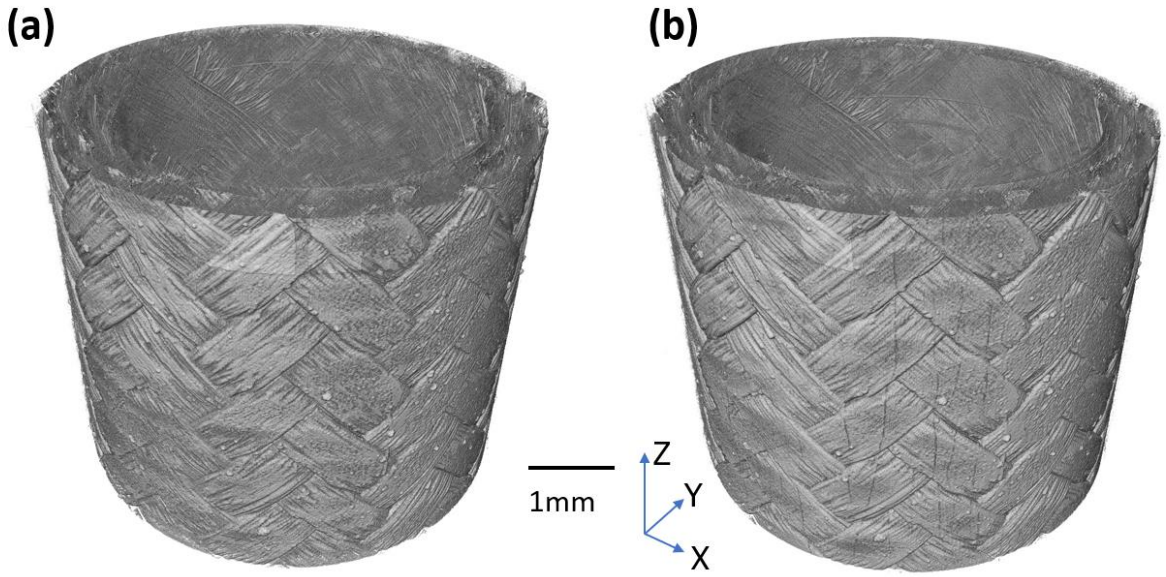


Figure 5.6: (a) The 3D rendered volume of the composite at the original state and (b) the volume of the composite just before the fracture (3800N). (data from scans with a resolution of 7.91μm)

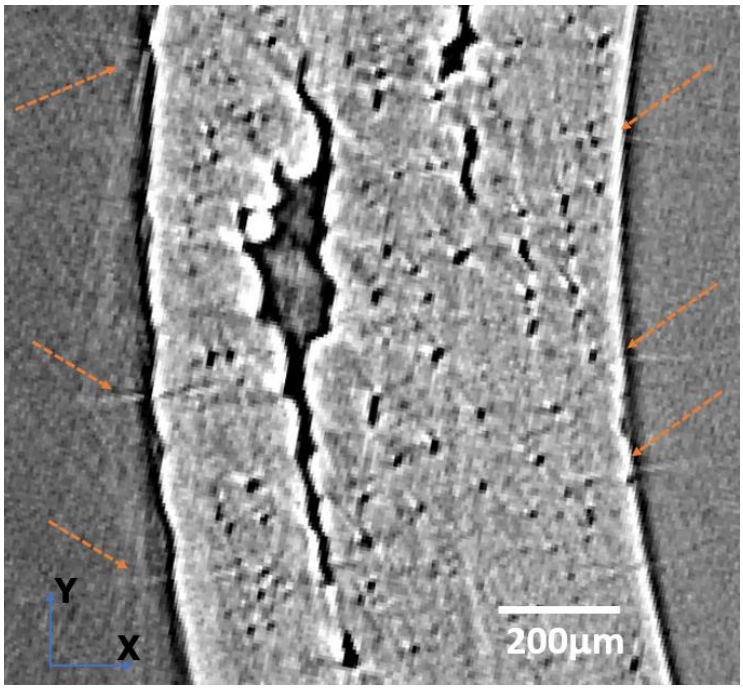


Figure 5.7: The horizontal (X-Y) virtual slice of the *in situ* tomographic images at load (2000N) showing the surface cracks at both outside and inside surface. (data from 7.91μm scan at the stage of 2000N)

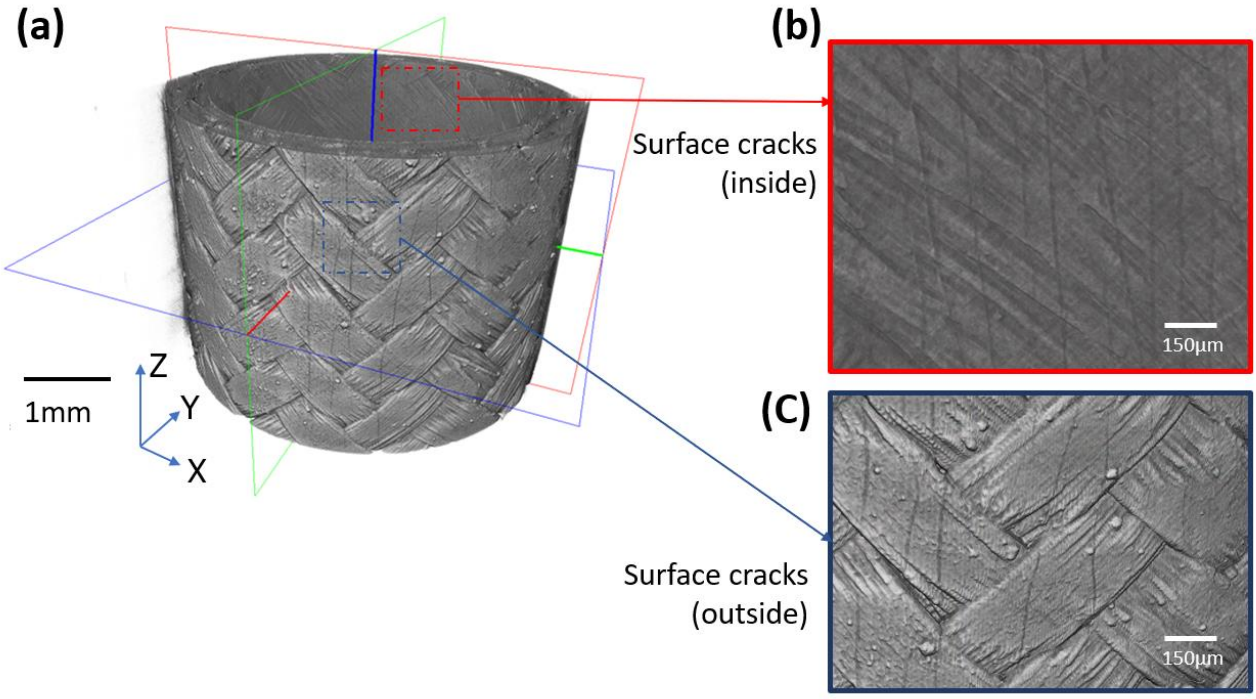


Figure 5.8 (a) The *in situ* 3D rendering view of the composite showing the surface cracks, (b) the enlarged view showing the cracks at the inside surface, and (c) outer surface. Images from the 7.91μm scan at the stage of 2000N.

From the *in situ* tomographic images of each stage (as shown in figure 5.8), the number of the cracks can be measured. The crack densities on the inside surface (IS) and outside surface (OS) were measured over the entire sample with an area of 171.5 mm^2 and 215.6 mm^2 respectively. They show a different statistic number. The IS cracks always have a higher density over the OS crack density at each loading state (figure 5.9). The highest crack density observed in this study was about 4 mm^{-1} but the OS crack density only reached around 2.5 mm^{-1} and it shows a reduced rate of increment after it passed 2 mm^{-1}.

The matrix cracks spanning axially along the entire sample height (figure 5.8), but they were distributed heterogeneously at different angular directions. Figure 5.10 shows the crack density on the outside surface and inside surface along the full angles (X-Y plane). Those crack numbers

were counted in each angular unit of 30°, which yield a unit sampling area of 14.3 mm^2 and 18 mm^2 for the inside surface and outside surface respectively. As shown in figure 5.10, the heterogeneity (difference) along the full angles is higher in the insider layer. Moreover, more heterogeneity was observed at higher loading stage.

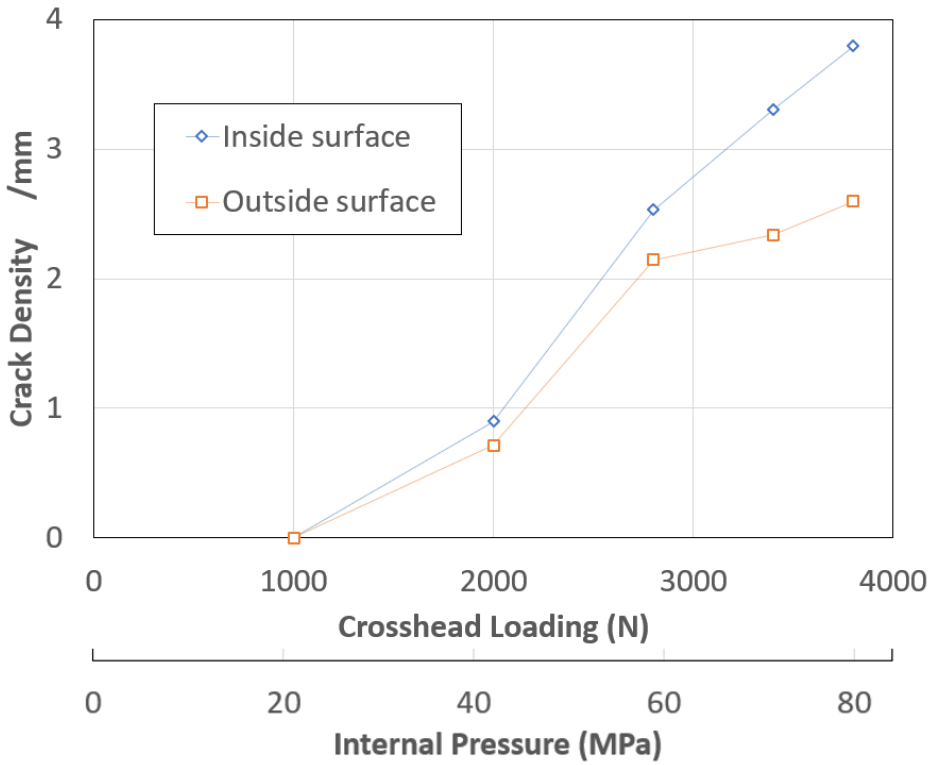


Figure 5.9: The crack densities at the inside surface and outside surface at different loading states

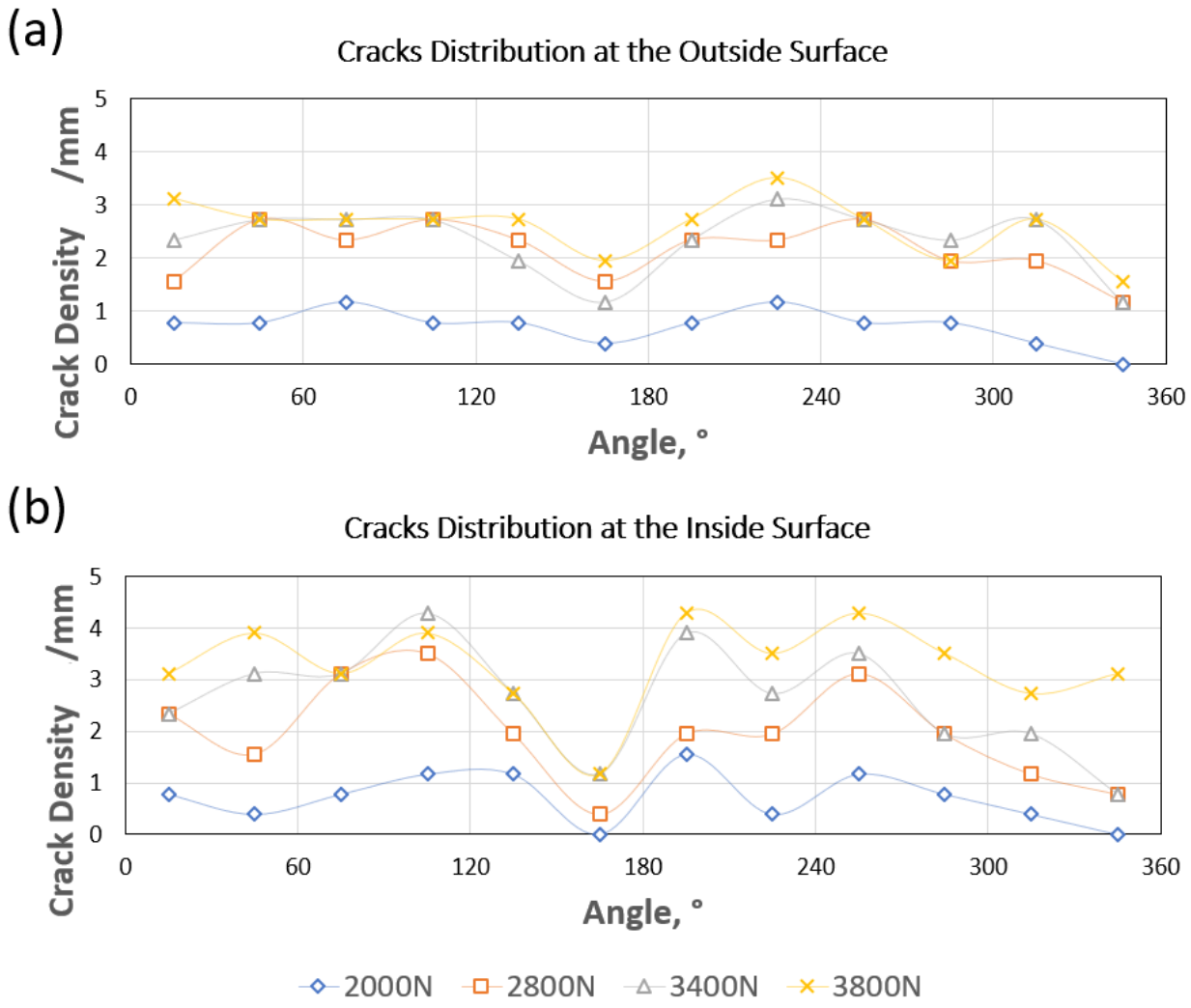


Figure 5.10: The distribution of the matrix cracks at (a) the outside layer and (b) the inside layer along different radial directions in different loading stages (final fracture occurred at 350°)

5.3.3 Microscale damage evolution

Figure 5.11 present the damage evolution as the localized strain features from the DVC results superimposed with the tube microstructure from the tomographic images. Two different patterns of a heterogeneous strain distribution were observed. At the beginning, the local strain that was relatively small (< 0.01) within the tube was preferably distributed along the fibre tows. The strain

pattern then gradually changed to cluster axially, showing a different type of damage. With further increased loading, those axially distributed strain features remain and progressed extensively. Additionally, the section view (figure 5.12) of the tube before the final fracture (3800 N) shows that the localized strain is not constant along the radius. Its distribution is related to the microstructure. Those damage initiating from the surface was deflected between the ply layers. The highest strain region was observed near the fibre tow crossover points.

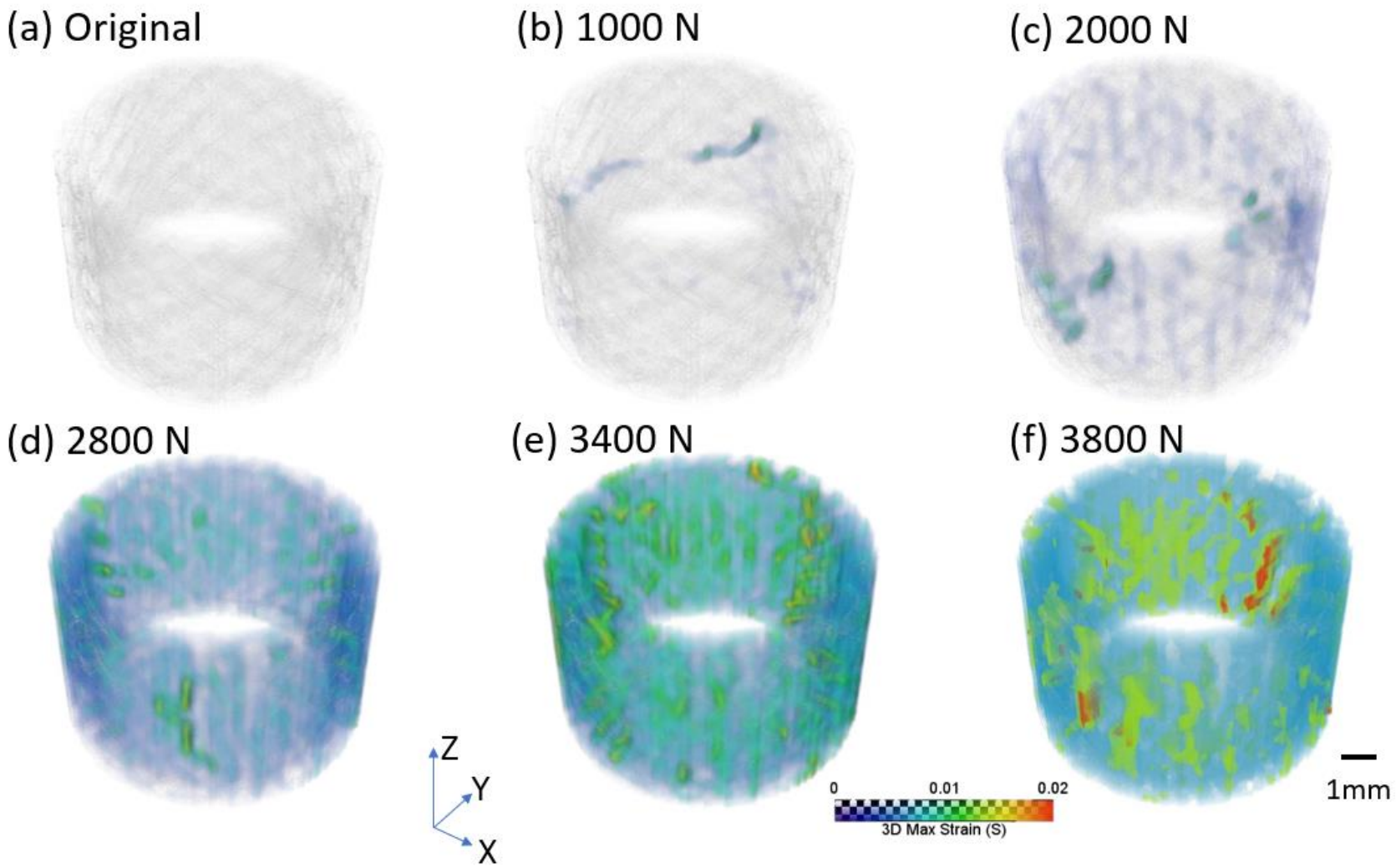


Figure 5.11: 3D visualization of the localized strains distribution with the microstructure of the tube showing the damage evolution. The strains were calculated from the displacement field measured relative to the original state and the opacity of the microstructure is set to be 1%. Data from 7.91 μm scans.

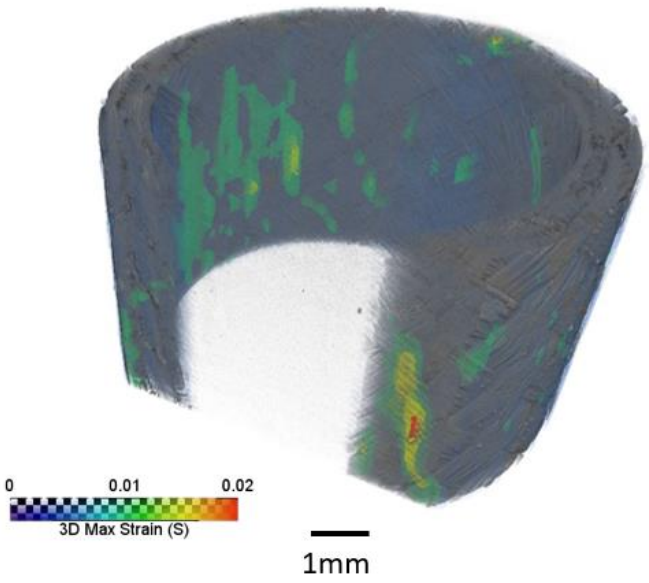


Figure 5.12: The sectioning view of the tube under 3800N showing the strain distribution along the tube radius

At the peak load (4052N), the through-thickness crack caused the final fracture of the composite tube. Figure 5.13 shows the 3D rendered shape of the fractured composite (8.2 µm voxel size in an *ex situ* laboratory tomographic scan) due to the critical crack. The strain map evolution of this critical crack path was then shown in the figure 5.14. It demonstrates the *in situ* damage development of the same location that became the final cracks path before the final fracture (blue rectangular region in figure 5.13). The DVC and tomographic image data were from the localized synchrotron *in situ* scans with a 3.25 µm voxel size. With the adjacent microstructure figures, figure 5.14(a) shows the strain distribution was firstly regulated by the fibre tows architecture. However, as the load increased, the localized strain features (figure 5.14(c)) corresponded to the path of the axial cracks, which then finally become the final crack path (figure 5.14(e)).

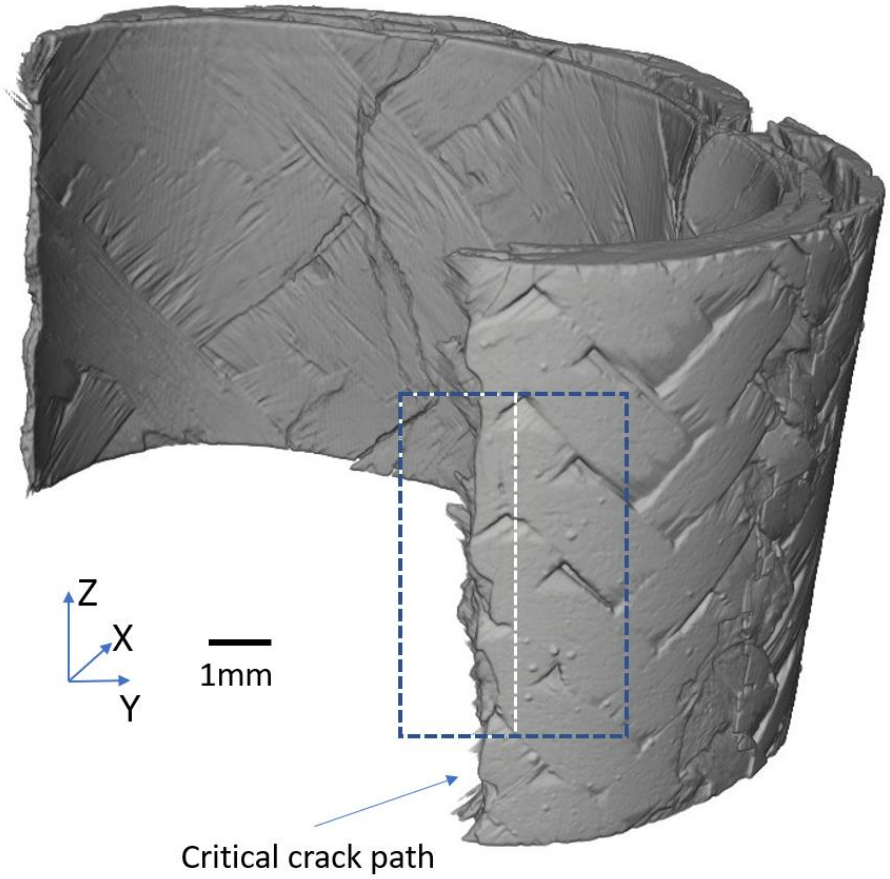


Figure 5.13: 3D rendered view of the fractured sample, Data from 8.2 µm scan (the strain evolution of the critical crack as in the blue box shown in the following figure 5.14)

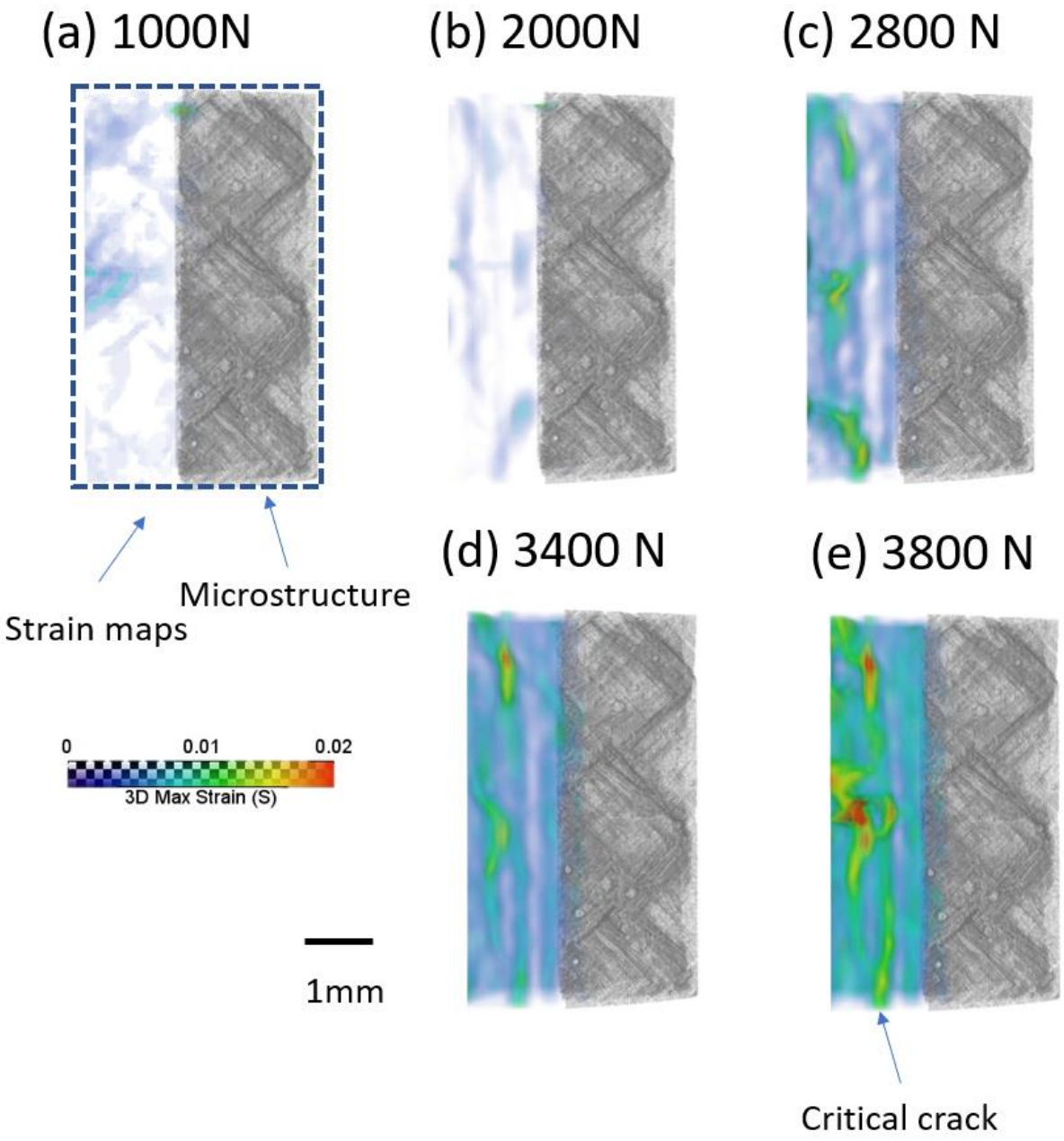


Figure 5.14: The strain distribution at the final critical region (blue rectangular in figure 5.13) with the adjacent microstructure, Data from 3.25 µm scans

5.3.4 Quantitative study of the deformation

The mechanical response of the composite tube can be quantified using the full-field displacement maps from the DVC calculation at different length scales. Unlike other traditional extensometers or surface 2D technologies, the DVC captures deformation of the entire sample at any direction. In this section, the macroscale and mesoscale deformation was investigated using the results from the scan that captured the entire tube sample (7.91 µm voxel size).

5.3.4.1 Coordinate system conversion and rigid body movement

Before showing the results, it is important to address the different coordinate systems (more details in Section 3.2.3). To demonstrate how the cylindrical tube deforms under the internal pressure, the target is to register the sample in the tube cylindrical coordinate system, where the origin is the centre of the cylindrical tube on the basal plane. By contrast, the DVC results in a Cartesian coordinate make the further eigen-decomposition of the hoop, radial and longitudinal deformation complicated. Therefore, the displacement results in Cartesian coordinates were transformed to the tube cylindrical coordinate system to demonstrate the nature of the sample deformation as in the following:

The DVC in the DaVis StrainMaster 8.2 cannot correct the subvoxel rigid body movement of the registered images sets and the resolution of the displacement depends on the final interrogation window size. As in the *in situ* experiment, the relative positions of the camera and rotation stages were fixed. However, in this study the tube sample under the internal pressure has no fixed end that is attached to the loading fixture. Therefore, the tube can tilt freely to a certain degree, which could generate a 3D rigid body translation and rotation. Those small movements are not negligible in comparison to the displacements within the material and need to be properly considered and corrected. A previous study by M. Mostafavi [111] demonstrated that correction of this rigid body

movement correlation can reduce the uncertainty in the displacement measurement to the scale about half of the voxel size. In this study an add-on in-house MATLAB code, based on Mostafavi's code [111], were developed to correct the rigid body movement and achieve the coordinates conversion. The original code focused on the translation. The developed code in this study corrected translation first. Then the sample rotation was corrected and the corresponding eigen-decomposition displacement in the cylindric coordinate systems was defined.

The code first corrects the rigid body translation. The original 3D tomographic pictures have the Cartesian coordinate system with reference registered with the tomographic camera and sample rotation centre. With respect to this system, the raw DVC results include the relative displacement vectors $[U_i] = \left[u_i^x, u_i^y, u_i^z\right]$ at each central point ($[A_i^o] = [x_i^o, y_i^o, z_i^o]$) of the correlation window. Therefore, the deformed location of each correlation window can be represented as $[A_i^1] = [A_i^o] + [U_i] = [x_i^1, y_i^1, z_i^1]$. The rigid body translation correlation is therefore removed as $[A_i^1] - [\overline{U}_i]$ (the average of all the displacement vectors). This rigid body translation was normally tens of voxel dimensions in this study.

Then, the centre of the rigid body rotation is corrected with respect to the center of the cylindric tube. The Euler rotation value $[\alpha, \beta, \gamma]$ is calculated from subdividing the translation correlated matrix and deformed location matrix. After the inverse rotation using Shoemaker's method [172], the rotation is corrected. After the rotation correction, the highest Euler rotation angle was less than 0.3°. The phenomena of the rotation can be demonstrated by the sinusoid pattern of the axial displacement along different angular directions (figure 5.15) of the entire tube. Examples of the axial distribution at different loading stages before and after the correlation are shown in the figure 5.15(b) and (c) respectively.

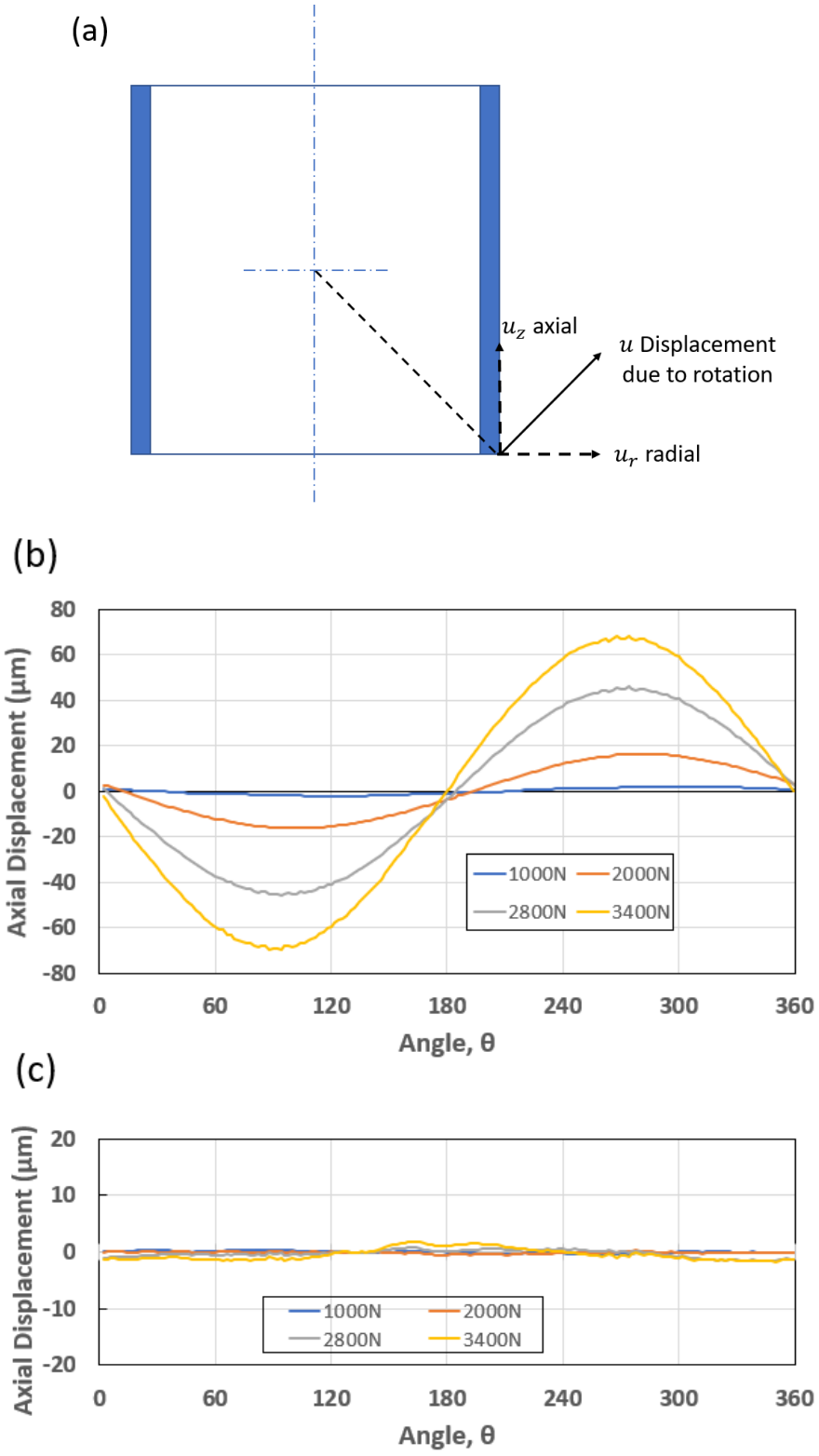


Figure 5.15: (a) The geometric relation of the rotation effect on axial and radial displacement; the axial displacement distribution (b) before correlation and (c) after eliminating the rotation effect.

5.3.4.2 Macroscale deformation

The macroscale mechanical response of the composite tube at different stages is shown in figure 5.16 after the coordinate conversion and correction of the rigid body translation and rotation. The displacement field DVC results were calculated from the scan that captured the entire sample (7.91μm voxel size). The deformation was illustrated as the displacement from the DVC analysis. At this macroscale, the displacements were the average across the thickness (1mm).

Figure 5.16(b) shows the distribution of displacement along the tube height. At the load of 1000 N, the tube experiences a relatively uniform dilation along its height. However, from the stage where matrix cracking was observed (2000N), tube started more extensive deformation, especially at the middle height. The difference between the two ends and the middle part can be as large as 40% at the higher loading stage. This observed pattern of displacement along the tube height indicates more extensive deformation at the middle part of the composite tube, which could also mitigate the possible effect of the cutting damage from the sample preparation.

Figure 5.16(c) shows the unwrapped radial displacement of the tube at each loading stage. The centre was defined as the physical centre of the cylindric composite tube. The data at each angle was a binning of the displacement through tube thickness and along the entire tube height. As shown in the figure, when the loading was 1000 N, the magnitude of the radial displacement is very limited and hardly being seen compared with the degree of the deformation in the higher loading stages. The zoomed figure 5.16(d) of the radial displacement at 1000 N shows a relatively uniform dilation (about 0.4 μm) at all angles. Two local maxima are witnessed at the angles of approximately 50° and 270°. Nevertheless, at this stage there is no extensive variation along different directions.

When the load reached 2000 N, the radial displacement (figure 5.16(c)) started to show an elliptical deformation from the original circular shape. This elliptical deformation can be divided into two types of deformation: dilation and ovalization (figure 5.17). The positive average radial displacement at each stage indicates a dilation. The sinusoidal patterns (figure 5.16c) with two full cycles at different radial directions illustrate the ovalization. After 2000 N, the radial displacement patterns at the later higher stages remains. An increasing degree of dilation and ovalization in general was demonstrated. The variation along the different direction is also increasing, indicating a further amplified anisotropic deformation ('ovalization'). Furthermore, those ellipses due to the ovalization share the similar major axis aligned at the direction around (50 ± 6°).

In summary, the statistical analysis of the macroscale tube deformation is relatively smooth and uniform at the beginning. It then deforms differently at different directions. The degree of the anisotropy in deformation is also amplified at higher loading states. It is noteworthy that in the ideal expansion of a homogeneous cylindric tube the distribution of the radial displacement is uniform at any angular direction and the circumferential displacement should be zero as situation of dilation in figure 5.17. However, the full-field analysis shows that the ideal situation might not apply to the composite tube. Further analysis of the deformation will then be addressed.

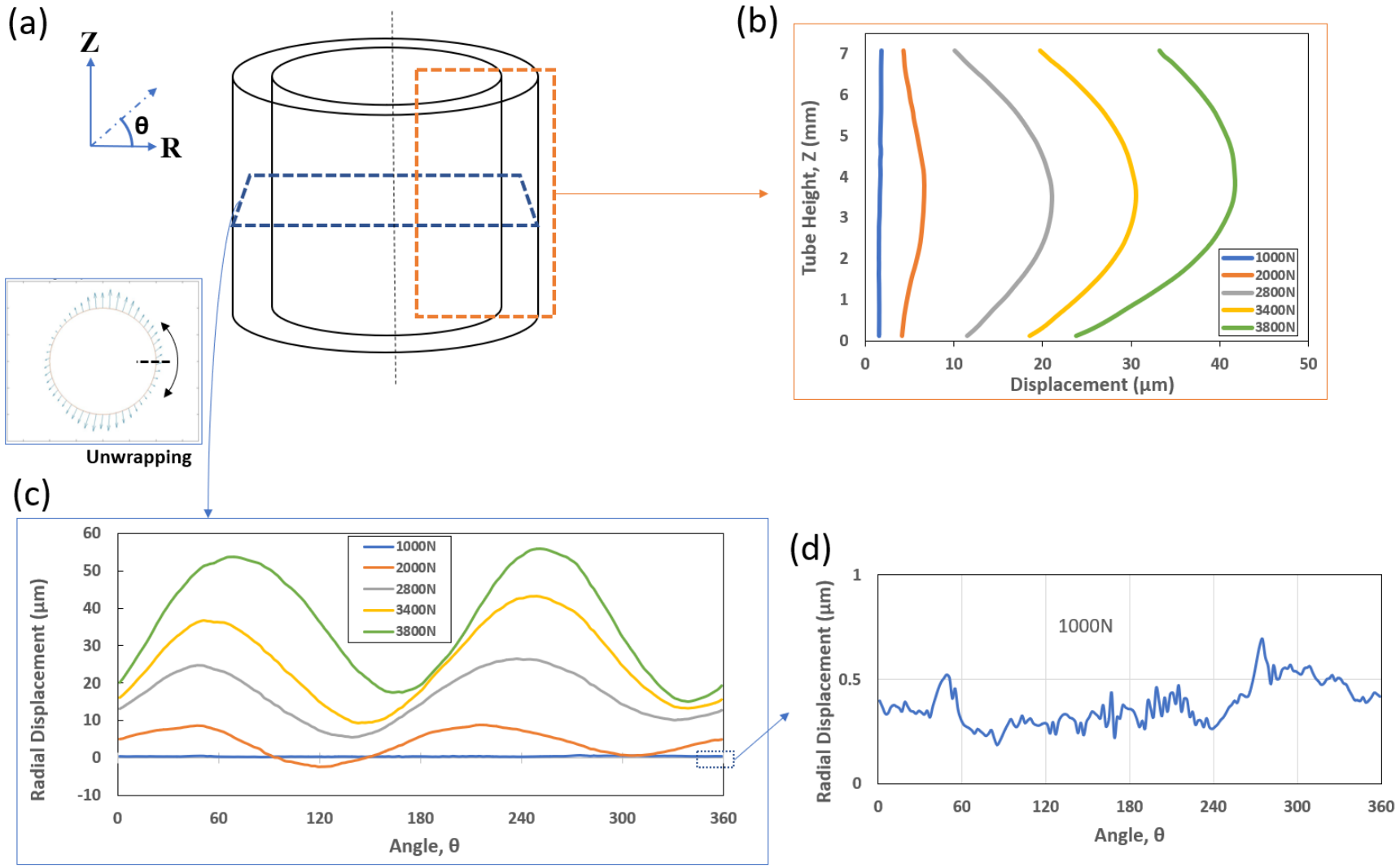


Figure 5.16 (a) The macroscale deformation of the cylindric tube (b) along the tube height, Z and (c) at different angle θ. (d) is the enlarged view of the radial displacement at different angle at the load of 1000N.

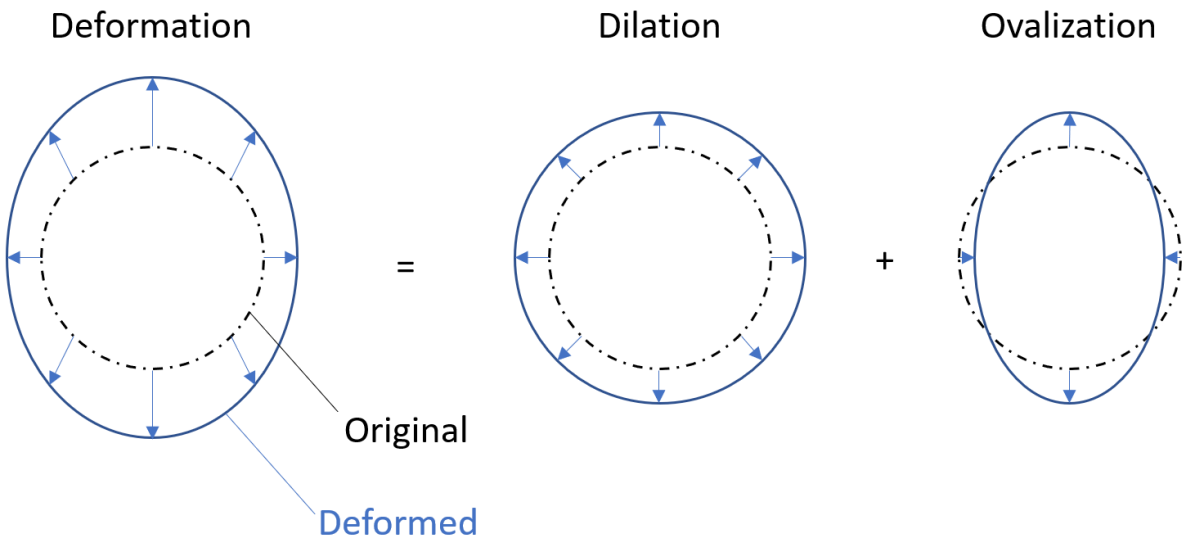


Figure 5.17: The two types deformation observed in the composite tube, dilation and ovalization shown as the radial displacement in the horizontal (X-Y) plan

.

5.3.4.3 Displacement field and hoop strain measurement

The overall macroscale deformation of the tube, as illustrated in 5.16, is anisotropic at different angular directions, which means the ideal strain equation for cylindric tubes with the homogeneous and isotropic assumptions of the material should not be applied in this study. Mathematically, the hoop strain is determined by two displacement-dependent terms in cylindrical coordinates (equation 5.1[173]), of which u_r is the axial displacement and u_θ is the circumferential displacement. With the help of the *in situ* tomographs coupled with DVC of the entire sample, the displacement terms at radial and circumferential were measured. Using the similar method as in the macroscale deformation analysis, here both two terms are illustrated in the mesoscale at each position in each stage. The radial term resulting from the radial displacement is understood to be the expansion of the tube (dilation), while the circumferential displacement shows the extent of the ovalization or uneven deformation.

$$\varepsilon_{\theta\theta} = \frac{u_r}{r} + \frac{\partial u_\theta}{\mathrm{r}\,\partial\theta} \tag{5.1}$$

Radial displacement

Figure 5.18 shows the radial displacement of the cylindric tube at different stages from the DVC measurement. At the beginning (1000 N), the distribution of the radial displacement shows a distinctive pattern compared with that of all the other loading stages. The radial dilation (about 0.5 μm) locates at the middle height of the tube and is relatively constant at different angle directions. At 2000 N, a pattern of the radial displacement appears where the contour map points out the two highest dilation directions. They are located at the positions of approximately 40° and 240°, which is also the major axis of the ellipse (ovalization deformation) as previously described. The minor axis is situated in the perpendicular direction. The pattern of the radial displacement field stays until the final scan before the failure at 3800 N.

Circumferential displacement

Figure 5.19 shows the circumferential displacement maps of the deformed tube at each stage. At 1000 N, the circumference displacement is generally small and there is no regular pattern of the distribution. By contrast, the circumferential displacement maps in the situation with higher loads show a similar distribution along the tube height. This type of contour maps suggests a similar magnitude and pattern of deformation on each transverse plane. This pattern of the circumferential displacement is typically generated from the ovalization of the cylindric tube (figure 5.17). The position with no (zero) circumferential displacement corresponds to the position of the major and minor axis of the ovalization as shown in the axial displacement maps.

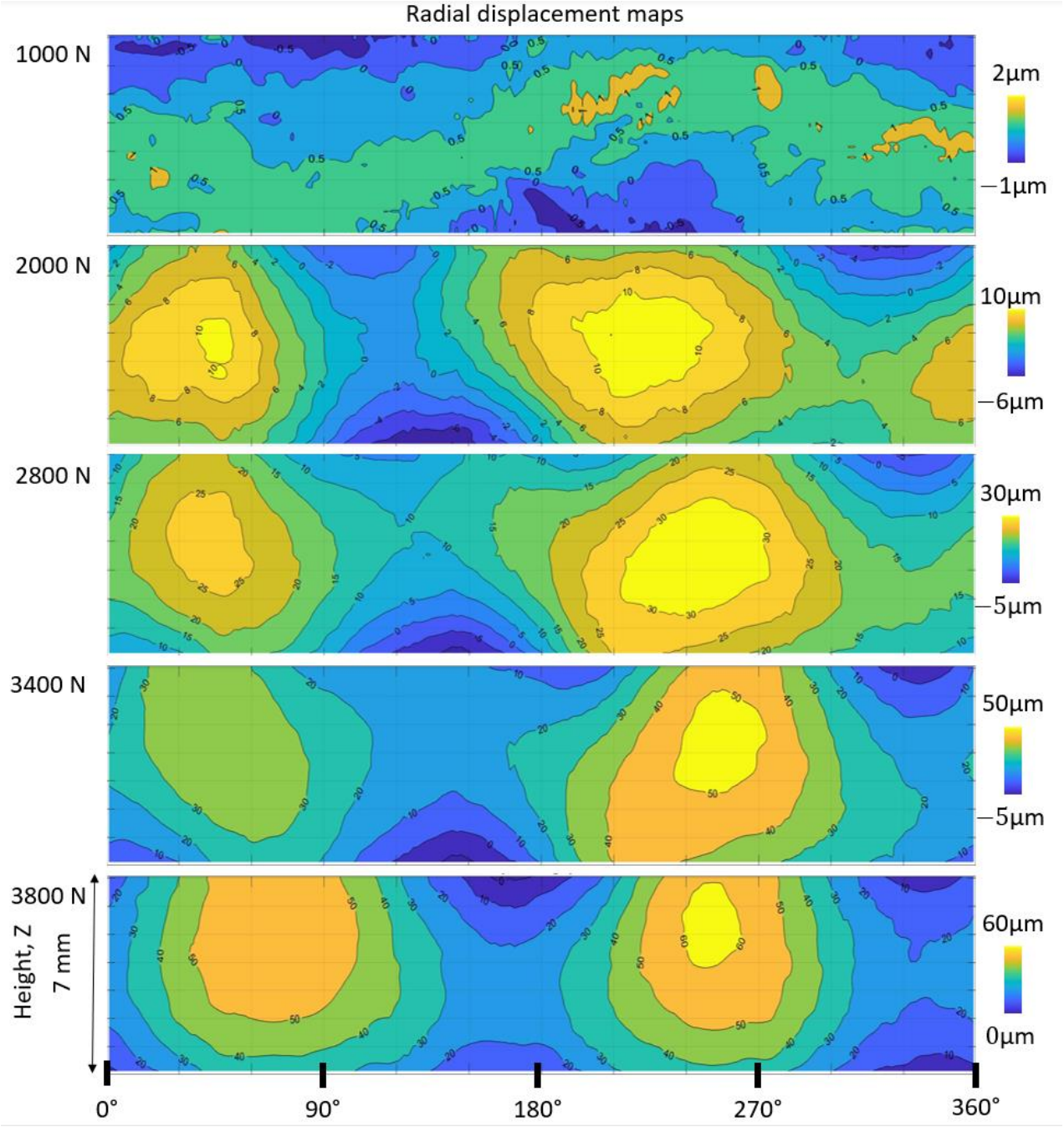


Figure 5.18: The unwrapped radial displacement maps at each loading stages

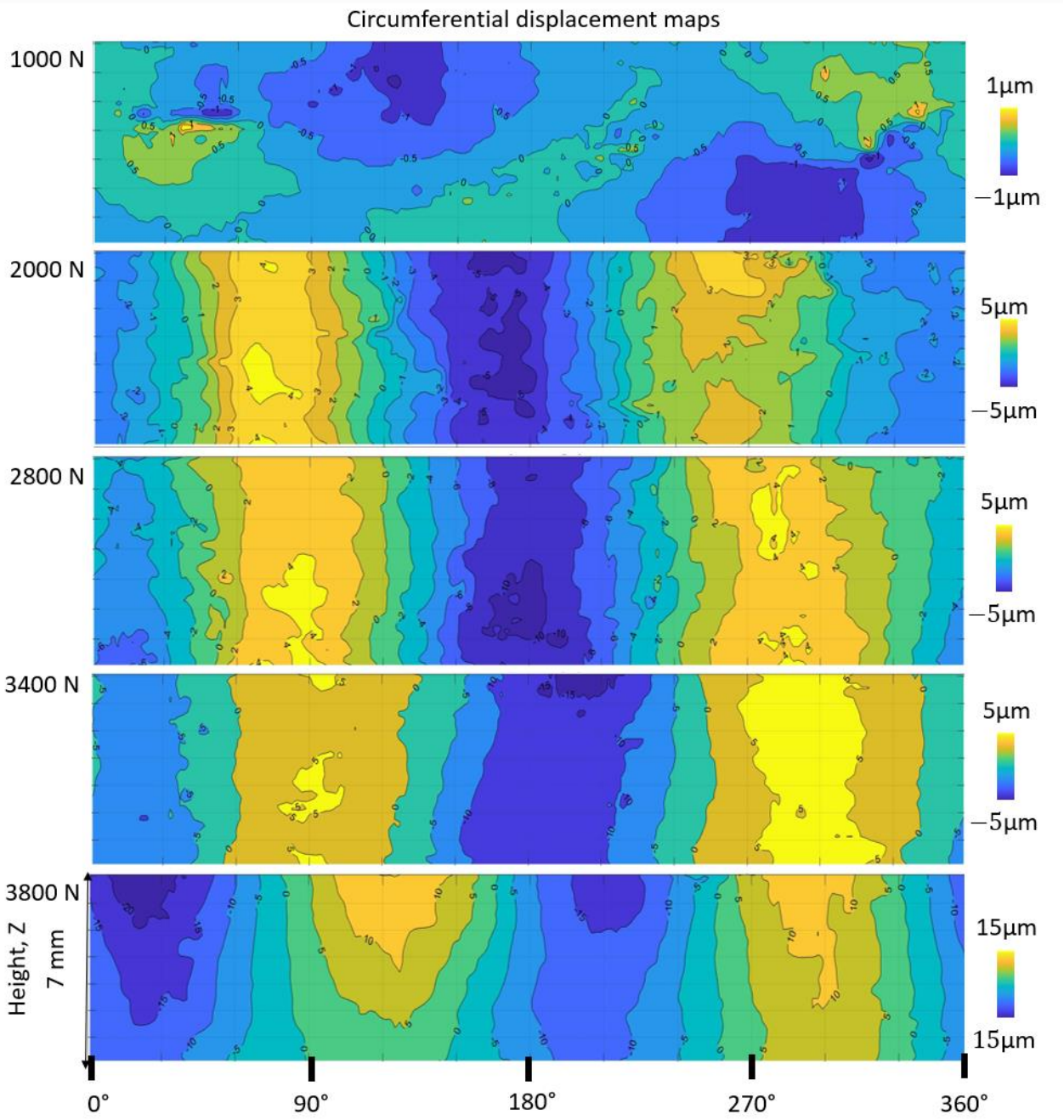


Figure 5.19: The unwrapped circumferential displacement maps at each loading stages

Hoop strain

With the measured value of the previous two terms, using the equation. 5.1, the hoop strain of the entire tube was calculated. In the equation, the radius r is taken as the average radius of the tube. Taking a typical example of the result at 3400 N, figure 5.20 illustrates the hoop strain map (figure 5.19(c)) of the tube though combining the radial displacement term (figure 5.20(a)) and the derivative of the circumferential displacement at θ (figure 5.20(b)) together. The two terms both have a noticeable contribution to the final hoop strain distribution of the cylindric tube. Furthermore, the highest hoop strained region at the same location was observed to be at 40° and approximately 240°.

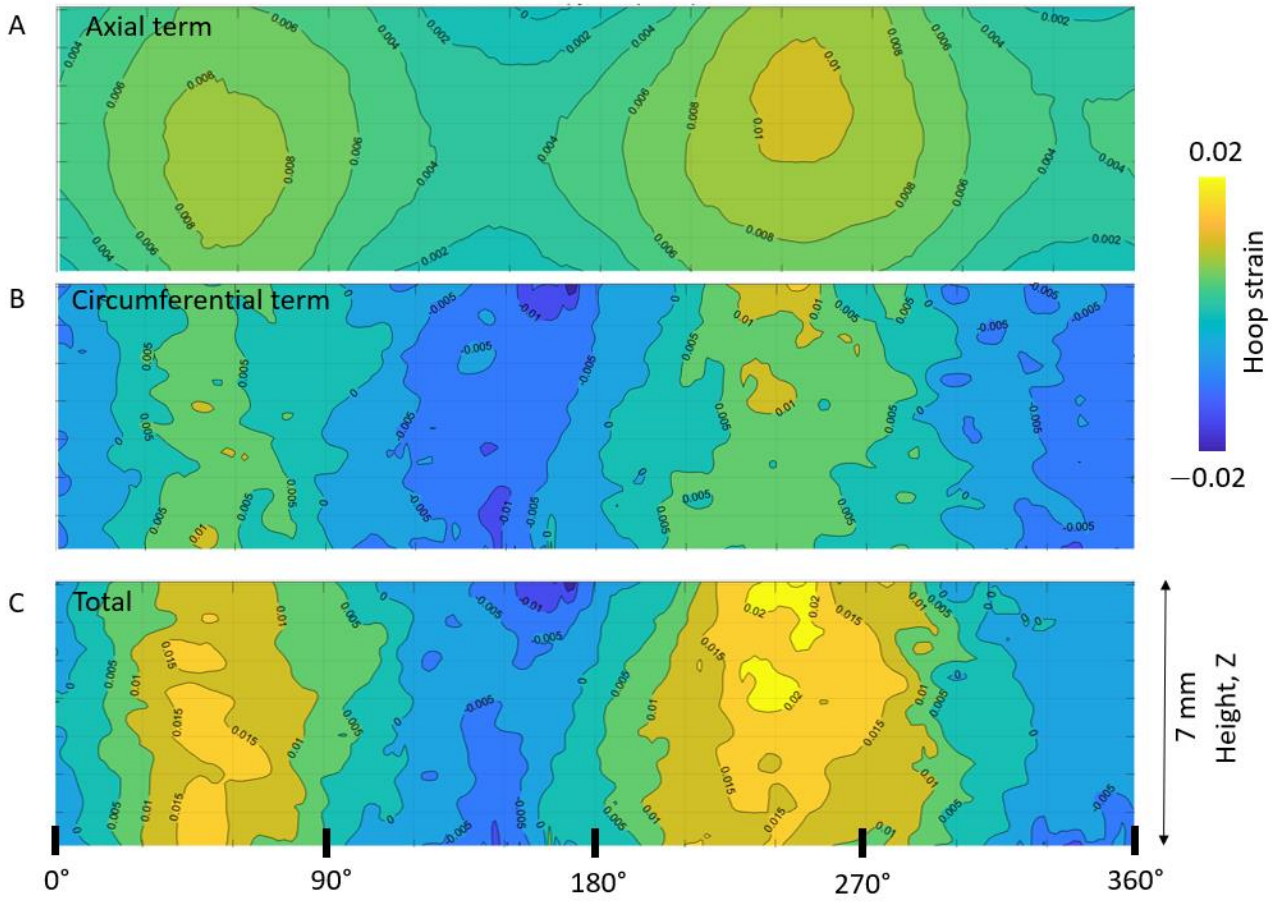


Figure 5.20: The (c) overall hoop strain maps from (a) the axial term and (b) the circumferential term at the stage of 3400 N.

5.3.5 Non-linear stress-strain behaviour

In the hoop pressurization test, the rubber insert under axial compression generates an internal pressure within the composite tube. The thickness and the radius of the composite tube are 1 mm and 5 mm respectively, while the maximum radial displacement was around 50 µm. The deformation of the cylinder is relatively small compared with its original geometry and the tube thickness is one fifth of its radius. Thus, by treating the composite tube as a thick-wall cylinder, the pressure can then be converted to the hoop stress. The Lamé Equation was used to calculate the hoop stress, as in the ASTM standard test C1819 - 15[174]. The adapted Lamé equation varies in different studies [5], [145], [168]. The equation used in this study is shown in equation 5.2, and is the same as that in the ASTM standard C1819-15 [174].

$$\sigma_r = \frac{r_i^2 P}{r_0^2 - r_i^2}\left(1 + \frac{r_0^2}{r^2}\right) \tag{5.2}$$

In equation 5.2, r is the radius of sample, where r_i is the interior radius, r_i is the outer radius and P is the internal pressure. All the parameters and variables were relatively easily to measure from the macroscale mechanical tests.

Using the average stress from the Lamé equation and the average hoop strain from the DVC, Figure 5.21 displays the macroscale stress-strain curve of the composite tube under internal pressure. The resulting proportional limit stress (PLS) and elastic modulus of the studied composites are approximately 135 MPa and 128 GPa respectively, using the offset method[174]. Other measurements and potential interesting parameters are summarised in Table 5.2

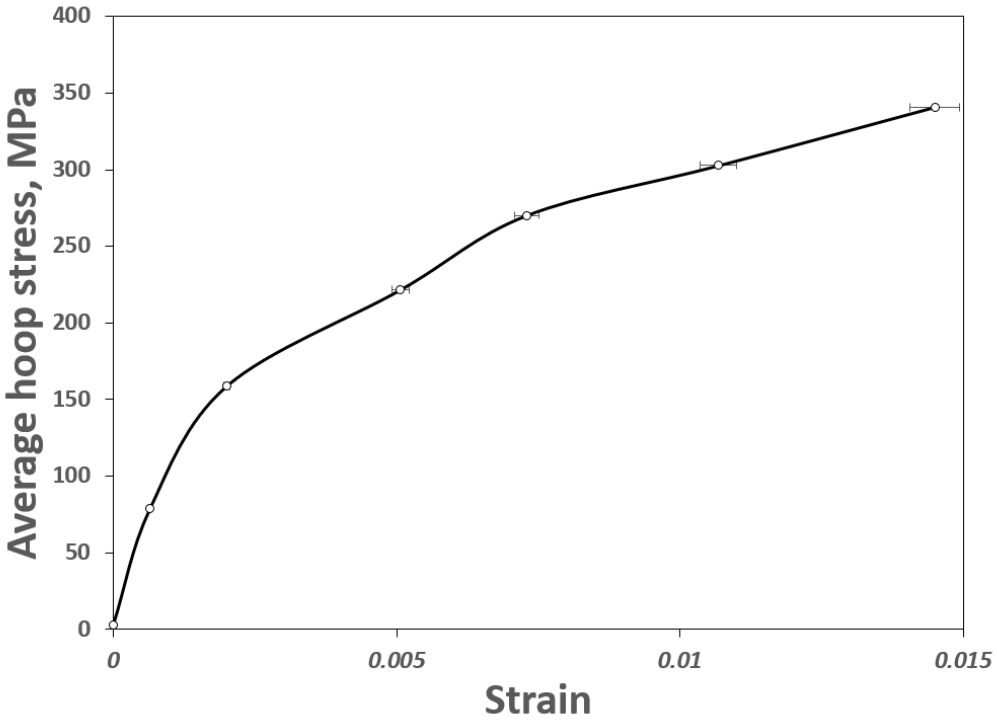


Figure 5.21: The average strain versus stress curve of the hoop pressurised composite tube, measured from the DVC.

Table 5.2 Measured material property of the tested SiC/SiC composite in this study

Modulus of elasticity, E (hoop)	Proportional limit stress, σ_o	Strain at proportional limit stress, ε_o	Stress at fracture, σ_f
128 ± 5 GPa	135 ± 10 MPa	0.0010 ± 0.0005	350 ± 10 MPa

5.4 Discussion

5.4.1 Anisotropic deformation behaviour

The rubber plug-in tests was first applied in the traditional cladding materials, such as Zr alloys [164], [167]. Compared with metal, a more complicated mechanical response should be expected in the ceramic composite [8], [44], [175]. However, the conventional macroscale method may only provide limited information. The *in situ* synchrotron micro-tomographs revealed the microstructure with the related heterogeneous deformation in the braided composites. The coupled DVC analysis further quantified the mechanical response at different scales, which is related the damage mechanism.

The conventional strain measurement methods were normally a 2D method. The method was either a physical attachment e.g. circumferential extensometers [5] and strain gauges [8], or a surface optical illumination [43], [60] . An attached gauge inevitably needs a further sample surface treatment as the ceramic composite normally exhibits a certain degree of surface roughness due to fibre crossover and porosity [174]. The non-destructive optical method avoids this problem but can only provide the strain at outer surface side [43]. It yields only the surface information, which may not be representative for the bulk behaviour[44]. An observation of the entire sample is essential in the composite tube because of its inherited high degree of anisotropy.

The macroscale deformation (figure 5.16) shows the overall non-uniform radial dilation soon after the matrix crack observed from the surface (at 2000 N) along the tube height and at different angular direction. Those data need to be interpreted with caution. A bulging barrel effect (figure 5.16(b)) was observed, which may be due to the lack of stress uniformity from the plug test along the axial direction. Similar bulging was also reported in the simulation and experimental results of

a homogenous metal [167], but are rarely discussed in the literature due to the lack of a suitable monitoring method (figure 5.22). However, bulging must be considered when discussing the loading state as this bulging barrel effect introduces a corresponding compressive stress at the inner surface and additional tension at outer surface. Therefore, the composite tube was subjected to a biaxial loading, even though the hoop strain is normally ten times larger than the axial strain in this study. A combination of dilation and ovalization was demonstrated in figure 5.16(c) as well with the occurrence of the matrix crack. This led to anisotropic expansion. The ellipses at different load stages due to ovalization share the same major axis aligned at the direction around (50 ± 6°). However, it is interesting to find that the overall ellipticity of the cylindrical tube is also increasing gradually with the higher loading, indicating a further amplified anisotropic deformation as the tube responses to an increase internal pressure.

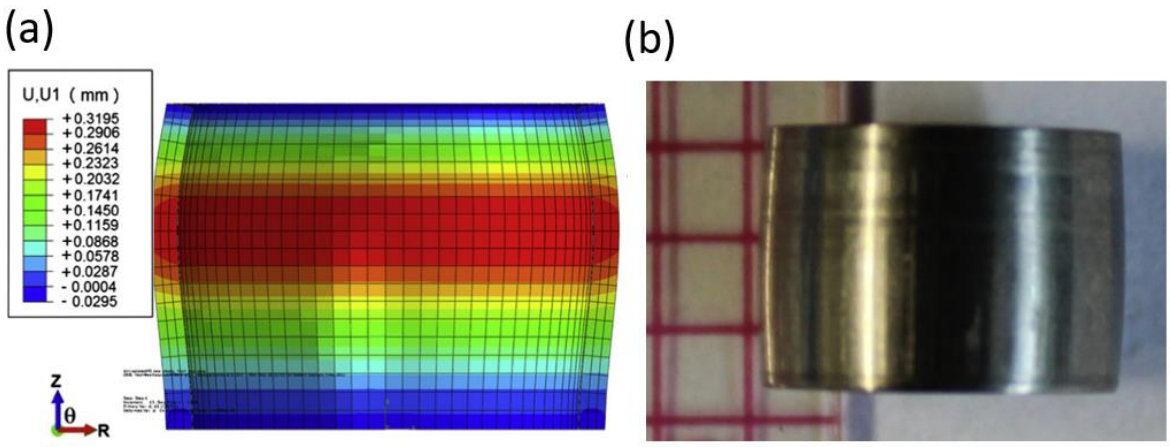


Figure 5.22: The radial dilation of the homogeneous Zr alloy cladding tube from internal pressure in reference [167], in (a) finite element simulation and (b) experiment.

The mesoscale deformation further reveals the mechanical response of the composite tube under internal pressure. This deformation includes a combination of uniform dilation and ovalization

that both contribute to the overall deformation (figure 5.16). In fact, it is interesting to find that the radial deformation and the hoop strain can be related to the architecture of fibre tows (figure 5.18). The radial displacement contour has its edge laying at approximately ± 45°, which is analogous to the structure of fibre tows braids. It may indicate how the woven fabric responds to the internal pressure. The highest mesoscale hoop strain still the most expanded region in the cylindric tube (figure 5.20), at which the circumference displacement (figure 5.19) due to ovalization plays an important role as well.

Most of the reported studies assumed a uniform expansion, such that only the radial deformation is accounted for the hoop strain calculation (equation. 5.1). For example, the *in situ* pressurization study[44] by Croom approximated the hoop strain only from the measured radial displacement while the circumferential displacement is assumed to be zero. Other studies [5], [93], [145] normally used the average value from surface strain measurements of a limited gauge area. However, the bulk deformation in this study shows a noticeable effect of the ovalization as the magnitude of circumferential displacement cannot be ignored, which means its associated term for macroscale strain calculation cannot be neglected or omitted for the approximation to have a precise result.

The ovalization deformation and the associated circumferential displacement was quantified in this full-field study. The observed non-uniform distribution of the circumferential displacement at different angular directions could also explain some reported results of other similar composites. For example, two orthogonal axial peaks of the strain distribution were presented in the pressurized tube with surface DIC technology (figure 5.23) of a woven SiC/SiC composite tube [93]. In addition, this non-uniform deformation might also be the reason of the large scattering in the radial displacement measurement from four surface-attached displacement transducers [5]. However,

without the full-field 3D technology to capture the entire sample, the quantified study of this anisotropic deformation is impossible.

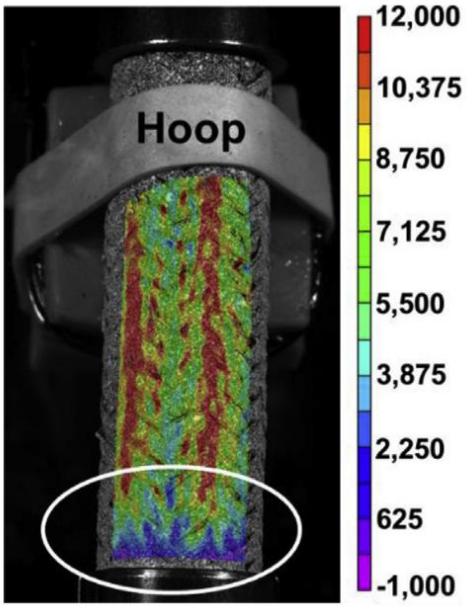


Figure 5.23: The DIC strain maps of a burst test in a of a woven SiC/SiC composite tube from reference [93] (units in μ)

The generalization of the ovalization behaviour in the pressurization test needs more *in situ* experiments of the composite tube for it to be confirmed. However, the non-uniform deformation can be discussed with the damage distribution. In this study, the spatial distribution of the surface matrix cracks (figure 5.10) was observed to be associated with the ovalization deformation. Further, the origin of this non-uniform deformation might due to the damage, such as the matrix cracks initiated before the 50% of the final loading (2000 N). This microscale damage of the matrix crack which makes the localized region prone to deformation. On the other hand, this ovalization played an important role in the localized strain distribution (figure 5.20(c)) itself. This local hoop tensile

strain might also lead to a strain-induced crack. The causality between the strain and damage requires further studies, but their relevant distribution was illustrated.

5.4.2 Damage evolution

The axial surface crack indicated a dominating hoop tensile stress. Those matrix cracks initiated from the outer and interior surface were quantified *in situ* for the first time. The crack density gradually increased with the applied load then reached to about 4 and 2.5 mm^{-1} for the outer and interior surface respectively (figure 5.9). The inside crack density is close to that in the previous C-ring test at room temperature (Chapter 4) and other reported studies[43], [57] where observed the saturation of the crack densities at the surface was about 2 mm^{-1} in a axial tension testing. However, the literature studies used the surface optical technology that only detected the outside cracks. The crack density at the outside surface in this study is close to that (4 mm^{-1}) observed in other *in situ* tomographic study of a single tow SiC/SiC composite[79]. Nevertheless, they were generally all in the same magnitude.

The situation of the inside cracks needs to be explained considering its more complex loading conditions. First, the inner surface is subjected to the contact force from the pressurized rubber directly while the outside surface is with no contact that is a plane stress condition. Further, the composite tubes have been ground smooth, so the local stress state should depend on roughness of the surface (i.e. surface breaking pores). Second, due to the bulging barrel effect, the inside surface is under compression at the axial direction compared with the axial tension at the outside surface.

It also needs to be mentioned that, in most hoop pressurization studies, the value of the hoop stress is an approximation, which is not directly measured. The hoop stress was normally calculated from the internal pressure via the Lamé Equation or its equivalent [5], [44], [145], [174]. Deviations could result from the damage or anisotropic behavior in the composite tubes. Therefore, it was

only used to approximates the average macroscale mechanical responses (figure 5.21). Using this method, the macroscale response of the average stress and strain in this study is shown in figure 5.24 with data from the literature obtained with surface measurement. Similar types of macroscale response and elastic properties (table 5.2) were observed. However, the elastic modulus measured in this study (~ 128 GPa) is smaller than that in the literature (~ 213 GPa) [57], [93] and the previous C-ring experiment (~ 335 GPa). This difference may be due to the fact that in this *in situ* experiment a very limited number of the scans was taken in the early linear region as the main target for this experiment was to observe the damage evolution in the hoop pressurization.

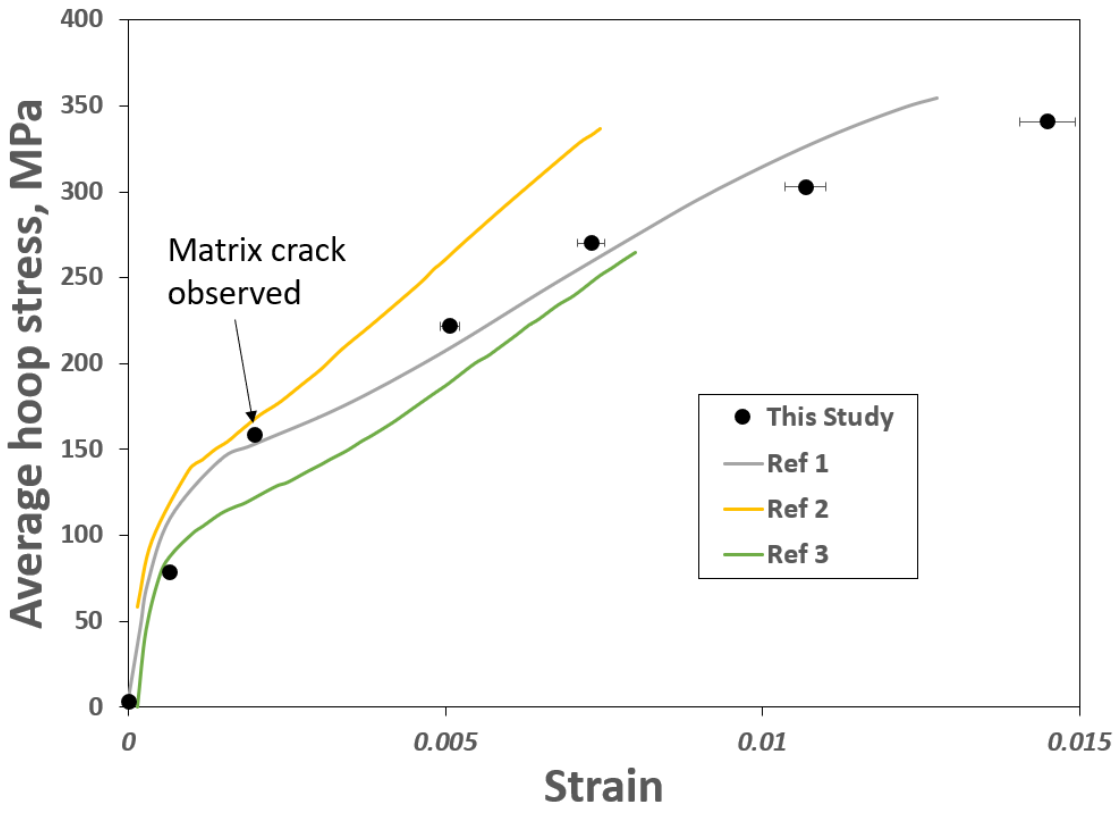


Figure 5.24: The measured strain versus stress curve of the composite tube under the increasing internal pressure. Compared with literature (Ref 1 [57], Ref 2 [93] in a plug-in test and Ref 3[93] in a burst test).

The damage evolution in the microscale was illustrated via the localized strain patterns (figure 5.11 and 5.14). Those localized strain due to a sudden change in the displacement field highlight the damage in the composite. Two different patterns were observed. At first, the deformation was regulated by the microstructure of the fibre tows. This may due to the 'textile effect' from the fire tow reorientation [43], or the strain concentration from the contacted local overlapping tows [163]. Other stochastic simulations of the composite also suggested that localized strain could be attributed to the distribution of local defects [176], [177], such as porosity in this case. It is hard to distinguish those two effects are either from the fibre textile or local defects as the distribution of the porosity is relevant to the fibre structure as shown in the previous Chapter 3. In contrast, the second strain pattern shows the redistributed localized strain axially spans along the tube, decorating the propagation of the axial matrix crack. Those damage also interacts with the microstructure along the tube radius, resulting a non-uniform through thickness distribution (figure 5.12).

The post-mortem tomographic image (figure 5.13) shows that the critical crack damage located at the direction around 350°. The final crack path is *not* at the direction with the highest macroscale hoop strain. The macroscale hoop strain was around 0.005 at this location compared with the highest value of 0.02 at approximately 40° and 240° figure 5.20. However, the microscale strain evolution of the final crack of figure 5.14 and other surface cracks (figure 5.11) showed that the local strain was generally higher the macroscale strain 0.02. It maybe because macroscale deformation results can only demonstrate how the composite tube response to the internal pressurization as an entire sample, but it cannot explain its microscale fracture behaviour and the origin of the damage. This is not surprising because the microstructure of the SiC/SiC involves a high degree of anisotropy from the fibric architecture, porosity, the number of layered structures,

etc. Furthermore, the early initiation of the cracks could alter the local stress distribution as well. All those are impractical to resolve at the macroscale level. Therefore, the fracture mechanism needs to be addressed at microscale.

Regarding the fracture mechanism, a combination of matrix cracking and fibre tow damage was observed. As for the matrix cracks, the final fracture path generally follows the path of one of the pre-existed axial matrix cracks (figure 5.14). However, there was no obvious different features observed in the crack that later became final fracture path compared with others (figure 5.11). It indicates the final fracture happened very rapidly. In the fractured sample, extensive fibre pull-out was observed (figure 5.13 and figure 5.25) next to the matrix cracking path. It shows fibre tows normally fractured at the crossovers. The fracture of the fibre tows is expected at the crossovers due to the different deformation of the fibre tows at their orientation. This is also supported by the *in situ* observation of localized strain situation at the fibre tow crossovers before the final fracture (figure 5.14).

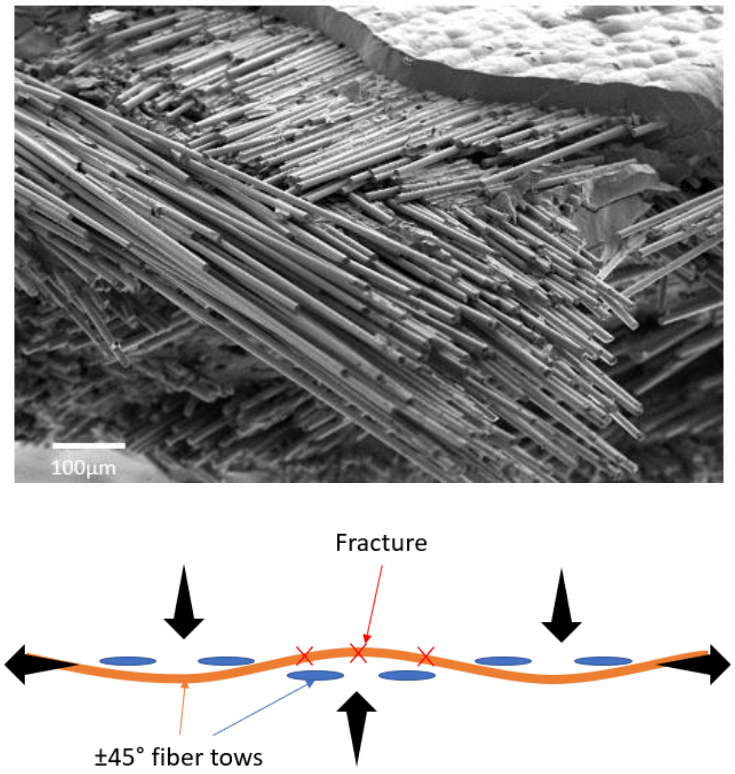


Figure 5.25: Scanning electron microscopic images of the fracture surface showing the extensive fibre pull-out with the schematic of fibre tow fracture mechanism.

5.5 Conclusions

This chapter present a study using the *in situ* synchrotron X-ray tomography to observe the damage evolution of the SiC-SiC composite tube under the internal pressure. A customized loading fixture was developed to generate the internal pressure using the plug-in insert. The damage was found initiated at both inside and outside surface from the tomographic images. The DVC of those *in situ* tomographic images allows the full-field measurement of the composite deformation. The anisotropic deformation of the composite tube at different directions was illustrated at macroscale. The local damage, such as the surface cracks, was associated with the occurrence of the non-uniform deformation of the composite tube. The final fracture of the composite tube is found to be reliant on the local crack evolution instead of the macroscale deformation, which demonstrates the importance of a multiscale observation method.

Chapter 6. 3D multiscale microstructure-based modelling of the fracture behaviour in nuclear graded SiC/SiC composite

6.1 Introduction

Numerical modelling is a widely used tool for industrial component design to assure in-service structure integrity. Numerical modelling can be used to predict the real engineering tests or to simulate the performance of a component in the operating conditions that can accelerate the materials selection in component design [178]. Experimental tests of components are not always practical due to the complex geometries and loading conditions or the limitations in the scale. Alternatively, the practice can be too expensive, especially in aerospace and nuclear industry, which makes the experimental reproduction impossible. In the meantime, computational modelling has the potential to evaluate the performance matrix of the components with an acceptable cost. To support this decision-making design, such a numerical model needs to have a high fidelity to provide a reliable virtual solution for a full-scale component in different operation environment with candidate materials [179].

The level of the fidelity and resolution in the virtual solution depends on the discretization in the numerical model. To serve the purpose of the component design, the computational method to evaluate the mechanical behaviours must have the level of the discretization that can address the critical microstructure and the damage evolution. In the application of the fracture simulation of an engineering structure, the discretization must be sufficiently fine to integrate the materials' features and the corresponding damage events in the critical micromechanical processes [177], [180]. For example, in the widely-used finite element (FE) method, the level of details in the simulated damage evolution is determined by the smallest discrete unit in the model, i.e. the size

of an individual element [181]. However, in the conventional FE method, a small discretization that describes the microscale features can substantially increase the computational cost, which makes the engineering scale model costly and time-consuming, if not impossible. The exact computational cost depends on the adapted algorithm and hardware. Generally, a reduced discretization size means a larger number of units which could lead to an rapid growth in the number of computational operations required.

Simplification to reduce the computational cost can be made by applying a coarse discretization with a homogenized microstructure or a generalized continuous material without a complex microstructure. This results in a relatively coarse discretization compared with the scale of the microstructure. In the cohesive models, a coarse mesh size could lead to inaccurate prediction of the energy released during the fracture process, as a accurately prediction in the cohesive zone model requires the mesh size to be less than the length of the cohesive zone [182]. Carpinteri and Colombo also pointed that when the finite element mesh is coarse, the cohesive force vectors in the model are too far from each other and therefore the fracture process cannot be simulated regularly [183]. Moreover, with a coarse discretization, the small-scale inherited material flaws are normally neglected or approximated in the large scales. Meanwhile, the mechanical behaviour of the composite is expected to involve a complex fracture mechanism that was observed to be related to the local strain concentration and microscale critical events [154],

Multiscale modelling offers a potential coupling strategy to simulate the large components based on fine-scale microstructure details efficiently [184], [185]. While several multiscale methods were proposed for intact material simulation where a small degree of deformation was assumed in a continuum [186], fewer methods are available for fracture simulation [184], [187]. One example of a multiscale model to simulate the behaviour of materials with a heterogenous microstructure

is through a representative volume element (RVE) [188], [189]. The RVE is the representative subscale sample of a larger scale material that includes the micro-heterogeneities [190]. The size of the RVE must exceed a critical value so that the simulation outcomes are insensitive to the dimension of the RVE and spatial distribution of the heterogeneous microstructure that the RVE includes. It can therefore simulate the mechanical behaviours that arise from complicated microstructures. However, to extend the RVE method to large engineering scales in the FEM, its simulation accuracy is still determined by the mesh size [191], [192].

For fracture simulation, the damage can be simulated using a cohesive law that may be obtained by the RVE or an explicit representation of the microstructure [193], [194]. The cohesive elements method can describe cracking via splitting of the meshes, where the generated faces are the crack surfaces [195]. Accordingly, the fidelity of the fracture process is sensitive to the mesh size [182]. To reduce the computational cost that is related to fine meshes, some multiscale models adopt local enrichments of the elements or nodes for mesh refinement during the fracture process to give a better prediction of the fracture behaviour. However, such an extended finite element method (XFEM) normally requires a pre-definition of the approximate crack path [196].

Other methods adapt the microstructure explicitly during the fracture process, such that a series of sub-models were developed in a multiscale model to address the importance at each scale. For example, Chakraborty and Rahman presented models where the microstructure constituents were described stochastically and the energy release within the microstructure was recalculated during the fracture process [197]. Thereby, the macroscale and microscale behaviours were coped with in different sub-models. The sub-models at different length scales could progressively interact with each other through the micromechanics-based homogenization. Normally, the computational cost of such multiscale models was very high due to the complex model architecture. The cost can be

substantially reduced via local enrichment of the microstructure near the crack propagation zone, such as the CAFE (cellular automata finite element) model where a FE model represents macroscale properties and a Cellular Automata (CA) describes the material microstructure properties [187], [198], [199].

Shterenlikht and Howard were the first to successfully use the CAFE method, by simulating the cleavage planes in the brittle fracture of a steel in a Charpy test [187], where the microstructure of the different grains was formed by different arrays of cells in the CA model. Following this method, in order to simulate materials with a more complex microstructure, a variation in representing the microstructure properties was achieved via another layer with a Meshfree sub-model, which bridged the relation between FE and CA models [200]. Subsequently, though the adaption of the microstructure-based Meshfree model (MAM), the Finite Element Microstructure Meshfree (FEMME) model was proposed by Saucedo-Mora [200], [201]. That is the model which has been used in this chapter.

The multiscale FEMME model can use a relatively coarse mesh size in the FE layer to describe the macroscale geometry. The microstructure information is described via the CA layer, which is connected to the FE layer using meshfree methods. The microstructure information in the model is only locally activated into the FE mesh when it is needed in order to achieve computational efficiency. The fracture path is therefore not pre-defined and can develop at the microscale in the CA layer.

In this chapter, the FEMME model will be used to simulate the damage development in the C-ring composite and tubular composite in the same scenarios as the previous experimental work. The novel *in situ* 3D characteristic techniques in the previous chapters provide the statistical results (size, shape etc.) needed for the microstructure inputs of the continuous fibre and heterogeneously

distributed porosity. The 3D quantitative analysis also demonstrated the fracture mechanisms and the damage accumulation in the SiC/SiC cladding tube in different loading conditions, which have been simulated using the FEMME model. The aim is to demonstrate the important aspects of the microstructure in a macroscale model and subsequently test the capability of the FEMME model. Firstly, the structure of the FEMME model and interaction between the different layers will be explained. The bulk response of the composite component and the development of the damage in the structure will then be compared with the 3D *in situ* experimental results.

6.2 Structure of the FEMME model [6]

The FEMME model consists of three layers: i) FE layer; ii) microstructure adapted meshfree (MAM) layer; and iii) CA layer. Each layer uses a distinctive simulation method to cope with the features at a different length scale, meanwhile they are interactively linked by energy homogenization [186], [202]. The microstructure is only locally enriched when it is necessary to achieve the computational efficiency. In this section, the structure of the FEMME model will be explained.

An example of the three layers in the FEMME model of a heterogenous material in a cylindric component that is compressed axially is shown in Figure 6.1. The macroscale geometry of the component is described the FE model. The grey constituent is a second phase in the heterogenous material that is different from the matrix. The second phase could be pores, impurities or strengthening particles. This heterogenous distribution of the second phase can be reproduced in the MAM layers as the particle domains. In a finer scale, the black shows the eroded cells in the

[6] The algorithm of the FEMME model was developed by L. Saucedo-Mora. I have further developed this model to simulate the *in situ* experiments presented in this study.

CA layer, which can describe the damage that has occurred locally, for instance due to the stress concentrations around the second phase.

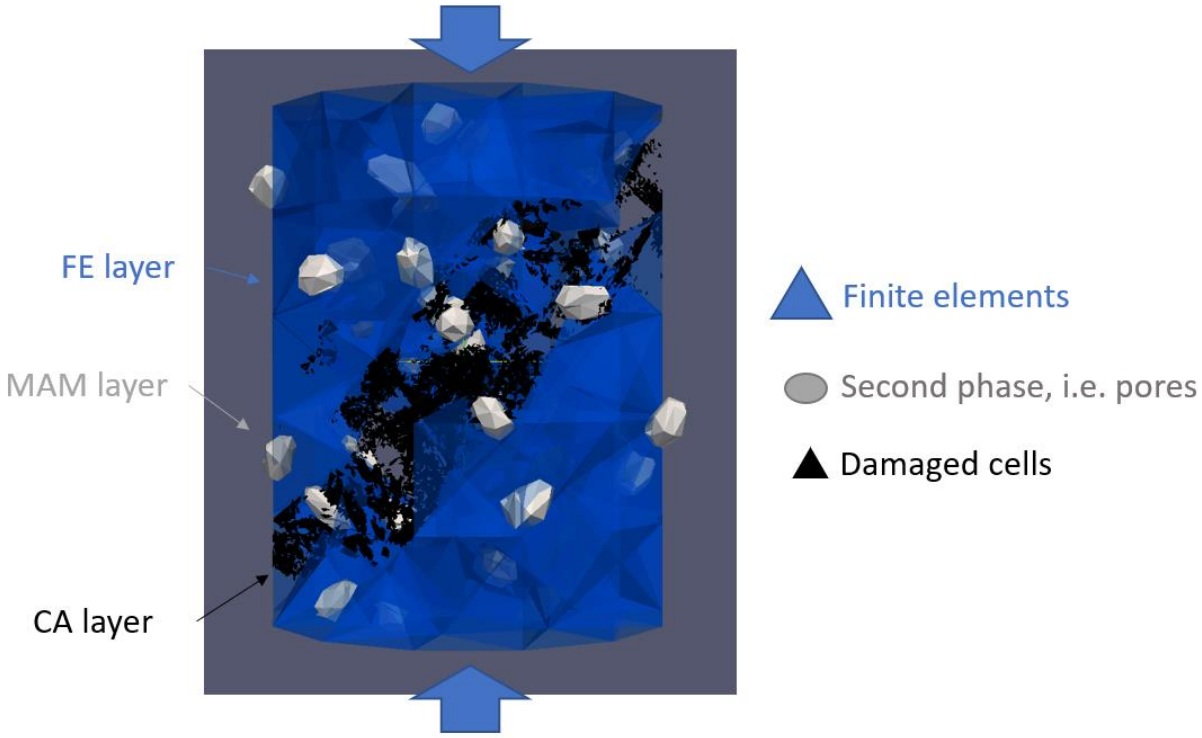


Figure 6.1: An example of a cylindric component FEMME model with three superimposed sub-layers

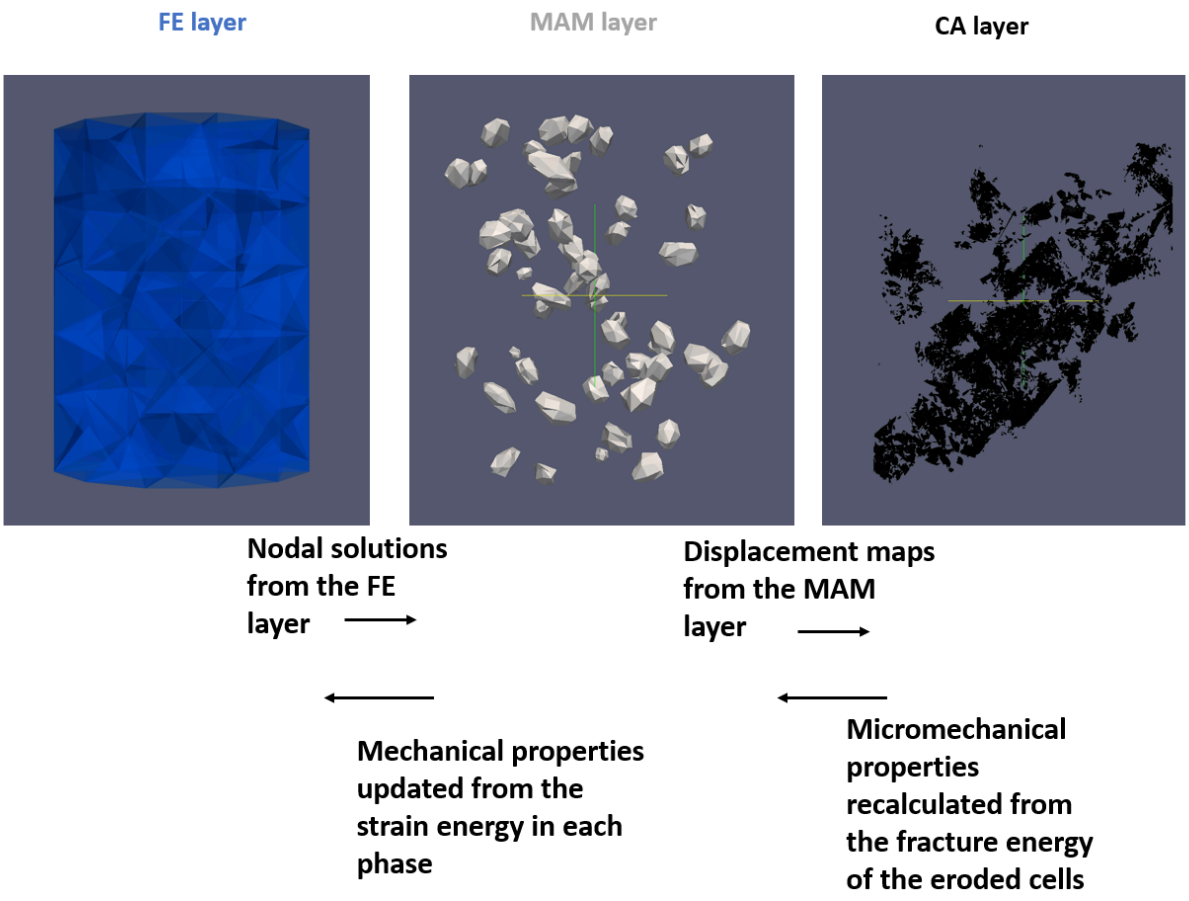


Figure 6.2: The architecture of the FEMME model and the interaction between the three layers

The FE model captures the macroscale geometry of the composite component. As illustrated in figure 6.2, an irregular tetrahedral mesh (in blue) was used, with a relatively coarse size. The FE model, to which the boundary conditions are applied, also represents the overall bulk mechanical response from the microstructure, as the properties of each finite element is affected by the development of damage within it. Namely, the macroscale mechanical properties depend on the damage that is described in the subsequent microstructure layer. To simulate the damage, a criterion is chosen such that if the strain of any element in the FE model reaches an arbitrarily defined critical strain this element is activated for local enrichment of the microstructure in the other two layers. The development of damage can then be simulated in the enriched region.

The first of two microstructure layers is the microstructure adaptive meshless (MAM) layer, where the heterogeneity, such as pores, particles or other phases, is mathematically defined by their approximate geometry (grey in figure 6.2). Once the microstructure is activated, the boundary conditions, such as displacement applied on each microstructure feature in the MAM layer, are calculated from the nodal solution in the FE layer.

The second microstructure layer, CA layer, consists of cells that can represent the different phases in the microstructure, regarding their spatial distribution in the MAM layer [200]. The location of each CA cell in MAM layer determines its assigned mechanical properties. During the simulation, the nodal solution in the MAM layer is shared with that in the CA layer and the strain at each cell is subsequently calculated. If the calculated strain of any cell reaches the assigned critical strain of such phase, the cell is eroded, resulting in a distribution of the damages in the model (black in figure 6.2). Accordingly, the erosion of the cells causes a release of the fracture energy. At each iterative step, the fracture energy of the eroded cells is summed through the energy homogenization to recalculate the mechanical properties of the MAM layer, which also affects the elastic properties of the host element in the FE layer [201]. In the FEMME model, the energy homogenization applies the Hill-Mandel method [202] to link the effects of the eroded cells in the microscale with the FE behaviour at macroscale. The fracture energy of eroded cells changes their material properties of the host domains in the MAM layer, which then changes the stiffness of the FE elements. The reduction in the FE element stiffness is proportional to the variation in the sum of the strain energy in the included domains in the MAM layer. Through this method, the macroscale mechanical response is simulated in the FEMME model, and it is sensitive to the damage evolution in the microstructural.

The damage behaviour is determined by the operations in the CA layer. The eroded cell can represent the damage in matrix, pores or other particles, depending on its assigned properties from the MAM layer. The resolution of the damage description is therefore affected by the size of the cells. The cells were subdivided from the FE tetrahedron elements. At each step of subdivision, the tetrahedron of the FE element was divided into four similar sized tetrahedrons cells. The size and number of the cells are dependent on the numbers of such repeated steps in the subdivision. With a sufficient subdivision (typically with 6 repetitions), the cellular description can be insensitive to the previous FE mesh [201]. Here, the size of the cells is fundamentally the resolution of the FEMME model.

Currently the FEMME model runs the FE layer in Abaqus, and the matrix operations for the MAM and CA layers are done using the NumPy package of Python 3.3. Overall, the kernel operation is carried out in the Abaqus with the subroutines script in Python for MAM and CA layers. The total computational time is predominantly determined by the sum of the time required for different layers. The connection between the different layers and operations of the FEMME model as in figure 6.2 can be summarized as follows:

1) Define the macroscale geometry in the FE model;
2) Describe the microstructure distribution in the MAM model with the materials properties for the CA model;
3) Evaluate the maximum principle stress in each FE element with initial properties and boundary conditions;
4) Once the maximum stress in any element in the FE model has reached the criterion value, the microstructure description is activated via the subdivision of the FE element;

5) The boundary conditions, as the nodal solutions from the FE model, are applied in the MAM model. The displacement solutions in the MAM are also mapped in the CA layer to calculate the strains in the cells;
6) If the calculated strain exceeds the defined failure strain of the cell's material in step 2, the cells were eroded; The displacement maps of the eroded cells are then updated; This iterative step in the CA layer is repeated until no cells reached the assigned value of the failure strain;
7) The mechanical properties of the MAM model and FE element that hosts the eroded cells are recalculated and updated for the step 3;

6.3 Image-informed reproduction of the SiC-SiC composite microstructure in the FEMME model

The FE model reproduced the approximate macroscale geometry of the composite tube based on the previous measurement of tomographic images. The inner diameter and the outer diameter of the tube are approximated to be 8 mm and 10 mm, respectively. 324 tetrahedral elements are generated for the C-ring sample with the width of 4 mm and 750 tetrahedral elements for the tube with a longitudinal length of 10 mm (Figure 6.3). The irregular tetrahedral elements were chosen as they can better represent the geometry of the woven fibres with fewer numbers of elements. Compared with hexahedral elements, the number of nodes in the tetrahedral elements required for the sufficient description of the fibre tows can be halved [203]. In the FEMME model this effect will be magnified as each FE element will be further subdivided in the CA layer for the microstructure description.

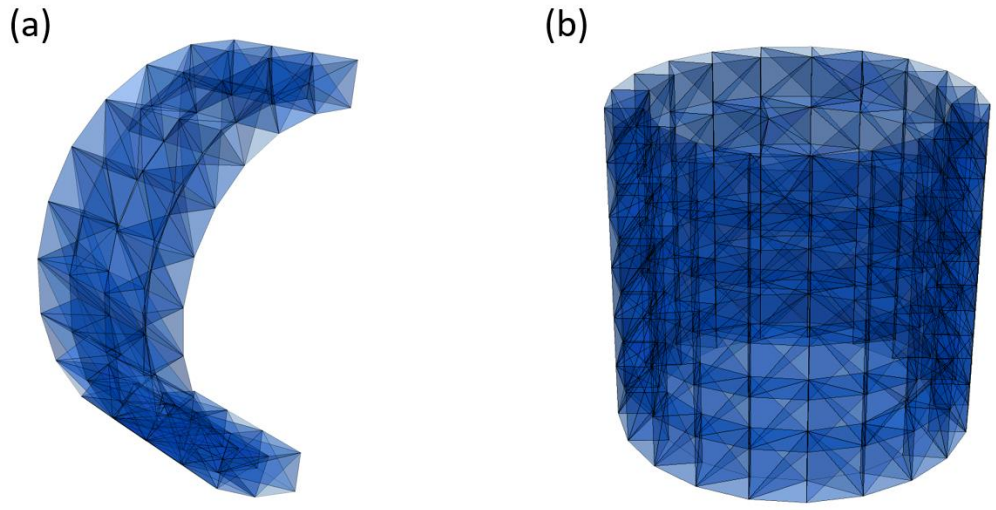


Figure 6.3: The FE model with (a) the 324 tetrahedral meshes for C-ring geometry and (b) 750 meshes for tubular geometry. The wall thickness is 1 mm.

The information between the FE layer and the CA layer is connected through the MAM framework. In the MAM layer, the microstructure of multi-phases needs to be defined (i.e. pores) [198]. It need to be mentioned that the methodology to describe and address the microstructure, such as pores and the fibres, for the FEMME model were developed by Saucedo-Mora [119], [204]. In this study, I edited the description of the microstructure based on the tomographic observation of the composite (Chapter 3) and applied this model to compare the *in situ* experiements. As for pores, the measured total porosity of composite tube from the tomographic image was about 5.5 vol.% (details in Chapter 3). The porosity consists of interconnected large pores and widely distributed small pores. Ideally the microstructure should be reproduced directly from the images. However, the complex structure of the pores makes the mathematical definition of real distribution impossible. Therefore, an approximation is required to describe the composite microstructure in

the simulation model. This approximation is based on the analysis of the previous tomographic images of the pores in the composite tube.

In the FEMME model, each pore is treated as a particle phase in the material. Its shape is fundamentally simplified as a 3D ellipsoid [200] with the assigned location, orientation and dimension (figure 6.4 (a)). In order to reproduce the pores structure with different ellipsoids, the shape and distribution of the pores from the tomographic characterization (from Chapter 3) are simplified into three categories in the MAM layer. The first two approximate the interconnected large pores (figure 6.4 (b)): they are broken into (1) the disc-shape pores that were between the fibre tow crossovers (3 vol.%) and (2) the needle-shape pores that were oriented along the fibre tows (2 vol.%). The third category describes (3) the randomly distributed small pores (0.5 vol.%). The different shapes and locations of the pores are mathematically defined based on their real statistical distribution. In the SiC/SiC composite tube, the interconnected pores were found between the three fibre plies. Accordingly, the location R, which is the centre point of the simplified ellipsoid, of the disc-shape pores and needle-shape pores is assigned at the boundary of the three fibre plies (at 4.33 and 4.66 mm). In the meanwhile, the small pores, which were generally widely distributed among the composite, were approximated by a uniform distribution among the sample radius (4.20 to 4.80 mm). In the model script, apart from the restriction of the radius position in the large and small pores, the angular and longitudinal positions of pores were randomly distributed among the sample area (function *numpy.random* in python to generate a uniform random distribution). Each pore was simplified to an ellipsoid in the model, to approximate the total network of the porosity. The axes (a, b, c) of the ellipsoid in different categories were chosen based on the real tomographic observation of the pores (figure 6.4 (b)). As the geometry of the porosity between the fibre boundless was found to be regulated by the fibre architecture, the

orientation of the such simulated needle-shape pores (a axis) is defined to be orientated ± 45° to the tube axis.

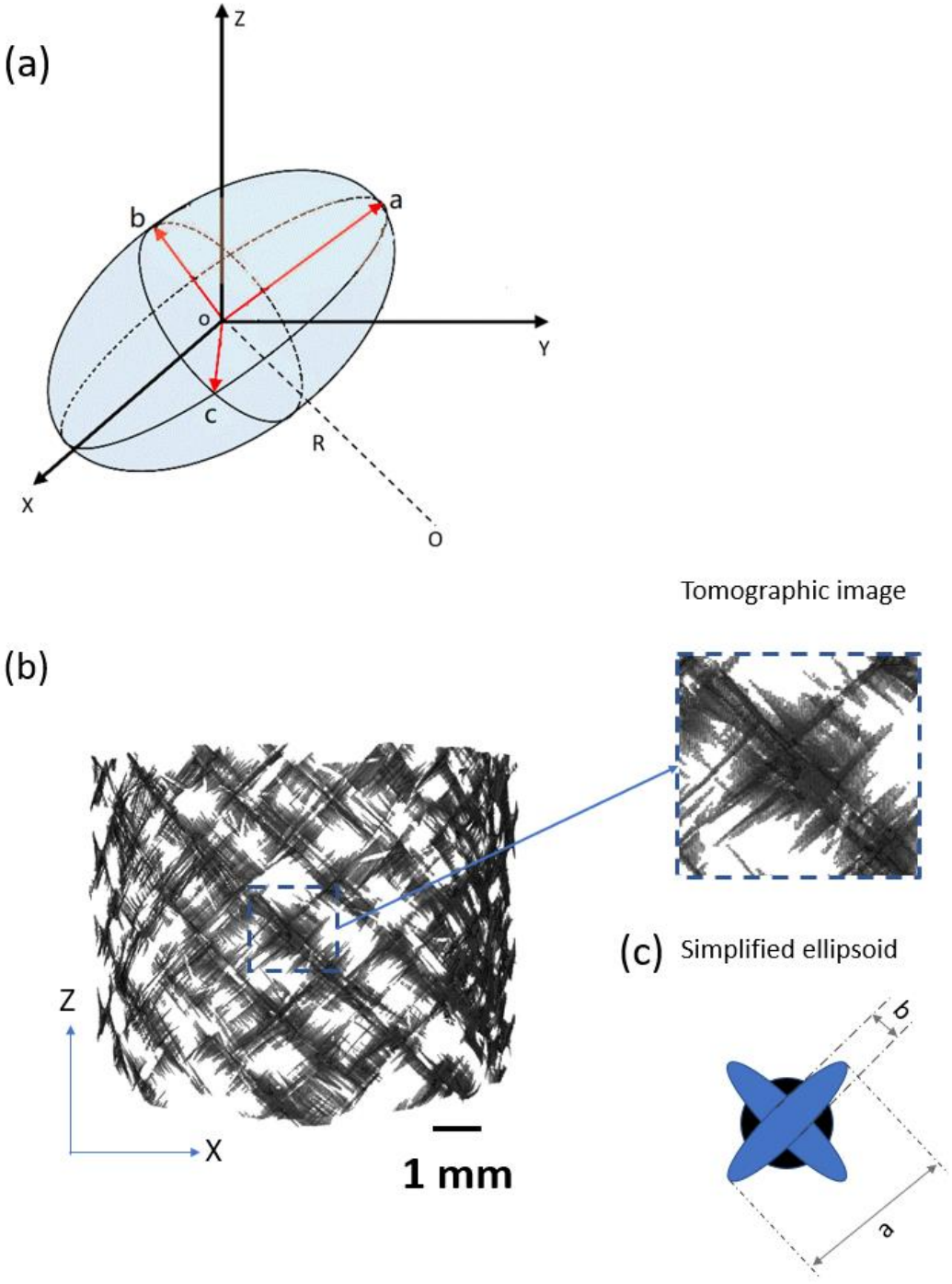
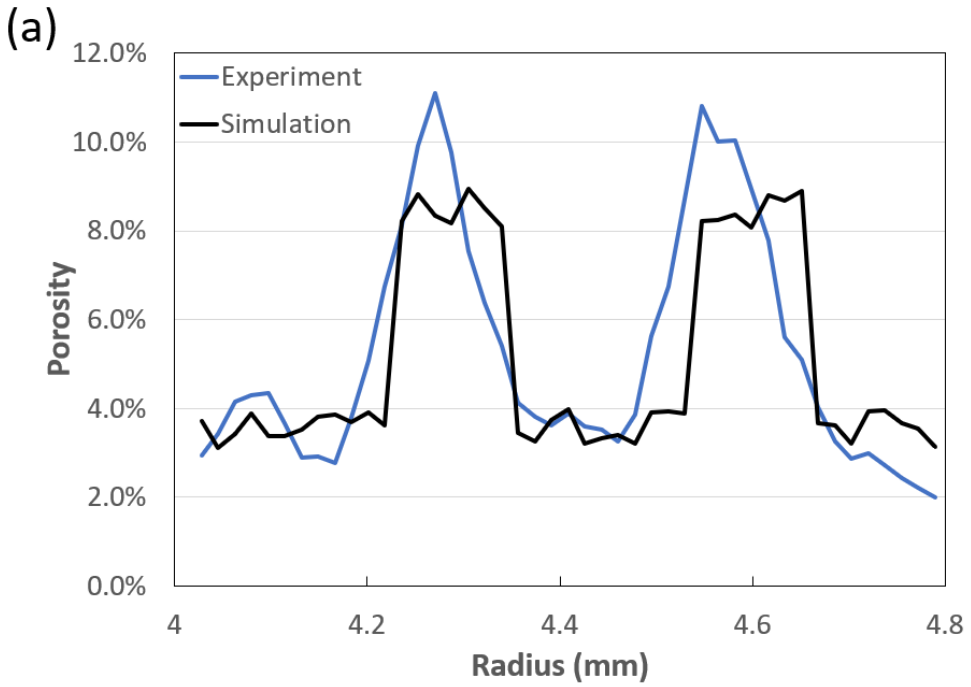


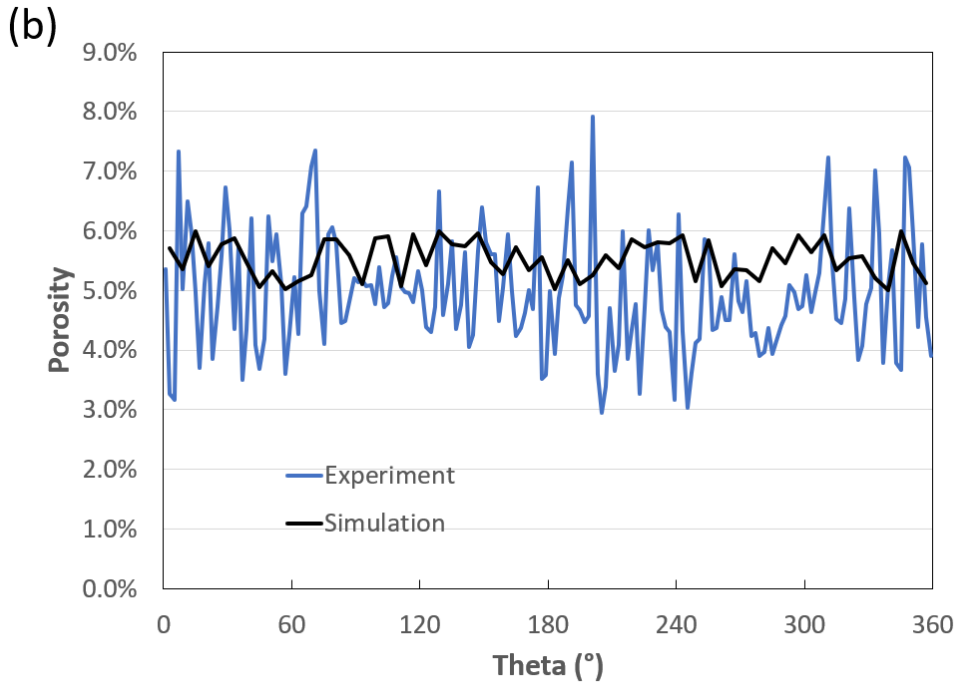
Figure 6.4: (a) The approximate description of a pore structure as an ellipsoid in the simulation model at MAM layer. (b) The tomographic image of the internal connected large pores (as in figure 3.9 from Chapter 3) and (c) the simplified ellipsoids for each pore in simulation (disk-shape in black and need shape in blue)

The designated parameters used in the model to generate the pores structure are listed in table 6.1. For such simulated results, the actual distribution of the pores along the radius direction is shown in the figure 6.5(a) and compared with the experimental data. The distributions of the simulated pores at other angular and longitude directions were relatively evenly distributed figure 6.5 (b) and (c) respectively. The general porosity distribution of the composite was approximated in the simulation model. Subsequently, the 3D visualization of the simulated pores generated is illustrated in figure 6.6 and compared with the tomographic image of the internal pores.

Table 6.1 The numerical input of geometric parameters in the model to describe the different pores observed from the tomographic experiment

Experiments	Large pores between the fibre tows		Small pores within each fibre tow
Numerical model	(1) disc-shape	(2) needle shape	(3) small pores
a (mm)	1.00 ± 0.10	3.00 ± 2.50	0.20 ± 0.05
b (mm)	1.00 ± 0.10	0.20 ± 0.05	0.20 ± 0.05
c (mm)	0.10 ± 0.05	0.20 ± 0.05	0.20 ± 0.05
R (mm)	4.33 and 4.66	4.33 and 4.66	4.20 to 4.80





(continue in the next page)

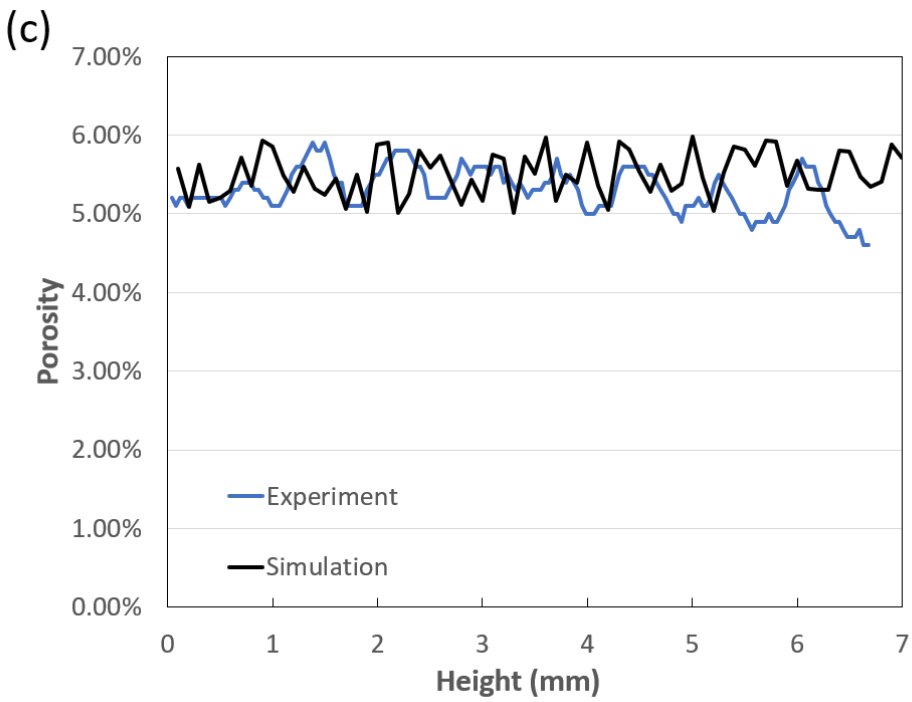


Figure 6.5: the spatial distribution of the porosity in the simulation at (a) radius, (b) angular and (c) longitudinal directions and with data from the experiment of the composite tube

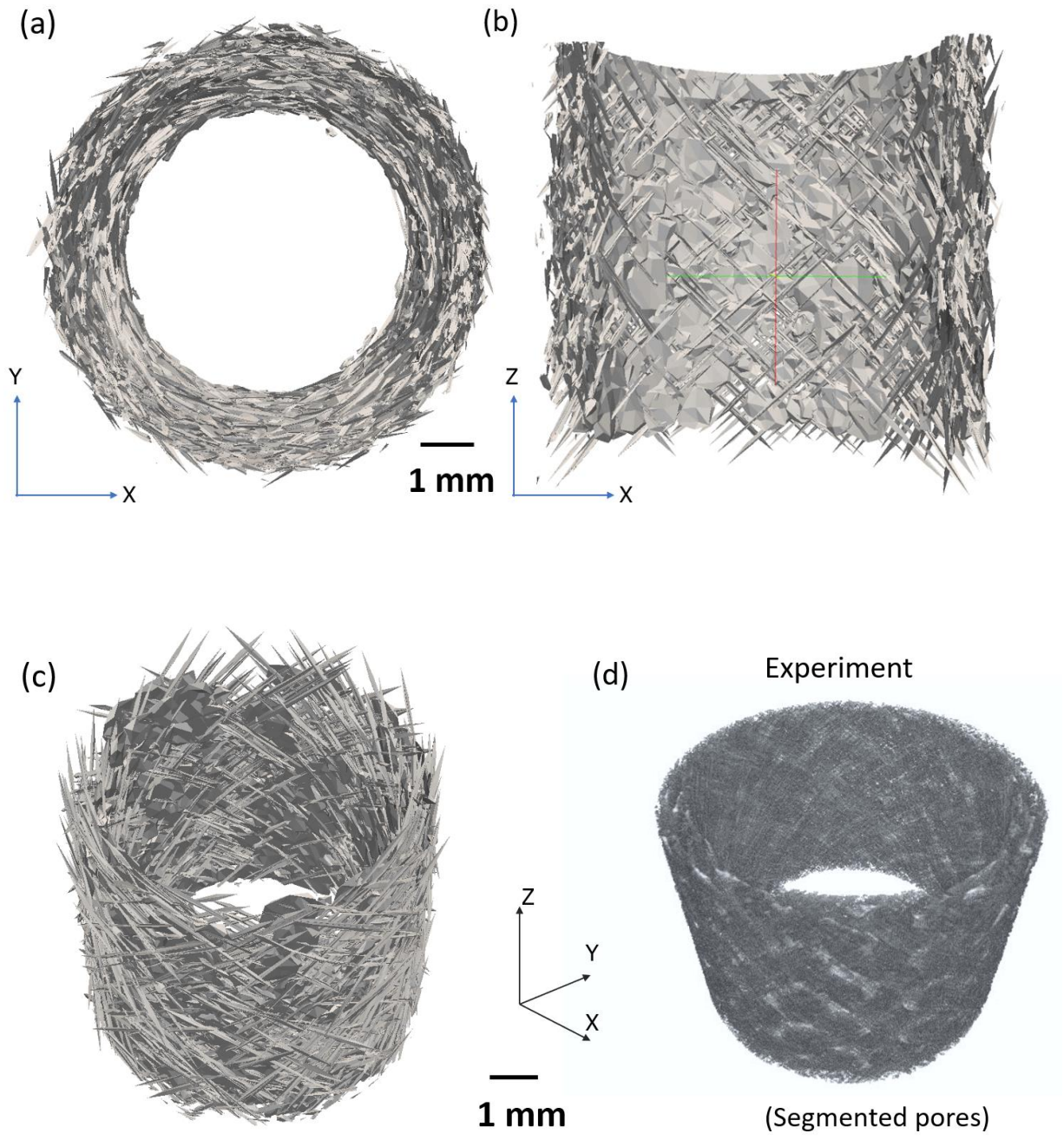


Figure 6.6: The numerical model of the pores generated in the model from different view (a), (b) and (C) comparison with (d) the tomographic image from the experiment characterization.

Each pore in the simulation model represents a particle domain (PD) in the MAM layer. The corresponding interparticle domain (IPD) has a truncated tetrahedron shape. Each triangular plane of the irregular tetrahedron is defined via the Delaunay triangularization function in the Paraview software 4.11[205], [206]. For each tetrahedron, the four vertices are the central points of four particle domains. Though this method, the microstructure with different types of porosities is reproduced in the MAM layer with all the nodal information. Even though, at this stage, the MAM layer is defined at the beginning of the model, the PD and IPD only become active when the host FE element at the same location reaches a critical stress value. In this study, the critical value was conservatively set to be 50% of the tensile stress of the material, which was judged to be below the level that the damage might start to occur.

Once the local microstructure is activated by exceeding this stress, the relevant tetrahedron FE element is subdivided into 4096 (4^6) smaller tetrahedra. The subdivided tetrahedra are the element cells in the CA layer. The cells in the CA layer are then identified to be within the PD or IPD in the MAM layer, so that their microstructure properties of the corresponding phases were assigned. The cells within the PD are the pores and the cells within the IPD are the matrix.

The fibres are explicitly inserted in the FEMME model through a mathematical description, which influences both the FE and MAM layers. The same algorithm was used to calculate the effect of the explicitly inserted fibre tows with the intersected elements as in the reference [204]. Figure 6.7(a) shows the relationship between the FE model and the one fibre tow. The shape of the fibre is simplified into a segmented straight line by the crossing points between the boundary of the FE elements and the fibre tow. It is assumed that the same strain fields within the FE element are shared with the intersecting fibre tow. The fibre tow may have anisotropic stiffness, so the reaction forces imposed from the fibre tows are introduced as additional stiffness into the element nodal

solution of the FE elements. The affected region from the fibre tows in the MAM layer is determined when the microstructure is activated. Since the PD and IPD subdivisions have been determined, their spatial relation with the fibre tows can be calculated. The affected region of the IPD domains are determined as there are fibres overlapped as shown in the figure 6.7(b). Therefore, the region of the MAM that is affected by the fibre is defined and the crossing points between the fibres and IPD boundaries are calculated. Accordingly, the micromechanical model is evaluated with the influence of the fibre tows. The nodal solution of the region that is affected by the stiffness of the fibres is calculated via this 'strengthening effect'. The general anisotropic mechanical behaviour of the model would therefore depend on the mathematical description of the fibres.

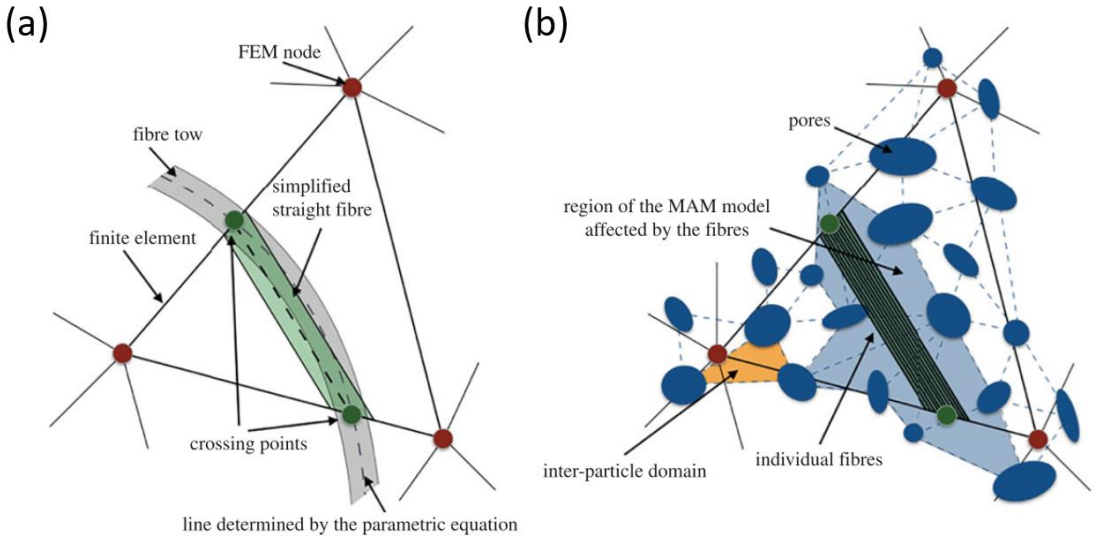


Figure 6.7: The special relationship between the (a) FE, the fibre tows and the microstructure in the (b) MAM layer [204]

Fibre tows that have a regular pattern can be reproduced using a mathematical representation [204]. The SiC/SiC composite used in this study has layers of braided fibres. The 2 X 2 (± 45°) braiding structure of fibre tows consists of repeating units. This braided structure in the tubular shape can

be duplicated though a combination of different sinusoidal curves. The mathematical equations (6.1-6.4) are used to describe the fibre tow braids with the starting point at u in Cartesian coordinates:

$$x = \pm R_{loc} \sin(A \cdot u) \quad (6.1);$$

$$y = \left(\frac{|\cos(A \cdot u)|}{\cos(A \cdot u)}\right)\sqrt{R_{loc}^2[1 - sin^2(A \cdot u)]} \quad (6.2);$$

$$z = u \pm c \quad (6.3);$$

where $$R_{loc} = R_{tube} \pm \Delta R \cos(\frac{A \cdot z}{d}) \quad (6.4).$$

In those equations, the parameter c defines the parallel fibres tows with different starting points; R_{tube} is the average radius of the braids layer; ΔR is the radius of each fibre; A and d describe the amplitudes of the representing sinusoidal for each fibre tow. The value of A ($2\pi/28$) is related to the larger sinusoidal variation that is relevant to the periodicity of the fibre architecture along the longitudinal direction. The d is related to the small sinusoidal that is related to the size of a woven unit. An example of the plot to describe one single fibre tow in this study is illustrated in figure 6.8, where the average radius R_{tube} = 4.84 mm, ΔR = 0.15 mm and A = $2\pi/28$ and d = 0.1.

Meanwhile, the plus and minus signs in the equations 6.1-6.4 are used to describe the two sets of fibre tows at ± 45° directions. Each set of fibre tows at plus or minus direction consist of a total number of 18 tows as counted through the tomographic image. The spacing of the 18 tows are evenly distributed among the angular direction. Figure 6.9 (a) shows the structure of those 18 tows in a braded layer that is reproduced in the simulation model. It is also compared with the experiment characterization of the fibre braids as shown in figure 6.9(b).

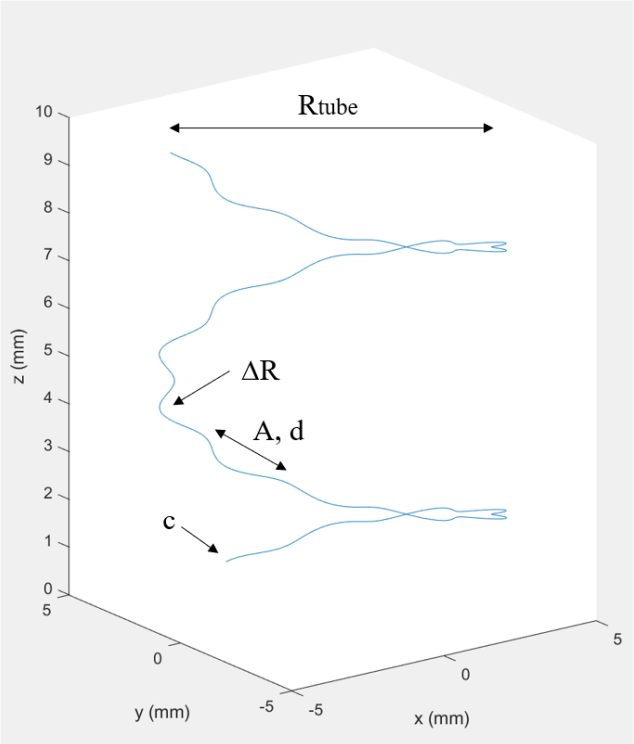


Figure: 6.8: The diagram of mathematical description of one fibre tow.

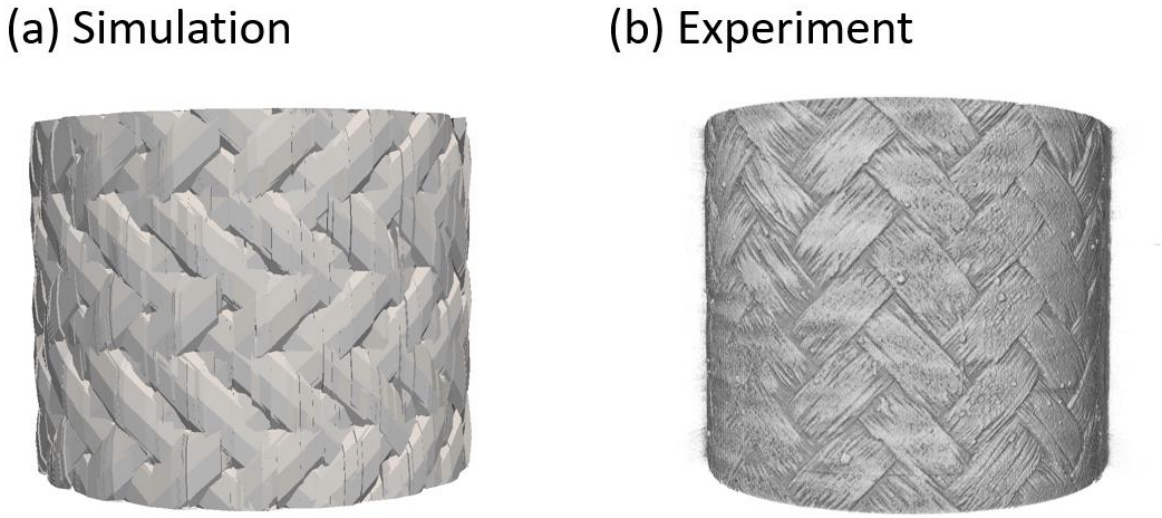


Figure 6.9: (a) The numerical model of fibres braids from the mathematical description, and the (b) comparison with the tomographic image of the fibre braids

6.4 C-ring Case Studies

The FEMME model is used to simulate a C-ring sample of under diametric compression, as in the experiments described in the previous experimental chapter 4. The geometry of the sample was generated at the FE layer in the Abaqus to obtain the meshes and nodal data with a tetrahedron mesh. This FE model approximates the C-ring sample with 1 mm wall thickness and 4 mm width. The C-ring has a total number of 324 tetrahedron mesh elements in the FE model, which yields an element size of approximate 1.1 mm. Within the same superimposed geometry, the microstructure of the SiC/SiC composite was described in the MAM layer and the CA layer, using the methodology described in section 6.3. A total of 4096 cells in the CA layer made up each of the FE tetrahedron elements, which allows a discretization size in the CA layer at around 60 μm.

In the FEMME model, the mechanical properties of each phase are input parameters, which are currently chosen based on a relatively subjective judgement. From the available literature data, the properties of the microstructure constituents are summarised in table 6.2. However, to reproduce the macroscale mechanical response from the experimental results (i.e. force vs displacement) those parameters are optimized, such that, for the matrix, the elastic modulus is 180 GPa with the elastic limit of 0.0003; the failure strain is 0.0012; and the Poisson's ratio is 0.25. For the pores, to avoid the computational error due to the divergence in each iterative run, instead of setting the elastic modulus being zero, it is chosen to be 10^{-6} GPa. For the fibres at room temperature, the elastic modulus is 400 GPa, the elastic strain limit is 0.0003, followed by linear decay until the failure strain at 0.01. At high temperature, the fibre failure strain was reduced to 0.001 with the same elastic strain limit. The optimized materials mechanical properties for the simulation are summarized in figure 6.10.

Table 6.2: The mechanical properties of the microstructure constituents and bulk properties of the SiC/SiC composite from the literature

Microstructure constituents	Elastic modulus (MPa)	Tensile strength (MPa)	Elongation (%)	Proportional limit stress (MPa)	Ref.
Generation III SiC fibres					
Hi-Nicalon Type-S	420	2600			[27], [37]
Tyranno SA3	375	2800	0.8		[27], [37]
Pure SiC (bulk)	450				[27]
SiC/SiC Minicomposite	420	880		280	[39]
SiC/SiC composite (bulk)	210	300		110	[27]
	248	269	1	125	[43]
	173		0.6		[93]

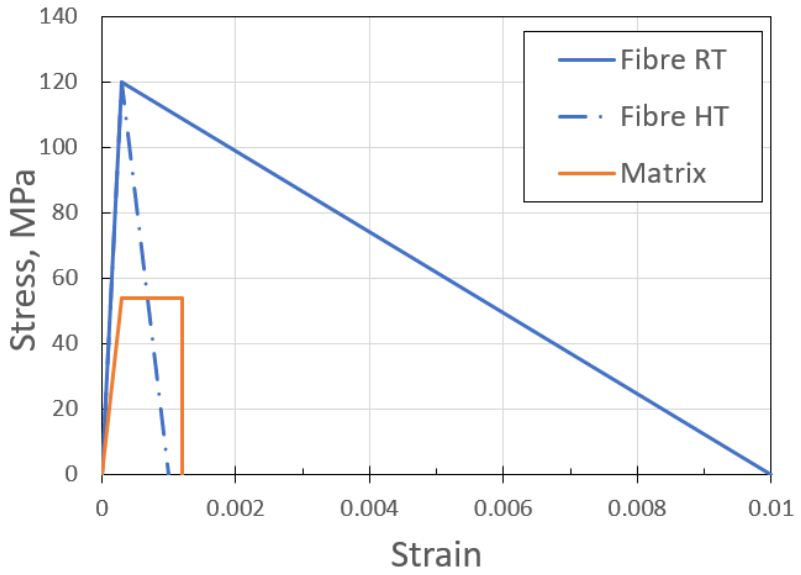


Figure 6.10: The optimized constituent phases properties of the fibre and matrix in the FEMME model

It should be noted that currently the microstructure inputs for different phases were optimised to fit the macroscale response of the macroscale component from the experiment. There was an optimization process that tunes the microstructure constituent properties to fit the experiment force vs displacement curve. The approximate values of the elastic modulus of the fibre and matrix were chosen based on the literature values, listed in table 6.2. As expected, the stiffness of the component was shown to be reliant on the elastic modulus of the fibres and matrix. The elastic limit of the matrix plays an important role in the overall magnitude of the mechanical response. Simulation 1 in figure 6.11 shows effect of increasing the elastic modulus limit of the matrix to 0.001. The values of the failure strain in matrix and fibres were tuned in a trial and error process, which also evaluated the sensitivity of each simulation input. The failure strain of the matrix and the elasticity of the fibre determine the ductility of the overall component model. Simulation 2 shows the result if the failure strain of the matrix is reduced to 0.0008, with a reduced ductility of the component. A reduced fibre elastic limit (0.0005) in Simulation 3 indicates the elastic strain limit of the fibre can lead to a noticeable increased ductility of the general component as well.

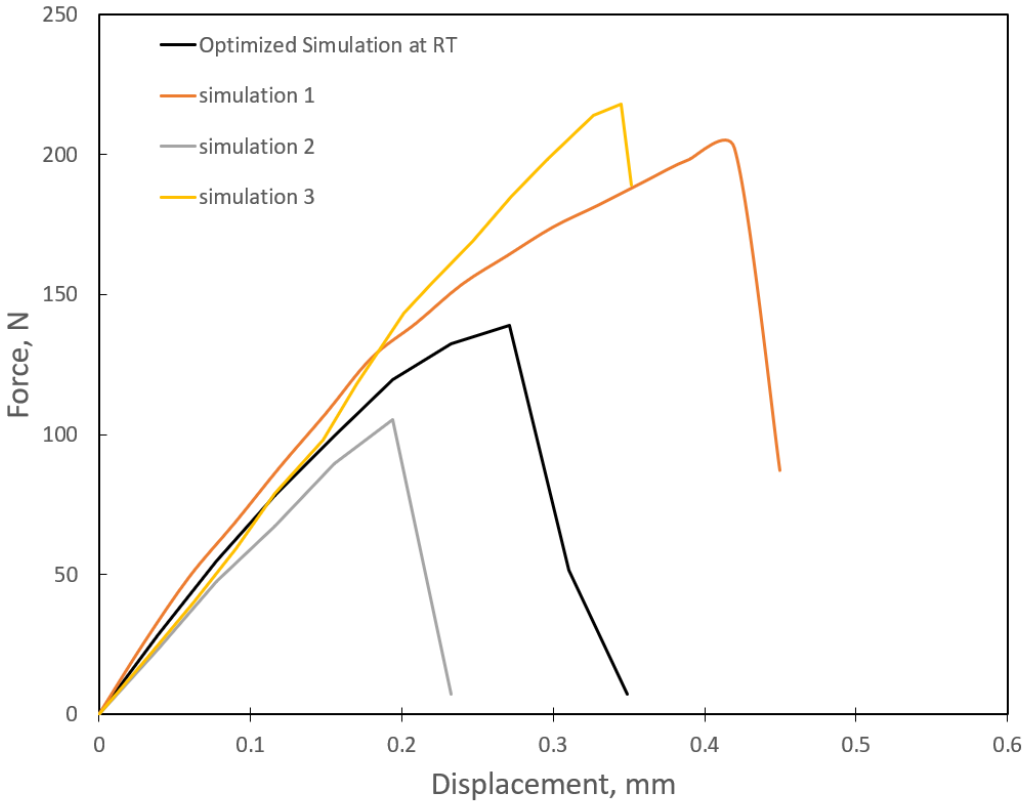


Figure 6.11: The simulation tests to optimize the simulation results to fit the macroscale mechanical response. The trails test in Simulation 1 (matrix elastic limit from 0.0003 to 0.001); Simulation 2 (matrix failure strain from 0.0012 to 0.0008); Simulation 3 (fibre elastic limit from 0.0003 to 0.0005).

In each modelling iteration, once the local strain within each constituent exceed the failure stain, the corresponding subdivided cell is eroded. Analogous with the cohesive model, the operation of eroded cells means the completely damage and the cells is therefore unable to transfer load in the model. The generated faces from the eroded cells describe the simulated damage path. Through this method, the FEMME model requires a computational time around 9 hr for 10 iterative steps in a workstation computer with an *Intel® Core™ i7-5820K* Processor and 56 GB installed memory.

At the macroscale, the optimised bulk response of the simulation model is compared with experimental results as shown in figure 6.12 by measuring the force and displacement at the top

of the C-ring. The FEMME model allows the reproduction of the non-linear behaviour in the ceramic composite via this optimization process. The departure from the linear region indicates a reduced macroscale elasticity that is due to the eroded cells as damage occurs. The damage evolution is therefore illustrated by the eroded cells, which can also influence the strain distribution in model as presented in the figure 6.13. The damage in the model as eroded cells in the CA model starts at the middle height and then there is a dispersed damage pattern found at higher load as the region of the eroded cells grow. At the same time, the simulated anisotropic strain distribution along each fibre tow is present in the magnified image of the sample. Figure 6.14(b) shows simulation results of the damage as matrix cracks with the surrounding pores structure. The matrix damage in the FEMME model was found to be associated with the spatial distribution of the pores in the component. However, compared with the experiment results (chapter 4) the FEMME model is not able to reproduce the periodic axial matrix cracks that span across the sample width. They were presented as a number of eroded regions in the model that was found to be influenced by the internal defects (as pores) in the microstructure.

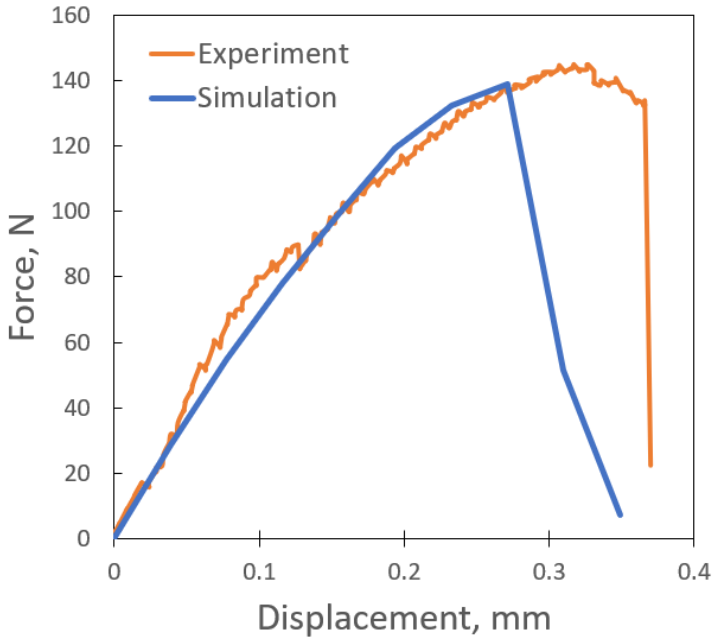


Figure 6.12: Comparison between the simulated force-displacement result (in blue) and that of the experiment results of the diametric compressed C-ring at room temperature. The displacement and the force were measured at the top of the diametric C-ring.

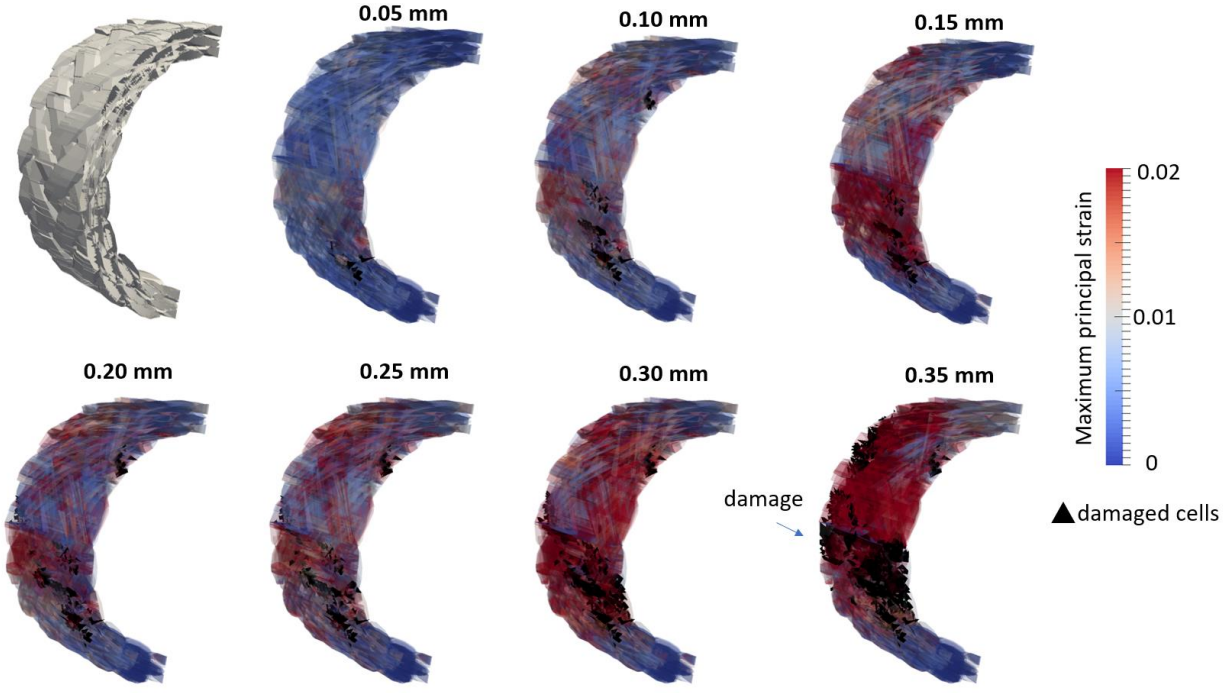


Figure 6.13: Simulation of strain and damage distributions in the diametric compressed C-ring at different crosshead displacement at room temperature.

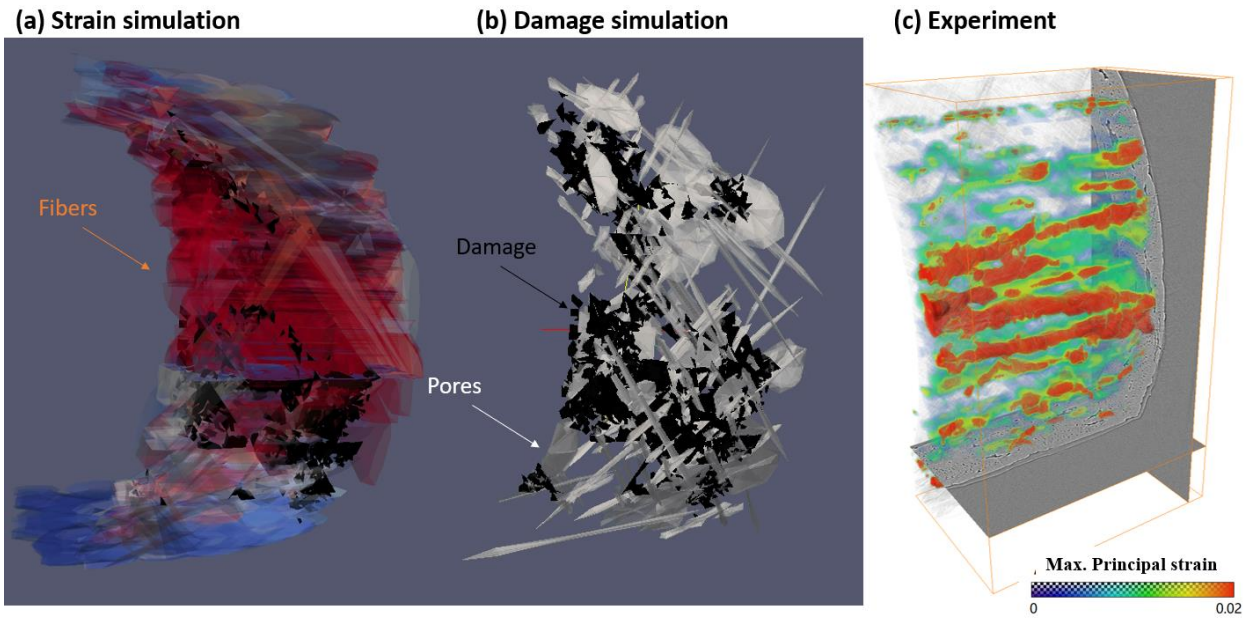


Figure 6.14: The magnified view of the simulation result with 0.35mm displacement showing (a) the fibres and damage, (b) the pores and the damage and (c) the experimental strain distribution.

At high temperature, the fractured SiC fibre was deemed to be unable to transfer stress due to the evaporation of PyC interphase in the air atmosphere (Chapter 4). In order to simulate the conditions at the high temperature, the failure strain of the fibre tows is reduced, from 0.01 to 0.001. The optimization of the virtual tests with the different fibre failure strain are shown in figure 6.15 where the fibre failure strain was set to be 0.005 and 0.0005 for virtual test 1 and 2, respectively. The fibre failure strain as a microstructure input can alter the overall magnitude of the macroscale mechanical response in the virtual C-ring component as shown in the figure 6.15. The same remaining mechanical properties were used for all the other parameters as the room temperature simulations (as shown in figure 6.10). When the optimization of the fibre failure strain is 0.001, the macroscale response of the same C-ring geometry with the same fibres and pores microstructure at the high temperature is shown in figure 6.16 to fit the experimental results.

Figure 6.17 shows the visualizations of the damage evolution from the optimized simulation at high temperature with strain distribution among the virtual component. It is interesting to note that the damage distribution is more concentrated, towards the central plane, and this is comparable to the strain concentration locations observed in the experimental work. Figure 6.18 shows the magnified images of the virtual components at high temperature. The tuned fibre failure strain can also influence the simulated distribution of the damaged cells, compared with the room temperature simulation results. Even though the matrix damage was only approximated as eroded cells in the model, with less 'strengthening' effects from the fibres, the damage propagated from the previous damaged cells and is regulated at similar height within the virtual component (compared with the room temperature results in figure 6.13). Though this method, the detailed composite behaviour at high temperature with the consideration of the microstructure was simulated in the FEMME model.

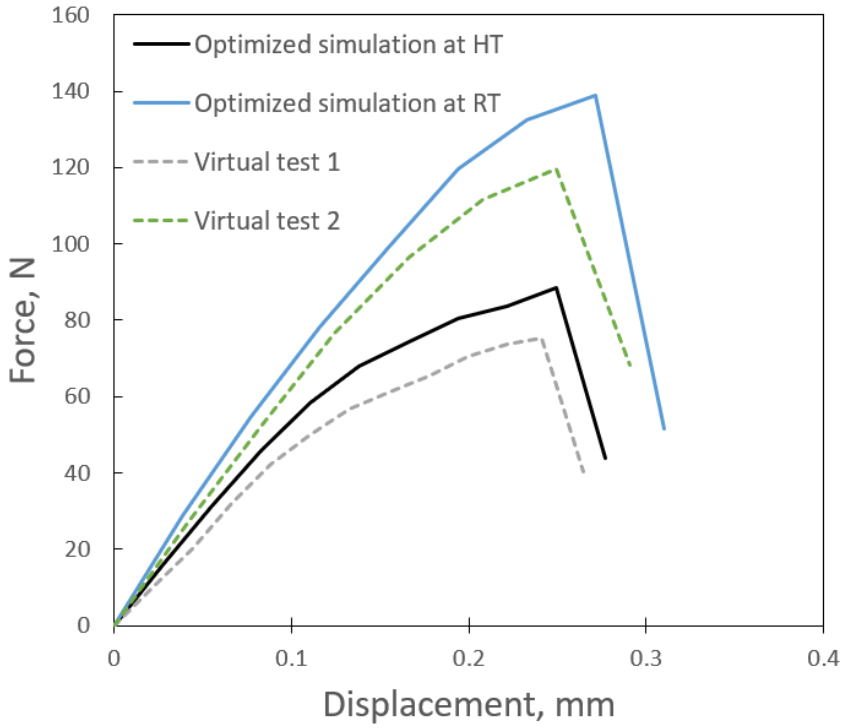


Figure 6.15: The optimization of the fibre failure strain in virtual tests to fit the macroscale mechanical response of the C-ring at high temperature. The failure strain of the fibre was 0.01 and 0.001 for the room temperature test and high temperature test, respectively. The virtual tests 1 and 2 have a fibre failure strain of 0.005 and 0.0005, respectively.

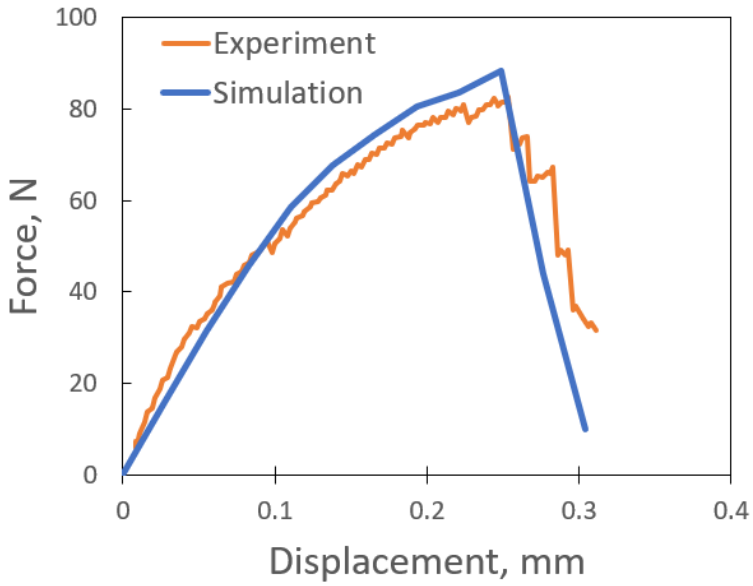


Figure 6.16: Comparison between the simulated force-displacement result (in blue) and that of the experiment results of the diametric compressed C-ring at elevated temperature

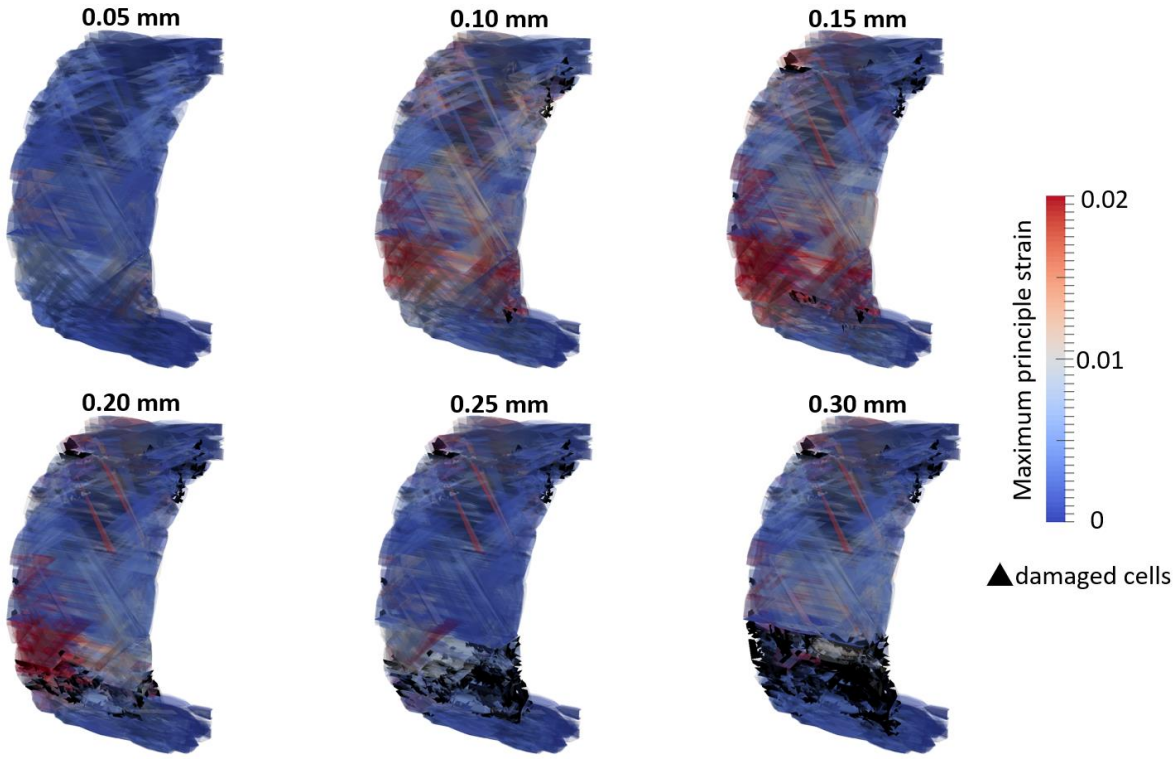


Figure 6.17: Simulation of strain and damage distributions in the diametric compressed C-ring at different crosshead displacement at elevated temperature.

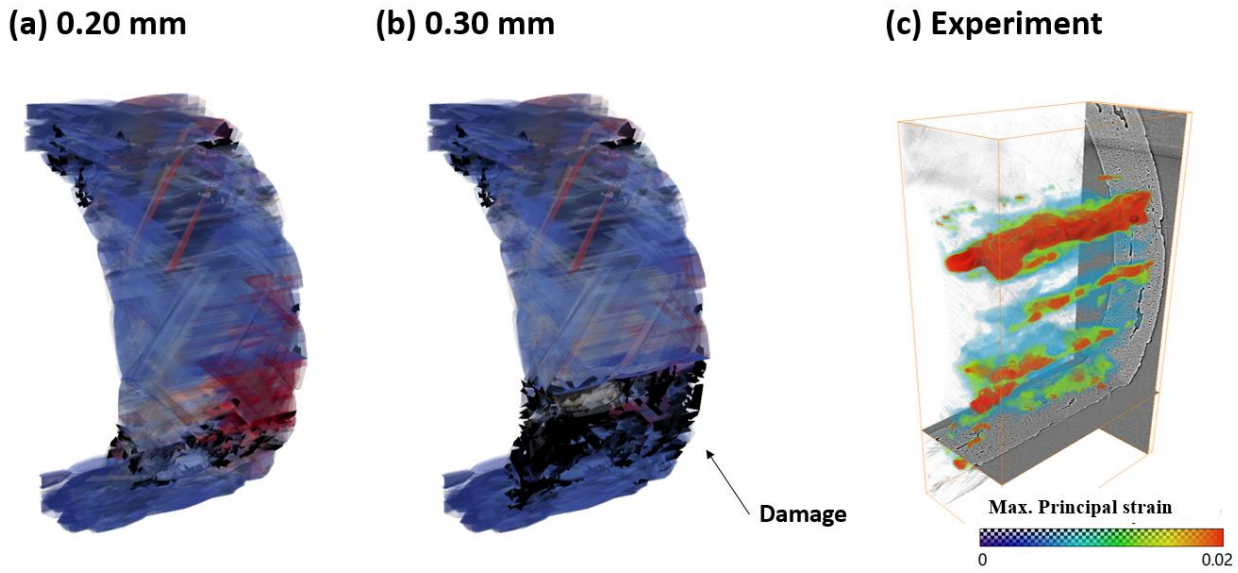


Figure 6.18: The magnified view of the simulation results C-ring diametric compression with a (a) 0.20mm and (b) 0.30mm displacement as in figure 6.12 and (c) the experimental results of the fractured sample at 0.28mm.

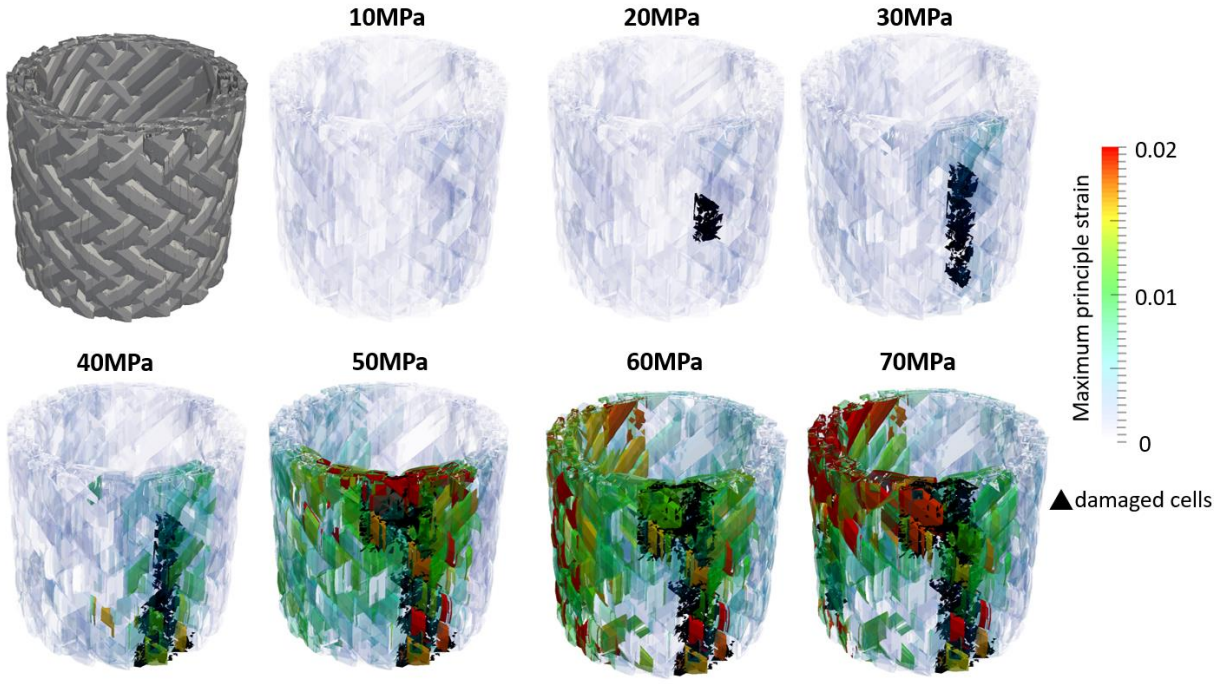
6.5 Internal Pressurization Case Study

The virtual C-ring diametric results demonstrate the capability of the FEMME model in simulating bulk response and damage evolution in a relatively concentrated loading state. The effects of the different loading state can also be performed. In the scenario of the tubular composite under internal pressure, the same microstructure description and micromechanical properties are used as that in the previous C-ring simulation at the room temperature. The internal pressure boundary conditions are applied on the inside surface of each FE element mesh. After the CA subdivision, the discretization of the cells structure is around 80 μm. The simulation time in this case was around 12 hr in 8 iterative steps on the same computer.

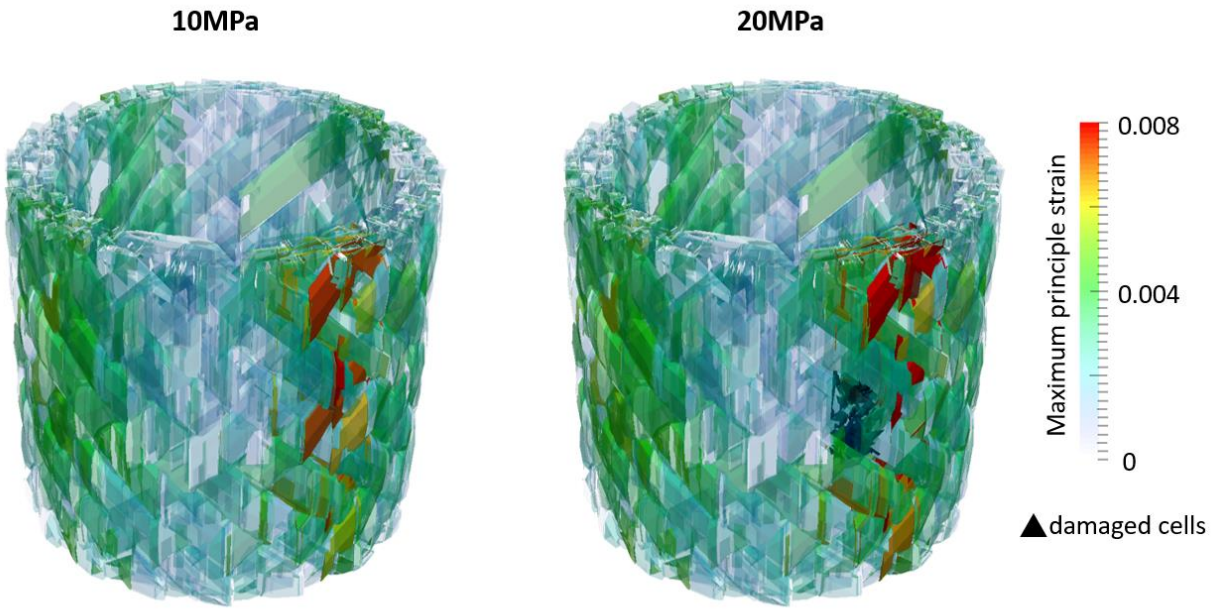
The virtual results of nucleation and propagation of the damage in the composite tube is shown in the figure 6.19, as the internal pressure is gradually increased to 70 MPa. The first damage appears when the pressure reaches 20 MPa, with the magnified images in figure 6.20. The propagated damage is aligned longitudinally under the hoop stress from the internal pressure. As internal pressure increases, a second longitudinal damage also nucleates at a different location (70 MPa in figure 6.19), which shows the potential to simulate multiple damages in the tubular component.

The deformation of the virtual composite tube was also anisotropic. Figure 6.21 shows the original and dilated tube as an example under 30 MPa (magnified displacement 5000×). Those dilation evolution of the composite tube at different angular direction under the internal pressure is shown in the figure 6.22. It was represented as the displacement maps from the nodal solutions in the FEMME model and compared with the original states. The data was binned at each 36° though the entire tube thickness. Even though the general degree of the deformation as magnitude of displacement was small compared with the geometry of the tube (few micrometres to millimetres), there was a noticeable anisotropic diameter change of the virtual cylindric tube under the internal

pressure at different angular directions as shown in the displacement plots. In those plots the maximum dilation was found constantly at around 280°. Those non-uniform dilations can lead to a non-zero circumferential displacement as shown in figure 6.23. This distribution pattern of displacement at circumferential direction (approximated as two sine waves) in the virtual test is comparable in the shape to the experimental observation of the ovalization defamation of the tube under internal pressure (Chapter 5). It notable that after 50 MPa due to the significant damage in the model (figure 6.22), the degree of the anisotropy is increased but the pattern stays. Nevertheless, in the FEMME model the macroscale deformation of the composite tube is also described.



6.19: Simulation of strain development and damage distribution in the composite tube with the increasing internal pressure.



6.20: The magnified strain distribution of the composite tube under internal pressure where the fibre damage is observed.

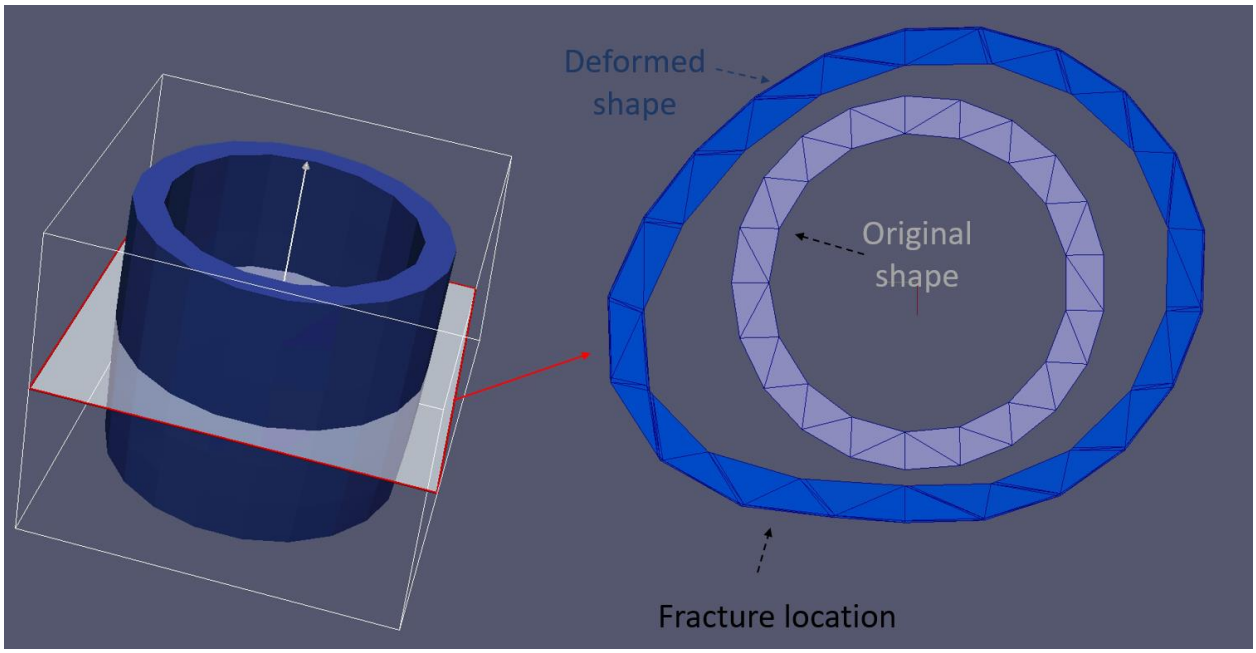


Figure 6.21: An example of the original shape and the deformed shape of the virtual cylindric tube under the internal pressure at 30MPa. (displacement magnified factor 5000×)

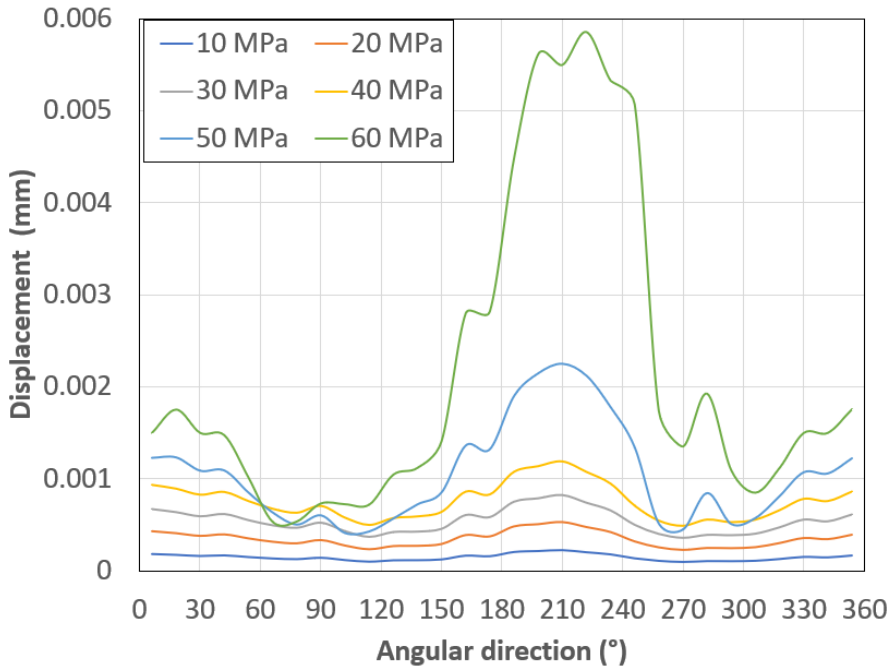


Figure 6.22: The anisotropic deformation of the cylindric tube at different angular directions under the internal pressure as displacement plots

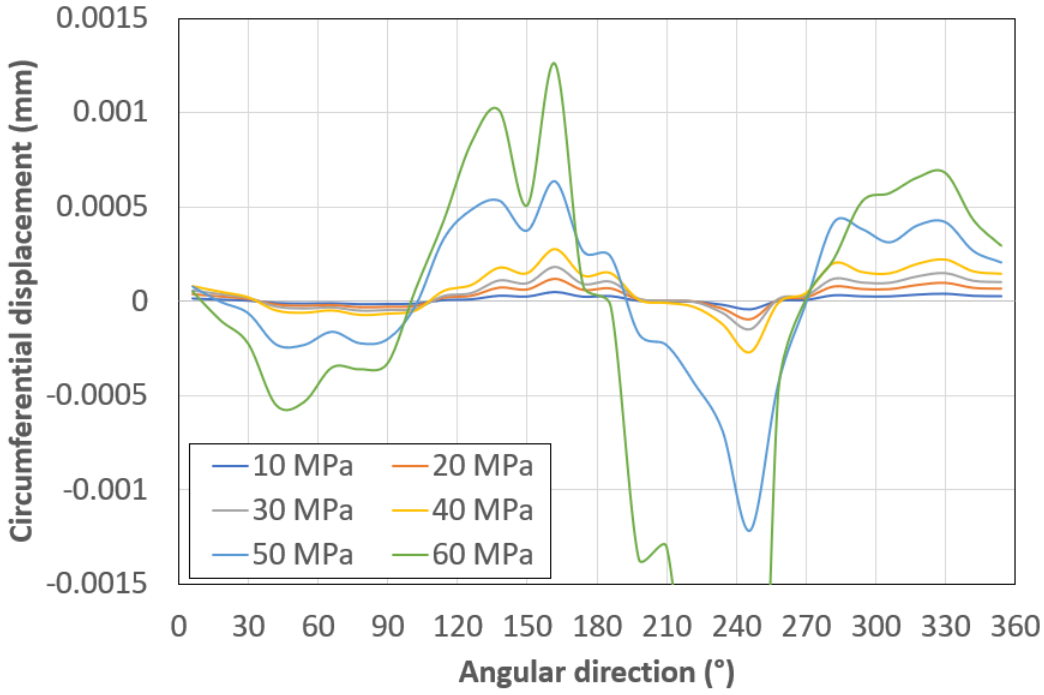


Figure 6.23: The circumferential displacement plots of the virtual composite tube under different internal pressure

6.6 Discussion

The aim of the application of the FEMME model in this study is to address the linkage between the macroscale component modelling and the microscale damage evolution in the composite. The microstructure information of the internal heterogeneity distribution can be described from the X-ray tomographic study of the composite. Informed by the tomographic images, the statistic distribution of the porosity is therefore approximated. The fibre tows are explicitly inserted, and these can hinder the damage propagation and influence the overall macroscale stiffness of the virtual component. Moreover, due to the different failure strains in the fibre and the matrix, the fibres can also transfer some load across the crack surface (illustrated as the eroded cells), which partially addresses the fibre pull-out effect in the composites. Currently, the microstructure is mathematically described in the model with the micromechanical properties as model inputs. The stiffness of the virtual component was reliant on the elastic parameters of each microstructure constituent. The failure strain of the fibre can also control the final ductility of the simulation results. With the tuning of the microstructure input, the model can successfully approximately reproduce the importance of the microstructure into a full-scale component model.

In this study, two cases of the damage evolution in the tubular composite component at different stress states were simulated with the effectiveness of the microstructure, such as pores and fibres. The predicted damage initiation location and damage development, which are not pre-defined in the model, are comparable with the *in situ* experimental results from both diametric C-ring compression and internal pressurization tests. The different damage distributions under the diametric compression and internal pressure demonstrates the influence of the loading state on the damage evolution. For example, relatively dispersed damage in the C-ring and the longitudinal

damage in the tubular component are presented in figure 6.13 and figure 6.19 respectively with the same constituents' properties at room temperature. Additionally, by tuning the microstructure properties, the high temperature fracture behaviour was also reproduced, which indicates the importance of the fibres in macroscale stiffness and damage propagation resistance in such simulation model. In the virtual simulation, the same material properties are used for both C-ring compression and internal pressurization simulation at room temperature. Those materials property inputs were optimized for the C-ring using the experimental study at room temperature. The anisotropic defamation of the composite tube under internal pressure was successfully reproduced in the FEMME model, while the microstructure was randomly described. Even though the magnitude of the dilation deformation (few micrometres) was generally only one tenth in what was observed in the experiment, the general pattern of the dilation at different angular direction under internal pressure was successfully reproduced at macroscale.

The macroscale response in the C-ring was obtained by optimization via changing the microstructure constituents' inputs. Thereinto, the elastic modulus of the fibre tow (400 GPa) falls within range (~360 to 430 GPa) from the reported experimental results of the minicomposite studies with the third generation fibres [39], [41], [207]. However, the elastic limit of the fibre at 0.03 % strain (i.e. 120 MPa) is relatively low compared with that in the experiments, which are generally larger than 400 MPa. Furthermore, the onset of the matrix crack (~0.03%) was also set to be earlier than that in the experimental studies (approximate 0.1% strain). At current stage, the materials properties in the FEMME model that give a good agreement in macroscale response have a noticeable difference compared with the experiential data, even though they fall in the same magnitude.

These differences between the simulation and experiments can be explained by the fact that the FEMME model was mainly designed to incorporate the significance of the stress concentration due to the pores and defects between the fibre tows within the composites [200], [201]. The interphase between the fibre and matrix is not integrated in the model but has been argued to have an important role in the composite mechanical properties[50], [75], [81]. The influence of such damage in the interphase and fibre pull-out are not directly reproduced, which means the sliding stress of the broken fibre was not considered. This effect is approximated by the earlier matrix damage strain that is arbitrarily chosen in the FEMME model at which the interphase damage may start to occur and the micromechanical properties of the matrix input was assumed to follow an elastic plastic stress-strain law where there was a constant stress from the elastic limit until the final failure. All of those are different from what occurred in the real situation of the damage evolution in the composites, which might explain the difference between experimental results and the results in the FEMME model.

Moreover, it also needs to be mentioned that the periodic distribution of the matrix cracks as observed in the experiment were not presented in the FEMME model in both C-ring and entire tubes. It might be the resolution limit of the model as the smallest discretization is around 60μm while experimental observed matrix crack opening was only few micrometres with a typical spacing of 500 μm. Furthermore, the microstructure of the pores, matrix and fibres was still an approximation in the model via the mathematical description. The periodic matrix cracks were typically observed in the experiment at the surface where it was a very thin layer (approximately 50 μm), which was not considered in the simulation model. Additionally, in the FEMME model, once the damage occurred (as eroded cells), the local strain energy is recalculated. The reduced

local elasticity that might be overestimated due to the size of the cells makes the damaged region prone to further damage development.

Therefore, the complex matrix damage evolution in the FEMME model is an approximation. As shown in the internal pressure results, the damage model also tends to give a slower virtual damage propagation. It may explain why the macroscale response of the force/displacement curve is smoother than that from the experiments. Thus, in order to relate the drops and the gradient changes to the onset of matrix cracking or the deflection of crack propagation, higher resolution modelling is required for the future development. Ideally, the model in the future development can directly reproduce the real structure of the fibres and the interphase from the experimental observation and have a resolution generally less than one micrometre for the damage simulation that is able to capture the detailed matrix cracks in the composite.

6.7 Conclusion

The advanced high-fidelity FEMME model has been used to simulate virtual tests of the nuclear graded SiC/SiC composite in different environment and stress state. The microstructure information was obtained from X-ray tomographic studies. The statistic distribution of the pores and the woven fibre tows are mathematically described in the model to address the importance of the microstructure. The local activation of the microstructure in the multi-scale model provides the computational efficiency of the complex damage evolution, where the damage was found associated with the pores. The effective simulation of the damage behaviour that is sensitive to the composite microstructure was demonstrated in the cases of C-ring diametric compression and tube under internal pressure. The simulations performed in the environments of the *in situ* experiments showed a good agreement in macroscale response and the damage evolution. Further development

in a higher fidelity model that can represent individual matrix cracking and fibre pull-out requires a higher resolution in the microstructure description, which would push the current limits of the FEMME model.

Chapter 7. Conclusions and future work

7.1 Conclusions

The work presented in this thesis has been devoted to the study of the damage evolution in the SiC/SiC composite that was developed for advanced nuclear fuel cladding. The method, based on the X-ray tomography and the digital volume correlation to detect the damage *in situ*, was developed and applied to mechanical tests of C-ring diametric compression and hoop pressurization of the entire tube. The 3D characterization and modelling provide the multiscale investigation of the relationships between the damage, microstructure, and macroscale deformation.

The 3D tomography image (Chapter 3) revealed the internal structure non-destructively, with special focus on the fibres and porosities. The large pores were found spatially interconnected and located between the fibre ply layers. In the case of C-ring diametric compression (Chapter 4), the *in situ* tomographic method has been developed that permits the continuous observation of the composite sample at both room temperature and high temperature. Crack propagation at room temperature was found to be regulated by the fibre architecture. High temperature (900°C) with air atmosphere degenerates the mechanical properties of the SiC/SiC composite where a smoother crack path was found. The damage evolution that is related to the microstructure and macroscale deformation was also quantified though the digital volume correlation to provide full-field studies. Further, a larger sampling volume as the entire composite tube was examined in the hoop pressurization test (Chapter 5). The matrix cracks were found to have initiated at both inside and outside surface. The densities of both cracks increased with the increased internal pressure, but they were distributed heterogeneously among the tube sample. The corresponding heterogenous deformation of the tube under internal pressure was quantified, where the dilation was combined

with the ovalization effect. Moreover, a more accurate method to measure the hoop strain was presented. The final critical crack was found as a development of the local crack instead of a consequence of the macroscale deformation. The general macroscale deformation of those experimental results can be reproduced in the multiscale FEMME model (Chapter 6) via tuning of the microstructure properties. The microstructure of the composite was approximated via mathematical descriptions based on the 3D experimental observation. The general damage evolution was reproduced in the virtual tests with the 3D strain pattern. The macroscale deformation depends on the inputs of the microstructure constituents. The damage was found relevant to the local defects such as pores within the simulation model.

7.2 Suggestions for future work

The feasibility of the coupled X-ray tomography and digital volume correlation has been demonstrated in the thesis. This method provides a more reliable measurement of the mechanical properties in the SiC/SiC composite cladding tubes and facilitates the component design. However, there were few limitations associated with the current methods that may also point out the potential directions for future work.

(1) The spatial resolution of the common tomography used has a limit close to 1 μm, while the interphase in the composite has a thickness in the scale of the nanometres. Considering the importance of the interphase reported in the literature, it is worthwhile to push the resolution limits of the tomographic images, such as the use of the nanotomography [208], to observe the damage in the interphase. A *in situ* study of the damage in the interphase would be invaluable.

(2) Due to the limited accessibility of synchrotron tomography, there were a small number of samples examined. The generalization of some observations, such as the ovalization in the

composite tube under internal pressure, requires much more numbers of tests on the composite samples. Some experiments might be repeated using the laboratory tomography.[7]

(3) The continuous tomography reveals the entire story of mechanical response in the sample, but the available loading rig limits the volume of the sample that can be observed. Further development of the experimental method might be done to investigate a larger sampling area in the composite with the continuous monitoring and also its performance at high temperature.

(4) In the virtual test, the microstructure was approximated in the FEMME model. Ideally, the microstructure observed in the tomography should be directly reproduced in the model. Moreover, currently the microstructure properties were tuned to fit the experimental results. The microstructure inputs in the future should be obtained directly from the results of the real micromechanical tests of each material constituent [209].

(5) Another important factor in the composite modelling is the behaviour of its interphase, which can transfer the load between fibre and the matrix. The incorporation of the interphase behaviour requires further discretization in the model, so that the computation algorithm needs to be optimized to reduce the computational cost, e.g. parallelization of computing.

[7] The Deben CT5000 5kN in-situ tensile stage was used with the Xradia 510 for the internal pressurization test, but the sample stage became unstable after around 2kN load.

Bibliography

[1] A. Kohyama, M. Seki, K. Abe, T. Muroga, H. Matsui, S. Jitsukawa, *et al.*, "Interactions between fusion materials R&D and other technologies," *J. Nucl. Mater.*, vol. 283–287, no. PART I, pp. 20–27, 2000.

[2] T. Taguchi, T. Nozawa, N. Igawa, Y. Katoh, S. Jitsukawa, a. Kohyama, *et al.*, "Fabrication of advanced SiC fiber/F-CVI SiC matrix composites with SiC/C multi-layer interphase," *J. Nucl. Mater.*, vol. 329–333, no. 1–3 PART A, pp. 572–576, 2004.

[3] Y. Katoh, L. L. Snead, C. H. Henager, a. Hasegawa, a. Kohyama, B. Riccardi, *et al.*, "Current status and critical issues for development of SiC composites for fusion applications," *J. Nucl. Mater.*, vol. 367–370 A, no. SPEC. ISS., pp. 659–671, 2007.

[4] W. J. Kim, D. Kim, and J. Y. Park, "Fabrication and material issues for the application of SiC composites to LWR fuel cladding," *Nucl. Eng. Technol.*, vol. 45, no. 4, pp. 565–572, 2013.

[5] D. Kim, H. G. Lee, J. Y. Park, and W. J. Kim, "Fabrication and measurement of hoop strength of SiC triplex tube for nuclear fuel cladding applications," *J. Nucl. Mater.*, vol. 458, pp. 29–36, 2015.

[6] F. Carre, P. Yvon, P. Anzieu, N. Chauvin, and J. Y. Malo, "Update of the French R&D strategy on gas-cooled reactors," *Nucl. Eng. Des.*, vol. 240, no. 10, pp. 2401–2408, 2010.

[7] A. Ž. Iveković, S. Novak, G. Dražić, D. Blagoeva, and S. G. de Vicente, "Current status and prospects of SiCf/SiC for fusion structural applications," *J. Eur. Ceram. Soc.*, vol. 33, no. 10, pp. 1577–1589, 2013.

[8] C. P. Deck, G. M. Jacobsen, J. Sheeder, O. Gutierrez, J. Zhang, J. Stone, *et al.*, "Characterization of SiC-SiC composites for accident tolerant fuel cladding," *J. Nucl. Mater.*, vol. 466, pp. 667–681, 2015.

[9] T. Nozawa, S. Kim, K. Ozawa, and H. Tanigawa, "Stress envelope of silicon carbide composites at elevated temperatures," *Fusion Eng. Des.*, vol. 89, no. 7–8, pp. 1723–1727, 2014.

[10] C. Cabet, A. Michaux, C. Fazio, L. Malerba, M. F. Maday, M. Serrano, *et al.*, "The new EC FP7 MatISSE project: materials' innovations for a safe and sustainable nuclear in Europe," in *SMINS-3, Structural Materials for Innovative Nuclear Systems (SMINS-3) - Workshop Proceedings, Idaho National Laboratory, Idaho Falls, United States, 7-10 October 2013*, 2013.

[11] C. R. F. Azevedo, "Selection of fuel cladding material for nuclear fission reactors," *Eng. Fail. Anal.*, vol. 18, no. 8, pp. 1943–1962, 2011.

[12] L. Hallstadius, S. Johnson, and E. Lahoda, "Cladding for high performance fuel," *Prog. Nucl. Energy*, vol. 57, pp. 71–76, 2012.

[13] NEA and OECD, "Status Report on Structural Materials for Advanced Nuclear Systems," 2013.

[14] NEA and OECD, “State-of-the-art Report on Innovative Fuels for Advanced Nuclear Systems,” 2014.

[15] P. Yvon and F. Carré, “Structural materials challenges for advanced reactor systems,” *J. Nucl. Mater.*, vol. 385, no. 2, pp. 217–222, 2009.

[16] S. J. Zinkle and J. T. Busby, “Structural materials for fission & fusion energy,” *Mater. Today*, vol. 12, no. 11, pp. 12–19, 2009.

[17] “Nuclear Fuel Fabrication.” [Online]. Available: http://www.world-nuclear.org/info/Nuclear-Fuel-Cycle/Conversion-Enrichment-and-Fabrication/Fuel-Fabrication/. [Accessed: 27-Sep-2017].

[18] “Nuclear Industry Pursues New Fuel Designs and Technologies | POWER Magazine.” [Online]. Available: http://www.powermag.com/nuclear-industry-pursues-new-fuel-designs-and-technologies/?pagenum=2. [Accessed: 27-Sep-2017].

[19] D. Shepherd, “Technology readiness level (TRL) assessment of cladding for advanced nuclear fuels,” *Struct. Mater. Innov. Nucl. Syst.*, pp. 108–116, 2013.

[20] S. J. Zinkle, K. A. Terrani, J. C. Gehin, L. J. Ott, and L. L. Snead, “Accident tolerant fuels for LWRs: A perspective,” *J. Nucl. Mater.*, vol. 448, no. 1–3, pp. 374–379, 2014.

[21] H. G. Kim, J. H. Yang, W. J. Kim, and Y. H. Koo, “Development Status of Accident-tolerant Fuel for Light Water Reactors in Korea,” *Nucl. Eng. Technol.*, vol. 48, no. 1, pp. 1–15, 2016.

[22] C. Sauder, J. Braun, A. MICHAUX, G. Loupias, and P. Billaud, “Assesment of SiC/SiC cladding for LWRs,” *LWR Fuel Perform. Meet. Top Fuel 2013*, 2013.

[23] K. Yueh and K. A. Terrani, “Silicon carbide composite for light water reactor fuel assembly applications,” *J. Nucl. Mater.*, vol. 448, no. 1–3, pp. 380–388, 2014.

[24] L. L. Snead and O. J. Schwarz, “Advanced SiC composites for fusion applications,” *J. Nucl. Mater.*, vol. 219, pp. 3–14, 1995.

[25] T. Ishikawa, “A Tough, Thermally Conductive Silicon Carbide Composite with High Strength up to 1600C in Air,” *Science (80-.).*, vol. 282, no. 5392, pp. 1295–1297, 1998.

[26] R. Naslain, “Design, preparation and properties of non-oxide CMCs for application in engines and nuclear reactors: An overview,” *Compos. Sci. Technol.*, vol. 64, no. 2, pp. 155–170, 2004.

[27] Y. Katoh, K. Ozawa, C. Shih, T. Nozawa, R. J. Shinavski, A. Hasegawa, *et al.*, “Continuous SiC fiber, CVI SiC matrix composites for nuclear applications: Properties and irradiation effects,” *J. Nucl. Mater.*, vol. 448, no. 1–3, pp. 448–476, 2014.

[28] L. H. Rovner and G. R. Hopkins, “Ceramic Materials for Fusion,” *Nucl. Technol.*, vol. 29, no. 3, pp. 274–302, Jun. 1976.

[29] L. L. Snead, T. Nozawa, Y. Katoh, T. S. Byun, S. Kondo, and D. a. Petti, “Handbook of SiC properties for fuel performance modeling,” *J. Nucl. Mater.*, vol. 371, no. 1–3, pp. 329–377, 2007.

[30] R. H. Jones and C. H. Henager, “Subcritical crack growth processes in SiC/SiC ceramic matrix composites,” *J. Eur. Ceram. Soc.*, vol. 25, no. 10 SPEC. ISS., pp. 1717–1722, 2005.

[31] R. H. Jones, D. Steiner, H. L. Heinisch, G. a. Newsome, and H. M. Kerch, “Radiation resistant ceramic matrix composites,” *J. Nucl. Mater.*, vol. 245, no. 2–3, pp. 87–107, 1997.

[32] R. R. Naslain, “The design of the fibre-matrix interfacial zone in ceramic matrix composites,” *Compos. Part A Appl. Sci. Manuf.*, vol. 29, no. 9–10, pp. 1145–1155, 1998.

[33] F. Rebillat, J. Lamon, R. Naslain, E. Lara-Curzio, M. K. Ferber, and T. M. Besmann, “Properties of Multilayered Interphases in SiC/SiC Chemical-Vapor-Infiltrated Composites with ‘Weak’ and ‘Strong’ Interfaces,” *J. Am. Ceram. Soc.*, vol. 81, no. 9, pp. 2315–2326, 1998.

[34] N. Carrère, E. Martin, and J. Lamon, “Influence of the interphase and associated interfaces on the deflection of matrix cracks in ceramic matrix composites,” *Compos. Part A Appl. Sci. Manuf.*, vol. 31, no. 11, pp. 1179–1190, 2000.

[35] K. Shimoda, J. S. Park, T. Hinoki, and A. Kohyama, “Influence of pyrolytic carbon interface thickness on microstructure and mechanical properties of SiC/SiC composites by NITE process,” *Compos. Sci. Technol.*, vol. 68, no. 1, pp. 98–105, 2008.

[36] T. Ishikawa, *Advances in inorganic fibers*. Springer Berlin Heidelberg, 2005.

[37] A. R. Bunsell and A. Piant, “A review of the development of three generations of small diameter silicon carbide fibres,” *J. Mater. Sci.*, vol. 41, no. 3, pp. 823–839, 2006.

[38] A. Hasegawa, A. Kohyama, R. H. Jones, L. L. Snead, B. Riccardi, and P. Fenici, “Critical issues and current status of SiC/SiC composites for fusion,” *J. Nucl. Mater.*, vol. 283–287, no. PART I, pp. 128–137, 2000.

[39] C. Sauder, A. Brusson, and J. Lamon, “Influence of interface characteristics on the mechanical properties of Hi-nicalon type-S or tyranno-SA3 fiber-reinforced SiC/SiC minicomposites,” *Int. J. Appl. Ceram. Technol.*, vol. 7, no. 3, pp. 291–303, 2010.

[40] Y. Katoh, L. L. Snead, T. Nozawa, S. Kondo, and J. T. Busby, “Thermophysical and mechanical properties of near-stoichiometric fiber CVI SiC/SiC composites after neutron irradiation at elevated temperatures,” *J. Nucl. Mater.*, vol. 403, no. 1–3, pp. 48–61, Aug. 2010.

[41] S. Bertrand, F. Philippe, R. Pailler, and L. Jacques, “Hi-Nicalon/SiC Minicomposites with (Pyrocarbon/SiC) nanoscale multilayered interphases,” *J. Am. Ceram. Soc.*, vol. 82, no. 9, pp. 2465–73, 1999.

[42] Y. Katoh, A. Kohyama, T. Nozawa, and M. Sato, “SiC/SiC composites through transient eutectic-phase route for fusion applications,” *J. Nucl. Mater.*, vol. 329–333, no. 1–3 PART A, pp. 587–591, Aug. 2004.

[43] F. Bernachy-Barbe, L. Gélébart, M. Bornert, J. Crépin, and C. Sauder, “Anisotropic damage behavior of SiC/SiC composite tubes: Multiaxial testing and damage characterization,” *Compos. Part A Appl. Sci. Manuf.*, vol. 76, pp. 281–288, 2015.

[44] B. P. Croom, P. Xu, E. J. Lahoda, C. P. Deck, and X. Li, "Quantifying the three-dimensional damage and stress redistribution mechanisms of braided SiC/SiC composites by in situ volumetric digital image correlation," *Submitted*, vol. 130, pp. 238–241, 2016.

[45] J. A. Dicarlo, "Advances in SiC / SiC Composites for Aero-Propulsion," 2013.

[46] F. Christin, "Design, Fabrication, and Application of Thermostructural Composites (TSC) like C/C, C/SiC, and SiC/SiC Composites," *Adv. Eng. Mater.*, vol. 4, no. 12, pp. 903–912, 2002.

[47] L. Chaffron, C. Sauder, C. Lorrette, L. BRIOTTET, A. Michaux, L. Gélébart, *et al.*, "Innovative SiC / SiC Composite for Nuclear applications," *EPJ Web Conf.*, vol. 51, p. 01003, 2012.

[48] R. J. Kerans and R. S. Hay, "Interface Design for Oxidation-Resistant Ceramic Composites," *J. Am. Ceram. Soc.*, vol. 85, pp. 2599–2632, 2002.

[49] R. R. Naslain, "SiC-matrix composites: Nonbrittle ceramics for thermo-structural application," *Int. J. Appl. Ceram. Technol.*, vol. 2, no. 2, pp. 75–84, 2005.

[50] R. R. Naslain, R. J. F. Pailler, and J. L. Lamon, "Single- and multilayered interphases in SiC/SiC composites exposed to severe environmental conditions: An overview," *Int. J. Appl. Ceram. Technol.*, vol. 7, no. 3, pp. 263–275, 2010.

[51] C. Droillard and J. Lamon, "Fracture Toughness of 2-D Woven SiC/SiC CVI-Composites with Multilayered Interphases," *J. Am. Ceram. Soc.*, vol. 79, no. 4, pp. 849–858, Apr. 1996.

[52] G. N. Morscher, H. M. Yun, and J. A. Dicarlo, "In-plane cracking behavior and ultimate strength for 2D woven and braided melt-infiltrated SiC/SiC composites tensile loaded in off-axis fiber directions," *J. Am. Ceram. Soc.*, vol. 90, no. 10, pp. 3185–3193, 2007.

[53] T. Nozawa, Y. Katoh, and A. Kohyama, "Evaluation of Tensile Properties of SiC/SiC Composites with Miniaturized Specimens," *Mater. Trans.*, vol. 46, no. 3, pp. 543–551, 2005.

[54] W. Yang, A. Kohyama, T. Noda, Y. Katoh, T. Hinoki, H. Araki, *et al.*, "Interfacial characterization of CVI-SiC/SiC composites," *J. Nucl. Mater.*, vol. 307–311, no. 2 SUPPL., pp. 1088–1092, 2002.

[55] A.G. Evans and D. B. Marshall, "Overview no. 85 The mechanical behavior of ceramic matrix composites," *Acta Metall.*, vol. 37, no. 10, pp. 2567–2583, 1989.

[56] C. Ayranci and J. Carey, "2D braided composites: A review for stiffness critical applications," *Compos. Struct.*, vol. 85, no. 1, pp. 43–58, 2008.

[57] F. Bernachy-Barbe, L. Gélébart, M. Bornert, J. Crépin, and C. Sauder, "Characterization of SiC/SiC composites damage mechanisms using Digital Image Correlation at the tow scale," *Compos. Part A Appl. Sci. Manuf.*, vol. 68, pp. 101–109, 2015.

[58] J. D. Stempien, D. M. Carpenter, G. Kohse, and M. S. Kazimi, "Characteristics of Composite Silicon Carbide Fuel Cladding after Irradiation under Simulated PWR Conditions," *Nucl. Technol.*, vol. 5450, 2017.

[59] C. P. Deck, H. E. Khalifa, B. Sammuli, T. Hilsabeck, and C. A. Back, "Fabrication of SiC-

SiC composites for fuel cladding in advanced reactor designs," *Prog. Nucl. Energy*, vol. 57, pp. 38–45, 2012.

[60] E. Rohmer, E. Martin, and C. Lorrette, "Mechanical properties of SiC/SiC braided tubes for fuel cladding," *J. Nucl. Mater.*, vol. 453, no. 1–3, pp. 16–21, 2014.

[61] Y. Katoh, L. L. Snead, T. Nozawa, T. Hinoki, A. Kohyama, N. Igawa, *et al.*, "Mechanical Properties of Chemically Vapor-Infiltrated Silicon Carbide Structural Composites with Thin Carbon Interphases for Fusion and Advanced Fission Applications," *Mater. Trans.*, vol. 46, no. 3, pp. 527–535, 2005.

[62] H. Araki, W. Yang, H. Suzuki, Q. Hu, C. Busabok, and T. Noda, "Fabrication and flexural properties of Tyranno-SA/SiC composites with carbon interlayer by CVI," *J. Nucl. Mater.*, vol. 329–333, no. 1–3 PART A, pp. 567–571, 2004.

[63] W. Yang, H. Araki, A. Kohyama, S. Thaveethavorn, H. Suzuki, and T. Noda, "Fabrication in-situ SiC nanowires/SiC matrix composite by chemical vapour infiltration process," *Mater. Lett.*, vol. 58, no. 25, pp. 3145–3148, 2004.

[64] P. Dupel, R. Pailler, and F. Langlais, "Pulse chemical vapour deposition and infiltration of pyrocarbon in model pores with rectangular cross-sections - Part II Study of the infiltration," *J. Mater. Sci.*, vol. 29, no. 5, pp. 1341–1347, 1994.

[65] D. Lespiaux, F. Langlais, R. Naslain, S. Schamm, and J. Sevely, "Correlations between gas phase supersaturation, nucleation process and physico-chemical characteristics of silicon carbide deposited from Si-C-H-Cl system on silica substrates," *J. Mater. Sci.*, vol. 30, no. 6, pp. 1500–1510, 1995.

[66] K. Sugiyama and E. Yamamoto, "Reinforcement and antioxidizing of porous carbon by pulse CVI of SiC," *J. Mater. Sci.*, vol. 24, no. 10, pp. 3756–3762, 1989.

[67] L. Gélébart, C. Chateau, M. Bornert, J. Crépin, and E. Boller, "X-ray tomographic characterization of the macroscopic porosity of chemical vapor infiltration SIC/SIC composites: Effects on the elastic behavior," *Int. J. Appl. Ceram. Technol.*, vol. 7, no. 3, pp. 348–360, Jan. 2010.

[68] S. P. Lee, J. O. Jin, J. S. Park, a. Kohyama, Y. Katoh, H. K. Yoon, *et al.*, "High temperature characterization of reaction sintered SiC based materials," *J. Nucl. Mater.*, vol. 329–333, no. 1–3 PART A, pp. 534–538, 2004.

[69] K. Luthra and G. Corman, "Melt infiltrated (MI) SiC/SiC composites for gas turbine applications," *DER Peer Rev. Microturbine …*, 2002.

[70] K. N. Lee, D. S. Fox, and N. P. Bansal, "Rare earth silicate environmental barrier coatings for SiC/SiC composites and Si3N4 ceramics," *J. Eur. Ceram. Soc.*, vol. 25, no. 10, pp. 1705–1715, Jan. 2005.

[71] A. G. Evans and F. W. Zok, "The physics and mechanics of fibre-reinforced brittle matrix composites," *J. Mater. Sci.*, vol. 29, no. 15, pp. 3857–3896, 1994.

[72] W. A. Curtin, "Theory of Mechanical Properties of Ceramic-Matrix Composites," *J. Am. Ceram. Soc.*, vol. 74, no. 11, pp. 2837–2845, Nov. 1991.

[73] P. Lawrence, “Some theoretical considerations of fibre pull-out from an elastic matrix,” *J. Mater. Sci.*, vol. 7, no. 1, pp. 1–6, Jan. 1972.

[74] V. Kostopoulos and Y. Z. Pappas, “Toughening Mechanisms in Long Fiber Ceramic Matrix Composites,” *Compr. Compos. Mater.*, pp. 95–114, 2000.

[75] M. D. Thouless and a. G. Evans, “Effects of pull-out on the mechanical properties of ceramic-matrix composites,” *Acta Metall.*, vol. 36, no. 3, pp. 517–522, 1988.

[76] N. Lissart and J. Lamon, “Damage and failure in ceramic matrix minicomposites: Experimental study and model,” *Acta Mater.*, vol. 45, no. 3, pp. 1025–1044, 1997.

[77] J. Martinez-Fernandez and G. N. Morscher, “Room and Elevated Carbon Temperature Tensile Properties of Single Tow Hi- CVI SiC Matrix Minicomposites,” *J. Eur. Ceram. Soc.*, vol. 20, pp. 2627–2636, 2000.

[78] J. Lamon, “A micromechanics-based approach to the mechanical behavior of brittle-matrix composites,” *Compos. Sci. Technol.*, vol. 61, no. 15, pp. 2259–2272, 2001.

[79] C. Chateau, L. Gélébart, M. Bornert, J. Crépin, E. Boller, C. Sauder, *et al.*, “In situ X-ray microtomography characterization of damage in SiCf/SiC minicomposites,” *Compos. Sci. Technol.*, vol. 71, no. 6, pp. 916–924, Apr. 2011.

[80] C. Chateau, L. Gélébart, M. Bornert, and J. Crépin, “Modeling of damage in unidirectional ceramic matrix composites and multi-scale experimental validation on third generation SiC / SiC minicomposites,” *J. Mech. Phys. Solids*, vol. 63, pp. 298–319, 2014.

[81] H. A. Bale, A. Haboub, A. A. Macdowell, J. R. Nasiatka, D. Y. Parkinson, B. N. Cox, *et al.*, “Real-time quantitative imaging of failure events in materials under load at temperatures above 1,600°C,” *Nat. Mater.*, vol. 12, no. 1, pp. 40–46, 2013.

[82] C.-H. Hsueh, “Interfacial debonding and fiber pull-out stresses of fiber-reinforced composites,” *Mater. Sci. Eng. A*, vol. 165, no. 2, pp. 1–11, 1990.

[83] C.-H. Hsueh, “Crack-wake interfacial debonding criteria for fiber-reinforced ceramic composites,” *Acta Mater.*, vol. 44, no. 6, pp. 2211–2216, Jun. 1996.

[84] C. Liang and J. W. Hutchinson, “Mechanics of the fiber pushout test,” *Mech. Mater.*, vol. 14, no. 3, pp. 207–221, Jan. 1993.

[85] Y. Katoh, K. Ozawa, T. Hinoki, Y. Choi, L. L. Snead, and A. Hasegawa, “Mechanical properties of advanced SiC fiber composites irradiated at very high temperatures,” *J. Nucl. Mater.*, vol. 417, no. 1–3, pp. 416–420, 2011.

[86] G. N. Morscher, “Modeling the elastic modulus of 2D woven CVI SiC composites,” *Compos. Sci. Technol.*, vol. 66, no. 15, pp. 2804–2814, Dec. 2006.

[87] T. Ishikawa, K. Bansaku, N. Watanabe, Y. Nomura, M. Shibuya, and T. Hirokawa, “Experimental stress/strain behavior of SiC-matrix composites reinforced with Si-Ti-C-O fibers and estimation of matrix elastic modulus,” *Compos. Sci. Technol.*, vol. 58, no. 1, pp. 51–63, 1998.

[88] T. Nozawa, K. Ozawa, Y. B. Choi, A. Kohyama, and H. Tanigawa, “Determination and

prediction of axial/off-axial mechanical properties of SiC/SiC composites," *Fusion Eng. Des.*, vol. 87, no. 5–6, pp. 803–807, 2012.

[89] W. Yang, H. Araki, A. Kohyama, Q. Yang, Y. Xu, J. Yu, *et al.*, "The effect of SiC nanowires on the flexural properties of CVI-SiC/SiC composites," *J. Nucl. Mater.*, vol. 367–370 A, no. SPEC. ISS., pp. 708–712, 2007.

[90] S. Zhu, M. Mizuno, Y. Kagawa, and Y. Mutoh, "Monotonic tension, fatigue and creep behavior of SiC-fiber-reinforced SiC-matrix composites: A review," *Compos. Sci. Technol.*, vol. 59, no. 6 SPEC. SEC., pp. 833–851, 1999.

[91] J. S. Park, A. Kohyama, T. Hinoki, K. Shimoda, and Y. H. Park, "Efforts on large scale production of NITE-SiC/SiC composites," *J. Nucl. Mater.*, vol. 367–370 A, no. SPEC. ISS., pp. 719–724, 2007.

[92] A. G. Evans, J. Domergue, and E. Vagaggini, "Methodology for Relating the Tensile Constitutive Behavior of Ceramic-Matrix Composites to Constituent Properties," *J. Am. Ceram. Soc.*, vol. 77, no. 6, pp. 1425–35, 1994.

[93] K. Shapovalov, G. M. Jacobsen, L. Alva, N. Truesdale, C. P. Deck, and X. Huang, "Strength of SiCf-SiCm composite tube under uniaxial and multiaxial loading," *J. Nucl. Mater.*, vol. 500, pp. 280–294, 2018.

[94] American Society for Metals. and ASM International. Handbook Committee., *Nondestructive evaluation and quality control*. ASM International, 1989.

[95] T. Whitlow, E. Jones, and C. Przybyla, "In-situ damage monitoring of a SiC/SiC ceramic matrix composite using acoustic emission and digital image correlation," *Compos. Struct.*, vol. 158, pp. 245–251, 2016.

[96] M. Shiwa, O. Y. Chen, T. Kishi, S. Carpenter, S. Mitsuno, H. Ichikawa, *et al.*, "Fracture Mechanisms in Unnotched and Notched SiC/SiC Composites Studied by Acoustic Emission Analysis," *Mater. Trans. JIM*, vol. 36, no. 4, pp. 511–517, 1995.

[97] G. N. Morscher, "Modal acoustic emission of damage accumulation in a woven SiC / SiC composite," *Compos. Sci. Technol.*, vol. 59, no. 5, pp. 687–697, 1999.

[98] M. J. Eaton, R. Pullin, and K. M. Holford, "Acoustic emission source location in composite materials using Delta T Mapping," *Compos. Part A Appl. Sci. Manuf.*, vol. 43, no. 6, pp. 856–863, 2012.

[99] L. Alva, K. Shapovalov, G. M. Jacobsen, C. A. Back, and X. Huang, "Experimental study of thermo-mechanical behavior of SiC composite tubing under high temperature gradient using solid surrogate," *J. Nucl. Mater.*, vol. 466, pp. 698–711, 2015.

[100] J. M. Tracy, "Multi-scale Investigation of Damage Mechanisms in SiC/SiC Ceramic Matrix Composites.," University of Michigan, 2014.

[101] V. P. Rajan, M. N. Rossol, and F. W. Zok, "Optimization of Digital Image Correlation for High-Resolution Strain Mapping of Ceramic Composites," *Exp. Mech.*, vol. 52, no. 9, pp. 1407–1421, 2012.

[102] ASTM, “Standard Guide for Computed Tomography (CT) Imaging,” 100 Barr Harbor Drive, West Conshohocken, PA 19428-2959, United States., 2000.

[103] L. Salvo, P. Cloetens, E. Maire, S. Zabler, J. J. Blandin, J. Y. Buffière, *et al.*, “X-ray micro-tomography: an attractive characterization technique in materials science,” *Nucl. Instruments Methods Phys.*, vol. 200, pp. 273–286, 2003.

[104] J. Banhart, *Advanced tomographic methods in materials research and engineering*. Oxford University Press, 2008.

[105] P. Cloetens, W. Ludwig, J. Baruchel, D. Van Dyck, J. Van Landuyt, J. P. Guigay, *et al.*, “Holotomography: Quantitative phase tomography with micrometer resolution using hard synchrotron radiation x rays,” *Appl. Phys. Lett.*, vol. 75, no. 19, pp. 2912–2914, 1999.

[106] S. R. Stock, F. De Carlo, and J. D. Almer, “High energy X-ray scattering tomography applied to bone.,” *J. Struct. Biol.*, vol. 161, no. 2, pp. 144–50, Feb. 2008.

[107] E. Maire and P. J. Withers, “Quantitative X-ray tomography,” *Int. Mater. Rev.*, vol. 59, no. 1, pp. 1–43, 2014.

[108] M. Drakopoulos, T. Connolley, C. Reinhard, R. Atwood, O. Magdysyuk, N. Vo, *et al.*, “I12: The Joint Engineering, Environment and Processing (JEEP) beamline at Diamond Light Source,” *J. Synchrotron Radiat.*, vol. 22, no. 2015, pp. 828–838, 2015.

[109] S. R. Stock, “X-ray microtomography of materials,” *Int. Mater. Rev.*, vol. 44, no. 4, pp. 141–164, 1999.

[110] S. R. Stock, “Recent advances in X-ray microtomography applied to materials,” *Int. Mater. Rev.*, vol. 53, no. 3, pp. 129–181, 2008.

[111] M. Mostafavi, D. M. Collins, B. Cai, R. Bradley, R. C. Atwood, C. Reinhard, *et al.*, “Yield behavior beneath hardness indentations in ductile metals, measured by three-dimensional computed X-ray tomography and digital volume correlation,” *Acta Mater.*, vol. 82, pp. 468–482, 2015.

[112] B. Yu, R. S. Bradley, C. Soutis, P. J. Hogg, and P. J. Withers, “2D and 3D imaging of fatigue failure mechanisms of 3D woven composites,” *Compos. Part A Appl. Sci. Manuf.*, vol. 77, pp. 37–49, 2015.

[113] B. Yu, R. Blanc, C. Soutis, and P. J. Withers, “Evolution of damage during the fatigue of 3D woven glass-fibre reinforced composites subjected to tension-tension loading observed by time-lapse X-ray tomography,” *Compos. Part A Appl. Sci. Manuf.*, 2015.

[114] P. Potluri, P. Hogg, M. Arshad, D. Jetavat, and P. Jamshidi, “Influence of fibre architecture on impact damage tolerance in 3D woven composites,” *Appl. Compos. Mater.*, vol. 19, no. 5, pp. 799–812, 2012.

[115] J. H. Kinney, T. M. Breunig, T. L. Starr, D. Haupt, M. C. Nichols, S. R. Stock, *et al.*, “X-ray Tomographic Study of Chemical Vapor Infiltration Processing of Ceramic Composites.,” *Science*, vol. 260, no. 5109, pp. 789–792, 1993.

[116] A. Morales-Rodríguez, P. Reynaud, G. Fantozzi, J. Adrien, and E. Maire, “Porosity analysis

of long-fiber-reinforced ceramic matrix composites using X-ray tomography," *Scr. Mater.*, vol. 60, no. 6, pp. 388–390, 2009.

[117] A. Morales-Rodriguez, P. Reynaud, G. Fantozzi, J. Adrien, and E. Maire, "3D-Porosity structural analysis of long -fiber- renforced ceramic matrix composites using X-ray tomography," *13th Eur. Congr. Compos. Mater. Stock.*, vol. 1, no. C, pp. 3–4, 2008.

[118] J. Marrow, C. Reinhard, Y. Vertyagina, L. Saucedo-Mora, D. Collins, and M. Mostafavi, "3D Studies of Damage by Combined X-ray Tomography and Digital Volume Correlation," *Procedia Mater. Sci.*, vol. 3, pp. 1554–1559, 2014.

[119] L. Saucedo-mora, M. Mostafavi, D. Khoshkhou, C. Reinhard, R. Atwood, S. Zhao, *et al.*, "Observation and simulation of indentation damage in a SiC – SiC fi bre ceramic matrix composite," *Finite Elem. Anal. Des.*, vol. 110, pp. 11–19, 2016.

[120] S. Barhli, D. Hollis, B. Wieneke, M. Mostafavi, and T. J. Marrow, "Advanced 2D and 3D Digital Image Correlation of the Full Field Displacements of Cracks and Defects," *ASTM Int.*, vol. Evaluation, 2015.

[121] Y. Vertyagina, M. Mostafavi, C. Reinhard, R. Atwood, and T. J. Marrow, "In situ quantitative three-dimensional characterisation of sub-indentation cracking in polycrystalline alumina," *J. Eur. Ceram. Soc.*, vol. 34, no. 12, pp. 3127–3132, 2014.

[122] B. Pan, K. Qian, H. Xie, and A. Asundi, "Two-dimensional digital image correlation for in-plane displacement and strain measurement: A review," *Meas. Sci. Technol.*, vol. 20, no. 6, 2009.

[123] B. Pan, D. Wu, and Z. Wang, "Internal displacement and strain measurement using digital volume correlation: A least-squares framework," *Meas. Sci. Technol.*, vol. 23, no. 4, 2012.

[124] B. K. Bay, T. S. Smith, D. P. Fyhrie, and M. Saad, "Digital volume correlation: Three-dimensional strain mapping using X-ray tomography," *Exp. Mech.*, vol. 39, no. 3, pp. 217–226, 1999.

[125] T. S. Smith, B. K. Bay, and M. M. Rashid, "Digital volume correlation including rotational degrees of freedom during minimization," *Exp. Mech.*, vol. 42, no. 3, pp. 272–278, 2002.

[126] D. P. Finegan, E. Tudisco, M. Scheel, J. B. Robinson, O. O. Taiwo, D. S. Eastwood, *et al.*, "Quantifying bulk electrode strain and material displacement within lithium batteries via high-speed operando tomography and digital volume correlation," *Adv. Sci.*, vol. 3, no. 3, pp. 1–11, 2015.

[127] K. Madi, G. Tozzi, Q. H. Zhang, J. Tong, A. Cossey, A. Au, *et al.*, "Computation of full-field displacements in a scaffold implant using digital volume correlation and finite element analysis," *Med. Eng. Phys.*, vol. 35, no. 9, pp. 1298–1312, 2013.

[128] S. Roux, J. Réthoré, and F. Hild, "Digital image correlation and fracture: an advanced technique for estimating stress intensity factors of 2D and 3D cracks," *J. Phys. D. Appl. Phys.*, vol. 42, no. 21, p. 214004, 2009.

[129] N. Lenoir, M. Bornert, J. Desrues, P. Be´suelle, and G. Viggiani, "Volumetric Digital Image Correlation Applied to X-ray Microtomography Images from Triaxial Compression Tests

on Argillaceous Rock," *Strain*, vol. 43, pp. 193–205, 2007.

[130] LaVision, "LaVision GmbH, StrainMasterDVC DaVis 8.4," 2018.

[131] G. Tozzi, E. Dall'Ara, M. Palanca, M. Curto, F. Innocente, and L. Cristofolini, "Strain uncertainties from two digital volume correlation approaches in prophylactically augmented vertebrae: Local analysis on bone and cement-bone microstructures," *J. Mech. Behav. Biomed. Mater.*, vol. 67, no. November 2016, pp. 117–126, 2017.

[132] M. Palanca, G. Tozzi, L. Cristofolini, M. Viceconti, and E. Dall'Ara, "Three-Dimensional Local Measurements of Bone Strain and Displacement: Comparison of Three Digital Volume Correlation Approaches," *J. Biomech. Eng.*, vol. 137, no. 7, p. 071006, 2015.

[133] S. A. McDonald, L. C. R. Schneider, A. C. F. Cocks, and P. J. Withers, "Particle movement during the deep penetration of a granular material studied by X-ray microtomography," *Scr. Mater.*, vol. 54, no. 2, pp. 191–196, 2006.

[134] M. Ye, H. M. Sanchez, M. Hultz, Z. Yang, M. Bogorad, A. D. Wong, *et al.*, "Brain microvascular endothelial cells resist elongation due to curvature and shear stress," *Sci. Rep.*, vol. 4, pp. 1–6, 2014.

[135] G. Taubin, "Estimation of planar curves, surfaces, and nonplanar space curves defined by implicit equations with applications to edge and range image segmentation," *IEEE Trans. Pattern Anal. Mach. Intell.*, pp. 1115–1138, 1991.

[136] P. Fenici, A. J. Frias Rebelo, R. H. Jones, A. Kohyama, and L. L. Snead, "Current status of SiC/SiC composites R&D," *J. Nucl. Mater.*, vol. 258–263, no. PART 1 A, pp. 215–225, 1998.

[137] Y. Feng, Z. Feng, S. Li, W. Zhang, X. Luan, Y. Liu, *et al.*, "Micro-CT characterization on porosity structure of 3D Cf/ SiCmcomposite," *Compos. Part A Appl. Sci. Manuf.*, vol. 42, no. 11, pp. 1645–1650, 2011.

[138] Y. Nikishkov, L. Airoldi, and A. Makeev, "Measurement of voids in composites by X-ray Computed Tomography," *Compos. Sci. Technol.*, vol. 89, pp. 89–97, 2013.

[139] Y. Gao, Y. Wang, X. Yang, M. Liu, H. Xia, P. Huai, *et al.*, "Synchrotron X-ray tomographic characterization of CVI engineered 2D-woven and 3D-braided SiCf/SiC composites," *Ceram. Int.*, vol. 42, no. 15, pp. 17137–17147, 2016.

[140] E. S. Pino, A. Y. Abe, and C. Giovedi, "The quest for safe and reliable fuel cladding materials," in *2015 International Nuclear Atlantic Conference - INAC 2015*, 2015.

[141] W. C. ASTM International, "ASTM C1275 - 18 Standard Test Method for Monotonic Tensile Behavior of Continuous Fiber-Reinforced Advanced Ceramics with Solid Rectangular Cross-Section Test Specimens at Ambient Temperature," 2018.

[142] M. K. Ferber, V. J. Tennery, S. B. Waters, and J. Ogle, "Fracture strength characterization of tubular ceramic materials using a simple c-ring geometry," *J. Mater. Sci.*, vol. 21, no. 8, pp. 2628–2632, 1986.

[143] D. L. Shelleman, O. M. Jadaan, J. C. Conway, and J. J. Mecholsky, "Prediction of the

Strength of Ceramic Tubular Components: Part II—Experimental Verification," *J. Test. Eval.*, vol. 19, no. 3, pp. 192–200, 1991.

[144] A. International, "Standard Test Method for Ultimate Strength of Advanced Ceramics with Diametrally Compressed C-Ring Specimens at Ambient Temperature," *C1323 − 10 Stand.*, vol. 96, no. Reapproved, pp. 1–6, 2001.

[145] G. M. Jacobsen, J. D. Stone, H. E. Khalifa, C. P. Deck, and C. A. Back, "Investigation of the C-ring test for measuring hoop tensile strength of nuclear grade ceramic composites," *J. Nucl. Mater.*, vol. 452, no. 1–3, pp. 125–132, 2014.

[146] D. Zhang and D. R. Hayhurst, "Stress–strain and fracture behaviour of 0°/90° and plain weave ceramic matrix composites from tow multi-axial properties," *Int. J. Solids Struct.*, vol. 47, no. 21, pp. 2958–2969, 2010.

[147] A. Macdowell, "X-Ray micro-Tomography,", *International Society for Optics and Photonics*. 2007.

[148] C. Puncreobutr, P. D. Lee, and R. W. Hamilton, "Quantitative 3D Characterization of Solidification Structure and Defect Evolution in Al Alloys Quantitative 3D Characterization of Solidification Structure and Defect Evolution in Al Alloys," no. January 2012, 2014.

[149] B. Cai, S. Karagadde, L. Yuan, T. J. Marrow, T. Connolley, and P. D. Lee, "In situ synchrotron tomographic quantification of granular and intragranular deformation during semi-solid compression of an equiaxed dendritic Al–Cu alloy," *Acta Mater.*, vol. 76, pp. 371–380, Sep. 2014.

[150] S. Titarenko, P. J. Withers, and A. Yagola, "An analytical formula for ring artefact suppression in X-ray tomography," *Appl. Math. Lett.*, vol. 23, no. 12, pp. 1489–1495, 2010.

[151] E. Vagaggini, J.-M. M. Domergue, and A. G. Evans, "Relationships between Hysteresis Measurements and the Constituent Properties of Ceramic Matrix Composites: I, Theory," *J. Am. Ceram. Soc.*, vol. 78, no. 10, pp. 2709–2720, Oct. 1995.

[152] K. Hironaka, T. Nozawa, T. Hinoki, N. Igawa, Y. Katoh, L. L. Snead, *et al.*, "High-temperature tensile strength of near-stoichiometric SiC/SiC composites," *J. Nucl. Mater.*, vol. 307–311, no. 2 SUPPL., pp. 1093–1097, 2002.

[153] J. El Yagoubi, J. Lamon, J. C. Batsale, J. Dhote, and M. Le Flem, "Multiscale Thermal Characterization of Mechanically Loaded Ceramic Matrix Composite: Estimation of Thermal Diffusivity at Micro/Mesoscale," *Exp. Mech.*, vol. 55, no. 4, pp. 783–794, 2015.

[154] P. J. Withers, "3D crack-tip microscopy: Illuminating micro-scale effects on crack-tip behavior," *Adv. Eng. Mater.*, vol. 13, no. 12, pp. 1096–1100, 2011.

[155] R. O. Ritchie, "Mechanisms of fatigue-crack propagation in ductile and brittle solids," *Int. J. Fract.*, vol. 100, pp. 55–83, 1999.

[156] K. T. V. Rao, W. O. Soboyejo, and R. O. Ritchie, "Ductile-phase toughening and Fatigue-Crack Growth in Nb-Reinforced Molybdenum Disilicide Intermetallic Composites," *Metall. Trans. A*, vol. 23, no. 8, pp. 2249–2257, 1992.

[157] G. N. Morscher, “Stress-dependent matrix cracking in 2D woven SiC-fiber reinforced melt-infiltrated SiC matrix composites,” *Compos. Sci. Technol.*, vol. 64, no. 9, pp. 1311–1319, 2004.

[158] V. Mazars, O. Caty, G. Couégnat, A. Bouterf, S. Roux, S. Denneulin, *et al.*, “Damage investigation and modeling of 3D woven ceramic matrix composites from X-ray tomography in-situ tensile tests,” *Acta Mater.*, vol. 140, pp. 130–139, 2017.

[159] R. Naslain, A. Guette, F. Rebillat, S. Le Gallet, F. Lamouroux, L. Filipuzzi, *et al.*, “Oxidation mechanisms and kinetics of SiC-matrix composites and their constituents,” *J. Mater. Sci.*, vol. 39, no. 24, pp. 7303–7316, 2004.

[160] L. Filipuzzi, G. Camus, and R. Naslain, “Oxidation Mechanisms and Kinetics of 1 D-SiC/C/SiC Composite Materials: I, An Experimental Approach,” *J. Am. Ceram. Soc.*, vol. 47, no. 2, pp. 459–466, 1994.

[161] Y. Gowayed, G. Ojard, R. Miller, U. Santhosh, J. Ahmad, and R. John, “Correlation of elastic properties of melt infiltrated SiC/SiC composites to in situ properties of constituent phases,” *Compos. Sci. Technol.*, vol. 70, no. 3, pp. 435–441, 2010.

[162] G. N. Morscher, “Tensile Stress Rupture of SiC f/SiCm Minicomposites with Carbon and Boron Nitride Interphases at Elevated Temperatures in Air,” *J. Am. Ceram. Soc.*, vol. 42, no. 8, pp. 2029–2042, 1997.

[163] M. N. Rossol, V. P. Rajan, and F. W. Zok, “Effects of weave architecture on mechanical response of 2D ceramic composites,” *Compos. Part A Appl. Sci. Manuf.*, vol. 74, pp. 141–152, 2015.

[164] K. Mosley, “The stressing for test purposes of materials in tubular form using elastomeric inserts—experimental and theoretical development,” *Arch. Proc. Inst. Mech. Eng. 1847-1982 (vols 1-196)*, vol. 196, no. 1982, pp. 123–139, Dec. 1982.

[165] R. A. Jaramillo, W. R. Hendrich, and N. H. Packan, *Tensile Hoop Behavior of Irradiated Zircaloy-4 Nuclear Fuel Cladding*, no. December. OAK RIDGE NATIONAL LABORATORY Oak Ridge, Tennessee 37831-6283, 2006.

[166] M. N. Gussev, T. S. Byun, Y. Yamamoto, S. A. Maloy, and K. A. Terrani, “In-situ tube burst testing and high-temperature deformation behavior of candidate materials for accident tolerant fuel cladding,” *J. Nucl. Mater.*, vol. 466, pp. 417–425, 2015.

[167] H. Jiang and J. A. J. Wang, “Methodology for mechanical property testing of fuel cladding using an expanding plug wedge test,” *J. Nucl. Mater.*, vol. 446, no. 1–3, pp. 27–37, 2014.

[168] T. S. Byun, E. Lara-Curzio, R. A. Lowden, L. L. Snead, and Y. Katoh, “Miniaturized fracture stress tests for thin-walled tubular SiC specimens,” *J. Nucl. Mater.*, vol. 367–370 A, no. SPEC. ISS., pp. 653–658, 2007.

[169] J. A. J. Wang and H. Jiang, *Methodology for mechanical property testing of fuel cladding using an expanding plug wedge test*, vol. ORNL/TM-20, no. U.S. DEPARTMENT OF ENERGY under contract DE-AC05-00OR22725. 2013.

[170] P. H. Mott and C. M. Roland, “Limits to Poisson’s ratio in isotropic materials,” *Phys. Rev.*

B, vol. 80, no. 13, p. 132104, Oct. 2009.

[171] B. Münch, P. Trtik, F. Marone, and M. Stampanoni, "Stripe and ring artifact removal with combined wavelet-Fourier filtering," *Opt. Soc. Am.*, vol. 17, no. 2009–2010, pp. 34–35, 2009.

[172] K. Shoemake, "Animating rotation with quaternion curves," *ACM SIGGRAPH Comput. Graph.*, vol. 19, no. 3, pp. 245–254, 1985.

[173] H. R. Hamidzadeh and R. N. Jazar, *Vibrations of Thick Cylindrical Structures*. Boston, MA: Springer US, 2010.

[174] ASTM C1819-15, "Standard Test Method for Tensile Hoop Strength of Continuous Fiber-Reinforced Advanced Ceramic Tubular Specimens at Ambient Temperatures Using Elastomeric Insert," *ASTM Int. West Conshohocken, PA*, pp. 1–17, 2015.

[175] F. W. Zok and S. M. Spearing, "Matrix crack spacing in brittle matrix composites," *Acta Metall. Mater.*, vol. 40, no. 8, pp. 2033–2043, Aug. 1992.

[176] M. Blacklock, J. H. Shaw, F. W. Zok, and B. N. Cox, "Virtual specimens for analyzing strain distributions in textile ceramic composites," *Compos. Part A Appl. Sci. Manuf.*, vol. 85, pp. 40–51, 2016.

[177] B. N. Cox, H. A. Bale, M. Begley, M. Blacklock, B.-C. Do, T. Fast, *et al.*, "Stochastic Virtual Tests for High-Temperature Ceramic Matrix Composites," *Annu. Rev. Mater. Res.*, vol. 44, no. 1, pp. 479–529, 2014.

[178] J. H. Panchal, S. R. Kalidindi, and D. L. McDowell, "Key computational modeling issues in Integrated Computational Materials Engineering," *CAD Comput. Aided Des.*, vol. 45, no. 1, pp. 4–25, 2013.

[179] F. Roters, P. Eisenlohr, L. Hantcherli, D. D. Tjahjanto, T. R. Bieler, and D. Raabe, "Overview of constitutive laws, kinematics, homogenization and multiscale methods in crystal plasticity finite-element modeling: Theory, experiments, applications," *Acta Mater.*, vol. 58, no. 4, pp. 1152–1211, 2010.

[180] R. K. Nalla, J. H. Kinney, and R. O. Ritchie, "Mechanistic fracture criteria for the failure of human cortical bone," *Nat. Mater.*, vol. 2, no. 3, pp. 164–168, 2003.

[181] R. Talreja, "Multi-scale modeling in damage mechanics of composite materials," *J. Mater. Sci.*, vol. 41, no. 20, pp. 6800–6812, 2006.

[182] A. Turon, C. G. Dávila, P. P. Camanho, and J. Costa, "An engineering solution for mesh size effects in the simulation of delamination using cohesive zone models," *Eng. Fract. Mech.*, vol. 74, no. 10, pp. 1665–1682, Jul. 2007.

[183] A. Carpinteri and G. Colombo, "Numerical analysis of catastrophic softening behaviour (snap-back instability)," *Comput. Struct.*, vol. 31, no. 4, pp. 607–636, 1989.

[184] H. Talebi, M. Silani, S. P. a Bordas, P. Kerfriden, and T. Rabczuk, "A computational library for multiscale modeling of material failure," *Comput. Mech.*, vol. 53, no. 5, pp. 1047–1071, 2014.

[185] E. Weinan, “Principles of Multiscale Modeling,” *Phys. Today*, p. 510, 2011.

[186] J. Fish and Z. Yuan, “Multiscale enrichment based on partition of unity,” *Int. J. Numer. Methods Eng.*, vol. 62, no. 2, pp. 1341–1359, 2005.

[187] A. Shterenlikht and I. C. Howard, “The CAFE model of fracture - Application to a TMCR steel,” *Fatigue Fract. Eng. Mater. Struct.*, vol. 29, no. 9–10, pp. 770–787, 2006.

[188] J. Segurado, C. González, and J. LLorca, “A numerical investigation of the effect of particle clustering on the mechanical properties of composites,” *Acta Mater.*, vol. 51, no. 8, pp. 2355–2369, 2003.

[189] H. J. Böhm, A. Eckschlager, and W. Han, “Multi-inclusion unit cell models for metal matrix composites with randomly oriented discontinuous reinforcements,” *Comput. Mater. Sci.*, vol. 25, no. 1–2, pp. 42–53, 2002.

[190] K. Runesson, P. Steinmann, M. Ekh, A. Menzel, and F. Larsson, “Homogenized Material Properties,” *Const. Model. Eng. Mater. – Theory Comput. Vol. I. Gen. Concepts Inelasticity*, vol. 1, pp. 339–364, 2011.

[191] T. Kanit, S. Forest, I. Galliet, V. Mounoury, D. Jeulin, M.-S. Kang, *et al.*, “Determination of the size of the representative volume element for random composites: statistical and numerical approach,” *Int. J. Solids Struct.*, vol. 40, no. 13–14, pp. 3647–3679, 2003.

[192] V. Uthaisangsuk, U. Prahl, and W. Bleck, “Stretch-flangeability characterisation of multiphase steel using a microstructure based failure modelling,” *Comput. Mater. Sci.*, vol. 45, no. 3, pp. 617–623, 2009.

[193] N. Moës and T. Belytschko, “Extended finite element method for cohesive crack growth,” *Eng. Fract. Mech.*, vol. 69, no. 7, pp. 813–833, 2002.

[194] R. C. Yu, L. Saucedo, and G. Ruiz, “Finite-element study of the diagonal-tension failure in reinforced concrete beams,” *Int. J. Fract.*, vol. 169, no. 2, pp. 169–182, 2011.

[195] M. Ortiz and A. Pandolfi, “Finite-deformation irreversible cohesive elements for three-dimensional crack-propagation analysis,” *Int. J. Numer. Methods*, vol. 44, no. 9, pp. 1267–1282, 1999.

[196] J. Oliver, A. E. Huespe, and P. J. Sánchez, “A comparative study on finite elements for capturing strong discontinuities: E-FEM vs X-FEM,” *Comput. Methods Appl. Mech. Eng.*, vol. 195, no. 37–40, pp. 4732–4752, 2006.

[197] A. Chakraborty and S. Rahman, “Stochastic multiscale models for fracture analysis of functionally graded materials,” *Eng. Fract. Mech.*, vol. 75, no. 8, pp. 2062–2086, 2008.

[198] L. Saucedo, M. Mostafavi, D. Khoshkhou, C. Reinhard, R. Atwood, S. Zhao, *et al.*, “3D cellular automata finite element (CAFE) modelling and experimental observation of damage in quasi-brittle nuclear materials: Indentation of a SiC-SiCfibre ceramic matrix composite,” *Smins-3*, vol. c, 2013.

[199] C. A. Gandin, J. L. Desbiolles, M. Rappaz, and P. Thévoz, “A three-dimensional cellular automaton-finite element model for the prediction of solidification grain structures,” *Metall.*

Mater. Trans. A Phys. Metall. Mater. Sci., vol. 30, no. 12, pp. 3153–3165, 1999.

[200] L. Saucedo-Mora and T. James Marrow, "Method for the explicit insertion of microstructure in Cellular Automata Finite Element (CAFE) models based on an irregular tetrahedral Finite Element mesh: Application in a multi-scale Finite Element Microstructure MEshfree framework (FEMME)," *Finite Elem. Anal. Des.*, vol. 105, pp. 56–62, 2015.

[201] L. Saucedo-Mora and T. J. Marrow, "FEMME: A multi-scale Finite Element Microstructure MEshfree fracture model for quasi-brittle materials with complex microstructures," *Eng. Fract. Mech.*, vol. 147, pp. 355–372, 2015.

[202] R. Hill, "On the micro-to-macro transition in constitutive analyses of elastoplastic response at finite strain," *Math. Proc. Cambridge Philos. Soc.*, vol. 98, no. 3, pp. 579–590, 1985.

[203] A. Doitrand, C. Fagiano, F. X. Irisarri, and M. Hirsekorn, "Comparison between voxel and consistent meso-scale models of woven composites," *Compos. Part A Appl. Sci. Manuf.*, vol. 73, pp. 143–154, 2015.

[204] L. Saucedo-Mora and T. J. Marrow, "Multi-scale damage modelling in a ceramic matrix composite using a finite-element microstructure meshfree methodology," *Philos. Trans. R. Soc. A Math. Phys. Eng. Sci.*, vol. 374, no. 2071, p. 20150276, 2016.

[205] D. T. Lee and B. J. Schachter, "Two algorithms for constructing a Delaunay triangulation," *Int. J. Comput. Inf. Sci.*, vol. 9, no. 3, pp. 219–242, 1980.

[206] U. Ayachit, *The ParaView Guide: A Parallel Visualization Application*. USA: Kitware, Inc., 2015.

[207] S. Bertrand, R. Pailler, and J. Lamon, "Influence of Strong Fiber/Coating Interfaces on the Mechanical Behavior and Lifetime of Hi-Nicalon/(PyC/SiC)n/SiC Minicomposites," *J. Am. Ceram. Soc.*, vol. 84, no. 4, pp. 787–794, 2001.

[208] P. J. Withers, "X-ray nanotomography," *Mater. Today*, vol. 10, no. 12, pp. 26–34, 2007.

[209] Y. Zayachuk, D. Armstrong, S. Roberts, and P. Hosemann, "Room temperature and high temperature micromechanical testing of SiC- SiC fiber composites for nuclear fuel cladding applications," *dc.engconfintl.org*, 2017.